Experimental and numerical study on heat transfer and pressure drop during mPCM slurry flow in microchannels

A thesis submitted by

Rabia Shaukat

in part fulfilment of the requirements for the degree of

Doctor of Philosophy

in the

School of Engineering and Material Science

Queen Mary University of London

Mile End Road

London, E1 4NS

UK

(2015)

Dedicated to my husband

Mr. Muhammad Asif

Declarations

I, Rabia Shaukat, confirm that the research included within this thesis is my own work or that where it has been carried out in collaboration with, or supported by others, that this is duly acknowledged below and my contribution indicated. Previously published material is also acknowledged below.

I attest that I have exercised reasonable care to ensure that the work is original, and does not to the best of my knowledge break any UK law, infringe any third party's copyright or other Intellectual Property Right, or contain any confidential material.

I accept that the College has the right to use plagiarism detection software to check the electronic version of the thesis.

I confirm that this thesis has not been previously submitted for the award of a degree by this or any other university.

Print Name: Rabia Shaukat

Signature:

Date:

Abstract

Microencapsulated phase change material (mPCM) slurries have been used as the working fluids for enhancement of convective heat transfer, thermal energy storage and thermal energy transport due to their high latent heat and almost constant temperature during the change of phase between liquid and solid. This project aimed at investigating experimentally and numerically heat transfer and pressure drop characteristics during mPCM slurry flow in microchannels.

A test rig has been designed and built. The test section consists of six microchannels of length 500 mm, width 1 mm and height 1.5 mm, machined inside the aluminum blocks. Local surface temperature and local heat flux along the channel were determined, from temperatures measured at 98 precisely-known locations in the aluminum blocks, by the inverse solution of the two-dimensional (2-D) heat conduction (Yu et al. (2014)).

Experiments were performed using pure water to validate the experimental setup and the data are also used for comparison with mPCM slurry. For mPCM slurry, experiments were conducted at mass concentrations of 5% and 10%, with Reynolds number ranging from 340 to 1800. The effects of mass concentration on local surface temperature, local heat flux, local Nusselt number, average Nusselt number, bulk temperature rise and pressure drop, were investigated. Moreover, the effect of Stefan number on heat transfer performance of mPCM slurry flow was also investigated. The average Nusselt numbers at Re = 1200 for 5% and 10% mass concentrations were 12.1% and 28.3% higher than those of pure water, respectively. For the same heat transfer rate of 400 W, the fluid temperature rise was found to be 1.03 K and 2.68 K lower at mass concentrations of 5% and 10% as compared to water. The pressure drop for mPCM slurry was found to be

lower at same heat transfer rate than pure water. An empirical correlation was also developed and all experimental data can be predicted within ±15%.

Moreover, numerical simulations of three-dimensional conjugated heat transfer during the melting and freezing of mPCM slurry flow in microchannels were carried out. Numerical model was validated with experimental data and found to be in a good agreement within maximum 15%. The bulk temperature rise in case of mPCM slurry was lower than that of pure water. Furthermore, the delay in thermal boundary layer development was observed for mPCM slurry.

Numerical simulations of three-dimensional conjugated heat transfer of mPCM slurry in microchannel heat sink was performed. The effects of geometrical parameters including height and width of separating wall of the channel on surface temperature, bulk temperature, thermal resistance and heat transfer rate were investigated. The numerical results show that: (i) increase in width from 1.2 to 4.0 resulted in 38.5%, 48%, 41% and 51% increase in surface temperature, bulk temperature, thermal resistance and heat transfer rate, respectively, (ii) Increase in height shows more uniform surface temperature. Furthermore, the effect of circular, square and rectangular cross sectional shapes of channel on heat transfer and pressure drop was examined. It is found that the rectangular shape showed 67% lower thermal resistance but circular shape transferred 62% more heat per unit pumping power.

Keywords: Microencapsulated phase change material, Slurry, Microchannel, Heat transfer, Heat sink, Inverse heat conduction, Latent heat, Thermal Energy storage, Air conditioning, Refrigeration, Electronics cooling.

Acknowledgements

First of all I would like to thanks Allah Almighty for giving me strength and courage to complete this task. I wish to express my sincere thanks to Dr Hua Sheng Wang for his kind supervision throughout the duration of project. This project would have been not possible without his continuous support, encouragement and guidance.

I am really grateful to Dr. Lei Chai and Dr. Jei Sun for providing me the assistance, academic discussions and suggestions about my project. I am also very obliged to Dr. Muhammad Sajid Kamran, Saqib Raza Jivani for their help during the experiments. Saima and Tabinda, for being very encouraging friends through thick and thin. I would also like to acknowledge Dennis Ife, Mike Collins, Roger Nelson and Jun Ma for their help in building and maintenance of the experimental setup.

I am also very grateful to my family especially parents, siblings, mother in law, father in law, sister in laws, brother in law, my husband Asif for their affection and emotional support throughout this period. I am highly obliged to them for taking care of my children during this duration.

Finally, I would like to acknowledge University of Engineering and Technology, Lahore, Pakistan and Higher Education Commission of Pakistan for providing PhD studentship. Moreover, EU research grant FP7-2010-IRSES-269205 and EPSRC research grant EP/L001233/1 are gratefully acknowledged.

Contents

Nomenclature

A_c	Cross-sectional area of microchannel
a	Short side of rectangular cross-section
b	Long side of rectangular cross-section
c	Mass concentration of mPCM slurry, %
C	Specific heat capacity, J/kgK
D	Diameter of microchannel
D_h	Hydraulic diameter of microchannel
h	Heat transfer coefficient
h_{fg}	Latent heat of phase change
k	Thermal conductivity, W/m K
L	Length of microchannel
L_1	Length of solid region
L_2	Length of phase change region
L_3	Length of liquid region
m	Mass flow rate
n	Number of microchannels
ΔP	Pressure drop over the length of microchannel

q_w	Heat flux at wall
Q	Heat transfer rate
R	Radius of circular channel
R_{th}	Thermal resistance, K/W
T	Temperature, K
T_1	Start point at which phase change begins
T_2	End point at which phase change completes
T_{max}	Maximum temperature at top surface of the heat sink
U	Velocity in x-direction
V	Velocity in y-direction
w	Velocity in z-direction

Abbreviations

CFD	Computational fluid dynamics
CST	Constant surface temperature
CHF	Constant heat flux
FD	Fully developed flow
PAO	Poly-alpha-olefin
SEM	Scanning electron microscope

mPCM	Microencapsulated phase change material
NEPCM	Nanoencapsulated phase change material

Greek letters

α	Aspect ratio, b/a
φ	Volumetric concentration of phase change particles
θ	Dimensionless temperature
ρ	Density, kg/m^3
μ	Dynamic viscosity, kg/m s
λ	Heat transfer enhancement (%)

Subscripts

b	Bulk fluid (mPCM slurry)
i	Inlet
o	Outlet
f	Working fluid
p	Particles of phase change material
s	Wall of heat sink
w	Water
h	Hot water

Dimensionless numbers

Nu	Nusselt number, hD_h/k
Pr	Prandtl number, $C_b\mu_b/k_b$
Re	Reynolds number,$\rho_b v D_h/\mu_b$
Ste	Stefan number, q/mh_{fg} – *1*
z^+	Dimensionless axial length, *(z/rRePr)*

List of Figures

List of Tables

Chapter 1

Introduction

Rapid increase in world energy consumption has raised issues of exhaustion of non-renewable energy resources and environmental impacts (greenhouse gases, ozone depletion, adverse climatic changes, etc.). In developed countries buildings sector, both residential and commercial, consumes 20% to 40% of the total energy consumption. This demand will continue to increase in near future due to growing population, and demand for building services. Improvement in building energy design, thermal energy storage devices and use of renewable energy resources has the potential to make a major contribution to reduce the dependency on fossil fuels (Pérez-Lombard et al. (2008).

Moreover, due to advancement in technology, emerging electronic devices are becoming smaller in sizes. One of the major issues with the design of these smaller devices is the high heat removal and maintaining them at safe operating temperature. Current cooling technologies of air cooling, water cooling, heat pipes, thermoelectric cooling have reached to their limits of cooling (Song et al. (2013b)). Therefore, there is a need to explore more efficient innovative cooling technologies. Microchannel heat exchangers, compact in size and very high in efficiency, can play an important role in these applications.

Microencapsulated phase change material (mPCM) slurries as heat transfer fluid in microchannels have attracted the attention owing to their higher heat absorption capability. The potential benefits of mPCM slurry are high heat absorption during phase

change and increase of the effective thermal conductivity due to more particle-particle and particle to fluid interaction.

Earlier experimental and numerical studies on heat transfer characteristics of mPCM slurry showed enhanced convective heat transfer as compared to pure water, leading to compact thermal energy storage system, and reduced pumping power. Experimental and numerical studies are available for analysing the heat transfer characteristics of mPCM slurry. A few experimental studies have been found for evaluating the heat transfer performance of mPCM slurry in microchannels. All of these studies were carried out under constant heat flux boundary condition. In practical applications, the local surface heat flux varies along the flow direction of the channel. Therefore, investigations are needed for the case under the convective boundary condition. To the author's knowledge, literature survey shows that no experimental study has been reported for analysing the heat transfer parameters under convective boundary condition. In the present investigation, convective boundary condition is considered for heat transfer of mPCM slurry flow in microchannels.

In earlier experimental studies of mPCM slurry flow in microchannels, heat transfer performance of mPCM slurry is obtained by measuring the overall heat transfer rate. No experimental data have been reported for obtaining the local heat transfer behaviour of mPCM slurry flow in microchannels. Examining the local heat transfer characteristics makes it possible to identify the melting and solidifying states of mPCM slurry along the microchannel. This enables the analysis of mechanisms during the melting and solidifying and enhancement of the solid-liquid phase change heat transfer. This study was therefore motivated to design and build a test rig to provide accurate local heat transfer measurements. The local surface temperature and local heat flux along the microchannel are determined from temperatures measured at 98 precisely known locations by the

inverse solution of 2-D heat conduction equation (Yu et al. (2014)) and linear fittings. An empirical correlation has been developed to predict the heat transfer characteristics of mPCM slurry under convective boundary condition based on the experimental data obtained.

Numerical simulation is a reliable and cost effective method and able to investigate a wide range of different parameters. Numerical simulations of three-dimensional conjugated heat transfer analysis of entire geometry of the test section has been carried out to examine the melting and freezing of mPCM slurry flow in microchannels. Numerical results are compared with experimental data.

Heat conduction through wall plays an important role in heat transfer of microchannel heat sink. Few numerical studies have considered the effect of wall heat conduction on heat transfer of mPCM slurry flow in microchannel heat sinks. The effects of thickness and height of separating wall of the microchannel on thermal performance of heat sink have not been investigated. Moreover, the previous studies (Dammel and Stephan (2011), Rao et al. (2007), Ho et al. (2013), Sabbah et al. (2008), and Kuravi et al. (2009)) were conducted for mPCM slurry in rectangular microchannels. In the present study, effects of different geometrical shapes (square, circular and rectangular) of microchannel on thermal and hydraulic performance on heat sinks are also numerically investigated.

1.1 Thesis overview

The mPCM slurry has attracted much attention during the past decade because of its higher latent heat and almost constant temperature during its phase change from solid to liquid or vice versa. The current study involves both the experimental and numerical investigation. A test rig has been designed and built to provide the accurate local heat transfer characteristics of mPCM slurry flow in microchannels. Experiments have been

conducted on pure water and mPCM slurry of mass concentration 5% and 10%. Numerically, commercially available software FLUENT has been used to predict the melting and solidification characteristics of mPCM slurry flow in microchannels. Furthermore, the effects of geometrical parameters on heat transfer and pressure drop have been investigated.

To achieve the overall objectives, following sub-objectives were accomplished.

1.1.1 Experimental investigation

The objectives of this part includes:

1. To design and build a test rig to provide accurate local heat transfer measurements for mPCM slurry flow in microchannels.

2. To obtain data for heat transfer and pressure drop characteristics of pure water for the purpose of validity and comparison.

3. To obtain data for local heat transfer and pressure drop characteristic of mPCM slurry at mass concentrations of 5% and 10% for mass flow rates ranging from 4.9g/s to 10.7g/s.

4. To compare new data with the data available in literature.

5. To further investigate the effects of mass concentration of mPCM slurry on local surface temperature, local heat flux, local Nusselt number, Stefan number, bulk temperature rise and pressure drop.

6. To investigate the surface morphology of mPCM slurry before and after the experiments.

7. To develop a prediction method for laminar mPCM slurry flow in microchannel under the convective boundary condition.

1.1.2 Numerical Investigation

Compared with experiment, numerical simulation is a reliable and cheap method and able to investigate a wide range of different parameters. The numerical simulations will include:

1.1.2.1 Numerical simulation of test section to examine mechanisms inside the test section

1. To perform numerical simulation of three dimensional heat conduction for the entire geometry of the test section.

2. To investigate the mechanisms under different boundary conditions of constant heat flux and constant surface temperature.

1.1.2.2 Numerical simulation of heat transfer characteristics during melting and freezing of mPCM slurry flow in microchannels

Numerical study is chosen for the analysis of heat transfer characteristics during freezing and melting of mPCM slurry flow in microchannels. The objectives of this part includes:

1. To numerically simulate three dimensional conjugated heat transfer of entire geometry of the test section.

2. To validate the numerical model with fanning friction factor correlations available.

3. To compare numerical results with present experimental data.

4. To examine the mechanisms during the melting and solidification of mPCM slurry flow in microchannel.

1.1.2.3 Numerical investigation of mPCM slurry flow in microchannel heat sink

Owing to very small size of microchannels, wall conduction plays very important role in heat transfer of the heat sinks. Numerical simulations of three-dimensional conjugated heat transfer will be conducted to analyse the enhanced heat transfer performance.

The objectives of this part includes:

1. To analyse the effects of mass concentration, inlet temperature of mPCM slurry and Stefan number on the heat transfer performance of mPCM slurry.
2. To analyse the effects of height and width of separating wall of microchannel and cross sectional shape of microchannel on the heat transfer performance of heat sink.

The thesis is structured as follows. Chapter 1 illustrates the introduction, and aim and objectives. The Chapter 2 includes the detailed literature review of manufacturing, applications and heat transfer and pressure drop of mPCM slurry in macro and microchannel. Chapter 3 describes the test rig, test section and experiment methodology. Data processing for experimental and numerical investigations have been covered in Chapter 4. Experimental results for pure water and mPCM slurry are presented in Chapter 5 and 6 respectively.

Numerical simulation of 3D conjugated heat transfer of pure water in entire geometry of aluminium test blocks are discussed in Chapter 7. The melting and freezing characteristics of mPCM slurry flow in microchannels have been numerically investigated in Chapter 8 and 9 respectively. The parametric study of geometrical effects of microchannel shape and separating wall have been discussed in Chapter 10. The conclusions and future work have been complied in Chapter 11.

Chapter 2

Literature Review

2.1 Phase change materials

Phase change materials (PCMs) have attracted the attention of researchers and scientists because of their capability to store more energy due to high latent heat. PCMs absorb and release energy during their phase change at a constant temperature. As compared to the sensible thermal energy storage systems, PCMs have much higher energy densities. This chapter provides an extensive literature review about the types, formation, thermophysical properties, applications, heat transfer and pressure drop characteristics of mPCM slurry.

PCMs are mainly classified into two groups: organic and inorganic materials. A wide range of PCMs, their properties and applications are reviewed by Zalba et al. (2003). The advantages and disadvantages of the organic and inorganic materials are highlighted in Table 2.1.

Table 2.1 Comparison of organic and inorganic materials for thermal energy storage (Zalba et al. (2003))

Organics	**Inorganics**
Advantages	Advantages
Non corrosives	Greater phase change enthalpy
Low or none undercooling	
Chemical and thermal stability	
Disadvantages	Disadvantages
Lower phase change enthalpy	Undercooling
Low thermal conductivity	Corrosion
Inflammability	Phase separation
	Lack of thermal stability

2.2 Selection of PCM

Following are key parameters that are generally considered for the selection of PCMs for any application (Mehling and Cabeza (2008)).

1. Phase change temperature:

   A suitable phase change temperature depends on the temperature of heat source/sink.

2. Latent heat of phase change:

   A large latent heat is desired.

3. Cycling stability of the PCM particles:

   This maintains the performance of the PCM particles for a sufficiently long period of time required.

4. Subcooling:

   No subcooling or small subcooling is desired.

5. High thermal conductivity:

   A high thermal conductivity enhances the heat transfer during charging and discharging.

6. Volume change during phase change:

   A low volume change during phase change is desired.

Paraffin has been widely used as PCM because of its stable chemical, thermal properties and low cost. A wide range of its melting temperature from -57 ºC to80 ºC makes paraffin attractive for many applications (Chen et al. (2014)).

2.3 Types of PCM slurries

PCM slurry is a fluid that mixes PCMs (e.g. PCM particles) in a carrier fluid (e.g. water). PCM slurries can be used to easily transport thermal energy with both the latent heat of the PCM and sensible heat of carrier fluid. There are five types of PCM slurries.

i) Ice slurry

Ice slurry is a mixture of ice crystals, water and additive like salt, alcohol or glycol. These additives are used to lower the melting point. Currently, ice slurries are widely used on industrial and commercial level. The application of ice slurry is limited due to its melting point.

ii) Clathrate hydrate slurry

In these slurries, a special molecular structure is formed and decomposed by heating and cooling of aqueous solution. The heat is associated with formation and breakdown of molecular structure.

iii) Phase change emulsion

PCMs are directly mixed into the carrier fluid. This type of slurry can cause the agglomeration and clogging of pipes. Surfactants are added into mixture to reduce the clogging.

iv) Shape stabilized slurry

PCMs are soaked into the polyethylene and then dispersed into the carrier fluid.

v) Microencapsulated PCM slurry

This is a more advanced form of PCM slurry. PCMs are encapsulated in polymer shells to form microencapsulated phase change materials (mPCM). Formation of mPCM is illustrated in Section 2.4. These microcapsules are dispersed into carrier fluid. The mPCM have many benefits over traditional PCM slurries. The mPCM have more convective heat transfer due to particle-particle and particle-fluid interaction. The mPCM slurries are more stable and have low volume expansion during the change of phase. The encapsulation of PCMs decreases the potential of agglomeration and clogging. On the other hand, mPCM are expensive and may leak from shells due to shear force of pumping.

2.4 Formation of mPCM

The mPCMs are microcapsules having core PCM inside the polymer shell. The selection of core PCM depends on the application. There are some requirements for the shell as well: the shell material should be elastic, able to stand required temperature and pump shear force and to seal tightly (Chen et al. (2014)). There are many methods available for the production of mPCM. A detailed review about the different methods available for the production of mPCM has been given by Jamekhorshid et al. (2014). The production methods are mainly classified into three categories.

i. Physical methods

ii. Physical-chemical methods

iii. Chemical methods

2.4.1 Physical methods

Physical methods include spray dying, spray cooling, air suspension coating, solvent evaporation, vibrational nozzle and centrifugal extrusion. In these methods, shell polymer

is applied to core PCM by mechanical means. These methods cannot produce microcapsules of size smaller than 100μm.

2.4.2 Physical chemical methods

These methods produce solid and stable particles. Advantages and disadvantages of different manufacturing methods are summarized by Jamekhorshid et al. (2014). Chemical methods include in situ polymerization, interfacial polymerization, coacervation and cross link method. The In situ polymerization is the most common method used for manufacturing of microencapsulated particles. It produces particles in range of 5-100μm. Different methods have different impacts on the size and morphology of mPCM. Increase in speed of the mixer produces more uniform and smaller particles. Different shell materials produce different shapes. Higher polymerization temperature produces better morphology. There should be appropriate proportion of shell and core materials. The lower quality shell may cause leakage of PCM and results in clogging of the system. On the other hand, thick shells may cause higher thermal resistance.

2.5 Problems of mPCM slurry

There are certain problems associated with mPCM. These are subcooling, durability and stability of mPCM particles.

2.5.1 Subcooling

Subcooling is the phenomenon that delays the freezing point of mPCM particles. This phenomenon is mostly common in mPCM particles of size smaller than 100μm. Nucleating agents are usually added to mPCM particles as catalyst to increase the crystallization. These nucleating agents affect the morphology and concentration of mPCM particles. A new method has been introduced by Cao and Yang (2014) for

minimizing subcooling effect by optimizing the composition of resin shell. They managed to reduce the subcooling while maintaining the specific heat capacity of paraffin.

2.5.2 Durability and stability

Another major issue regarding the mPCM particles is their durability and stability. The continuous pumping of mPCM particles cause the rupture of shells. This will result in clogging of pipes and a further rise in pumping power.

2.5.3 Agglomeration

The separation of mPCM particles and base fluid (e.g. water) is also one of the major shortcoming of mPCM slurry. The continuous stirring of the mPCM slurry diminishes this effect.

2.6 Applications of PCM

PCMs are widely used in textile, space heating and cooling (thermal energy storage) device, microelectronics etc. (Mehling and Cabeza (2008))

1. In textile industries, mPCMs are incorporated into the inner side of garments to improve the thermo-regulating properties of garments. PCMs are also used in aerospace textile to protect astronauts from extreme weather conditions in space. They are also widely used in blankets, medical garments, insulation etc.

2. Space cooling: For keeping space cool, the temperature should not be raised above the certain level. This could be achieved in three ways, improving heat rejection from space, reducing temperature fluctuations, and reducing heat input to the space. Space cooling can be achieved by three natural cooling methods: (i) by utilizing lower night ambient temperature, (ii) by rejecting heat to the ground, (iii)

by rejecting heat to latent heat storage system. These natural cooling methods are efficient because of no power consumption but they are dependent on ambient conditions. .

3. Space heating: Space heating is to keep the temperature within thermal comfort zone range. This could be achieved in three ways, by reducing temperature fluctuations, minimizing heat loss and by supplying heat if the temperature falls below the comfort range. Heat is stored by PCM as latent heat during the day time and by night when temperature drops, the stored energy is released into space. The selection of PCM for space heating is dependent on the ambient conditions.

4. Microelectronics: Due to advancement in technology, emerging electronic devices are becoming smaller in sizes. One of the major issues with the design of these smaller devices is the high heat removal and maintaining them at safe operating temperature. Current cooling technologies of air cooling, water cooling, heat pipes, thermoelectric cooling have reached their limit of cooling (Song et al. (2013b)). Microchannel heat exchangers are compact in size and can dissipate more heat due to their small size channels and higher heat transfer area. The application of PCM slurry in microchannel heat exchangers as coolant has attracted the attention of researchers due to their high latent heat. The potential benefits of PCM slurry are high heat absorption during phase change and increase of effective thermal conductivity due to more particle-particle and particle to fluid interaction. Due to large effective heat capacity of phase change material, temperature of the fluid remains constant during the melting or solidification of phase change particles, which results in the constant surface temperature of electronic devices and bulk temperature.

2.7 Thermophysical properties of mPCM slurry

The thermophysical properties of mPCM slurry are evaluated by Eqs. A.1-A.5 given in Appendix A. The local bulk temperature of pure water can be calculated by assuming linear increase of temperature along the test section. However, the local bulk temperature of the fluid containing mPCM particles is not linear. In previous experimental studies the local bulk temperature of the mPCM slurry was calculated using three region model (Huang et al., (2012))

For $0 \leq x \leq L_1$

$$T_{\mathrm{b}} = T_{\mathrm{b,i}} + \frac{T_1 - T_{\mathrm{i}}}{L_1} x \tag{2.1}$$

For $L_1 \leq x \leq L_1 + L_2$

$$T_{\mathrm{b}} = T_1 + \frac{T_2 - T_1}{L_2} (x - L_1) \tag{2.2}$$

For $L_1 + L_2 \leq x \leq L$

$$T_{\mathrm{b}} = T_2 + \frac{T_{\mathrm{o}} - T_2}{L_3} (x - L_1 - L_2) \tag{2.3}$$

where T_{i} and T_{o} are the inlet and outlet temperature of mPCM slurry, L_1, L_2, and L_3 are the lengths of the test section respectively, which are defined by Eqs. (2.4) to (2.6).

For Region 1 (solid region):

$$L_1 = \frac{\dot{m} C_{\mathrm{pb}} (T_1 - T_{\mathrm{i}})}{Q} L \tag{2.4}$$

For Region 2 (phase change region)

$$L_2 = L - L_1 - L_3 \tag{2.5}$$

For Region 3 (Liquid region)

$$L_1 = \frac{\dot{m} C_{\mathrm{pb}} (T_{\mathrm{o}} - T_2)}{Q} L \tag{2.6}$$

where $\dot{m}$ is the mass flowrate of mPCM slurry, where C_{pb} is the specific heat capacity of mPCM slurry and Q is the heat transfer rate for the mPCM slurry.

2.8 Heat transfer and pressure drop characteristics of mPCM slurry

So far, a number of experimental and numerical studies have been conducted to analyse the heat transfer and pressure drop characteristics of mPCM slurry in macrochannels and microchannels. The details of the experimental conditions, thermophysical properties of mPCM slurry, heat transfer, pressure drop correlations and proposed correlations are summarised in Table 2.2 to Table 2.6.

2.8.1 Heat transfer and pressure drop of mPCM slurry in macrochannels

The melting heat transfer characteristics of turbulent mPCM slurry flow in circular channel under the constant heat flux boundary condition was experimentally investigated by Choi et al. (1994). A three-region melting model was developed for determination of local bulk temperature of mPCM slurry along the flow direction of the channel. This model had been frequently used for the estimation of local bulk temperature.

Goel et al. (1994) conducted an experimental study on heat transfer performance of mPCM slurry in a circular channel under constant heat flux boundary condition. The

effects of Stefan number, mass concentration of mPCM, diamater of mPCM particles and solution homogenity on the heat transfer performance of mPCM slurrry were investigated. It was found that Stefan number was the most dominant parameter for the heat transfer performance of mPCM slurry. A very good qualitative agreement between the theoretical results of Charunyakorn et al. (1991) and their experimental data was found. However, the quantitative agreement was not upto par. They believed that this could be due to the effect of melting temperature range of PCM. Charunyakorn et al. (1991) assumed one melting point where as mPCM particles melts within a range obtained by differential scanning calorimeter (DSC). Later, Roy and Avanic (1997) performed the experimental study on the same experimental system as that of Goel et al. (1994) to analyze the effect of mPCM shell walls on the heat transfer performance. An insignificant effect of the shell wall on the heat transfer performance of mPCM slurry was observed.

Moreover, Inaba et al. (2004) experimentally studied the heat transfer and pressure drop characteristics of mPCM slurry consisting of a mixture of two different size of mPCM particles under laminar and turbulent flow conditions. They observed a 2.8% increase in Nusselt number as compared to pure water due to increase in particle to particle interaction and higher latent heat of mPCM slurry. An experimental setup was built by Delgado et al. (2012) to measure the local heat transfer measurements of mPCM slurry flow in a circular channel under constant heat flux boundary condition. Eleven thermocouples were installed along the flow direction to measure the local surface temperature by solution of 1-D heat conduction equation. The measured surface temperatures were compared with surface temperature predicted by Kays and Crawford (1993) correlation given in Eq. (2.7)

$$Nu = 4.36 + \frac{0.023 \times Gz_{\mathrm{x}}}{1 + 0.0012 \times Gz_{\mathrm{x}}} \tag{2.7}$$

where $Gz_{\mathrm{x}} = DRePr/x$ is dimensionless Graetz number, D is the diameter of circular channel, Re is the Reynolds number and , Pr is the Prandtl number.

Delgado et al. (2012) found about 15% deviation between the measured and predicted surface temperature. It was believed that the possible reasons for this deviation could be due to the interference of heat flux by insertion of thermocouples, influence of wall heat flux on thermocouples, or heat losses from thermocouples to surroundings. While considering all of these parameters, a theoretical model was developed for correction of surface temperature measurements. This resulted in increase of local heat transfer coefficient by 26% and drop in surface and bulk temperature of slurry as compared to pure water. It was examined that the operating temperature range should be adjusted to take the full advantage of latent heat of mPCM slurry. In another study, Delgado et al. (2014) examined the thermal and rheological properties of mPCM slurry. It was found that 20% mass concentrations of mPCM slurry showed the higher heat transfer performance. No rupture was observed after the consecutive two weeks of thermal cycling of mPCM slurry.

Several experiments were conducted by Wang et al. (2007) to analyse the heat transfer performance during melting of mPCM slurry in copper tube of length 1.46 m and diameter 4 mm respectively. Experiments were conducted for laminar and low turbulent flows. It was reported that the local heat transfer coefficients for mPCM slurry was always higher as compared to the pure water in laminar flow. However, in turbulent flow the variation of the local heat transfer coefficient was dependent on heating rate. A simple correlation given in Eq. (2.43) was proposed for mPCM slurry in thermally developing region under the constant heat flux boundary condition. Their experimental results were found to be in

good agreement ± 15% with the proposed correlation. In another experimental study, Wang et al. (2008) proposed two new correlations given by Eqs. (2.44) and (2.45) for predicting the average Nusselt number for laminar and turbulent flow in circular channels. Chen et al. (2008) carried out experimental study for mPCM slurry during laminar flow on the same apparatus as that of Wang et al. (2007). They observed 1.2 times higher heat transfer enhancement of mPCM slurry as compared to pure water. However, 67.5% reduction in power consumption as compared to pure water at same heat transfer rate was observed as shown in Figure 2.1.

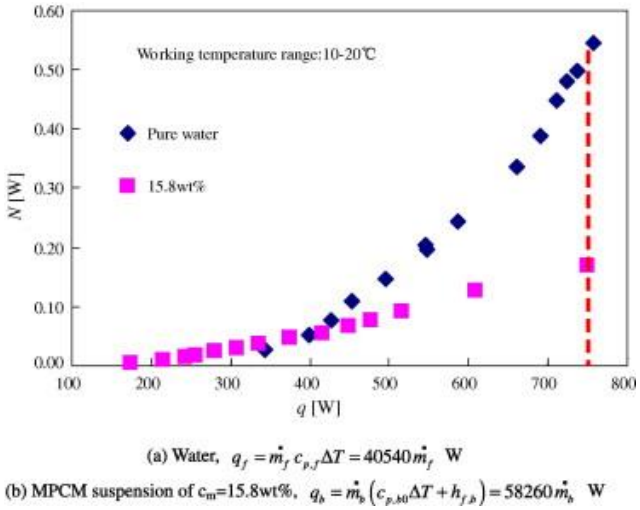

Figure 2.1 Power consumption *vs* heat transfer rate Chen et al. (2008)

The effects of Stefan number, melting temperature range of mPCM slurry, mass concentration of mPCM slurry and Reynolds number on dimensionless surface temperature was numerically investigated by Zeng et al. (2009). The effects of mass concentration of mPCM slurry and Reynolds number were not very much significant but decrease in Stefan number and melting temperature range resulted in lower dimensionless surface temperature.

Another experimental study to examine the heat transfer characteristics of mPCM slurry flow in circular channel was reported by Yamagishi et al. (1999). In previous experimental studies, bulk temperature was measured by three region melting model

which assumes that all the mPCM particles start or end phase change simultaneously. However, in practice mPCM particles near the surface melts first and then melting proceed to the core of the channel. To decrease the uncertainty in bulk temperature measurement they designed and built the test section into ten equal segments. Constant heat flux was applied to each segment separately. The local bulk temperature determined by energy balance was compared with local bulk temperature predicted by three-region melting model. It was observed that the local bulk temperature by energy balance was lower in region 1 and higher in region 3 compared to three region model as shown in Figure 2.2. They explained that three region melting model assumes that there is no subcooling phenomena and all mPCM particles melt and solidify simultaneously. The measured bulk temperature was considered more accurate because subcooling and melting temperature range was taken into account. Another interesting result of pressure drop with increase of mPCM concentration was observed as shown in Figure 2.3. This could be owing to increase in slurry viscosity resulted in linearization of mPCM slurry at higher mass concentration.

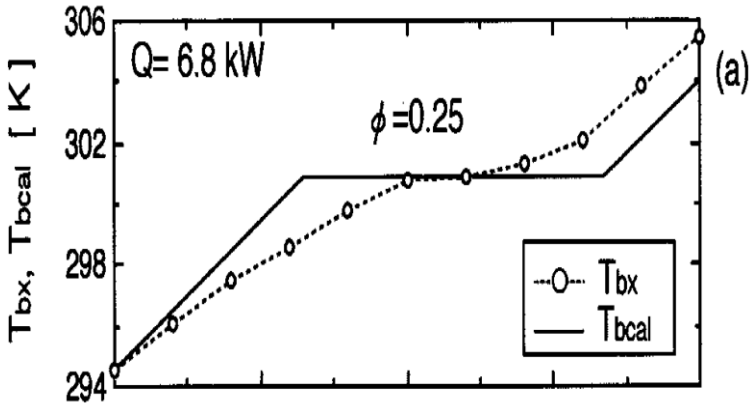

Figure 2.2 Comparison of measured and calculated bulk temperature (Yamagishi et al. (1999))

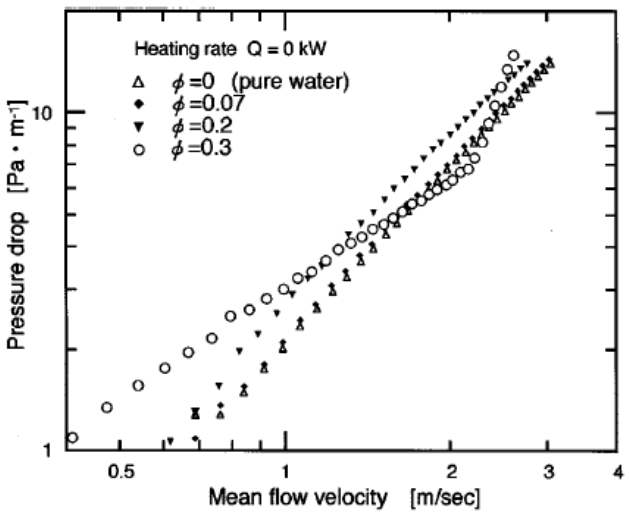

Figure 2.3 Pressure drop *vs* mean flow velocity for pure water and MCPCM slurries at 298 K. Yamagishi et al. (1999)

Huang et al. (2012) proposed the addition of magnetic material inside the mPCM particles to further enhance the convective heat transfer characteristics of mPCM. They did experimental study to examine heat transfer characteristics of magnetic mPCM slurry under external magnetic field applied to the segment of test section. A significant increase in heat transfer coefficient and reduction in surface temperature in the external magnetic field region was found, because of movement of the mPCM particles towards the channel surface. This movement of mPCM particles resulted in thinning of boundary layer hence, increasing heat transfer. This heat transfer enhancement also resulted in lower pump power consumption.

2.8.2 Heat transfer and pressure drop of mPCM slurry in microchannels

Microchannels are favourable for high heat absorption due to their large contact area. A few experimental and numerical studies have been found regarding the heat transfer performance of mPCM slurry flow in microchannels.

Kondle et al. (2013) did a numerical study of mPCM slurry flow in microchannels of three different aspect ratios under CST, CHF H1 and CHF H2 boundary conditions. Flow

was considered hydro-dynamically and thermally fully developed. Fully developed Nusselt numbers for different aspect ratios under different boundary conditions were compared with numerical results to validate numerical model. Heat flux was adjusted so that the phase change occurs when the flow was fully developed. It was found that the Nusselt number increases at the start of phase change and then decreases when melting of mPCM slurry completed as shown in Figure 2.4.

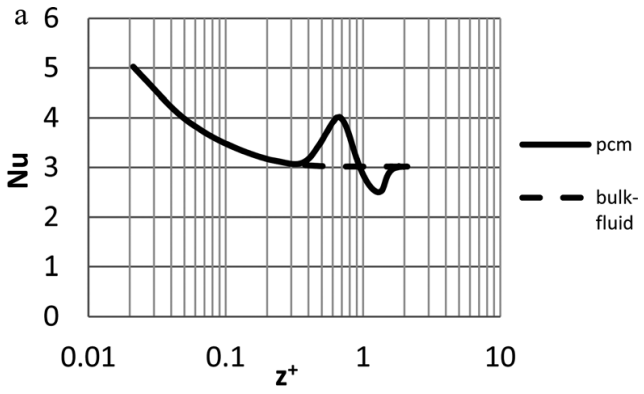

Figure 2.4 Variation of Nusselt number along dimensionless axial distance (Kondle et al. (2013))

After complete melting of the mPCM slurry Nusselt number was found to be less than the pure water because in solid and liquid state specific heat capacity of mPCM slurry was lower than pure water. Similar increase and then decrease in Nusselt number was also examined by Ravi (2008) and Zeng et al. (2009). They analysed the effects of melting temperature range of mPCM particles and Stefan number on the heat transfer performance of mPCM slurry. It was found that heat transfer enhances with the decrease in Stefan number and melting temperature range.

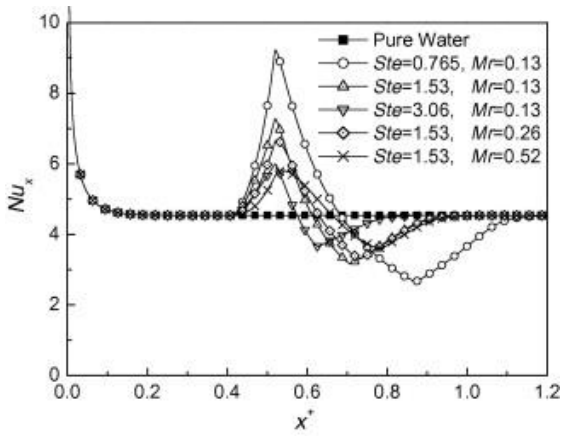

Figure 2.5 Effect of Stefan number and melting temperature range on the performance of mPCM slurry (Zeng et al. (2009)).

A two-phase numerical model for mPCM slurry flow in circular microchannel was developed by Xing et al. (2005). The mass, momentum and energy equations were solved separately for solid and liquid phase. The results showed that there exist an optimum heat flux for every given Reynolds number which enhances the heat transfer performance of mPCM slurry. It was reported that the ratio of heat transfer rate to pumping power was higher at low Reynolds number. Therefore, optimum mass flow rate and heat flux should be considered while designing the microchannel heat sinks. Numerical results were compared with experimental data of Goel et al. (1994) and reported to be very sensitive to inlet temperature of mPCM slurry.

A novel way of enhancing heat transfer of mPCM slurry has been proposed by Song et al. (2013b). They proposed the mixture of liquid metal with mPCM particles as heat transfer fluid. The proposed fluid had higher thermal conductivity and effective specific heat capacity. The numerical study of liquid metal mPCM slurry flow in channel showed higher heat transfer coefficients for liquid metal slurry as compared to water mPCM slurry as shown in Figure 2.6. The effect of higher pressure drop due to the higher viscosity of liquid metal, was not investigated.

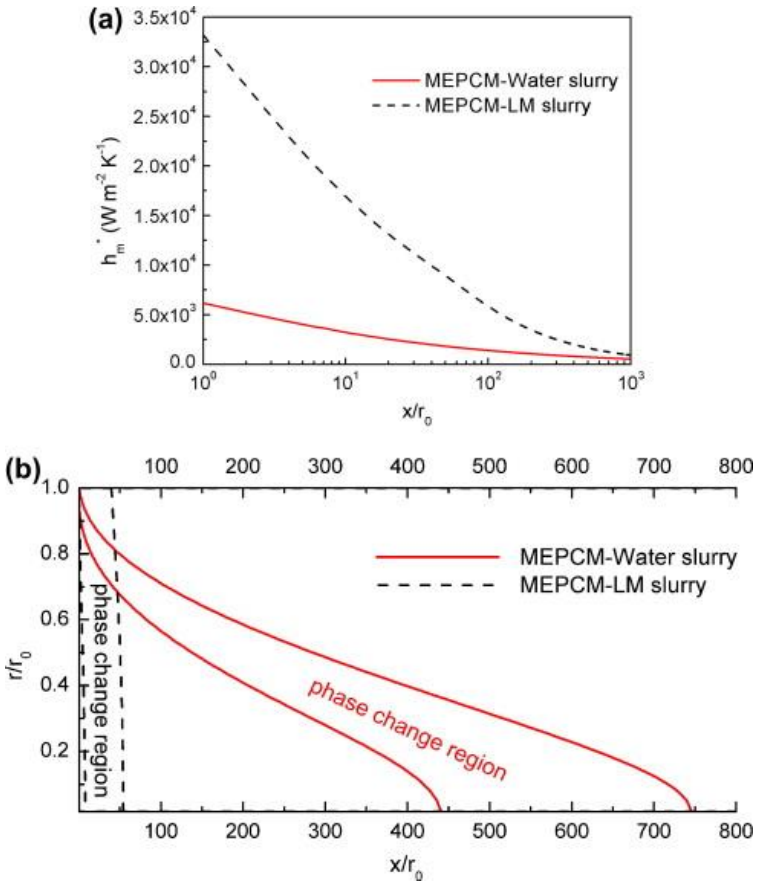

Figure 2.6 Effect of carrying fluid on (a) heat transfer enhancement (b) the distribution of phase change region of slurries (Song et al. (2013b))

Another heat transfer enhancement technique was also proposed by Song et al. (2013a) by introducing the twisted tape inserts inside the channel. The heat transfer performance for the mPCM slurry in the tube with twisted tape insert were found to be much higher than that for the normal tube because of latent heat of mPCM and swirl flow caused by twisted tape. Kuravi et al. (2009) numerically simulated 3D manifold microchannel heat sink. The physical model of their simulation is shown in Figure 2.7.

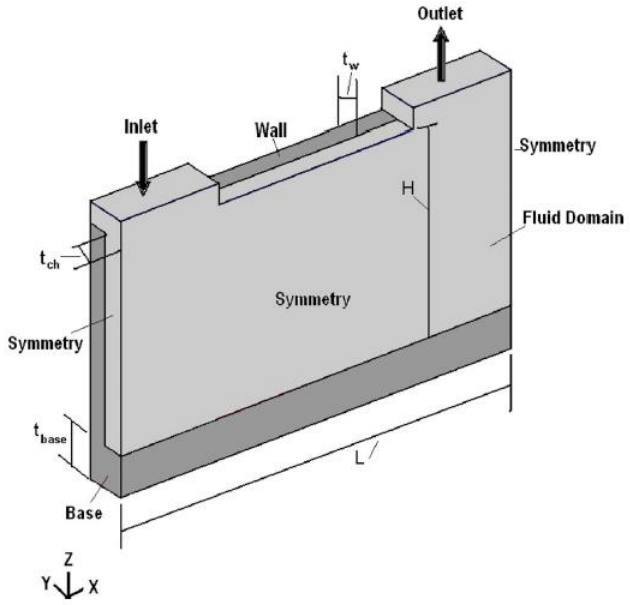

Figure 2.7 Physical model of single microchannel used for numerical simulation (Kuravi et al. (2009))

They analysed the performance of NEPCM slurry flow in the manifold microchannel heat sink and compared it with single phase fluid. The thermophysical properties of slurry were taken constant except specific heat capacity and thermal conductivity. The NEPCM slurry showed better heat transfer performance as compared to PAO due to its high latent heat of fusion. The bulk temperature of NEPCM was found to be lower than PAO and it further decreases with increase of mass concentration of NEPCM slurry. It was reported that for NEPCM, effective thermal conductivity has insignificant effect on the heat transfer performance. However, effective thermal conductivity effect is more prominent for large size of mPCM particles.

A numerical study on three dimensional conjugated heat transfer for mPCM slurry flow in rectangular microchannel heat sink was performed by Sabbah et al. (2008). The physical model and boundary conditions are shown in Figure 2.8

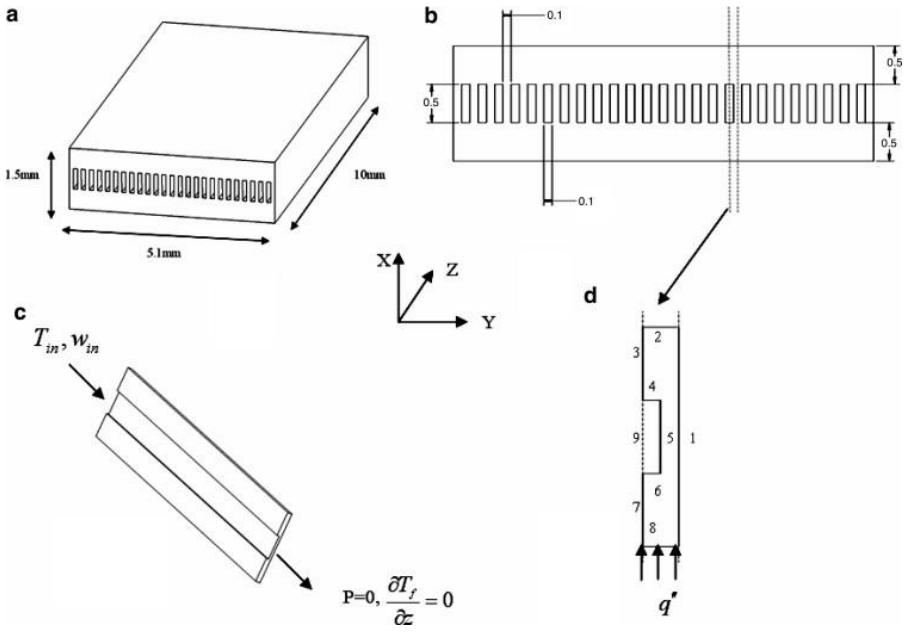

Figure 2.8 (a) Heat sink three dimensional isometric and front view (b) Isometric and front view of part modelled in simulation (Sabbah et al. (2008))

In their study, effective thermal conductivity and temperature dependent water properties were considered. The results showed underestimation of the required cooling load when temperature dependent properties of water were neglected. The influence of the material of heat sink was analysed and it was found that copper heat sinks showed enhanced heat transfer performance as compared to aluminium. In another numerical study, Sabbah et al. (2011) explored the effect of mPCM slurry flow on thermal boundary layer. It was observed that thermal boundary layer extends in case of mPCM layer and they suggested it may be because mPCM particles act as a heat sink which slowed the growth of the thermal boundary layer. The thickness of boundary layer depends on melting zone. This delay in boundary layer thickness has also been observed by Seyf et al. (2013).

A novel approach of tangential impingement of mPCM slurry in microtube heat sink has been numerically simulated by Seyf et al. (2013). The schematic diagram of microtube heat sink with tangential impingement is shown in Figure 2.9.

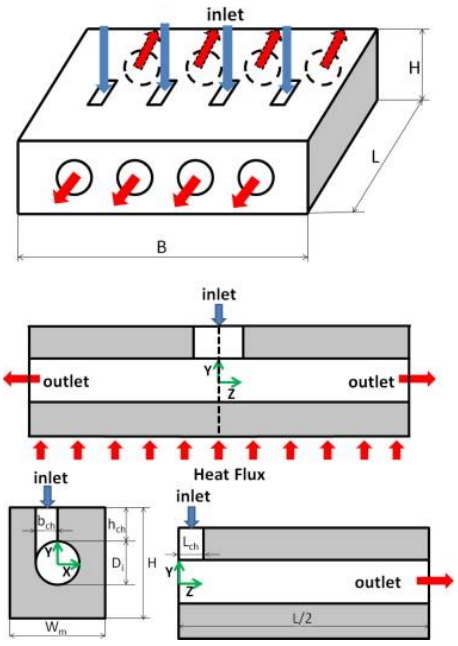

Figure 2.9 Schematic of micro-tube heat sink with tangential impingement (Seyf et al. (2013))

They investigated the effects of melting temperature range, inlet Reynolds number, mass concentration of mPCM slurry, thermal resistance, temperature uniformity and total entropy generation in microtube heat sinks. It was reported that increase in the inlet Reynolds number increases the cooling performance of heat sinks. Reduction in thermal resistance and temperature uniformity of heat sink surface was also observed with increase in mass concentration and inlet Reynolds number. Contrary to Ravi (2008) and Zeng et al. (2009) their results showed that increase in melting temperature range enhanced the cooling capability of heat sink. The overall entropy generation decreased with the increase of Reynolds number, mass concentration and melting temperature range.

In numerical studies, it is very easy to obtain the local temperatures and heat fluxes. But as far as experimental studies on microchannels are concerned, it is very difficult to obtain the local surface temperature and local heat flux due to very small size of microchannels. Researchers used different methods to obtain the surface temperature of microchannels. Rao et al. (2007) experimentally investigated convective heat transfer performance of mPCM slurry flow in rectangular minichannels (4.2 mm height, 2 mm width and 150 mm

length) under boundary condition of constant heat flux and found that mPCM slurry with 5% mass concentration showed higher Nusselt number and heat transfer coefficient with respect to water within the considered mass flow rates ranging from 0.05 to 0.35 kg/min. Six thermocouples have been placed along the flow direction of channel inside the copper block at a certain distance beneath the microchannel bottom surface. The inner local surface temperature of microchannel was calculated by assuming 1-D heat conduction in the copper block beneath the minichannels.

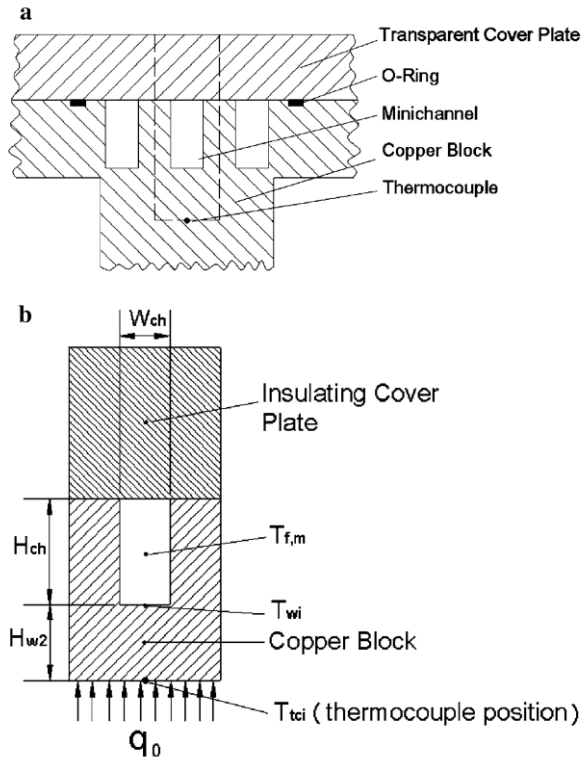

Figure 2.10 Cross sectional view of minichannels (Rao et al. (2007))

Later, Dammel and Stephan (2011) modified the length of the test section of Rao et al. (2007) to increase residence time of mPCM slurry in microchannels. They examined that in order to take the maximum advantage of latent heat of mPCM slurry, optimum inlet temperature and the mass flow rate should be considered. Wu et al. (2013) experimentally analysed the heat transfer performance of bare and silica NEPCM dispersed with PAO (poly alpha olefin) in the microchannel heat exchanger. Their results showed that at the same velocity NEPCM slurry showed 2 times better heat transfer as compared to pure

PAO. Ho et al. (2013) carried out experimental study to examine the convective heat transfer characteristics of mPCM slurry in minichannels of 1.5 mm height and 1 mm width. It was found heat transfer enhancement of about 52% at *Re* = 133. The local surface temperature of microchannel was calculated by the same method as Rao et al. (2006). In another study, Ho et al. (2014a) developed correlation given in Eq.(2.4) for mPCM slurry flow in microchannels. Wang and Lin (2012) did an experimental study on convective heat transfer characteristics of mPCM slurry flow in a rectangular channel of 0.14 aspect ratio. Surface temperature was measured by welding eight thermocouples to the shorter side of rectangular tube along the flow direction. Dimensionless surface temperature was reduced by 16% for 20% mass concentration of mPCM slurry as compared to water.

Recently, a numerical study was performed by Rajabi Far et al. (2015) to enhance the convective heat transfer of microchannel heat sink with oblique fins. These oblique fins were used to interrupt the development of hydrodynamic and thermal boundary layer which resulted in the heat transfer enhancement. It was found that the Nusselt number increased with the NEPCM slurry flow in microchannel heat sink. The increase in Euler number was also observed due to higher viscosity and resistance during working fluid flow. The effect of tip clearance was also investigated. Their results showed that for tip clearance to channel width ratio ranging from 0.20 to 0.375 gave higher Nusselt number and Euler numbers. In this project, the local surface temperature and local heat flux were determined and compared by two methods:

1. By inverse heat conduction solution of Yu et al. (2014)

2. Linear and polynomial fittings of temperature measured at ninety eight locations.

Yu et al. (2014) proposed a meshless inverse method for determining the local surface temperature and heat flux by measuring temperatures in the outside wall boundary. The points where temperature and heat flux are known are defined as field points (fp). The

points where surface temperature and heat flux are to be determined are known as source points (sp) as shown in Figure 2.11.

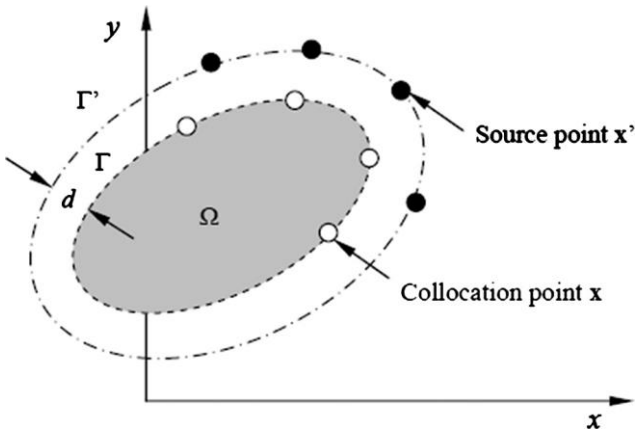

Figure 2.11 The method of fundamental solution and fictitious boundary (Yu et al. (2014)).

The surface temperature and heat flux at source points were determined by solving simultaneous solving Eqs. (2.8) and (2.9) by singular value decomposition method.

$$\sum_{i=1}^{n_{\mathrm{sp}}} \beta_{\mathrm{i}} u^{*}\left(x_{\mathrm{i}}, x_{\mathrm{j}}\right)=T_{\mathrm{j}},(j=1, \ldots \ldots, n_{\mathrm{fp}}^{\mathrm{T}}) \tag{2.8}$$

where T_{j} is the temperature measured and $n_{\mathrm{fp}}^{\mathrm{T}}$ are the number of points (ninety eight thermocouples) with known temperatures. The heat flux at field point *j* is represented by Eq. (2.9).

$$\sum_{i=1}^{n_{\mathrm{sp}}} \beta_{\mathrm{i}} q^{*}\left(x_{\mathrm{i}}, x_{\mathrm{j}}\right)=Q_{\mathrm{j}},(j=1, \ldots \ldots, n_{\mathrm{fp}}^{\mathrm{Q}}) \tag{2.9}$$

where Q_{j} is the heat flux and $n_{\mathrm{fp}}^{\mathrm{Q}}$ are the number of points with known heat flux.

Temperatures measured at 98 locations were used as input to the Fortran code to find the local surface temperature and local heat flux along the flow direction of the microchannel.

The inverse solution of Yu et al. (2014) was based on 2-D steady state heat conduction problem. The effects of lateral sides and adiabatic regions near the upstream and downstream of the microchannel test section were ignored. So, the local surface temperature and local heat flux were also determined by linear and polynomial fittings of temperatures measured inside the block. Figure 2.12 to Figure 2.16 show the comparison of local surface temperature and local heat flux determined by linear and polynomial fittings. The local surface temperature obtained by three polynomial fitting methods does not vary a lot. However, for local heat flux measurements, linear fittings give more reasonable and closer results to inverse heat conduction solution of Yu et al. (2014) as compared to higher order polynomial fittings. This also shows that local heat flux measurements are very sensitive to the temperature measurements.

Figure 2.13 depicts that local heat flux obtained by linear fittings and inverse conduction solution are in good agreement from $z = 0.14$ to $z = 0.36$. At $z = 0.085$ m and $z = 0.415$ m the local heat flux is higher than local heat flux obtained by inverse solution. It seems possible that these differences are due to the following factors:

1. The adiabatic upstream and downstream parts of the test section were not considered by inverse heat conduction (Yu et al. (2014)).
2. The inverse solution proposed by Yu et al. (2014) was for 2-D steady state heat conduction. The effects of the lateral sides of the test section were neglected.
3. The hot water entered into upper and lower jackets by jet impingement. The increase in local heat flux near the upstream and downstream of test section could be the results of enhanced heating by jet impingement.

Hence, considering all of the above stated factors, linear fittings were opted for measurement of local surface temperature and local heat flux. The local surface

temperature and heat flux measurements by linear fittings considered the effects of adiabatic parts of the test section and jet impingement.

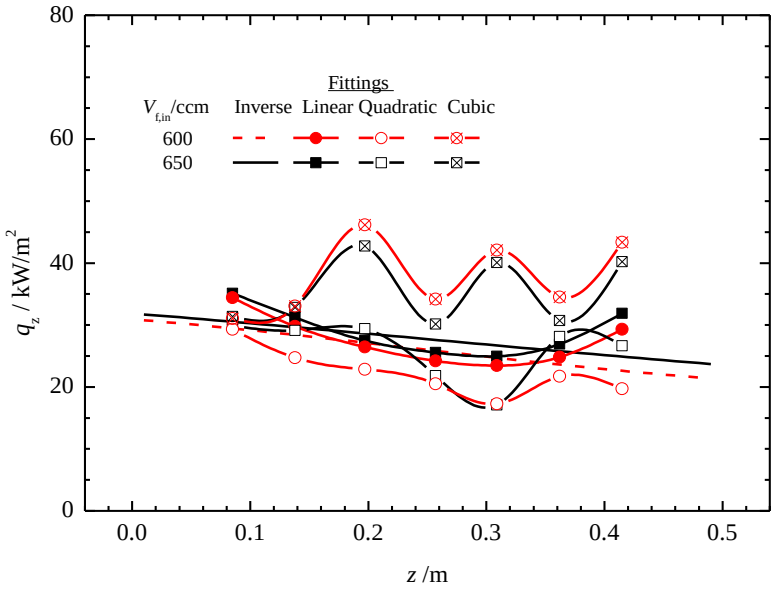

Figure 2.12 Variation of local heat flux by inverse method (Yu et al. (2014)) linear and polynomial fittings

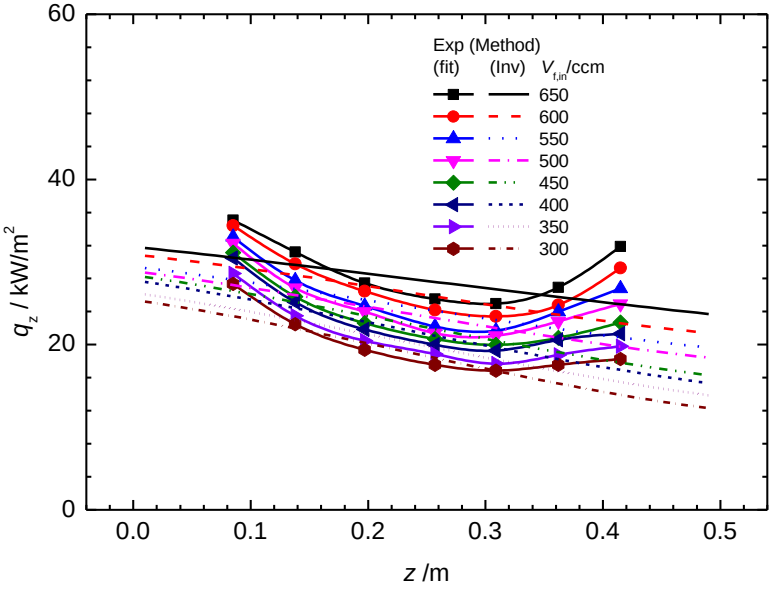

Figure 2.13 Variation of local heat flux by inverse method (Yu et al. (2014)) and linear fittings

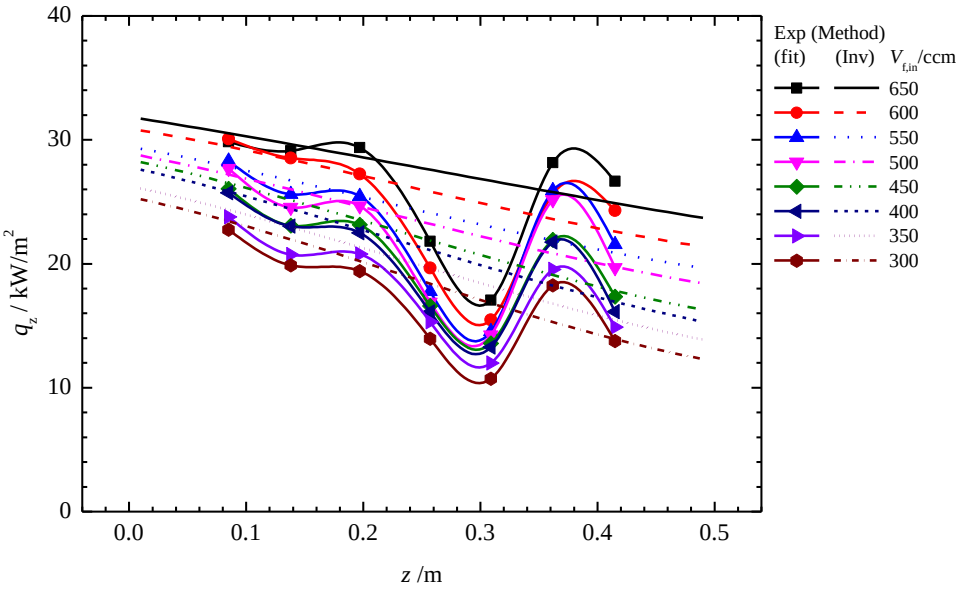

Figure 2.14 Comparison of local wall heat flux determined by inverse method (Yu et al. (2014)) and quadratic polynomial fitting

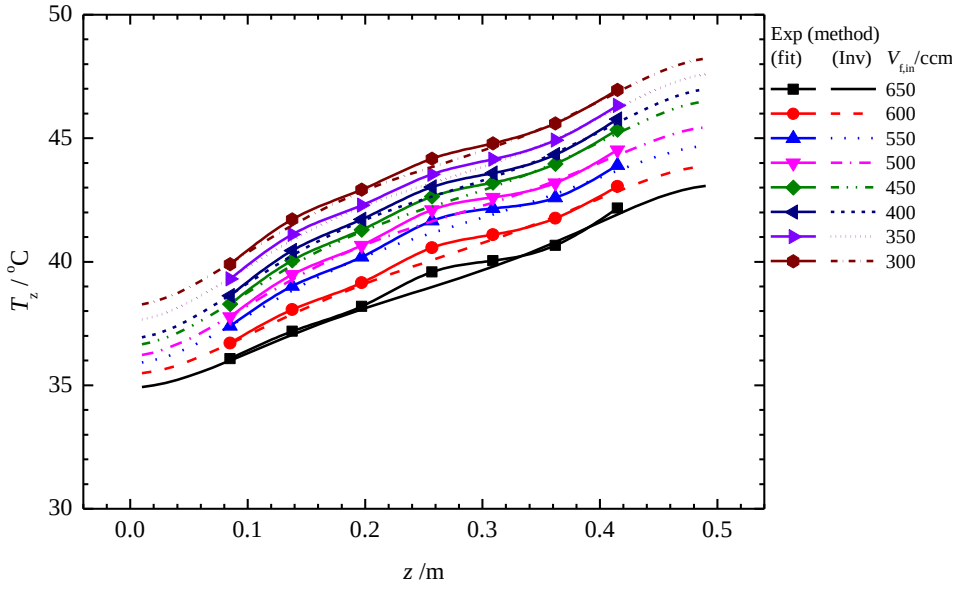

Figure 2.15 Comparison of local surface temperature determined by inverse method (Yu et al. (2014)) and linear fitting

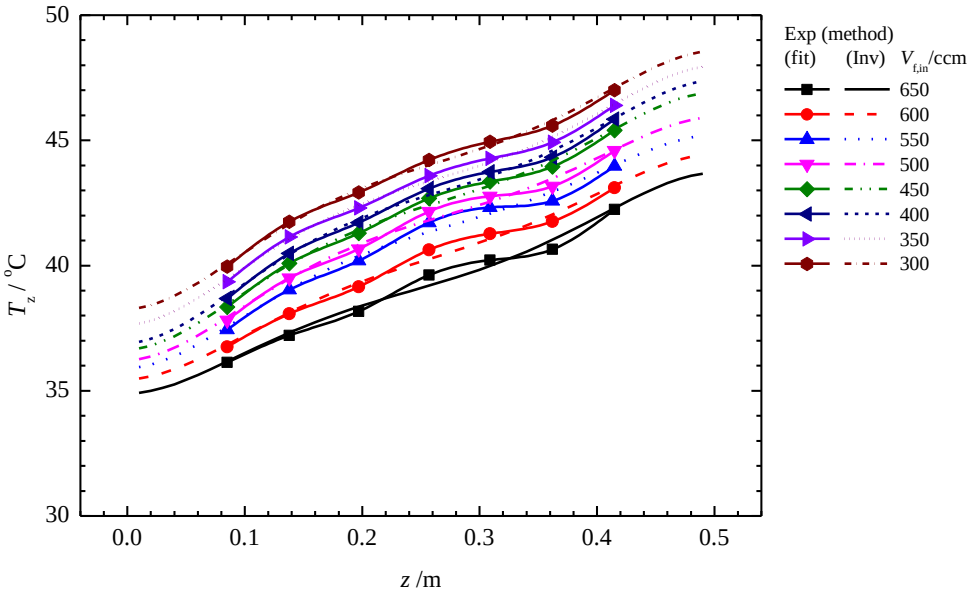

Figure 2.16 Comparison of local surface temperature determined by inverse method (Yu et al. (2014)) and quadratic polynomial fitting

Table 2.2 Summary of conditions for heat transfer of mPCM slurries flow in microchannels

	Study type	mPCM c %	Channel geometry material	Test section mm	B.C	Flow regime Re	Claimed uncertainty %	Parameters	Validation	Comments
Macrochannels										
Choi et al. (1994)	Exp	c_m 0,10	Circular Stainless steel	I.D=10 L=1000	CHF	13230 for water	Not mentioned	T_b, h_x,	Blausius Dittus Boelter Petukhov	Proposed three-region melting model for measurement of local bulk temperature for mPCM slurry
Goel et al. (1994)	Exp	c_v 5,10,15, 20	Circular Copper	L=30 I.D=3.14 O.D =4.76	CHF	Laminar	Not mentioned	θ_w, Ste,d_p,c, suspension homogeneity	Charunyakorn et al. (1991)	About 50% dimensionless surface temperature reduction was observed with mPCM slurry as compared to water. Stefan number had a very significant effect on heat transfer performance of mPCM slurry.
Yamagishi et al. (1999)	Exp	c_v 7, 12, 15, 25, 30	Circular Stainless steel	I.D=10.1 WT=1.0 L=8000	CHF	Laminar & turbulent	Within ±15	T_w,f,h_x, T_b	Blausius Eq. Hagen-Poiseuille,	Found pressure drop for mPCM of c = 30% lower than water in velocity range 2-2.5m/s. Local bulk temp calculated by energy balance was compared by predicted from three-region model Measured surface temp by 1-D conduction Decrease in bulk temp and increase in h_x was observed.

										Examined the thermal stability and morphology of used mPCM after 5000 thermal cycling

Table 2.2 Continued

	Study type	mPCM c %	Channel geometry material	Test section mm	B.C	Flow regime Re	Claimed uncertainty %	Parameters	Validation %	Comments
Roy and Avanic (1997)	Exp	c_v upto 30	Circular Brass	L=30 $I.D$=3.26	CHF	Laminar	Not mentioned	θ_w	Empirical correlation Eq. (2.25)	Found an insignificant effect of mPCM shell wall on heat transfer performance.
Hu and Zhang (2002)	Num	<25	Circular		CHF	laminar	None	Ste,MR, d_p, Re	Exp data of Goel et al. (1994)	Proposed modified Nusselt number to consider phase change of mPCM slurry
Inaba et al. (2004)	Exp	c_m 20	Circular Stainless steel	$I.D$ = 15 $W.T$= 0.8 L= 5850	CHF	500<Re< 6000	±5	Nu_x, T_w,f	Hagen-Poiseuille, Blausius Eq.	Found 2 to 2.8 times heat transfer enhancements compared to pure water
Chen et al. (2006)	Exp	c_m 5-40	Circular Perspex	L=2000 $I.D$= 10 $O.D$=14		Laminar	7.2	Nu_x, $T_{w,x}$,$T_{b,x}$	Shah & London Eq.(2.38)	Nu_x for mPCM slurry was found to be 1.2 times higher than pure water. Pump consumption for mPCM slurry was 67.5% lower than pure water at same heat transfer rate
Wang et al. (2007)	Exp	c_m 5-27.6	Circular stainless steel	L=1460 D=4 $W.T$=1	CHF	2100<Re <4000	8.14	T_w ,f, h_x , Nu_x , T_b	Shah & London Eq.(2.38)	Conducted experiments for laminar and turbulent flow. h_x increases in laminar regime for all three regions

									Choi & Cho Eq. (2.39)	In turbulent regime, h_x depends on the heating rate. Proposed new correlation for mPCM slurry flow

Table 2.2 Continued

	Study type	mPCM c %	Channel geometry material	Test section mm	B.C	Flow regime Re	Claimed uncertainty %	Parameters	Validation %	Comments
Chen et al. (2008)	Exp & Num	c_m 5, 10, 15.8	Circular Stainless steel	L=1460 $I.D$=4.0 $W.T$=1.0	CHF	400<Re<1900			Shah & London Eq.(2.38)	Nu_x for mPCM slurry was found to be 1.2-2.4 times higher than pure water.
Zeng et al. (2009)	Exp	c_m 5, 10, 15.8	Circular Stainless steel	L=1460 $I.D$=4.0 $W.T$=1.0	CHF	Laminar	None	Ste, T_m , T_{in} , Re,c, d_p	Exp data of (Zeng et al.(2009))	Physical properties of water were taken as independent of temperature. Used enthalpy model for consideration of phase change. Observed that heat transfer enhancement increases with decrease in Ste and Mr.
Zou et al. (2010)	Exp	c_m 10, 20, 30	Circular	$I.D$ =12 L=1200		Turbulant		ΔP,N_p		Compared the pressure drop of mPCM slurry with pure water. They observed 73% reduction in pumping power for v=0.6 m/s, c=30%
Delgado et al. (2012)	Exp	c_m 10	Circular	$O.D$=10 L=1.82	CHF	Laminar	Not mentioned	T_w,f,h_x,	Hagen-Poiseuille, Blausius Eq	Proposed theoretical model for correction of surface temp measurements. Found reduction in surface temperature, increase in heat transfer coefficient for mPCM slurry

Table 2.2 Continued

	Study type	mPCM c %	Channel geometry material	Test section mm	B.C	Flow regime Re	Claimed uncertainty %	Parameters	Validation %	Comments
Delgado et al. (2014)	Exp	c_{m} 14,20,30	Circular	*O.D*=10 *L*=1820	CHF	None	Not mentioned	Morphology, enthalpy-temperature	None	Analyzed the morphology of mPCM particles after the two weeks of thermal cycling.
Mossaz et al. (2015)	Num	c_{m} 10	Circular Copper	*L*=1475 *I.D*=3.9 *O.D=6. 0*	CHF	2500<*Re* <25000		Measured thermophysical properties of fluid		Dis experimental setup validation by non encapsulated salt. Problems encountered were discussed.

Table 2.2 Continued

	Study type	mPCM c %	Channel geometry material	Test section mm	B.C	Flow regime Re	Claimed uncertainty %	Parameters	Validation %	Comments
					Microchannels					
Xing et al. (2005)	Num	<25	Circular		CHF	laminar	None	c, PI, PP, ε, h_x	Exp data of Goel et al. (1994)	Solved separately mass, momentum and energy equations for solid PCM and pure water. Found optimum heat flux for given *Re* Reported sensitivity of simulation results with inlet temp of mPCM slurry. Ignored wall conduction.
Wang and Lin (2012)	Exp	c_m 5 - 20	Rec. Aluminum	*W*= 12.8 *H*= 1.8 *L*= 900.2	7100 - 10000	$Re < 2000$		θ_w	Not mentioned	Observed the dimensionless surface temperature reduction for mPCM slurry as compared to water
Rao et al. (2007)	Exp	c_m 5,10,20	Rec. Copper	*W*=2.0 *H*=4.2 *L*=150.0 *n*=3.0 D_h = 2.7	19230 to 96150	$70 < Re < 3000$	*Nu* = 9.7 *h* = 6.7	h_{av},Nu_{av}	---------	Measured surface temperature by 1-D conduction through copper block. No local heat transfer coefficient measured.
Sabbah et al. (2008)	Num	c_v 5-25	Rec. Copper Aluminum	*W*=0.1 *H*=0.5 *L*=10.0 D_h = 0.16	1000000 , 5000000	80,158,236	None	*v*, heat sink material, T_{bulk}, θ_w	Exp data of Goel et al. (1994)	Considered temp dependent properties of water, wall conduction, developing flow, Effective thermal conductivity of mPCM slurry.

Table 2.2 Continued

	Study type	mPCM c %	Channel geometry material	test section mm	B.C	Flow regime Re	Claimed uncertainty %	Parameters	Validation %	Comments
Kuravi et al. (2009)	Num	c_m 30	Rec. Manifold	W=0.1 H=0.5 L=1.0 D_h= 0.16	1000000	Laminar	None	Nu,T_{in}, ΔT_m, c	Exp data of Goel et al.(1996) Goel et al. (1994)	Considered wall conduction effect of microchannel Flow was not fully developed Investigated effect of mass concentration, T_{in} , ΔT_m , and heat flux on mPCM performance. Found better performance of NEPCM with respect to PAO
Sabbah et al. (2011)	Num	c_v 5, 10, 15, 20, 25	Circular	-------	1460,3650,7300,10950	Laminar	None	Thermal boundary layer growth, α_x , enhancement index, surface temp reduction	-----	Implemented measured specific heat from DSC test into numerical model. Used effective thermal conductivity of slurry.
Hasan (2011)	Num	c_m 0-20	Rec. counterflow	n=25.0 W=0.1 H=0.5 L=10.0 $W.T$=0.1 D_h = 0.16	CHF 1000000	Laminar	None	Effectiveness, T_{bulk}, Performance index, pressure drop	Exp data of Farid et al. (2007)	Used source term for mPCM slurry numerical modelling. Used constant properties for pure water as base fluid. Heat transfer performance of exchanger was found better with mPCM slurry.

Table 2.2 Continued

	Study type	mPCM c %	Channel geometry material	Test section mm	B.C	Flow regime Re	Claimed uncertainty %	Parameters	Validation %	Comments
Alquaity et al. (2012)	Num	c_v 3,5,7,10	Rec.	H=0.05 L=35 W=2	8000-20000	691,1418	None	Performance index, optimum length, ratio of gain to losses and input, q, c,	Exp data of Goel et al. (1994) &Chen et al. (2008)	Effective specific heat model was used. They found that there was optimum heat flux and mass flow rate exists for complete utilization of latent heat of mPCM slurry.
Dammel and Stephan (2011)	Exp & Num	c_m 10,20	Rec. copper	W=2.0 H=4.2 L=390.0 n=9.0 D_h = 2.7	175,350,700	$19 < Re < 367$	Not mentioned	T_{wall}, ΔP, $P.P$	Exp data of Dammel and Stephan (2011)	Modified the test section of Rao et al. (2007) Calculated surface temperatures by 1-D heat conduction through copper block. Water physical properties were taken as independent of temperature. Found surface temperature reduction with mPCM slurry flow as compared to pure water.
Kondle et al. (2013)	Num	c_v 15	Rec. Circular	α=1:2,1:4,1:8 H=0.15 W varied	CHF	Re=700	None	h_x, T_{bulk}	Exp data of Chen et al. (2008)	Water physical properties were taken as independent of temperature. Effective thermal conductivity was used for simulation. Ignored wall conduction
Ho et al. (2013)	Exp	c_m 0-10	Rec. Copper	L=50.0 W=1.0 H=1.5 n=10.0 D_h = 1.2	CHF	$133 < Re < 1515$	f 16.5% Nu_{av} 16.6%	f, Nu_{av} effectiveness index, cost of performance	Exp data of Lee and Mudawar (2007)	Surface temperature was measured by 1-D conduction through copper block. Average heat transfer coefficient was measured.

Table 2.2 Continued

	Study type	mPCM c %	Channel geometry material	Test section mm	B.C	Flow regime Re	Claimed uncertainty %	Parameters	Validation %	Comments
Wu et al. (2013)	Exp	c_{m} 9,30	Rec. Copper	W=0.025,0.1 H=0.5,1.0 L=1.0	100000-500000	Laminar	Temp ±0.18 ºC, voltmeter ±1 μV, P <5%, flow rate ±3%	h_{av}, $T_{\mathrm{w}} - T_{in}$,	Compared heat transfer coefficient at different m with manufacturer's data	Measured surface temperature by 1-D conduction through copper block. Average heat transfer coefficient was calculated by taking arithmetic mean of inlet and outlet temperature. They found encapsulation of shells has no major impact on heat transfer performance.
Ho et al. (2014a)	Exp	c_{m} 0-10	Rec.	n=10 L=50 H=1.5 W=1 D_{h} = 1.2	CHF	$133 < Re < 1515$	For mpcm slurry α_{av}:4.8-16.4%, Nu_{av}: 4.5 − 16.5%	Nu_{av} effectiveness index	Exp data of Lee and Mudawar (2007)	Developed correlation for mPCM slurry flow, nanofluids and hybrid fluid (mPCM and nanofluids mixture)
Ho et al. (2014b)	Exp	c_{m} 0.1-1	Rec.	W=0.8 L=50 H=1.2 n=23,34 D_{h} = 0.96	CHF		Heating: α_{av}: 2.02 − 2.26% Nu_{av}: 21.9 − 30.8% Cooling: α_{av}: 7.7 − 8.7% Nu_{av}: 23.1 − 31.5%	h_{av},Nu_{av}		Designed and fabricated loop for natural circulation of mPCM slurry in microchannel heat exchangers; Surface temperatures of loop were measured by 11 thermocouples installed along loop;

Table 2.2 Continued

	Study type	mPCM c	Channel geometry material	Test section	B.C	Flow regime	Claimed uncertainty	Parameters	Validation	Comments
		%		mm		Re	%		%	
Seyf et al. (2013)	Num	c_m 10-30	Circular	D=9	CHF	Re = 200,400,600	None	Re, ΔP, entropy, R_{th}, ΔT_s	Num data of Lelea (2010)	Numerically simulated novel heat sink with tangential impingement. Found better cooling performance with increase Re, c_m and T_m Reported decrease in R_{th}, ΔT_s with increase in Re,c_m and T_m
Choi and Cho (2001)	Exp	c_m 0-10	Rec. Copper	A=0.1,0.2,0.33,0.5	CHF 100000,400000	Re=1500	Nu_x: $\pm$3.7 %	Enhancement factor, α_x	Blasius Eq. Jones (1976)	Examined the effect of aspect ratio on thermal performance of array of discrete heat sources. A=0.2 shows better performance
Rajabi Far et al. (2015)	Num	c_m 0-30	Heat sink with oblique fins	t/W_c=0 to 0.74	CHF,CST	Re<215	None	T_b,Euler number,Nu_x	Goel et al.(1994)	Used temperature dependent properties. Found that heat transfer performanc increases with mass concentration of NEPCM slurry but also increases the Euler number Observed the temperature, specific heat capacity, viscosity and pressure contours.

num;	Numerical	*Re;*	Reynolds number	R_{th};	Thermal resistance
exp;	Experimental	*A*;	Aspect ratio	*f;*	Friction factor
c_m;	Mass concentration	Nu_{av};	Mean Nusselt number	CHF;	Constant heat flux
c_v;	Volume concentration	Nu_x;	Local Nusselt number	*I.D;*	Inner diameter
D;	Diameter	α_{av};	Mean heat transfer coefficient	*O.D;*	Outer diameter
L;	Length of channel	α_x;	Local heat transfer coefficient	*W.T;*	Wall thickness
W;	Width of channel	T_m;	Meting range	*P.P;*	Pumping power
H;	Height of channel	T_{bulk};	Bulk temperature	*Mr;*	Melting temperature range
n;	Number of channels	T_s;	Surface temperature	*t*	Tip clearance
ΔP;	Pressure drop	*Ste;*	Stefan number	W_c	Channel width ratio

Table 2.3 Thermophysical properties of mPCM slurries used for experimental and numerical studies

	Type of study	Core material	Shell material	Particle size	Melting point	Latent heat
				μm	ºC	kJ/kg
Choi et al. (1994)	Exp	hexadecane		<0.1mm	16.5	___
Goel et al. (1994)	Exp	N eicosane $C_{20}H_{42}$	Amino formaldehyde	100,250	37.0	200
Roy and Avanic (1997)	Exp	n-octadecane	___	10	27.8	233
Yamagishi et al. (1999)	Exp	Octadecane (C_{18} H_{38})	Melamine formaldehyde	6.3	27.8	233
Hu and Zhang (2002)	Num	___	___	50, 100, 250	___	___
Zhang et al. (2003)	Num	___	___	___	___	___
Inaba et al. (2004)	Exp	Small pcm ($C_{14}H_{30}$) Large PCM ($C_{22}H_{46}$)	___	Small = 1.5 Large = 17	Small = 5.7 Large = 45	Small=229 Large=189
Xing et al. (2005)	Num	octadecane	Melamine formaldehyde	6.3	27.8	223
Chen et al. (2006)	Exp	$C_{14}H_{30}$	___	50.9	14.0	229
Rao et al. (2007)	Exp	N octadecane	polymethylmethacrylat)	4.97	28.0	241
Yang et al. (2003)	Exp	N octadecane $C_{18}H_{42}$	___	<10	___	___
Wang et al. (2007)	Exp	1-bromohexadecane	Amino plastics	10.1	14.3	160

Table 2.3 Continued

	Type of study	Core material	Shell material	Particle size	Melting point	Latent heat
				μm	ºC	kJ/kg
Balikowski and Mollendorf (2007)	Exp	1.Climsel 28 (C28) 2. Thermasorb 83(TY83)	___	___	C28= 28 TY83= 28.3	C28=126 TY83=186
Chen et al. (2008)	Exp & Num	1-bromohexadecane $C_{16}H_{33}Br$	urea formaldehyde	8.20	14.3	129.8
Royon and Guiffant (2008)	Num	___	___	Millimetric particles	___	___
Sabbah et al. (2008)	Num	___	___	___	26-32	___
Ma et al. (2009)	Exp	Rubitherm	Acrylic polymer	2.0	6	___
Zeng et al. (2009)	Exp	1-bromohexadecane $C_{16}H_{33}Br$	Amino plastics	8.20	14.3	130.0
Kuravi et al. (2009)	Num	C.F: Polyalphaolefin water	___	nano	28.7	244.0
Zou et al. (2010)	Exp	paraffin	___	0.30	87	203.9
Diaconu et al. (2010)	Exp	RT6	Polycyclic cell	2.24	___	___
Hassanipour and Lage (2010)	Exp	Octadecane paraffin	Melamine shell	3.0±0.5mm	26-36	___
Wang and Lin (2012)	Exp	N octadecane (C_{18} H_{38})	Melamine formaldehyde	2	28	32.4
Sabbah et al. (2011)	Num	___	___	___	26.8-31.8	___
Delgado et al. (2012)	Exp	paraffin	polymer	1-20	25.5-28.0	___
Hasan (2011)	Num	n-octadecane	polymethylmethacrylate	5	28	___

Table 2.3 Continued

	Type of study	Core material	Shell material	Particle size μm	Melting point °C	Latent heat kJ/kg
Alquaity et al. (2012)	Num	Lauric acid	___	50nm	___	___
Huang et al. (2012)	Exp	n-octadecane	Melamine urea formaldehyde with iron particles	38.5	31.0	139.7
Dammel and Stephan (2011)	Exp & Num	n-eicosane	PMMA	5.04	36.4	247.3
Song et al. (2013b)	Num	Eicosane	Melamine formaldehyde	___	___	90.2
Kondle et al. (2013)	Num	N-eicosane	___	___	36.8	230.0
Song et al. (2013a)	Num	1-bromohexadecane	Amino plastics	10.10	14.3	160.0
Ho et al. (2013)	Exp	___	___	___	___	___
Wu et al. (2013)	Exp	Indium C.F Polyalphaolefin	Bare & Silica	___d	157.0	Pure:28.5 Encapsulated:19.6
Ho et al. (2014a)	Exp	eicosane	Urea formaldehyde	150nm	___	___
Ho et al. (2014b)	Exp	eicosane	Urea formaldehyde	150nm	___	___
Rajabi Far et al. (2015)	Num	Octdecane	___	___	___	___
Mossaz et al. (2015)	Exp	NaOH KOH			175	207

Table 2.4 Summary of heat transfer correlations

---

1. Inaba et al. (2007)

$$Nu_{\mathrm{x}} = \frac{h_{\mathrm{x}} D}{k_{\mathrm{b}}} \tag{2.10}$$

where $h_{hx} = q/(T_{\mathrm{hw}} - T_{\mathrm{b}})$ is local heat transfer coefficient, q is the constant heat flux, T_{hw} is surface temperature, T_{b} is the bulk temperature of slurry, D is inside diameter of circular channel and k_b is bulk thermal conductivity of slurry. Nusselt number was analysed against the non-dimensional distance along the tube axis. $X = x/DRe'Pr'$ is non-dimensional axial distance, x is channel axial direction, Re' and Pr' are modified Reynolds and Prandtl numbers respectively.

$$Re' = 8^{1-n}\left(\frac{3n+1}{4n}\right)^{-n}\left(\frac{\rho_{\mathrm{b}} U^{2-n} D^{n}}{\mu_{\mathrm{b}}}\right), Pr' = \left(\frac{3n+1}{4n}\right)^{n}\left(\frac{8U}{D}\right)^{n-1}\left(\frac{Cp_{\mathrm{b}}\mu_{\mathrm{b}}}{k_{\mathrm{b}}}\right) \tag{2.11}$$

where *n* is power index of the pseudoplastic viscosity and ranged from $n = 0.92$ to 0.96, ρ_{b} is the bulk thermal conductivity of mPCM slurry, and *U* is flow velocity of mPCM slurry measured by ultrasonic velocity profiler, μ_{b} is bulk pseudoplasticity viscosity of mPCM slurry, and Cp_{b} is bulk specific heat capacity of mPCM slurry.

2. Rao et al. (2007):

$$Nu = \frac{h_{\mathrm{av}} D_{\mathrm{h}}}{k_{\mathrm{b}}} \tag{2.12}$$

where $h_{\mathrm{av}} = Q/nA\Delta T_{\mathrm{m}}$ is the average heat transfer coefficient of mPCM suspension, D_{h} is the hydraulic diameter of channel, k_{b} is the thermal conductivity of static suspension, $Q = UI$ is total electric heating power, *U* is the voltage and *I* is the current measured by

precision ammeter, n is total number of minichannels, A is effective heat transfer area, and ΔT_{m} is mean temperature difference evaluated by Eq. (2.13)

$$\Delta T_{\mathrm{m}} = \frac{1}{6}(T_{\mathrm{w1}} + T_{\mathrm{w2}} + T_{\mathrm{w3}} + T_{\mathrm{w4}} + T_{\mathrm{w5}} + T_{\mathrm{w6}}) - \frac{1}{2}(T_{\mathrm{out}} - T_{\mathrm{in}}) \tag{2.13}$$

where T_{in} and T_{out} are the inlet and outlet temperature of the mPCM slurry, $T_{\mathrm{w1}}, T_{\mathrm{w2}},$ to T_{w6} are the surface temperatures of the channel bottom calculated by assuming 1-D heat conduction in the copper block underneath the minichannels, T_{in} and T_{out} are the inlet and outlet temperature of the mPCM. The 1-D heat conduction equation for predicting inner surface temperature is given by Eq. (2.14)

$$T_{\mathrm{wi}} = T_{\mathrm{tci}} - \frac{q_0 H_{\mathrm{w2}}}{k_{\mathrm{cb}}} \tag{2.14}$$

where T_{tci} are the temperatures measured by six thermocouples, q_0 is the mean heat flux, H_{w2} is the distance between thermocouples and channel bottom surface, k_{cb} is the thermal conductivity of copper block.

3. Hu and Zhang (2002):

$$Nu^* = \frac{qD}{k_{\mathrm{b}}(T_{\mathrm{w}} - T_{\mathrm{i}})} = Re_{\mathrm{b}} Pr_{\mathrm{bo}} \int_{1-\delta t/r_o}^{1} r_1 C_{\mathrm{p}}^* (\overrightarrow{U_1}.\overrightarrow{\nabla\theta}) d_{r_1} \tag{2.15}$$

where D is diameter of circular channel, q is heat flux, k_{b} is the bulk thermal conductivity of mPCM slurry, T_{w} is surface temperature of channel, T_{i} is the inlet temperature of mPCM slurry, $Re_{\mathrm{b}} = D_{\mathrm{h}} u_{\mathrm{m}}/v_{\mathrm{b}}$ is Reynold number, u_{m} is mean axial velocity along the length of channel, v_{b} is the bulk kinematic viscosity of mPCM slurry, $Pr_{\mathrm{b0}} = v_{\mathrm{b}}/\alpha_{\mathrm{bo}} = \rho_{\mathrm{b}} C_{\mathrm{p,bo}} v_{\mathrm{b}}/k_{\mathrm{b}}$ is Prandtl number without phase change of slurry, α_{bo} is the thermal diffusivity of mPCM slurry without phase change, $\rho_{\mathrm{b}}$is the bulk density of mPCM slurry,

$C_{\mathrm{p,bo}}$ is the specific heat of slurry without phase change, $r_1$is the dimensionless radial coordinate, C_{p}^{*} is variable specific heat of mPCM slurry which is strongly temperature dependent, $\overrightarrow{U_1}.\overrightarrow{\nabla\theta}$ is dot product of dimensionless velocity and angle between dimensionless velocity and temperature gradient vectors.

4. Wang and Lin (2012):

$$Nu_{\mathrm{x}} = \frac{h_{\mathrm{x}} D_{\mathrm{h}}}{k_{\mathrm{b}}} \tag{2.16}$$

where Nu_{x} is local Nusselt number, h_{x} is local heat transfer coefficient, $D_{\mathrm{h}} = 2ab/(a + b)$ is the hydraulic diameter of rectangular duct, a and b are the width and height of rectangular cross section, k_{b} is the thermal conductivity of mPCM slurry. The dimensionless surface temperature is inversely proportional to Nusselt number was calculated by Eq. (2.17)

$$\theta_{\mathrm{x}} = \frac{1}{Nu_{\mathrm{x}}} + \frac{4\bar{x}}{1+\beta} \tag{2.17}$$

where θ_{x} is dimensionless surface temperarure, $\beta = b/a$ = 0.14 is aspect ratio, $\bar{x}$ is dimensionless axial distance along the rectangular duct and is given by Eq. (2.18)

$$\bar{x} = \frac{x}{D_{\mathrm{h}} RePr} = \frac{(1+\beta)^2}{4\beta} \frac{x k_b}{\dot{m} C_{\mathrm{p,b}}} \tag{2.18}$$

where x is distance from inlet of channel, Re is the Reynolds number, Pr is the Prandtl number, k_{b} is the thermal conductivity of mPCM slurry, $\dot{m}$ is the mass flow rate of mPCM slurry and $C_{\mathrm{p,b}}$ is the specific heat capacity of mPCM slurry.

5. Chen et al. (2008):

$$h_{\mathrm{x}} = \frac{q}{T_{\mathrm{w}} - T_{\mathrm{b}}} = \frac{UI/_{\pi DL}}{T_{\mathrm{w}} - T_{\mathrm{b}}} \tag{2.19}$$

$$Nu_{\mathrm{x}} = \frac{h_{\mathrm{x}} D}{k_{\mathrm{b}}} = \frac{UI/_{\pi L}}{(T_{\mathrm{w}} - T_{\mathrm{b}})k_{\mathrm{b}}} \tag{2.20}$$

where h_{x} is the local heat transfer coefficient, q is the wall heat flux, T_{w} is the surface temperature of tube, T_{b} is the bulk temperature of mPCM slurry, U is the voltage, I is the current, D and L are the diameter and length of circular channel respectively, Nu_{x} is the local Nusselt number and k_{b} is the thermal conductivity of mPCM slurry. Nusselt number and heat transfer coefficient were compared against dimensionless surface temperature and dimensionless axial distance along the length of tube given by Eqs (2.21) and (2.22)

$$\Theta_w = \frac{T_{\mathrm{w}} - T_{\mathrm{b,i}}}{q_{\mathrm{w}}^{\text{“}} r/k_{\mathrm{b}}} = \frac{(T_{\mathrm{w}} - T_{\mathrm{b},i})}{UI/_{2\pi L}} \tag{2.21}$$

$$X^{+} = \frac{x/_{r}}{Re_{\mathrm{b}} Pr_{\mathrm{bo}}} = \frac{x\tau\pi v_b \rho_{\mathrm{b}}}{2mPr_{\mathrm{bo}}} \tag{2.22}$$

where θ_{w} is dimensionless surface temperature, $T_{\mathrm{b,i}}$ is the inlet temperature of slurry, Re_{b} is the Reynolds number, Pr_{bo} is the Prandtl number of non phase change slurry, v_{b} and ρ_{b} are kinematic viscosity and density of slurry, respectively. Experimental setup was validated by comparing measured Nusselt number with predicted Nusselt number by Eq. (2.23)

$$Nu_{\mathrm{f,x}} = 5.364\left[(1 + \frac{110x_{\mathrm{f}}^{+}}{\pi})^{\frac{-10}{9}}\right]^{\frac{3}{10}} - 1.0 \tag{2.23}$$

where $x_{\mathrm{f}}^{+} = x/(rRe_{\mathrm{f}}Pr_{\mathrm{f}})$, Re_{f} is the Reynolds number and Pr_{f} is the Prandtl number.

6. Sabbah et al. (2011)

$$Nu_{\mathrm{x}} = \frac{h_{\mathrm{x}} D}{\mathrm{k_b}} \tag{2.24}$$

where Nu_{x} is local Nusselt number, $h_{\mathrm{x}} = q_{\mathrm{w}}^{"}/(T_{\mathrm{w}} - T_{\mathrm{m}})$ is the local heat transfer coefficient, $q_{\mathrm{w}}^{"}$ is wall heat flux, $\mathrm{T_w}$ is surface temperature, and $T_{\mathrm{m}} = \int_0^{R_{\mathrm{o}}} \rho_{\mathrm{eff}}\, u_{\mathrm{z}} C_{\mathrm{eff}} r T dr / \rho_{\mathrm{eff}} C_{\mathrm{eff}} U R_i^2$ is bulk temperature of mPCM slurry, ρ_{eff} is effective density of mPCM slurry, u_{z} is axial velocity along the length of channel, C_{eff} is the effective specific heat of mPCM slurry, R_{i} and R_{o} are inner and outer radius of tube, D is the diameter of circular channel, and $\mathrm{k_b}$ is thermal conductivity of slurry.

7. Roy and Avanic (1997):

$$\frac{T_{\mathrm{w,x}} - T_{\mathrm{i}}}{qD/k} = \left(\frac{1}{Nu_{\mathrm{x}}} + \frac{4(x/D)}{Pe}\right) \tag{2.25}$$

where $T_{\mathrm{w,x}}$ is the local surface temperature along the flow direction of channel, T_{i} is the inlet temperature of fluid, q is the local heat flux, $Nu_{\mathrm{x}} = h_x D/k = qD/(T_{\mathrm{w,x}} - T_{\mathrm{m,x}})$ is the local Nusset number, h_x is the local heat transfer coefficient, D is the diameter of circular channel, k is the thermal conductivity of fluid, $T_{\mathrm{m,x}}$ is the local bulk temperature of fluid, $Pe = vD/\alpha$ is the Peclet number, v is the fluid velocity and α is the thermal diffusivity of fluid. Nusselt number was also calculated by Eq. (2.26) for comparison.

$$Nu_{\mathrm{x}} = \left[\frac{1}{Nu_{\infty}} - \frac{1}{2}\sum \frac{\exp(-\frac{2\gamma_{\mathrm{m}}^4 \left(\frac{x}{D}\right)}{Pe}}{A_{\mathrm{m}} \gamma_{\mathrm{m}}^4}\right] \tag{2.26}$$

where Nu_{∞} is Nusslet number in fully developed flow region and its value is 4.364, A_{m} and γ_{m}^4 are values given in Roy and Avanic (1997)

8. Zeng et al. (2009):

$$Nu_{\mathrm{x}} = \frac{h_{\mathrm{x}} D}{k_{\mathrm{b}}} \tag{2.27}$$

where Nu_{x} is the local Nusselt number, $h_{\mathrm{x}} = q/(T_{\mathrm{w}} - T_{\mathrm{x}})$ is local heat transfer coefficient, q is the local wall heat flux, T_{w} is the local inner surface temperature, T_{x} is the local bulk temperature of fluid. Experimental results of local Nusselt number were compared by predicted Nusselt number correlation for single phase fluid (water) given by Eq. (2.28)

$$Nu_{\mathrm{f,x}} = 5.364\left[(1 + \frac{110x_{\mathrm{f}}^{+}}{\pi})^{\frac{-10}{9}}\right]^{\frac{3}{10}} - 1.0 \tag{2.28}$$

where $x_{\mathrm{f}}^{+} = x/(rRe_{\mathrm{f}}Pr_{\mathrm{f}})$, Re_{f} is the Reynolds number and Pr_{f} is the Prandtl number.

9. Delgado et al. (2012)

$$Nu = 4.36 + \frac{0.023 \times Gz_{\mathrm{x}}}{1 + 0.0012 \times Gz_{\mathrm{x}}} \tag{2.29}$$

where $Gz_{\mathrm{x}} = DRePr/x$ is dimensionless Graetz number, D is the diameter of circular tube, Re is the Reynolds number and , Pr is the Prandtl number.

10. Goel et al. (1994):

$$\theta_{\mathrm{wx}} = \frac{T_{\mathrm{w}} - T_{\mathrm{i}}}{qr_{\mathrm{d}}/k_{\mathrm{b}}} \tag{2.30}$$

where θ_{wx} is dimensionless surface temperature of tube, T_{w} is surface temperature of duct, T_{i} is the inlet temperature of mPCM slurry, q is the heat flux, r_{d} is the channel radius and k_{b} is the thermal conductivity of slurry.

11. Alvarado et al. (2007):

$$h_{\mathrm{exp}} = \frac{q}{T_{\mathrm{w}} - T_{\mathrm{b}}} \tag{2.31}$$

$$h_{\mathrm{cal}} = \frac{Nu_{\mathrm{d}} k}{D} \tag{2.32}$$

where h_{exp} is experimental heat transfer coefficient, T_{w} is the surface temperature of channel, T_{b} is the bulk temperature of mPCM slurry, h_{cal} is the predicted heat transfer coefficient, Nu_{d} is the Nusselt number calculated by Eq. (2.33), k is the thermal conductivity of mPCM slurry, and D is the diameter of circular channel.

The experimental setup was validated by comparing the experimental results with Eq. (2.33).

$$Nu_{\mathrm{d}} = \frac{\left(\frac{f}{8}\right)(Re_{\mathrm{d}} - 1000)Pr}{1 + 12.7\left(\frac{f}{8}\right)^{\frac{1}{2}}(Pr^{\frac{2}{3}} - 1)} \tag{2.33}$$

where f is friction factor, Re_{d} is the Reynolds number, Pr is the Prandtl number. Eq. (2.33) is valid for $0.5 < Pr < 2000$ and $3000 < Re < 5 \times 10^6$.

12. Roy and Avanic (2001):

$$Nu_{\mathrm{cal}} = 0.00425 Re_{\mathrm{z}}^{0.979} Pr_{\mathrm{z}}^{0.4} (\mu_{\mathrm{b}}/\mu_{\mathrm{w}})^{0.11} \tag{2.34}$$

where Nu_{cal} is the predicted Nusselt number, $Re_z = u_{\mathrm{m}} D/v$ is the local Reynolds number, u_{m} is the mean velocity of fluid, D is the diameter of circular channel, v is the kinematic viscosity of fluid, $Pr_z = v/\alpha$ is the Prandtl number, α is the thermal diffusivity of fluid, μ_{b} and μ_{w} are the dynamic viscosities of water and calculated at surface temperature respectively.

13. Sabbah et al. (2008):

$$h = \frac{q}{(T_{\mathrm{s}} - T_{\mathrm{m}})} \tag{2.35}$$

where h is heat transfer coefficient, $q = q_4^{"}A_4 + q_5^{"}A_5 + q_6^{"}A_6/A_4 + A_5 + A_6$ is area averaged surface heat flux, $q_4^{"}, q_5^{"}, q_6^{"}$ are the surface heat fluxes and computed by $q_{\mathrm{b}} = \int_{A_{\mathrm{b}}} q^{"} dA_{\mathrm{b}} / \int_{A_{\mathrm{b}}} dA_{\mathrm{b}}$, q is local heat flux which is averaged in the minor direction and represented as a function of the flow direction (*z*-direction) as shown in Figure 2.7, A_{b} is boundary surface area, $T_{\mathrm{s}} = T_4A_4 + T_5A_5 + T_6A_6/A_4 + A_5 + A_6$ is area averaged interface surface temperature, T_4, T_5, T_6 are the surface temperatures computed by $T_{\mathrm{b}} = \int_{A_{\mathrm{b}}} TdA_{\mathrm{b}} / \int_{A_{\mathrm{b}}} dA_{\mathrm{b}}$ and it is averaged in the minor direction and represented as a function of the flow direction (z-direction),

$T_{\mathrm{m}} = \int_{A_{\mathrm{c}}} \rho v C_{\mathrm{p}} T dA_{\mathrm{c}} / \int_{A_{\mathrm{b}}} \rho v C_{\mathrm{p}} dA_{\mathrm{c}}$ is the mean flow temperature and it is mass weighted averaged in the two minor directions (*x*,*y* directions) and represented as a function of the flow direction (*z*-direction), ρ is density of mPCM slurry, v is the component of velocity in y direction, C_{p} is the specific heat capacity of mPCM slurry, and A_{c} is cross section area of channel.

14. Yamagishi et al. (1999):

$$h = \frac{q}{(T_{\mathrm{s}} - T_{\mathrm{m}})} \tag{2.36}$$

$$Nu_{\mathrm{x}} = 0.00425 Re_{\mathrm{bx}}^{0.979} Pr_{\mathrm{bx}}^{0.4} \left(\frac{\eta_{\mathrm{wx}}}{\eta_{\mathrm{bx}}}\right)^{-0.11} \tag{2.37}$$

where h is the heat transfer coefficient, q is the heat flux, T_{s} is the surface temperature of channel, T_{m} is the mean temperature of slurry, Nu_{x} is the local Nusselt number, $Re_{\mathrm{bx}} = u_{\mathrm{bx}}D/v$ is the local Reynolds number, u_{bx} is the mean velocity of fluid, D is the diameter

of circular channel, v is the kinematic viscosity of fluid, $Pr_{\mathrm{bx}} = v/\alpha$ is the Prandtl number, α is the thermal diffusivity of fluid, μ_{b} and μ_{w} are the dynamic viscosities of slurry and calculated at surface temperature, respectively.

15. Wang et al. (2007):

Experimental results of local Nusselt number were compared by Shah and London (1978) empirical correlation for laminar flow given by Eq. (2.23)

$$Nu_{\mathrm{f,x}} = 5.364\left[(1+\frac{110x_{\mathrm{f}}^{+}}{\pi})^{\frac{-10}{9}}\right]^{\frac{3}{10}} - 1.0 \tag{2.38}$$

where $x_{\mathrm{f}}^{+} = x/(rRe_{\mathrm{f}}Pr_{\mathrm{f}})$, Re_{f} is the Reynolds number of single phase fluid and Pr_{f} is the Prandtl number of single phase fluid.

For turbulent flow, experimental setup was validated by empirical correlation proposed by Choi et al. (1994)

$$Nu_{\mathrm{x}} = 0.00425Re_{\mathrm{bx}}^{0.979}Pr_{\mathrm{bx}}^{0.4}(\frac{\eta_{\mathrm{wx}}}{\eta_{\mathrm{bx}}})^{-0.11} \tag{2.39}$$

The local heat transfer coefficient along the length of channel was evaluated by Eq. (2.40)

$$Nu_{\mathrm{x}} = \frac{h_{\mathrm{x}}D}{k_{\mathrm{b}}} \tag{2.40}$$

where Nu_{x} is the local Nusselt number, $h_{\mathrm{x}} = q/(T_{\mathrm{wx}} - T_{\mathrm{bx}})$ is the local heat transfer coefficient, q is the heat flux, T_{wx} is the local surface temperature and T_{bx} is the local temperature of slurry.

16. Ho et al. (2013)

$$Nu_{\mathrm{x}} = \frac{h_{\mathrm{x}} D}{k_{\mathrm{b}}} \tag{2.41}$$

where Nu_{x} is the local Nusselt number, $h_{\mathrm{x}} = q/(T_{\mathrm{wx}} - T_{\mathrm{bx}})$ is the average heat transfer coefficient, q is the heat flux at the wall, T_{wx} is the local surface temperature and T_{bx} is the local bulk temperature of slurry.

17. Rajabi Far et al. (2015)

$$h_{\mathrm{x}} = \frac{q}{A_{\mathrm{tot}} \Delta T_{\mathrm{lm}}} \tag{2.42}$$

where q is the heat flux at the wall, A_{tot} is the bottom surface area which is not covered by the oblique fins and ΔT_{lm} is the log mean temperature difference.

Table 2.5 Proposed new correlations for mPCM slurry flow

1. Wang et al. (2007)

They proposed new correlation related to Shah and London (1978) correlation (Eq. (2.38)) for developing single phase flow under the constant heat flux was given by Eq. (2.43).

$$\frac{Nu_{\mathrm{mPCM}}}{Nu_{\text{shah \& London}}} = c \tag{2.43}$$

2. Wang et al. (2008)

For laminar flow

$$Nu = 0.8148 Re_{\mathrm{m}}^{0.4593} Pr_{\mathrm{m}}^{0.4863} Ste^{-0.1277} [(L_1 + L_2/D)]^{0.3059} \tag{2.44}$$

For turbulent flow

$$Nu = 4.8527 \times 10^4 Re_{\mathrm{m}}^{0.7733} Pr_{\mathrm{m}}^{2.7941} Ste^{0.3159} [(L_1 + L_2)/D]^{-0.333} (\mu_{\mathrm{m}}/\mu_{\mathrm{w}})^{-2.4349} \tag{2.45}$$

where Nu is the Nusselt number, $Re_{\mathrm{m}} = u_{\mathrm{m}} D/v$, u_{m} is the mean fluid velocity, D is the diameter of circular channel, v is the kinematic viscosity of mPCM fluid, $Pr_{\mathrm{m}} = v/\alpha$ is the Prandtl number, α is the thermal diffusivity of mPCM slurry, Ste is the Stefan number, L_1 is the length of non-phase change region, L_2 is the length of phase change region, μ_{m} and μ_{w} are the dynamic viscosities of slurry and calculated at surface temperature respectively.

3. Ho et al. (2014a)

For mPCM suspension

$$Y = a\left(\frac{Pe_{\mathrm{bf}}}{L/D_{\mathrm{h}}}\right)\left(1+\frac{\omega_{\mathrm{pcm}}}{Ste^{*}_{\mathrm{bf}}(1+Sb^{*}_{\mathrm{in,bf}})}\right)^{c} \tag{2.46}$$

where *Y* stands for the averaged Nusselt number $\overline{Nu}$, or the surface temperature control effectiveness $\varepsilon_{\mathrm{Tw}}$, or the average thermal resistance reduction effectiveness $\varepsilon_{\mathrm{R_{avg}}}$, the values for constants and ranges can be obtained from Ho et al. (2014a), *a*, *b*, and *c*, are constants, Pe_{bf} is the Peclet number of base fluid, L is the length of the channel, D_{h} is the hydraulic diameter of the channel, ω_{pcm} is the mass fraction of mPCM slurry, Ste^{*}_{bf} is the Stefan number, $Sb^{*}_{\mathrm{in,bf}} = (T_{\mathrm{m}} - T_{\mathrm{in}})/\Delta T_{\mathrm{ref}}$ is the modified inlet subcooling parameter, T_{m} is the melting temperature, T_{in} is the inlet temperature of working fluid, ΔT_{ref} is the reference temperature difference.

Table 2.6 Summary of pressure drop correlations

---

1. Alvarado et al. (2007):

$$h_{\mathrm{f}} = f\frac{L}{d}\frac{V^2}{2g} \tag{2.47}$$

$$\frac{1}{\sqrt{f}} = 1.14 + 2\log\left(\frac{d}{\varepsilon}\right) - 2log\left[1 + \frac{9.3}{Re\left(\varepsilon/_d\right)\sqrt{f}}\right] \qquad \text{for } Re > 3000 \tag{2.48}$$

where h_{f} is friction head loss, L is the length of channel, V is fluid velocity, d is diameter channe, g is gravitational constant, f is friction factor, ϵ / d is relative roughness and Re is Reynolds number.

$$h_{\mathrm{f}} = \frac{\Delta P}{\rho g} \tag{2.49}$$

Eq. (2.49) is steady flow energy equation for horizontal pipes.

2. Chen et al. (2006):

$$f = \frac{\tau_{\mathrm{w}}}{\rho U^2/8} = \frac{\Delta P.D}{\rho L}\frac{2}{U^2} = \frac{\pi^2.\Delta p.D^5.\rho.\Delta T^2}{8.L.m^2} \tag{2.50}$$

where f is friction factor, $f = 64/Re$ for laminar flow, $f = 0.3164/Re^{0.25}$ for turbulent flow, τ_{w} is wall shear stress, m is mass, U is mean velocity and L is test section length.

3. Inaba et al. (2004):

$$f_{\mathrm{b}} = \frac{\Delta P_{\mathrm{b}}/l_{\mathrm{te}}}{\left(\frac{1}{2}\right)\rho_{\mathrm{b}}U_{\mathrm{b}}^2/D} \times \frac{1}{4}, \qquad f_{\mathrm{w}} = \frac{\Delta P_{\mathrm{w}}/l_{\mathrm{te}}}{\left(\frac{1}{2}\right)\rho_{\mathrm{w}}U_{\mathrm{b}}^2/D} \times \frac{1}{4} \tag{2.51}$$

where f_{b} is fanning friction factor, U is velocity, l_{te} is length of channel, D is diameter of circular channel, subscripts w and b stands for bulk and water respectively.

4. Wang et al. (2007):

$$f = (\frac{D\Delta P}{L})(2\rho_{\mathrm{b}}u_{\mathrm{m}}^2) \tag{2.52}$$

where $f = 0.12143\ Re^{-0.25}$ for $Re > 2200$, $f = 0.12143\ Re^{-0.25}$ for $Re < 1200$, ΔP is pressure drop, D is diameter of channel, L is length of channel, u_{m} is velocity and ρ_{b} is bulk density. Chen et al. (2008), Yamagishi et al. (1999) used the same correlation as Wang et al. (2007)

5. Delgado et al. (2012)

Pressure drop was measured and compared with the predictions by Darcy-Weisbach equation and steady flow energy equation given in Eqs. (2.47) and (2.49). Friction value for laminar flow was calculated by Hagen Poiseuille equation and for turbulent flow (3000<Re<20000) the Blasius equation was utilized.

6. Roy and Avanic (2001):

$$\frac{1}{\sqrt{f}} = 0.8686 \ln\left(\frac{Re}{1.964 \ln Re - 3.8215)}\right) \tag{2.53}$$

where $Re = u_{\mathrm{m}}D/\mu$ is Reynolds number, u_{m} is fluid velocity and D is diameter of circular channel.

2.9 Summary

The detailed literature review shows that the use of mPCM slurry as a heat transfer fluid enhances convective heat transfer. An extensive experimental and numerical data are available for analysing the heat transfer characteristics of mPCM slurry flow in macrochannels. A few experimental studies have been reported for evaluating the heat transfer performance of mPCM slurry in microchannels. These studies were carried out under constant heat flux boundary condition. In the present investigation, convective boundary condition is chosen to evaluate the heat transfer performance of mPCM slurry.

In previous experimental studies, heat transfer performance of mPCM slurry flow in microchannels was analysed by determining average heat transfer coefficients. No experimental data have been reported for analysing the local heat transfer behaviour of mPCM slurry flow in microchannels. In the present study, a test rig is designed and build to provide accurate methods for local heat transfer measurements. The local surface temperature and local heat flux along the flow direction of microchannel are determined using the inverse solution of heat conduction equation (Yu et al. (2014)) and linear fittings from temperatures measured at nighty eight precisely known locations. The literature review also depicts that three empirical correlations have been reported for the prediction of average Nusselt number for mPCM slurry flow in channels under constant heat flux boundary condition. An empirical correlation is developed for mPCM slurry flow in microchannels under convective boundary condition based on the experimental data obtained.

Moreover, three dimensional conjugated heat transfer numerical simulation of entire test section was also carried out to closely analyse the mechanisms of solidifying and melting of mPCM slurry flow inside the microchannels. Furthermore, the literature review shows

that heat transfer characteristics during the freezing of mPCM slurry in microchannels has not been investigated yet. Therefore, in this present study numerical simulation of three dimensional conjugated heat transfer during the freezing of mPCM slurry is also investigated. To further elaborate the effect of geometrical parameters of microchannel heat sink on heat transfer and pressure drop characteristics, a numerical study is conducted for various geometric cross sections of microchannels. The effect of height and width of separating wall of microchannel is also investigated.

Chapter 3

Apparatus and Experimental Procedure

This chapter describes the design, manufacturing, and assembly of the test section, loops of the mPCM slurry flow and heating water, measurements of flow rate, pressure drop and temperature and the data acquisition system.

3.1 Test system

The schematic of the apparatus for measuring heat transfer of mPCM slurry flow in microchannels is shown in Figure 3.1. The photograph of the apparatus is shown in Figure 3.2. The apparatus consists of two loops; the flow of the working fluid (e.g. mPCM slurry) inside the microchannels and the flow of the hot water inside the upper and lower jackets amounted to the test section. Two thermostat reservoirs, water mixers, mixing chambers, test section and flow meters were used. One reservoir thermostat (Ecogold 10) acted as mPCM slurry reservoir. The working fluid was pumped from the thermostat at a set temperature towards the upstream mixing chamber where the inlet temperature of working fluid was measured. An auxiliary coolant loop was placed inside the working fluid thermostat to remove the excess heat and kept the thermostat at a desired constant temperature . The mass flow rate of working fluid was controlled and measured with an acrylic flow meter. At the exit of the inlet mixing chamber, the working fluid entered in the test section and was distributed into six microchannels. The hot water flowed counter-current in the upper and lower nylon jackets mounted to the test section. The working fluid absorbed heat from the hot water. A differential pressure transducer was installed between the upstream and downstream of microchannels to measure the pressure drop

across the microchannels. The working fluid left the test section and returned back into the thermostat.

For the hot water loop, distilled water was controlled/maintained at a constant temperature set in the thermostat. The hot water was divided into two streams, the mass flow rates of the two water streams were controlled to be the same by two valves and two acrylic flow meters. At the exit of acrylic flow meter, hot water entered into water mixers for proper mixing of water. The inlet temperature of the hot water was measured inside the water mixers by two T-type thermocouples. The hot water left the water mixer and entered into upper and lower nylon jackets. At the exit from the nylon jackets, hot water flowed into downstream water mixers. The outlet temperature of hot water was measured by two T-type thermocouples. The hot water finally returned back to the thermostat.

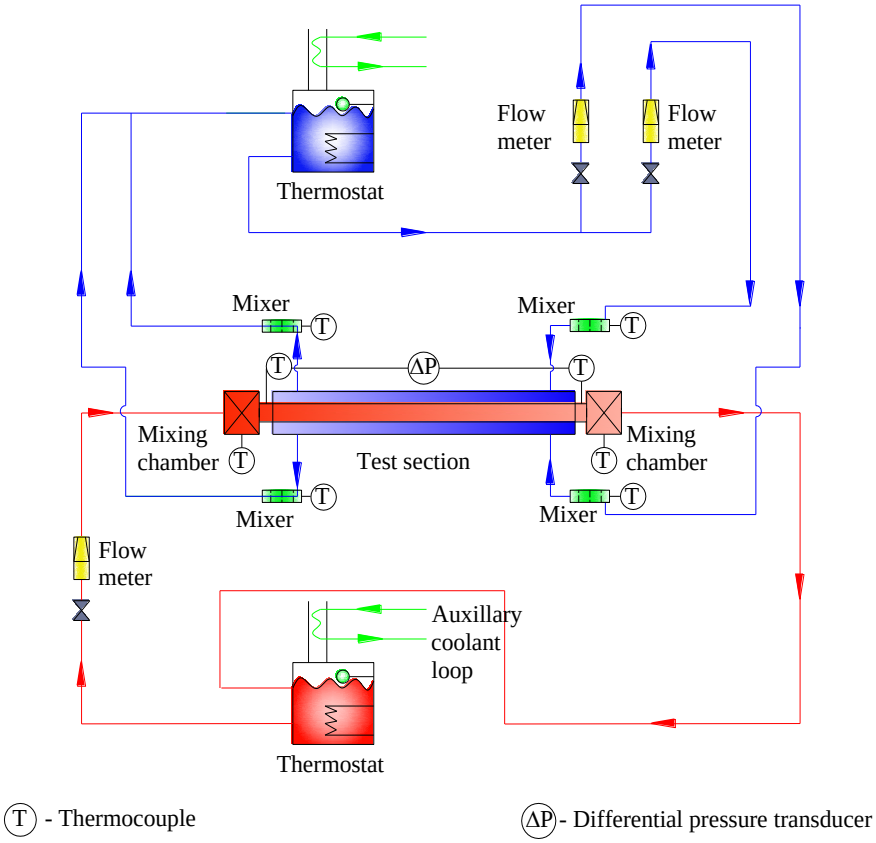

Figure 3.1 Schematic of test rig

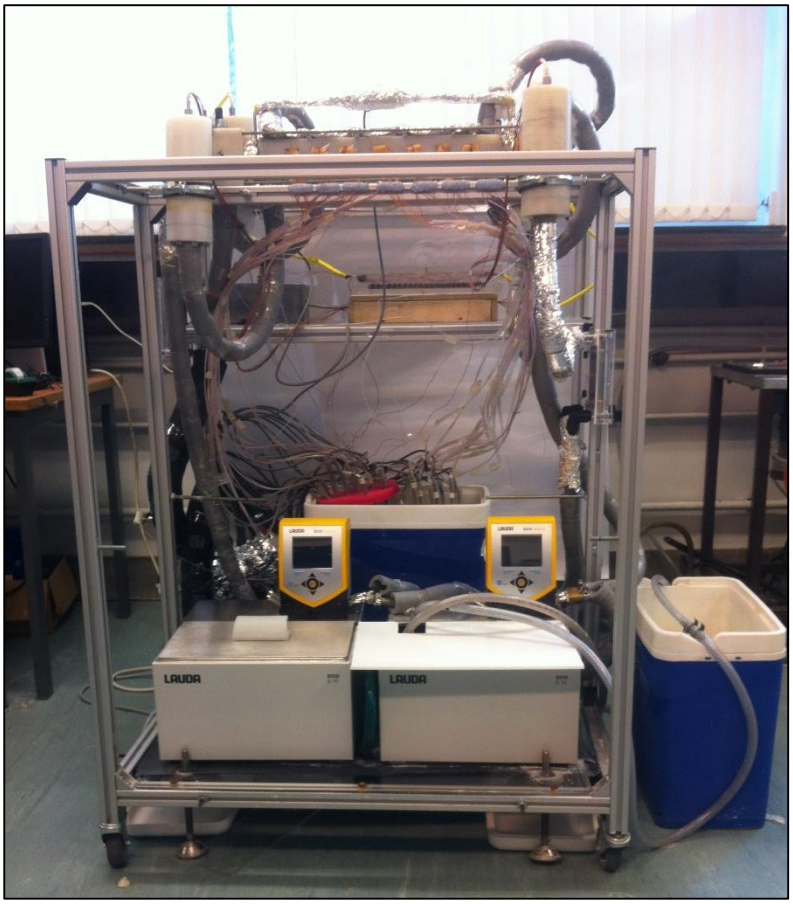

Figure 3.2 Photograph of test rig

3.2 Test section

Figure 3.3 and Figure 3.4 show the cross section and photograph of the test section. It consisted of two aluminium blocks (Part A and Part B) of length 500 mm, width 40 mm and height 15 mm as shown in Figure 3.5 to Figure 3.8. Six microchannels of width 1mm and height 1.5 mm were machined on the lower half (Part B) of the aluminium block as shown in Figure 3.8. The wall thickness between the microchannels was about 1.5 mm. Ninety eight thermocouple holes of diameter 0.6 mm were drilled at the depth of 20 mm at precisely known locations (z = 85, 138, 197, 257, 382, and 415 mm) along the length of the aluminium block. An O-ring was placed inside the matting blocks to prevent the leakage of working fluid.

The local heat flux and local surface temperature were obtained by the inverse heat conduction method based on temperature measurements inside the test block. In order to ensure the uniform temperature measurements along the depth of thermocouple holes, numerical simulation of three dimensional heat conduction for the entire geometry of the test section was carried out. The physical model and its coordinates are shown in Figure 3.9. The constant heat flux of 100 kW/m^2 and constant surface temperature of 297 K was applied to the hot water jackets and microchannel surfaces, respectively.

The temperature contours of numerically simulated symmetric half test section are shown in Figure 3.10. Figure 3.11 represents the isotherms inside the test section at z = 250 mm along the depth of thermocouple holes. The temperature variations along the depth of thermocouple holes at z = 250 mm is shown in Figure 3.12. It shows that the temperature suddenly drops towards the lateral walls of the test section. Thus, it is very important that thermocouples should be properly inserted till the depth of thermocouple holes to ensure the accurate temperature measurements.

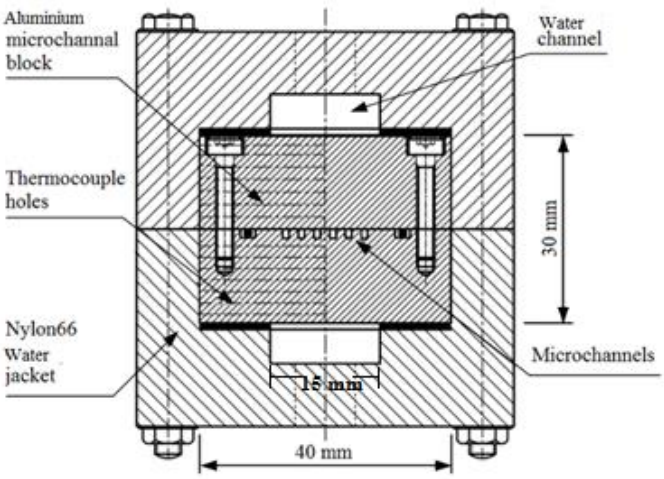

Figure 3.3 Cross section of test section

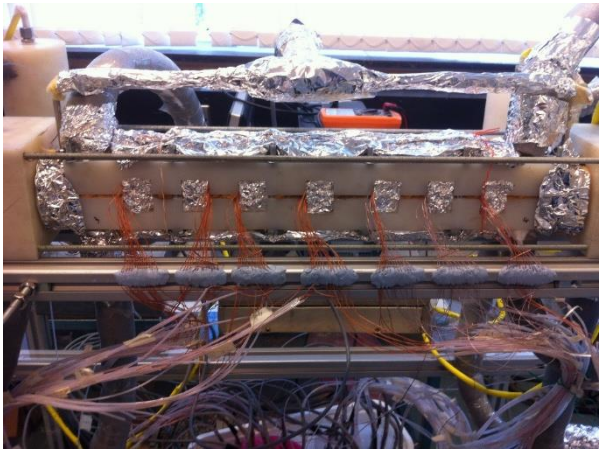

Figure 3.4 Photograph of test section

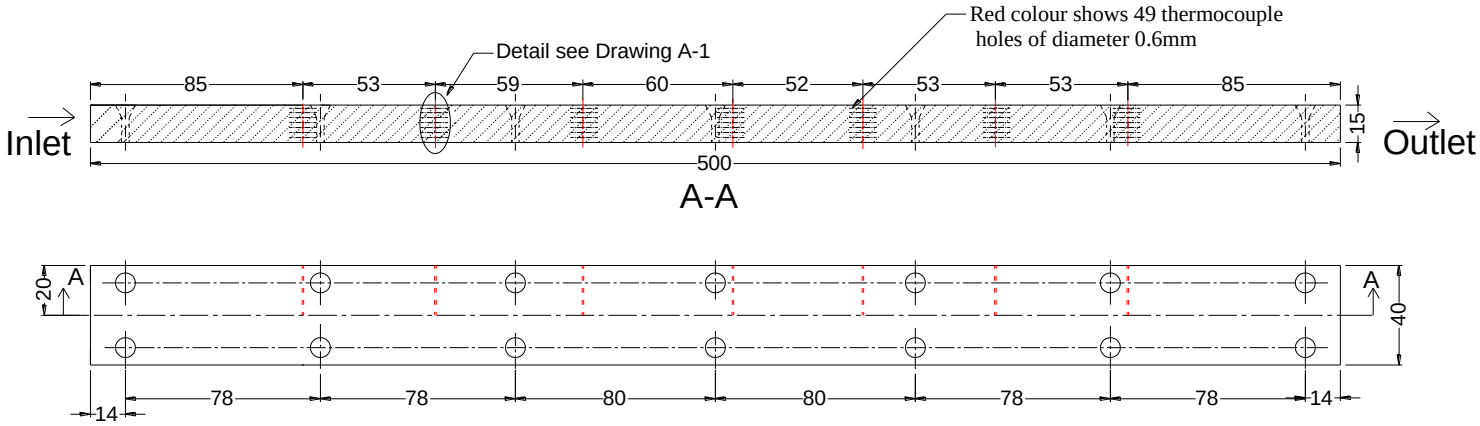

All dimensions are in mm
Tolerance of all dimensions is 0.01mm.

Figure 3.5 Drawing of Part A of aluminium block

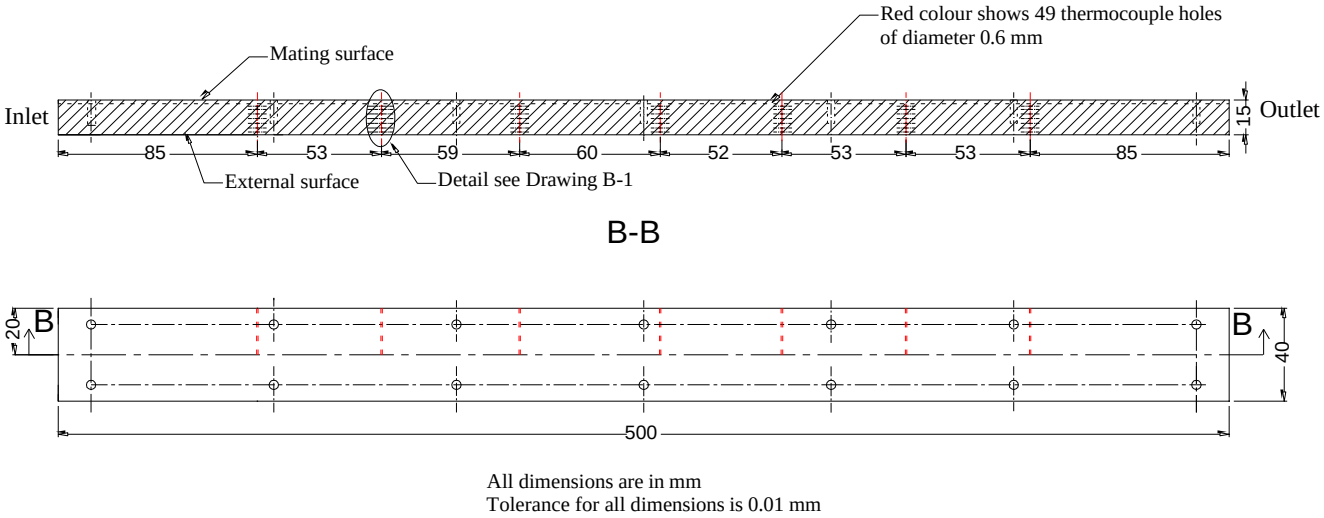

Figure 3.6 Drawing of part B of aluminium block

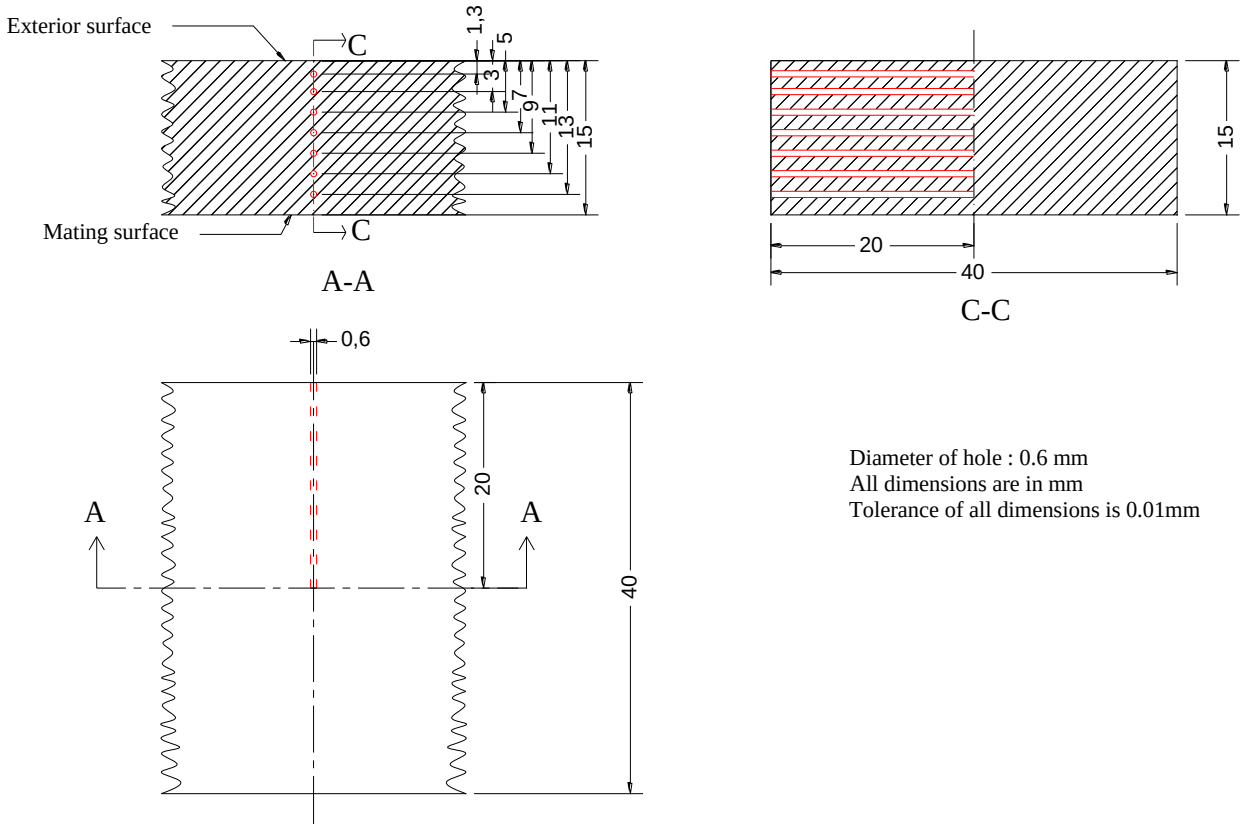

Figure 3.7 Drawing A-1: Details of thermocouple holes in part A

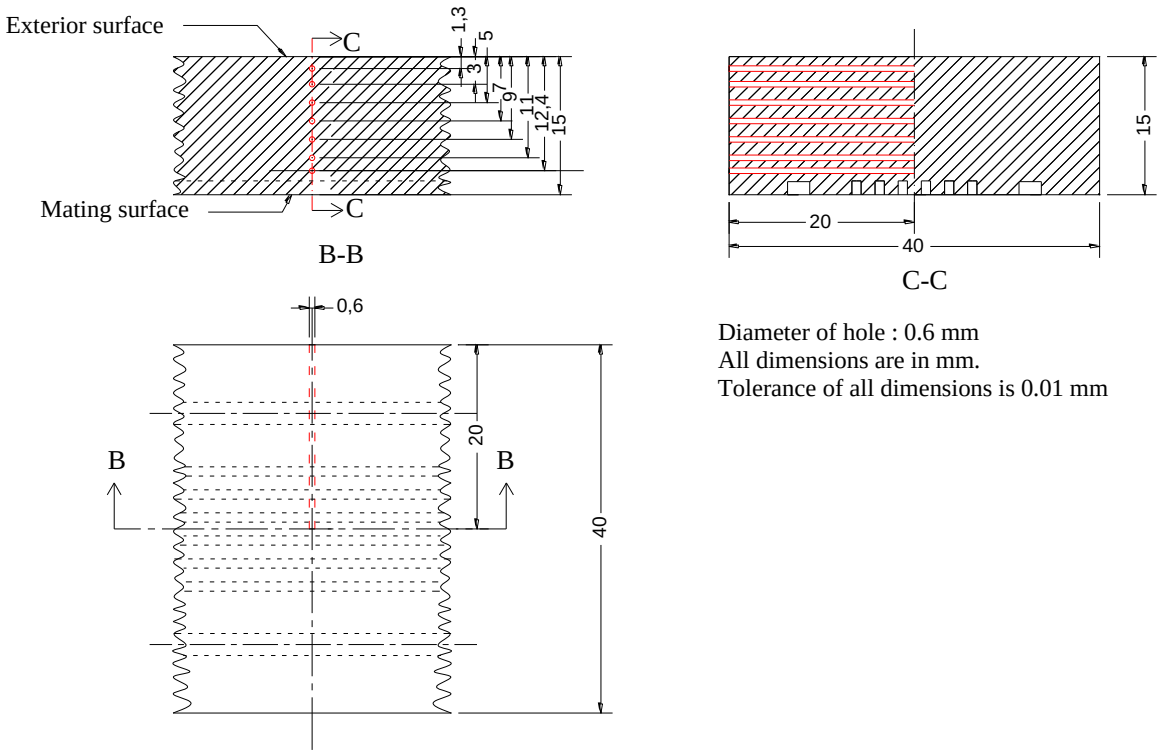

Figure 3.8 Drawing B-1: Details of thermocouple holes in Part B

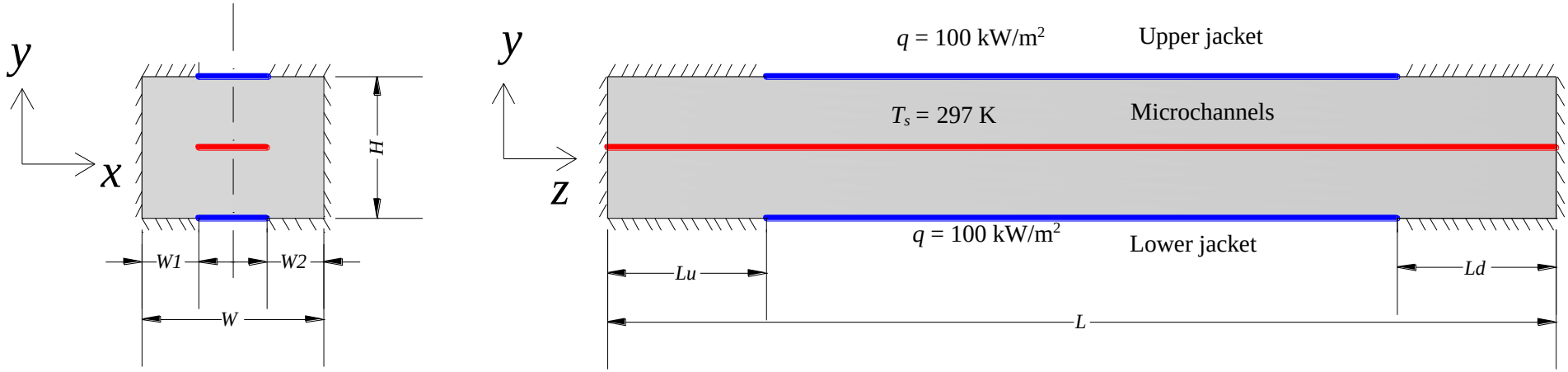

Figure 3.9 Physical model and coordinates

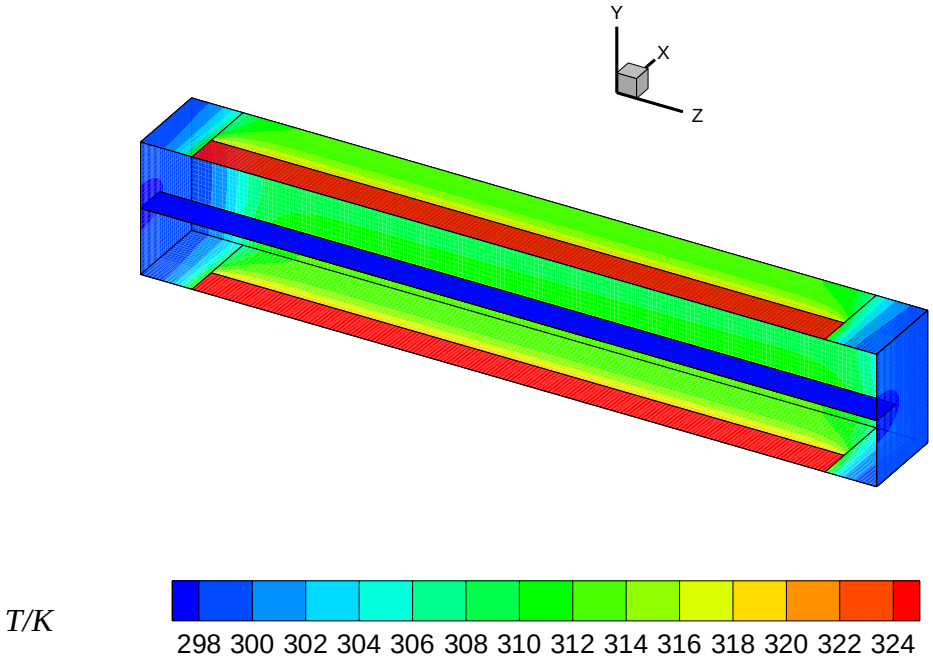

Figure 3.10 Temperature contours for numerically simulated half test section

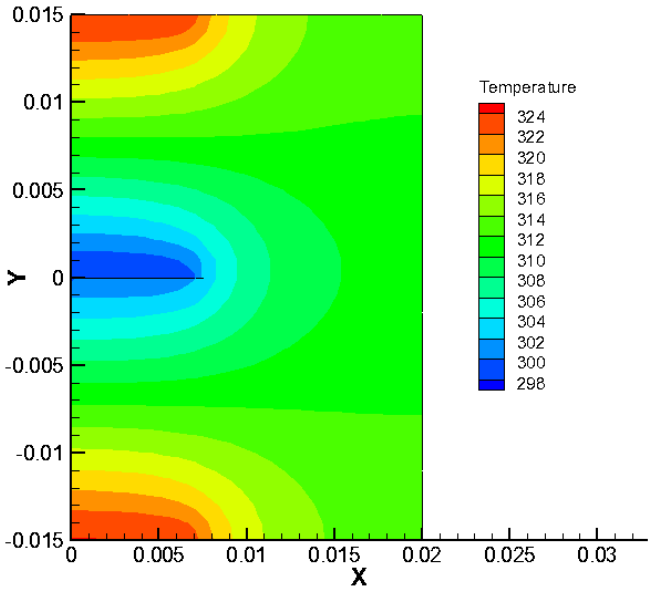

Figure 3.11 Temperature contours along *xy* plane at *z* = 250 mm

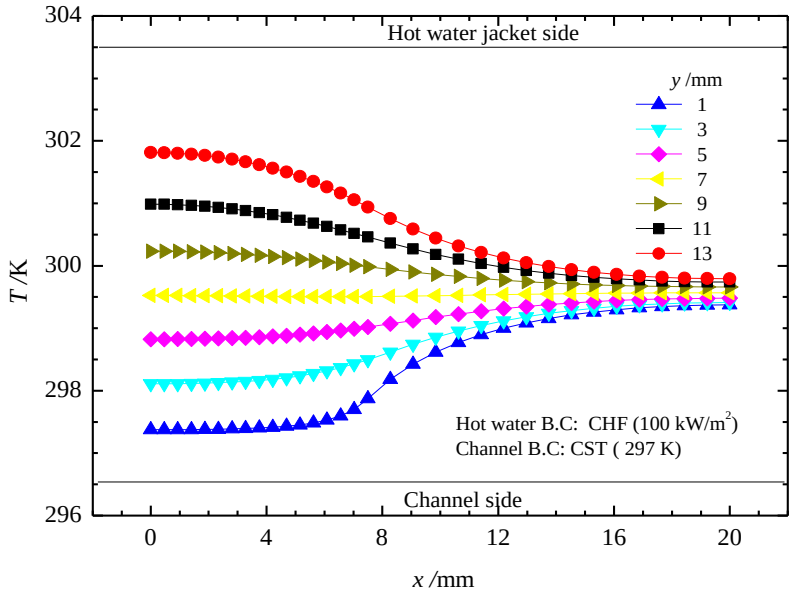

Figure 3.12 Temperature variation along *x* direction at *z* = 250 mm

3.3 Heating water loop

Two identical nylon jackets were manufactured for the flow of hot water at the upper and lower surfaces of aluminium block. Nylon was used to minimize the heat losses to the surroundings. The total length of hot water jacket was 440 mm. A slot of length 430 mm, depth 3 mm and width 15 mm was machined on the inner side of jacket for hot water flow. Gaskets were placed inside the nylon jackets to prevent leakages. The photograph of the nylon jackets amounted on the test section is shown in Figure 3.13. Further details of the cooling jacket are shown in Figure 3.14.

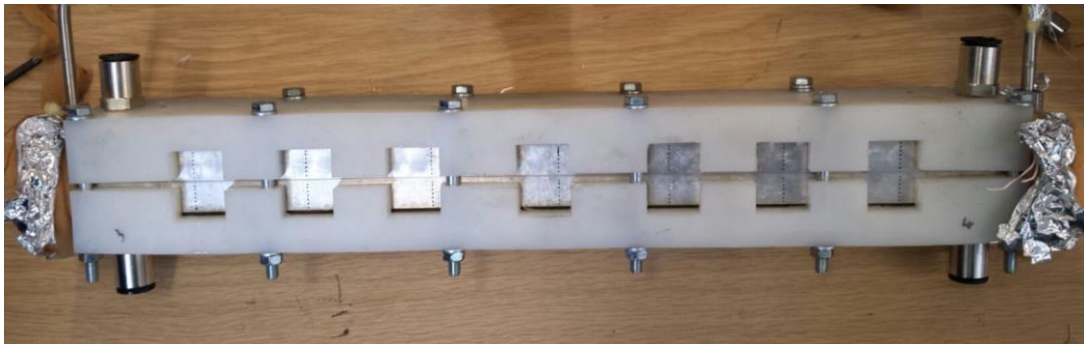

Figure 3.13 Photograph of upper and lower water jackets

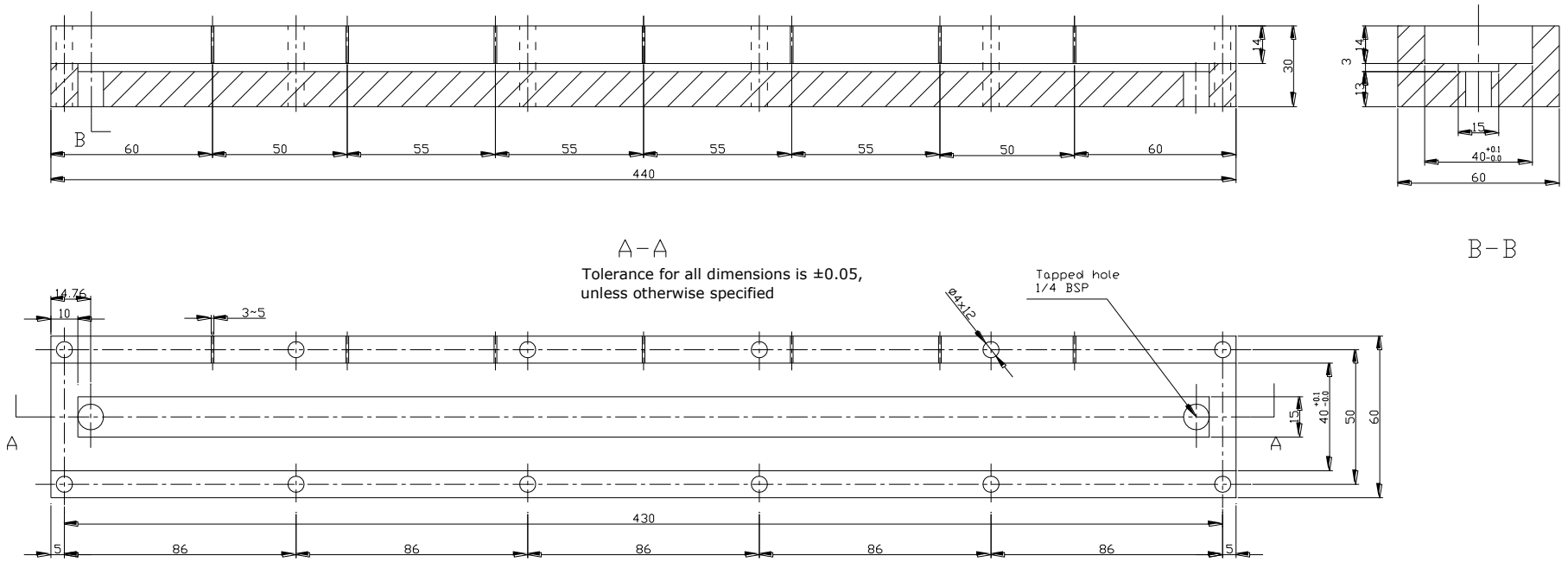

Figure 3.14 Drawing of cooling jacket

3.4 Mixing chambers

Two mixing chambers made up of nylon were manufactured to ensure the proper mixing of water/mPCM slurry. The temperature at the inlet and outlet of the microchannel were measured by two T-type thermocouples inserted inside the mixing chambers. The photograph of the mixing chamber is shown in Figure 3.15. The detailed drawings of the mixing chambers are shown in Figure 3.16 and Figure 3.17.

Figure 3.15 Photograph of mixing chamber

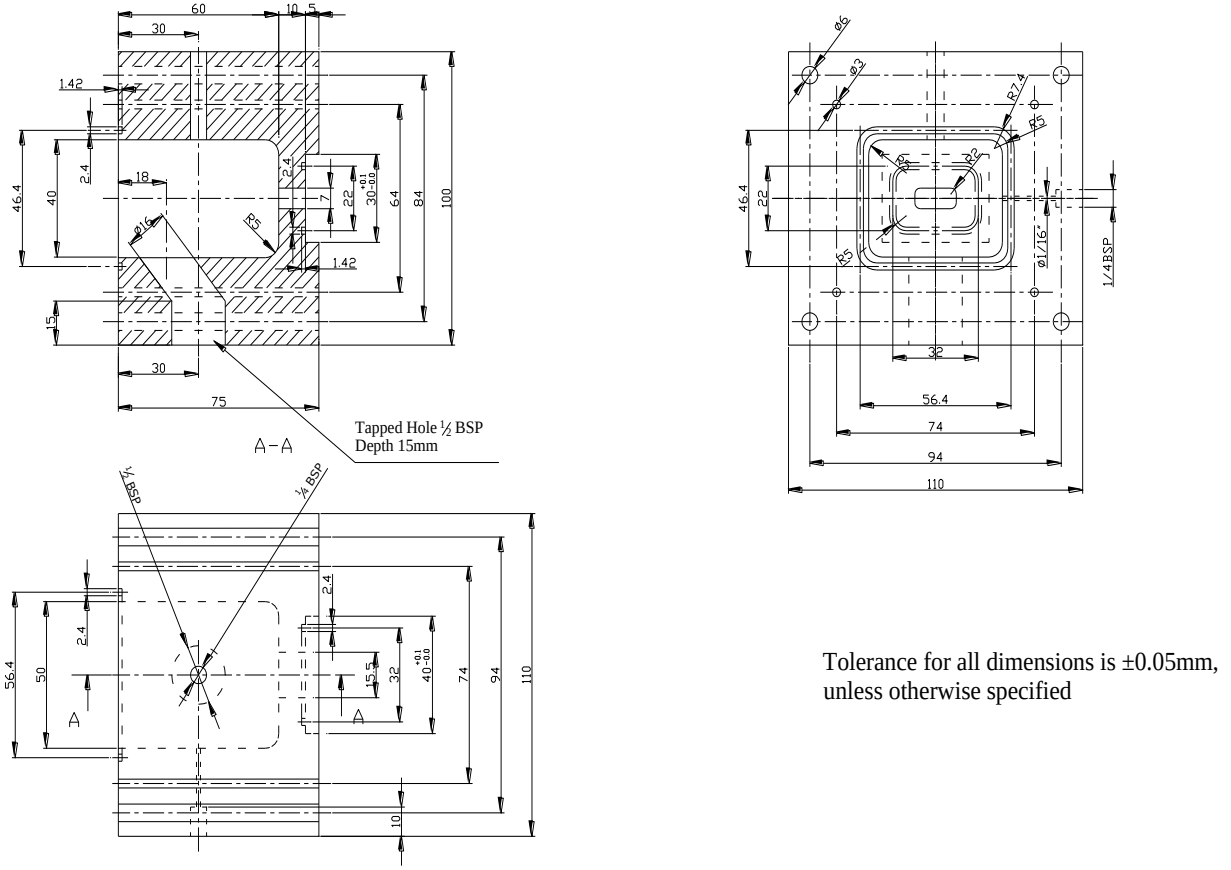

Tolerance for all dimensions is ±0.05mm,
unless otherwise specified

Figure 3.16 Drawing of inlet mixing chamber

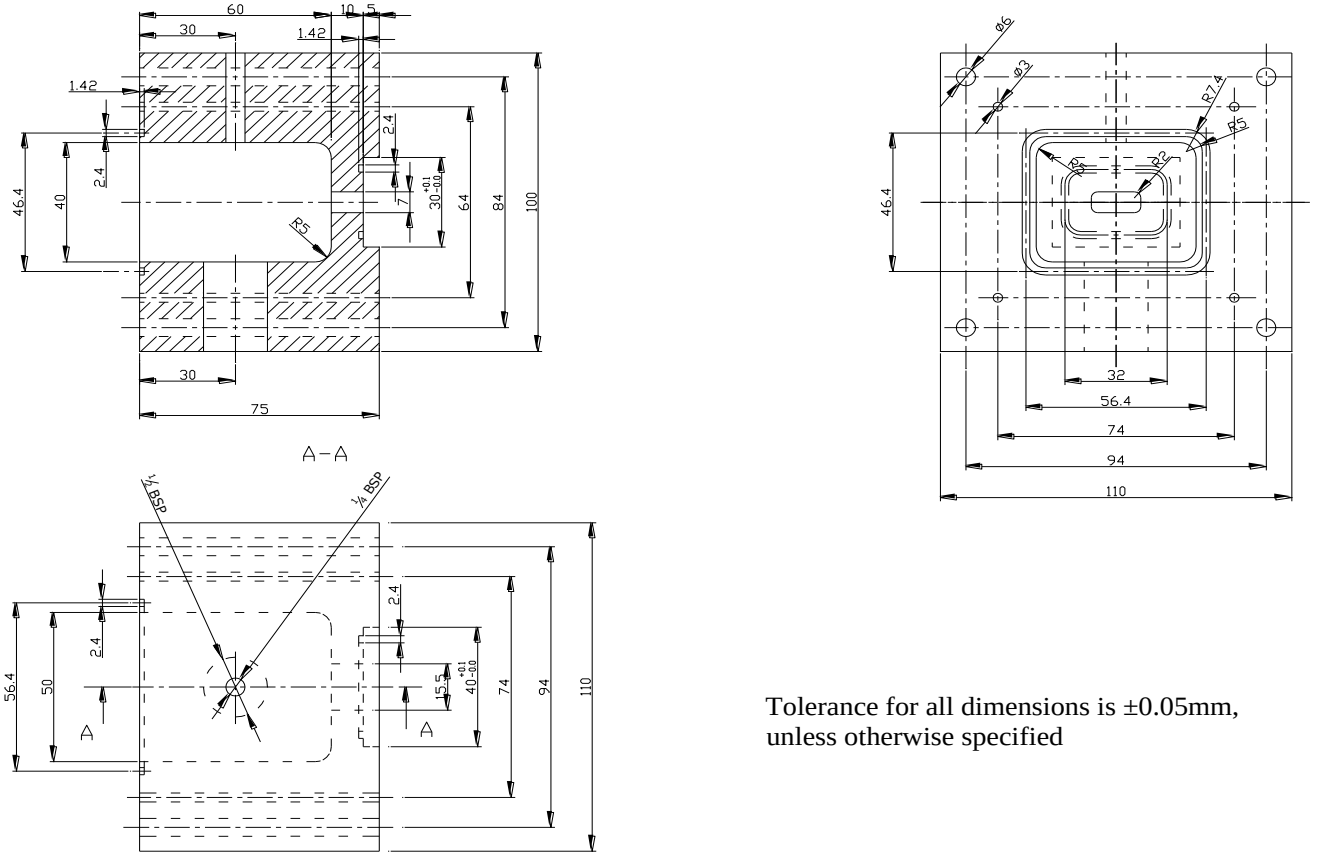

Tolerance for all dimensions is ±0.05mm, unless otherwise specified

Figure 3.17 Drawing of outlet mixing chamber

3.5 Heating water loop mixers

Two water mixers were used at the inlet and outlet of each jacket to ensure the proper mixing of water. The photograph of the water mixer is shown in Figure 3.18. These water mixers were originally designed by Krishnaswamy et al. (2005). They were made up of nylon to reduce the heat losses to the surroundings. The detailed drawing of water mixer is shown in Figure 3.19. It consisted of four baffle plates made of brass. Eight and five numbers of holes were drilled on baffle A and baffle B, respectively. The arrangement of the holes was such that it changed the direction of flow from the wall to the centre of the tube and vice versa. The baffle plates were placed at specific positions by using copper supports. Two T-type thermocouples were placed inside the water mixers to measure the temperature difference of hot water.

Figure 3.18 Photograph of water mixer

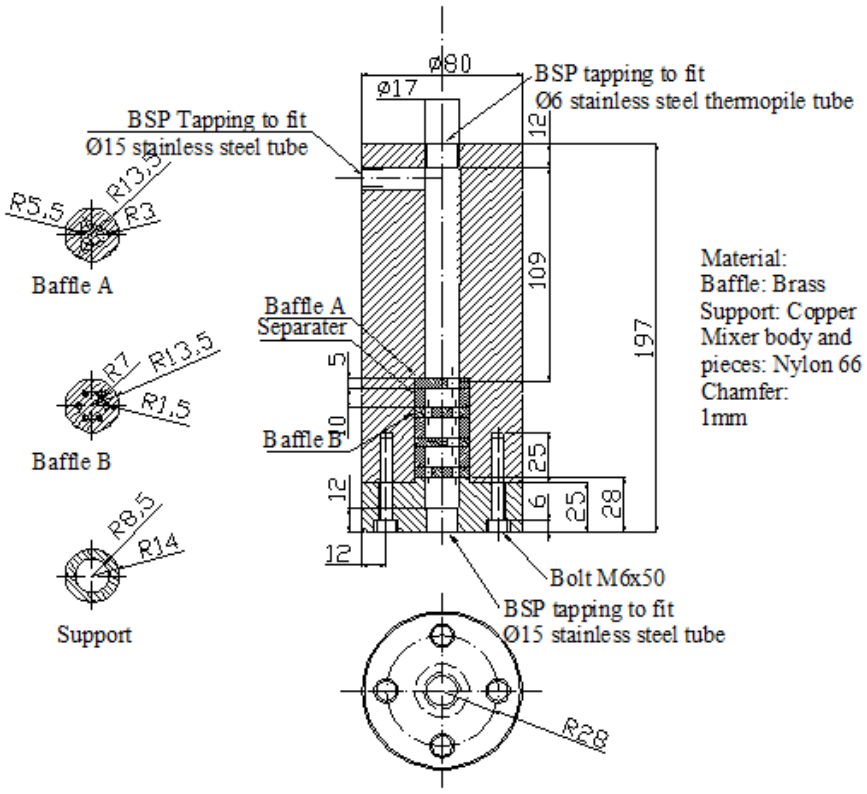

Figure 3.19 Drawing of water mixer

3.6 Thermocouples

T-type thermocouples were used for temperature measurement. Thermocouples were made from a reel of T type thermocouple wire from Omega. The nominal size of the wire was 0.4 mm × 0.7 mm. The wiring arrangement of thermocouple is shown in Figure 3.20. Copper and constantan wires of thermocouple were soldered to copper wires leading to the data logger. The soldered junctions were placed in glass tubes. These glass tubes were fully immersed in crushed ice and water mixture as shown in Figure 3.21. This ice junction removed any change in emf produced due to the copper lead wires. Thermocouples were calibrated (±0.02 K) against the platinum resistance thermometer accurate to 0.005 K, which was calibrated by the Universal Calibration Laboratories Ltd. (U.K.) in a high accuracy constant temperature bath.

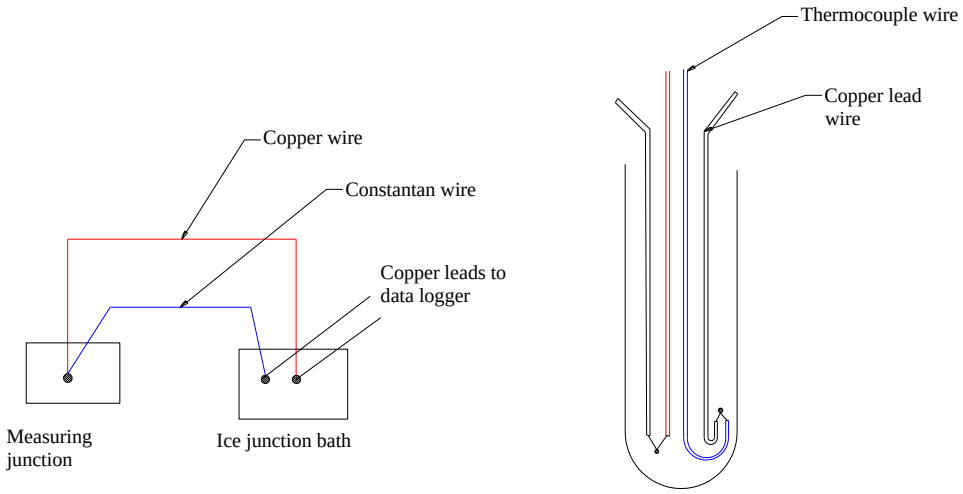

Figure 3.20 Wiring arrangement for thermocouples

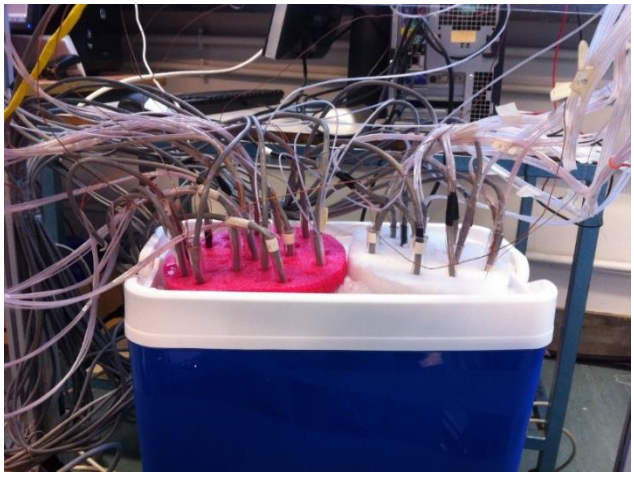

Figure 3.21 Photograph of ice junction

3.7 Pressure measurement

A differential pressure transducer (Druck, PMP 1400 series, accuracy ±0.04%, 0-1.5 bar) was used to measure the pressure drop across the microchannel. A slot of length 16 mm, width 6 mm and depth 4 mm was machined inside the aluminium block to access all microchannels by pressure tapings.

3.8 Flow rate measurement

Flow rates of the mPCM slurry and water were measured and controlled manually by durable acrylic flow meters (Key instruments, FR 4000 series). The range of mPCM slurry flow meter was from 100 ccm to 1500 ccm. The range of hot water flow meters was from 200 ccm to 3000 ccm. The full scale accuracy for both acrylic flow meters provided by manufacturer was ±2%.

3.9 Data acquisition

All measured data were recorded by Agilent 34980A data logger with two Agilent 34922A cards each having seventy channels. The photograph of the data logger is shown in Figure 3.22.

Figure 3.22 Photograph of Agilent 34980A model

All temperature and pressure measurements were recorded after the system reached to steady state. The steady state was usually achieved after thirty to forty minutes. The temperature and pressure measurements were monitored through Labview program. The screenshots of Lab view program is shown in Figure 3.23.

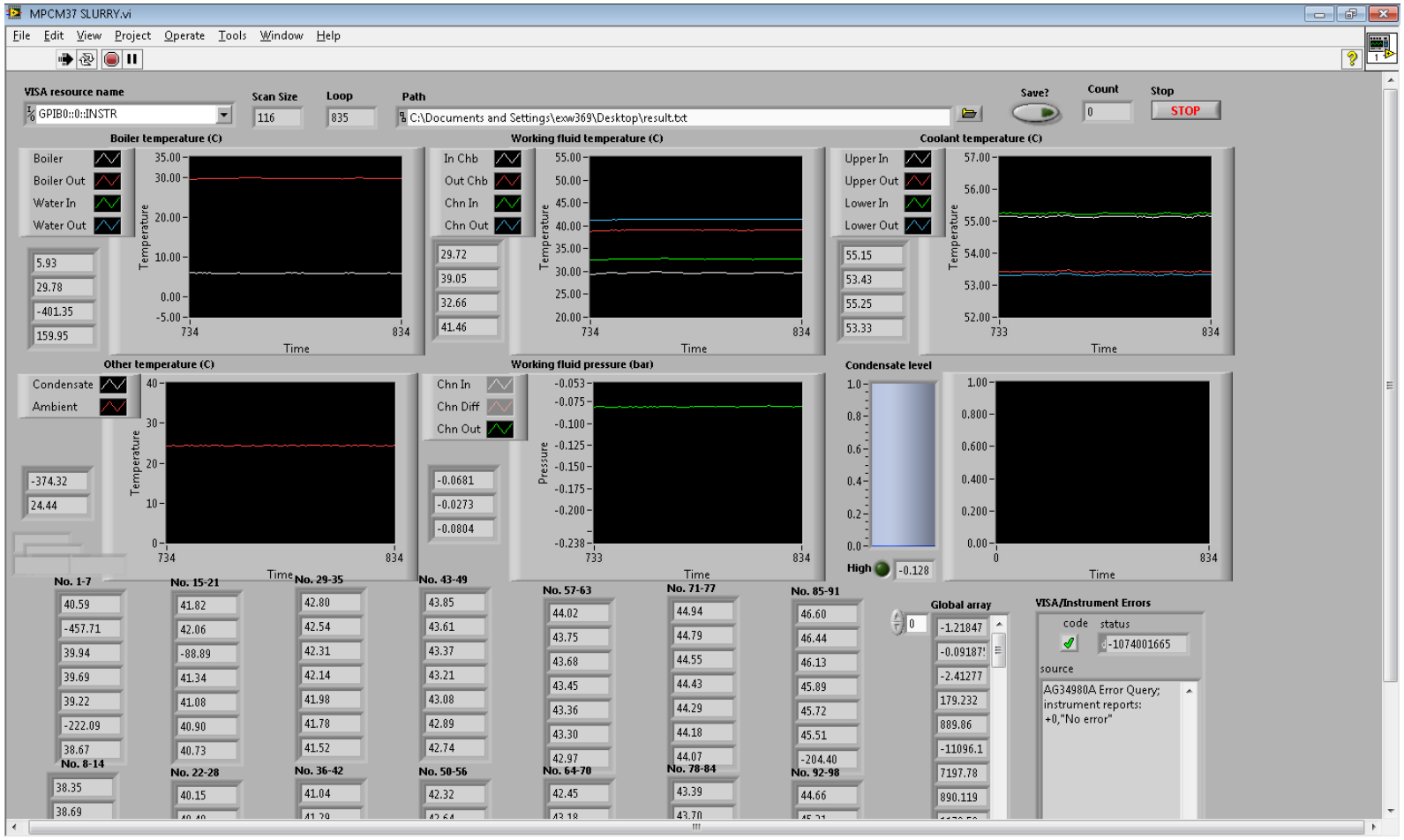

Figure 3.23 Screenshot of Labview program

3.10 Assembly of test rig

Valueframe aluminium profile (series 6) was chosen for making of supporting frame because of ease of mantle and dismantle. Profile 6 connectors (angle 30x30) were used to connect the profiles together. The components of test rig were connected together by nylon tubing of 10 mm diameter and quick fit fittings from RS online.

3.11 Commissioning of experimental setup

Before the start of the experiments, commission of test rig was done. Distilled water was circulated through both the jackets and microchannel loops. Leakage was observed between the mixing chamber and inlet side of microchannels. Gaskets were placed between mixing chambers and inlet side of microchannels to prevent the leakages. Test rig was run with distilled water in both loops for two days to make ensure there was no leakage. After leakage test, all thermocouples were marked at the depth of 20 mm to make sure that they were inserted till the depth of thermocouple holes. The marking and insertion of thermocouples is shown in Figure 3.24 and Figure 3.25.

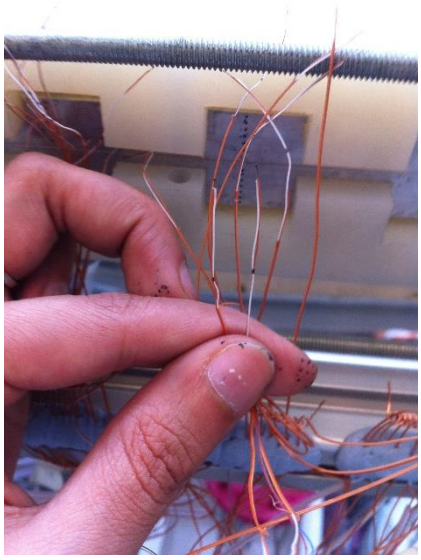

Figure 3.24 Photo of marking of thermocouple wires

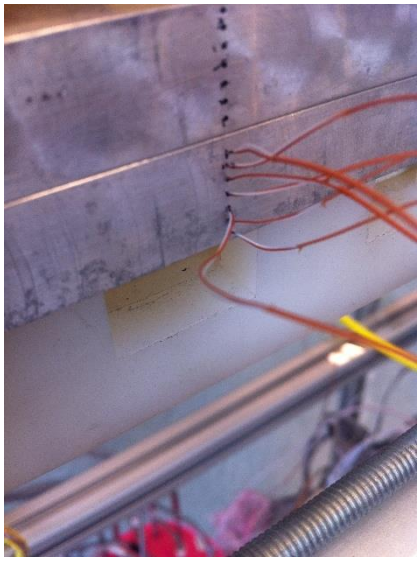

Figure 3.25 Photo of insertion of thermocouples

Then, the apparatus was thermally insulated with thick fibre glass insulation to reduce heat losses to the surroundings. Preliminary tests were performed to measure the heat loss from hot water jacket loop. The details of the heat loss tests are given in Appendix B.

3.12 Procedure for experiment with pure water

Both thermostat baths (Ecogold 10) were filled with distilled water. Thermocouple ice junction box was filled with a mixture of crushed ice and water. An extreme care was taken while setting the glass tubes inside the box so that they were separated from each other and completely immersed in a mixture of ice and water. On heating water loop, the inlet temperature of hot water inside the upper and lower jacket was set in thermostat. The hot water flow rates were adjusted and controlled to the required values by acrylic flow meters.

On working fluid loop, the inlet temperature of the working fluid (water) was set in thermostat. The ambient water temperature was circulated inside the water thermostat through an auxiliary heat exchanger to maintain the set water temperature inside the bath. A simple setup of a mixture of ice and water and heat exchanger was used to further drop down the ambient water temperature circulating inside the auxiliary heat exchanger.

All temperature and pressure readings were taken after the test system reached steady state. For first measurement, the apparatus was left to run for at least one and half hour to reach the steady state. The steady state of the apparatus was observed by Labview program. A normal day experiment consisted of sixteen set of experiments with three inlet temperature of hot water (40 ºC, 45 ºC and 50 ºC) at same mass flow rate (24 g/s) and eight different flow rates of working fluid water ranging from 4.9 g/s to 11.7 g/s.

After completing the full day experiment, the supply of ambient water inside the auxiliary heat exchanger and thermostats were switched off. Glass tubes were removed from the

ice and water junction to avoid the condensation inside the glass tubes. After two days experiments were repeated under similar conditions to verify the repeatability. A good repeatability results were obtained.

3.13 Procedure for experiment with mPCM slurry

Experiments were conducted with two types of mPCM slurries 1) Micronal DS5037X slurry 2) mPCM-37 slurry. Before starting experiments with mPCM slurry, mPCM slurry of required concentration of 5% and 10% was prepared by diluting the slurry with distilled water. The volume of diluted water for mPCM slurry was calculated by the following method.

Mass concentration of mPCM slurry is defined by Eq. (3.1)

$$c\ (\%) = \frac{m_{\mathrm{mPCM}}}{m_{\mathrm{slurry}}} \tag{3.1}$$

where $m_{\mathrm{mPCM}} = \rho_{\mathrm{p}} V_{\mathrm{p}}$ is the mass of mPCM particles, ρ_{p} and V_{p} are density and volume of mPCM particles, $m_{\mathrm{slurry}} = \rho_{\mathrm{p}} V_{\mathrm{p}} + \rho_{\mathrm{w}} V_{\mathrm{w}}$ is the mass of slurry, ρ_{w} and V_{w} are the density and volume of water.

$$c_1 = \frac{\rho_{\mathrm{p}} V_{\mathrm{p}}}{\rho_{\mathrm{p}} V_{\mathrm{p}} + \rho_{\mathrm{w}} V_{\mathrm{w}}} \tag{3.2}$$

where c_1 is the 42% and 37% mass concentration of slurry from suppliers BASF and Microtek, respectively, ρ_{p} and V_{p} are density and volume of mPCM slurry, ρ_{w} and V_{w} are the density and volume of water.

$$c_2 = \frac{\rho_p V_p}{\rho_p V_p + \rho_w (V_w + \Delta V_w)} \tag{3.3}$$

where c_2 is the required mass concentration of diluted sample, and ΔV_w is the volume of distilled water to be added in sample to make the required concentration. Mass of mPCM particles remains same in both the concentrations so by comparing Eqs. (3.2) and (3.3).

$$c_1(\rho_p V_p + \rho_w V_w) = c_2(\rho_p V_p + \rho_w V_w) + c_2(\rho_w \Delta V_w) \tag{3.4}$$

Dividing Eq. (3.4) by $\rho_p V_p + \rho_w V_w$

$$c_1 = c_2 + \frac{c_2(\rho_w \Delta V_w)}{\rho_p V_p + \rho_w V_w} \tag{3.5}$$

where $m_{slurry} = \rho_p V_p + \rho_w V_w = \rho_{slurry} V_{slurry}$, so Eq. (3.5) becomes

$$c_1 = c_2 + \frac{c_2(\rho_w \Delta V_w)}{\rho_{slurry} V_{slurry}} \tag{3.6}$$

The volume of the distilled water given by Eq. (3.7) was added to the mPCM slurry for making the required mass concentration.

$$\Delta V_w = \frac{(c_1 - c_2)\rho_{slurry} V_{slurry}}{c_2 \rho_w} \tag{3.7}$$

The improper mixing of mPCM slurry in diluted water may cause the blockage of microchannels. In order to form the uniform mixture of mPCM slurry, the mixing of mPCM slurry with distilled water was done by magnetic stirrer. The mixture of mPCM slurry and distilled water was stirred for twenty minutes. The photograph of stirring of mPCM slurry by magnetic stirrer is shown in Figure 3.26.

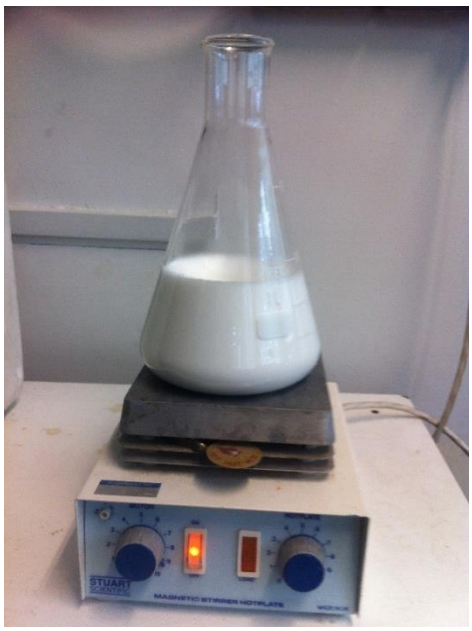

Figure 3.26 Photograph of dilution of mPCM slurry with magnetic stirrer

After preparation of mPCM slurry, thermostat bath was filled with mPCM slurry. The inlet temperature of mPCM slurry was set in thermostat panel. The volume flow rate of the mPCM slurry was adjusted and controlled by an acrylic flow meter ranging from 200 ccm to 1000 ccm. The experiments were performed under the same operating conditions as that of water. After one day of experiments with mPCM slurry, the drop in the volume flow rate on mPCM slurry loop was observed which indicated the possible blockage of microchannels. The microchannels was found to be blocked. The test section was opened and thoroughly cleaned with distilled water. After this incident at the end of the full day experiment, mPCM slurry was removed from thermostat bath. The apparatus was run for half an hour with distilled water to avoid any sort of mPCM slurry deposition inside the microchannels.

Chapter 4

Data Processing

This chapter describes the methods used for finding the various experimental parameters. The thermophysical properties of mPCM slurry were calculated by Eqs. A.1 to A.4 given in Appendix A.

4.1 Measured quantities

The following quantities were measured and recorded for each experimental test run.

1. Ambient temperature
2. Volume flow rates of hot water in upper and lower jackets
3. Volume flow rate of working fluid (Water/mPCMslurry)
4. Differential pressure drop across the microchannels
5. Temperatures at the inlet and outlet mixing chambers
6. Temperatures at the inlet and outlet of hot water upper and lower jackets
7. Temperature measurements at 98 locations using T-type thermocouple

4.2 Local surface temperature and local heat flux

The local surface temperature and local heat flux were determined and compared by two methods:

1. By inverse heat conduction solution of Yu et al. (2014)

2. Linear and polynomial fittings of temperature measured at 98 locations.

4.3 Energy balance

4.3.1 Heat transfer rate measured at microchannel side by inverse method

The heat transfer rate, $Q_{\mathrm{ch,inv}}$ measured at microchannel side by inverse method was calculated by Eq. (4.1)

$$Q_{\mathrm{ch,inv}} = 2n(a+b)\int_0^{L_{\mathrm{ch}}} q_{\mathrm{z,ch,inv}}\,dz \tag{4.1}$$

where n is the number of microchannels, a is the width of microchannel and b is the height of microchannel.

4.3.2 Heat transfer rate of jacket side by measuring flow rate and temperature rise

The heat transfer rate to the upper, $Q_{\mathrm{jac,up,\Delta T}}$, and lower, $Q_{\mathrm{jac,low,\Delta T}}$, jacket sides were calculated by Eqs. (4.2) and (4.3).

$$Q_{\mathrm{\Delta T,j,up}} = m_{\mathrm{h,in,up}} Cp_{\mathrm{w}} \Delta T_{\mathrm{j,up}} \tag{4.2}$$

$$Q_{\mathrm{\Delta T,j,low}} = m_{\mathrm{h,in,low}} Cp_{\mathrm{w}} \Delta T_{\mathrm{j,low}} \tag{4.3}$$

where $m_{\mathrm{h,in,up}}$ and $m_{\mathrm{h,in,low}}$ are the mass flow rates of hot water flowing in upper and lower jackets, respectively, Cp_{w} is the specific heat capacity of water, $\Delta T_{\mathrm{j,up}}$ and $\Delta T_{\mathrm{j,low}}$ are the temperature rise of water in upper and lower jackets, respectively.

4.3.3 Heat transfer rate of microchannel side by measuring flow rate and temperature rise

The heat transfer rate to the water, $Q_{\mathrm{\Delta T+l,ch}}$, was calculated by Eq. (4.4)

$$Q_{\Delta T+l,ch} = m_{f,in} Cp_w \left(T_{out,ch} - T_{in,ch}\right) + Q_{loss,jac} \quad (4.4)$$

where $m_{f,in}$ is the inlet mass flow rate of working fluid (water). $T_{out,ch}$ and $T_{in,ch}$ are the outlet and inlet temperatures of microchannel, respectively.

The heat transfer rate to the mPCM slurry is the combination of sensible heat and latent heat. The heat transfer rate to the mPCM slurry, $Q_{s,ch}$ was obtained by Eq. (4.5).

$$Q_{s,ch} = m_{f,in} Cp_b \left(T_{out,ch} - T_{in,ch}\right) + m_{f,in} ch_{fs} + Q_{loss,jac} \quad (4.5)$$

where $m_{f,in}$ is the inlet mass flow rate of working fluid (mPCM slurry), c is the mass concentration of mPCM slurry, and h_{fs} is the latent heat of mPCM slurry.

4.4 Local Nusselt number

The local heat Nusselt number, Nu_z, for working fluid was determined by Eq. (4.6)

$$Nu_z = \frac{q_z D_h}{(T_{w,z} - T_i) k_b} \quad (4.6)$$

where q_z is local heat flux determined by linear fitting, $T_{w,z}$ is local surface temperature determined by linear fittings of temperatures measured inside the block, and T_i is the inlet temperature of working fluid.

4.5 Average Nusselt number

Nusselt number based on average heat transfer coefficient is given by Eq. (4.7).

$$Nu = \frac{h_{\mathrm{av}} D_{\mathrm{h}}}{k_{\mathrm{b}}} \tag{4.7}$$

where $h_{\mathrm{av}} = q_{\mathrm{av}}/(T_{\mathrm{w,av}} - T_{\mathrm{b}})$ is average heat transfer coefficient of slurry, $D_{\mathrm{h}} = 2ab/(a+b)$ is the hydraulic diameter of microchannel, a and b are the width and height of microchannel respectively, k_{b} is bulk thermal conductivity of mPCM slurry.

4.6 Fanning friction factor

Hydraulic performance of mPCM slurry was evaluated by fanning friction factor given by Eq. (4.8)

$$f = \frac{D_{\mathrm{h}} \Delta P}{2 L \rho_{\mathrm{b}} u_{\mathrm{m}}^2} \tag{4.8}$$

where ΔP is pressure drop measured by differential pressure transducer, L is distance between two pressure tapings, ρ_{b} is bulk density of slurry, u_{m} is the mean fluid velocity in microchannel.

The working fluid properties was calculated by linear interpolation of thermophysical properties of water at bulk temperature given in Eq. (4.9)

$$T_{\mathrm{bulk}} = \frac{T_{\mathrm{ch,in}} + T_{\mathrm{ch,out}}}{2} \tag{4.9}$$

Mean fluid velocity of working fluid in microchannel was calculated by Eq. (4.10).

$$u_{\mathrm{m}} = \frac{m_{\mathrm{f,in}}}{n A_{\mathrm{ch}} \rho} \tag{4.10}$$

where $m_{\mathrm{f,in}}$ is mass flow rate of working fluid, n is number of microchannels, $A_{\mathrm{ch}} = ab$ is cross sectional area of microchannel, a is width of microchannel, b is height of microchannel and ρ is density of working fluid (water/mPCM).

4.7 Stefan number

Stefan number is one of the important parameter which influences the heat transfer of mPCM slurry. Stefan number is the ratio of sensible heat to the latent heat. It was evaluated by Eq. (4.11) (Zeng et al., (2009)).

$$Ste = \frac{Cp_{\mathrm{b}}(T_{\mathrm{ch,out}} - T_{\mathrm{ch,in}})}{ch_{\mathrm{fs}}} \tag{4.11}$$

where Cp_{b} is the bulk specific heat capacity of mPCM slurry, $T_{\mathrm{ch,out}}$ and $T_{\mathrm{ch,in}}$ are the outlet and inlet temperature of microchannel, *c* is the mass concentration of mPCM slurry and h_{fs} is the latent heat capacity of mPCM slurry.

4.8 Data proccessing for numerical simulation

The area-weighted average method had been used for calculating surface temperature and heat flux at inner wall of channel surface as given in Eqs. (4.12) and (4.13). It is computed by dividing the summation of the product of the selected field variable and facet area by the total area of the surface.

$$T_{\mathrm{w,z}} = \frac{1}{A}\int TdA = \sum_{i=1}^{n} T|A_{\mathrm{i}}| \tag{4.12}$$

$$q_{\mathrm{w,z}} = \frac{1}{A}\int qdA = \sum_{i=1}^{n} q|A_{\mathrm{i}}| \tag{4.13}$$

The average bulk temperature of the working fluid was calculated by the mass weighted average method as given in Eq. (4.14).

$$T_{\mathrm{b,av}} = \frac{\sum_{i=1}^{n} T_{\mathrm{i}} \rho_{\mathrm{i}} |w_{\mathrm{i}}.A_i|}{\sum_{i=1}^{n} \rho_{\mathrm{i}} |w_{\mathrm{i}}.A_i|} \tag{4.14}$$

The Stefan number was calculated by Eq (4.15).

$$Ste = \frac{q}{m h_{\mathrm{fg}}} - 1 \tag{4.15}$$

The dimensionless axial distance was obtained by Eq. (4.16).

$$z^{+} = \frac{z}{rRePr} \tag{4.16}$$

where z is the distance measured along the length of channel.

The local Nusselt number over the length of the microchannel is defined by Eq. (4.17).

$$Nu = \frac{q_{\mathrm{w,z}}\, D_{\mathrm{h}}}{(T_{\mathrm{w,z}} - T_{\mathrm{b,z}}) k_{\mathrm{f}}} \tag{4.17}$$

The heat transfer enhancement ratio due to mPCM slurry flow in microchannel as compared with water is defined as follows:

$$\varepsilon = \frac{h_{\mathrm{pcm}} - h_{\mathrm{w}}}{h_{\mathrm{w}}} \tag{4.18}$$

The thermal resistance for the total width W of the heat sink is determined by Eq. (4.19).

$$R_{\mathrm{th}} = \frac{T_{\mathrm{max}} - T_{\mathrm{in}}}{qWL} \tag{4.19}$$

where $T_{\max}$ is the maximum temperature at the top surface of the heat sink.

The pumping power is calculated by Eq. (4.20)

$$P_{\text{pump}} = nw_{\text{in}}A_{\text{c}}\Delta P \tag{4.20}$$

where A_{c} is the cross-sectional area of the channel, and ΔP is the pressure drop over the length of the channel.

Chapter 5

Heat Transfer and Friction Factor during Pure Water Flow in Microchannels

5.1 Introduction

Experiments were conducted with pure water under the same operating conditions as for mPCM slurry. The purpose of these experiments are as follows.

(a) To validate the experimental setup

(b) To provide data for comparison with data of mPCM slurry

Experiments were conducted with pure water under the same operating conditions as for two types of mPCM slurry i.e. Micronal DS5037X mPCM slurry and Microtek MPCM-37 slurry. On heating water loop the inlet temperature of hot water was varied from 40 ºC to 55 ºC. The mass flow rate of hot water was controlled and adjusted by acrylic flow meters at 17 g/s and 24 g/s. On a working fluid loop, the inlet temperature of the water was maintained at 22 ºC (for comparison with DS5037X slurry), 30ºC and 32 ºC (for comparison with MPCM-37 slurry). For each set of combination, mass flow rate of pure water inside the microchannel was varied from 5 g/s to 11 g/s. Temperature and pressure measurements were obtained after the experimental system reached the steady state.

5.2 Validation of experimental setup

First, the experimental setup was validated by using water as heat transfer fluid for laminar flow. The measured average Nusselt number was compared with available empirical correlations for laminar flow under the constant heat flux and constant surface temperature, respectively. The reliability of experimental setup was also checked by

comparing measured fanning friction factor with available empirical correlation of fanning friction factor for the fully developed flow.

In general, the known empirical correlations are mostly developed for circular channels, but they can be used for non-circular tubes by substituting the channel diameter to the hydraulic diameter $D_{h.}$ The empirical correlations used for comparison of the experimental data are as follows.

The average Nusselt number by Eq. (5.1) was proposed by Kays (1966).

$$Nu = 8.235(1 - 1.88/\alpha + 3.767/\alpha^2 - 5.814/\alpha^3 + 5.361/\alpha^4 - 2/\alpha^5) \quad (5.1)$$

where $\alpha = b/a$ is the aspect ratio of the microchannel, a is the short side of microchannel and b is the long side of the microchannel.

Equation (5.2) was proposed by Incropera and Witt (1996) for thermally developing laminar flow under the constant surface temperature boundary condition.

$$Nu = 3.66 + \frac{0.19(RePrD/L)^{0.8}}{1 + 0.117(RePrD/L)^{0.467}} \quad (5.2)$$

Experimental data were also compared with Shah and London (1978) correlation given by Eq. (5.3) for thermally developing flow under the constant heat flux boundary condition.

$$Nu = 4.364 + 0.0722RePrD/L \qquad \text{for } (\frac{RePrD}{L}) < 33.3 \quad (5.3)$$

where $Re = \rho vD/\mu$ is the Reynolds number and $Pr = C_p\mu/k$ is the Prandtl number.

The thermophysical properties of water were obtained at an average bulk temperature. The linear interpolation based on the water temperature range was used to determine the properties of water at a mean bulk temperature. For example, the inlet temperature of fluid is 23 ºC and the outlet temperature is 33 ºC. The thermophysical properties at average bulk of 28 ºC was obtained by linear interpolation.

Figure 5.1 illustrates the comparison of the calculated average Nusselt number by Eqs. (5.1) to (5.3) with the measured Nusselt number of pure water under the same operating conditions. It shows a good agreement for $Re < 1500$. For $Re > 1500$ it starts deviating from the empirical correlations. There are two likely causes for the differences between the measured and predicted Nusselt number.

1. At higher Reynolds number the flow was not fully developed, it was in thermally developing region due to the short length of the microchannel.
2. The available empirical correlations were based on constant heat flux and constant surface temperature boundary conditions. The present experimental data were obtained under convective boundary condition.

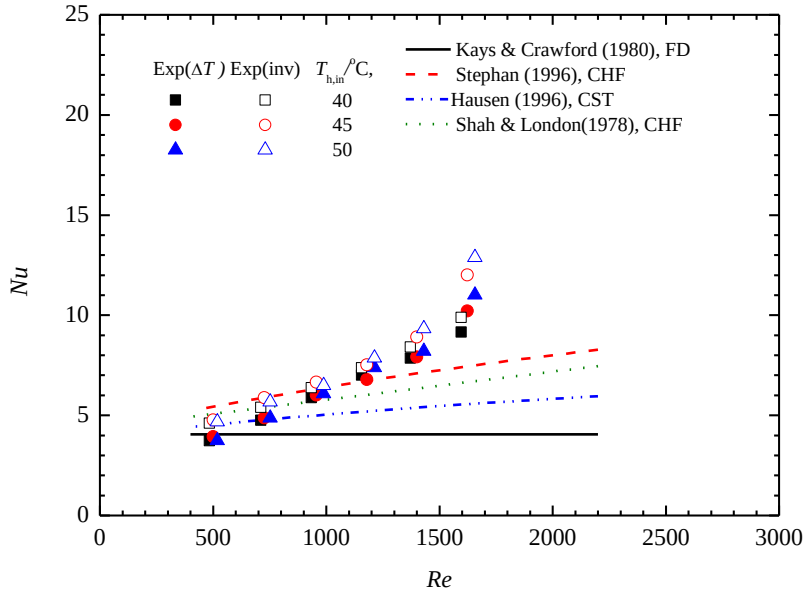

Figure 5.1 Comparison of measured *Nu* of water with empirical correlations (operating conditions for DS5037X slurry)

Figure 5.2 compares the measured Nusselt number of pure water under the same experimental conditions for MPCM-37 slurry with those predicted by Eqs. (5.1) to (5.3). For *Re* > 1500, the measured Nusselt number starts deviating from the empirical correlations because the flow was still developing due to small length of microchannels.

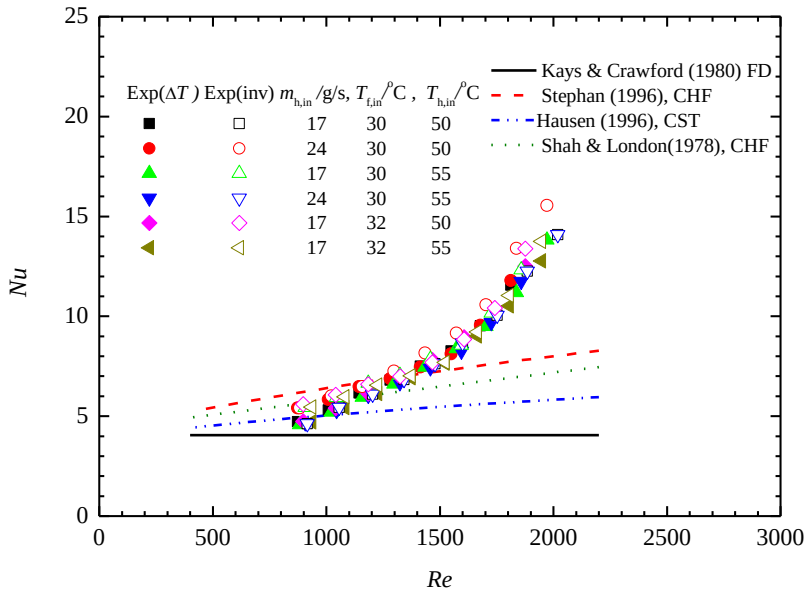

Figure 5.2 Comparison of measured average *Nu* of water under the same operating conditions as for MPCM-37 slurry with empirical correlations

5.3 Validation of pressure drop measurement

The experimental setup was also validated by comparing the fanning friction factor for rectangular and circular channels for fully developed flow given by Eqs. (5.4) and (5.5), respectively.

$$fRe = 0.6796 + 1.2197\alpha + 3.3089\alpha^2 - 9.5921\alpha^3 + 8.9089\alpha^4 - 2.99\alpha^5 \quad (5.4)$$

where α=*a/b* is the aspect ratio of microchannel, *a* is the short side and *b* is the long side of microchannel.

$$f = \frac{64}{Re} \quad (5.5)$$

For fully developed laminar flow, the pressure drop can be determined by Darcy Weisbach Eq. (5.4), given as follows:

$$f = \frac{D_{\mathrm{h}}\Delta P}{2L\rho_w u_{\mathrm{m}}^2} \quad (5.6)$$

where ΔP is the pressure drop measured by differential pressure transducer, L is the length of microchannel between the inlet and outlet pressure tappings, ρ_w is the density of water and u_{m} is the mean velocity of water flowing inside the microchannels.

Figure 5.3 and Figure 5.4 represent the comparison of measured fanning friction factor with the predicted fanning friction factor by Eq. (5.5). The maximum deviation of predicted and measured fanning friction factor was found to be 18.8%. It can be seen from Figure 5.4 that fanning friction factor starts increasing for *Re* > 1500. It is believed that at higher Reynolds number flow was not fully developed.

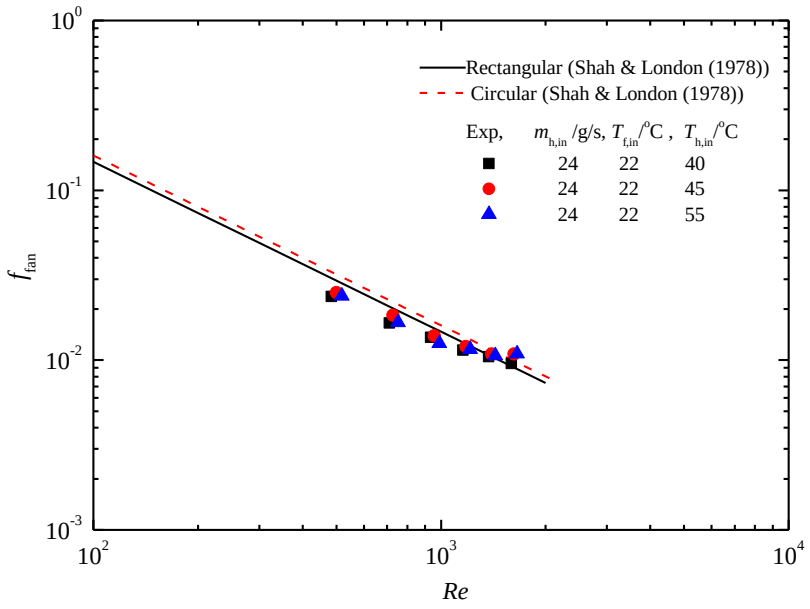

Figure 5.3 f_{fan} *vs Re* for pure water (operating conditions for DS5037X slurry)

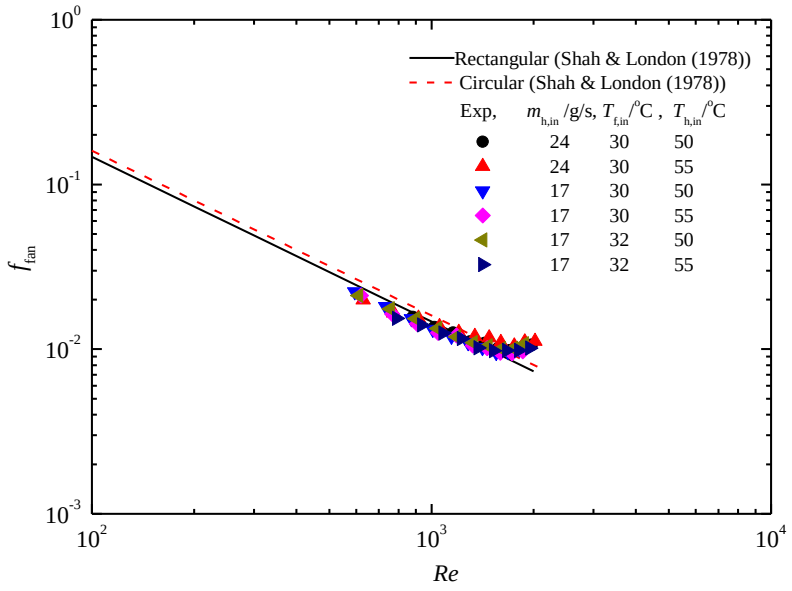

Figure 5.4 f_{fan} *vs Re* for pure water (operating conditions for MPCM-37 slurry)

The comparison of measured Nusselt number and fanning friction factor with available empirical correlations shows that the experimental setup is reliable for further experiments of mPCM slurry.

5.4 Energy balance

Preliminary experiments were conducted to examine the heat losses from the test section. The details of the heat loss experiment are given in Appendix B. The heat loss from test section to surroundings was found maximum 15.4% which cannot be ignored. This heat loss from hot water jacket ($Q_{l,tot}$) was added to the amount of heat ($Q_{\Delta T+l,ch}$) absorbed by working fluid. The amount of heat ($Q_{\Delta T+l,ch}$) absorbed by the working fluid flowing inside the microchannel should be equal to the sum of heat ($Q_{\Delta T,j,tot}$) supplied by hot water flowing inside the upper and lower jackets. The energy balance of the heat ($Q_{\Delta T,j,tot}$) emitted by hot fluid flowing inside the upper and lower jackets and heat ($Q_{\Delta T,ch+l}$) absorbed by the working fluid flowing inside microchannels was investigated. The energy balance difference ($Q_{\Delta T,j,tot} - Q_{\Delta T,ch+l}/Q_{\Delta T,ch+l}$) for pure water is given in Table C.2 and Table C.5. The energy balance difference was less than 11.1 % for higher mass flow rate of working fluid (11.5 g/s to 6.6 g/s) flowing inside microchannels. For lower mass flow rates (4.9 g/s and 3.9 g/s), the energy balance difference was maximum 26.3%. There are several possible explanations for this increase in energy balance difference at lower flow rates.

1. It could be due to the possible presence of air inside the system which eventually results in lower temperature measurements.
2. The other possible reason may be increased uncertainty of flow meter at lower flow rates.
3. During the experiments, it was observed that float of the flowmeter attains the steady state with difficulty at very low flow rates.

5.5 Local heat transfer characteristics of pure water

In the present investigation, the local Nusselt number of pure water is defined by the following Eq. (5.7).

$$Nu_{\mathrm{z}} = \left(\frac{q_{\mathrm{z}}}{T_{\mathrm{w,z}} - T_{\mathrm{b}}}\right)\frac{D_{\mathrm{h}}}{k} \tag{5.7}$$

where q_{z} is the local heat flux measured by the linear fitting, $T_{\mathrm{w,z}}$ is the local surface temperature measured by the linear fitting of temperatures measured inside the block, and $T_{\mathrm{b}} = (T_{\mathrm{mix,in}} + T_{\mathrm{ch,out}})/2$ is average bulk temperature of pure water, D_{h} is the hydraulic diameter of channel, and *k* is the thermal conductivity of water.

The temperature measurements for pure water (Run No. w-1) inside the aluminum block at 98 precisely locations are shown in Figure 5.5. The temperature gradients on the lower block are to some extent higher than the upper block. The observed increase in gradient on the lower block could be attributed to the thermal contact resistance between two lapped surfaces of the upper and lower blocks. The temperature profiles for pure water (Run Nos. w1-w18, operating conditions for DS5037X slurry) and (Run Nos.w-1a to w-65a, operating conditions for mPCM-37 slurry) are shown in Appendices D.1 to D.3 and Appendices D.11 to D.18, respectively.

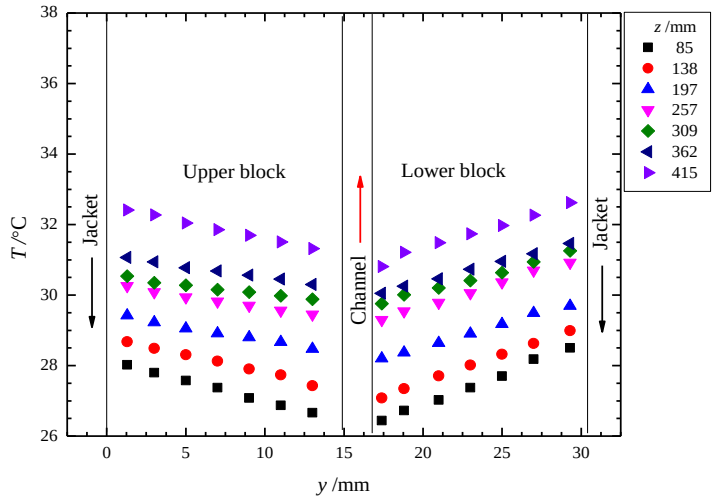

Figure 5.5 Temperature distributions inside the block. c = 0 %, $T_{h,in}$ = 40 °C, $T_{f,in}$ = 22 °C, $m_{h,in}$ = 24 g/s, $m_{f,in}$ = 11.5 g/s

The comparison of the local surface temperature and local heat flux measured by the linear fittings and inverse heat conduction solution of Yu et al. (2014) for pure water are shown in Figure 5.6 and Figure 5.7. The local surface temperatures determined by the two methods show very good agreement for all three cases. However, the local heat flux determined by the linear fitting is higher at z = 0.085m and z = 0.415 m. This could be due to the jet impingement of hot water and upstream and downstream adiabatic sides of microchannel.

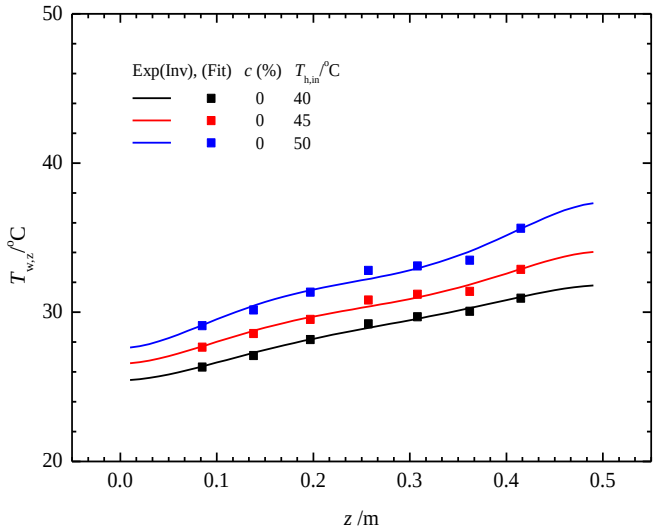

Figure 5.6 Variation of local surface temperature along the flow direction of microchannel. $T_{f,in}$ = 22 °C, $m_{h,in}$ = 24 g/s, $m_{f,in}$ = 11.5 g/s

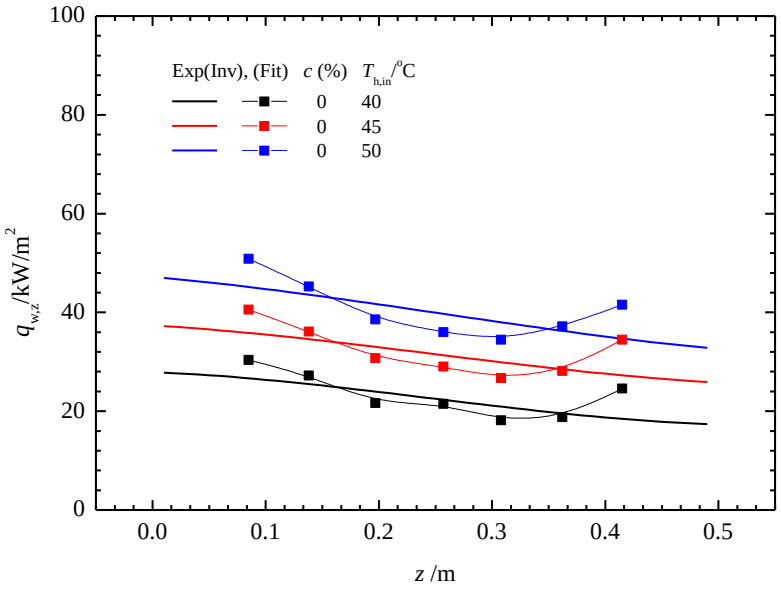

Figure 5.7 Variation of local heat flux along the flow direction of microchannel. $T_{f,in}$ = 22 ºC, $m_{f,in}$ = 11.5 g/s , $m_{h,in}$ = 24 g/s

The variation of the local Nusselt number along the flow direction of microchannel for pure water is shown in Figure 5.8. The variation of the local Nusselt number is very similar to the prediction by the empirical correlation of Shah and London (1978) given by Eq. (2.28) for thermally developing laminar flow . The local Nusselt number is higher at the beginning due to the entry region effect and then it starts decreasing due to the development of the thermal boundary layer.

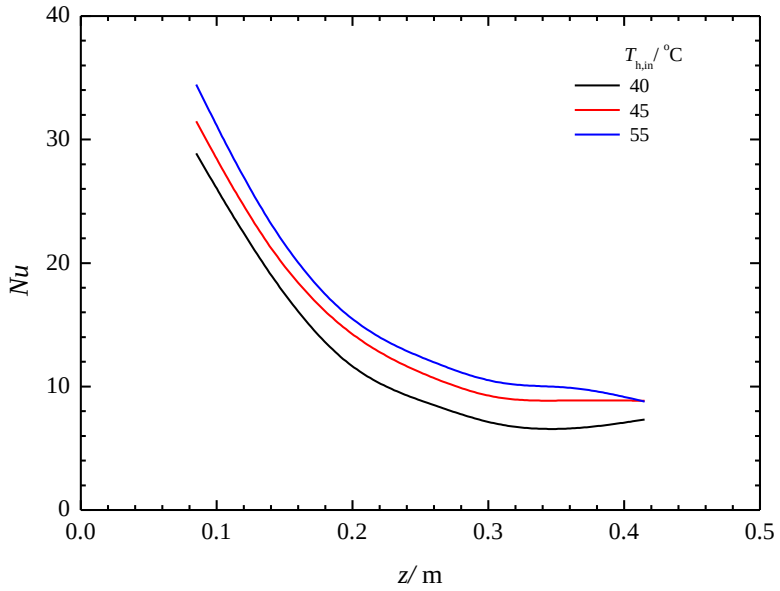

Figure 5.8 Variation of local *Nu* along the flow direction of microchannel. $T_{f,in}$ = 22 ºC, $m_{f,in}$ = 11.5 g/s , $m_{h,in}$ = 24 g/s

5.6 Conclusions

The experimental setup was validated by using pure water as the working fluid. The measured average Nusselt number and fanning friction factor were compared with available empirical correlations. The experimental results were in good agreement with the empirical correlations with maximum deviation of 18.8%. After the validation of experimental setup, the experiments were performed with mPCM slurry under the same operating conditions as pure water.

Chapter 6

Heat Transfer and Pressure Drop during Melting of mPCM Slurry Flow in Microchannels

Experiments were conducted with mPCM slurry of mass concentration ranging from 5% to 10% under similar operating conditions to those of pure water experiments. For the thermophysical properties of the mPCM slurry, specific heat capacity were measured by differential scanning calorimeter, thermal conductivity, density and dynamic viscosity were computed. Experimental data for mPCM slurry were compared with empirical correlations available. Subsequently, the local heat transfer characteristics of mPCM slurry were investigated. The effects of mass concentration of mPCM slurry on the local surface temperature, local heat flux, local Nusselt number, and bulk temperature rise and pressure drop were investigated and compared with experimental data of pure water.

6.1 Microencapsulated PCM slurry

Two types of mPCM slurries were used in the present investigation: one is Micronal DS5037X slurry and the other is MPCM-37 slurry. The Micronal DS 5037X and MPCM-37 slurry were provided by BASF and Microtek, respectively.

6.1.1 Micronal (DS5037X slurry)

The mass concentration of DS5037X slurry from supplier was 43%, which was diluted with distilled water to make the required concentration. The melting temperature of the mPCM particles was 26 ^{o}C. The scanning electron image of mPCM particles is shown in Figure 6.1. The nominal diameter of the particles was found to be from 5 to 11 μm. The

phase transition and latent heat capacity of mPCM particles were measured by DSC (differential scanning calorimeter, Mettler Toledo).

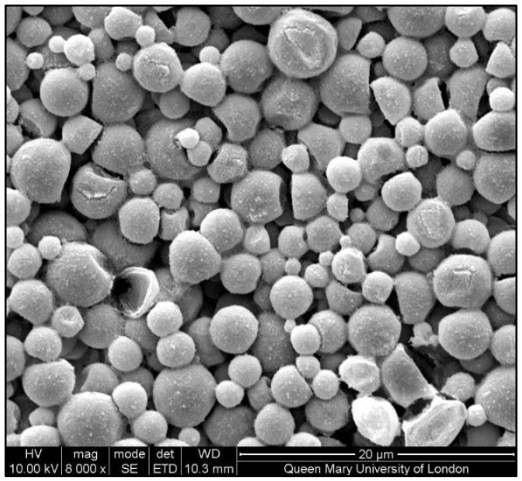

Figure 6.1 SEM image of Microencapsulated DS5037X slurry before thermal cycling

The test was conducted at constant heating and cooling rates of 5 °C/min. The mPCM particles were heated from -15 °C to 40 °C and then cooled down from 40 °C to -15 °C. As seen from Figure 6.2, the melting latent heat of mPCM particles was 80 J/g and melting temperature range was 23.3 ºC to 30.1ºC. The freezing latent heat of mPCM particles was 78 J/g and the freezing temperature range was 18.2 ºC to 25.1ºC as shown in Figure 6.3. For complete phase transition of mPCM particles, the outlet temperature of the mPCM slurry after heating should be higher than 30 ºC. The inlet temperature of slurry should be maintained less than 18 ºC to ensure the complete solidification of mPCM particles. However, the inlet temperature of the DS 5037X could only be maintained at 22 ºC due to insufficient cooling capacity. Thermophysical properties of DS5037X slurry are given in Table 6.1.

Table 6.1 Thermophysical properties of DS5037X slurry

Fluid	C %	ρ kg/m^3	k W/m K	C_p J/kg K	μ kg/m s
Pure water	0	998.0	0.6	4180	1.01×10^{-3}
mPCM slurry	5	989.6	0.57	4065	1.147×10^{-3}
mPCM slurry	10	982.3	0.54	3951	1.38×10^{-3}

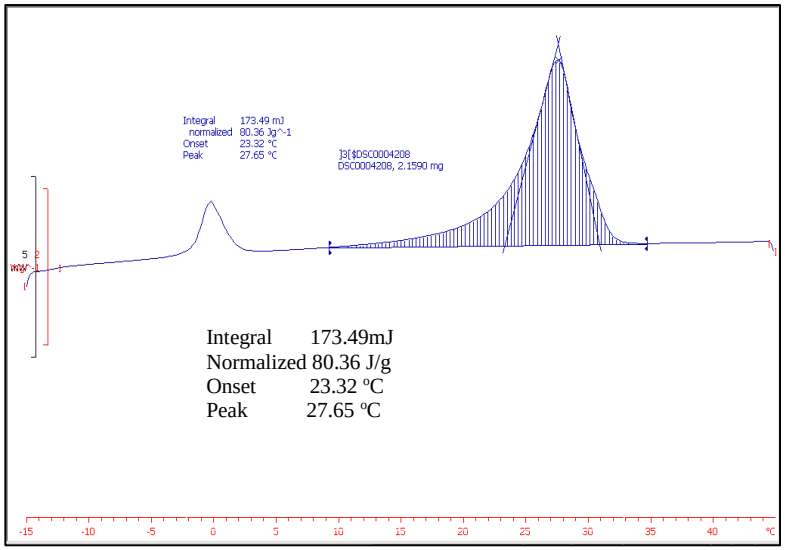

Figure 6.2 DSC curve of mPCM particles during heating cycle

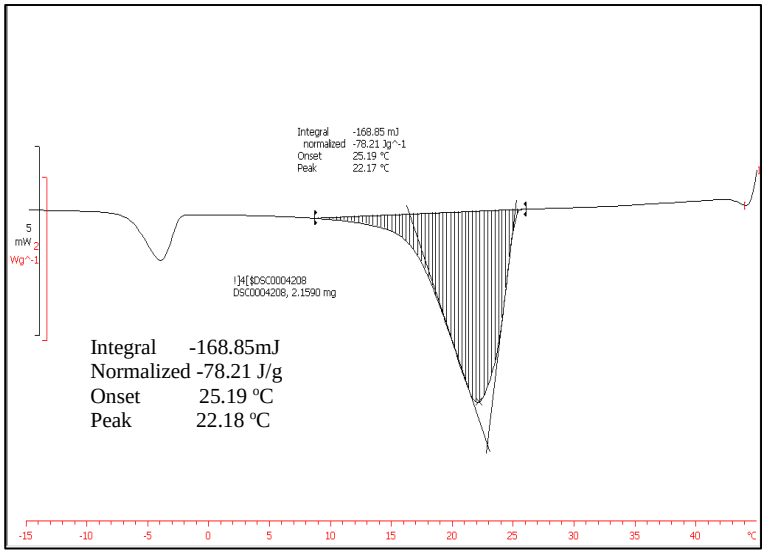

Figure 6.3 DSC curve of mPCM particles during cooling cycle

It is important to mention here that water at ambient temperature was circulated through the slurry reservoir to keep it at a set temperature. In order to further decrease the ambient water temperature flowing inside the auxiliary heat exchanger water and ice mixture was used as shown in Figure 6.4. It was likely that the solidification of mPCM particles was not completed before entering into the test section. To confirm this, experiments were performed using mPCM slurry with higher melting temperature of 37 ºC.

Figure 6.4 Photograph of ice and water mixture to drop the ambient water temperature

6.1.2 Microtek MPCM-37 slurry

The DSC curve for MPCM-37 slurry was provided by Microtek as shown in Figure 6.5. During melting cycle, the latent heat of mPCM particles was 178 J/g and the phase change transition range was 32.87 to 39.9 ºC. It appeared there was a subcooling of around 7.8 ºC for MPCM-37 slurry. The complete freezing temperature range of mPCM particles was 33.14 to 25 ºC. The thermophysical properties of MPCM-37 slurry are given in Table 6.2.

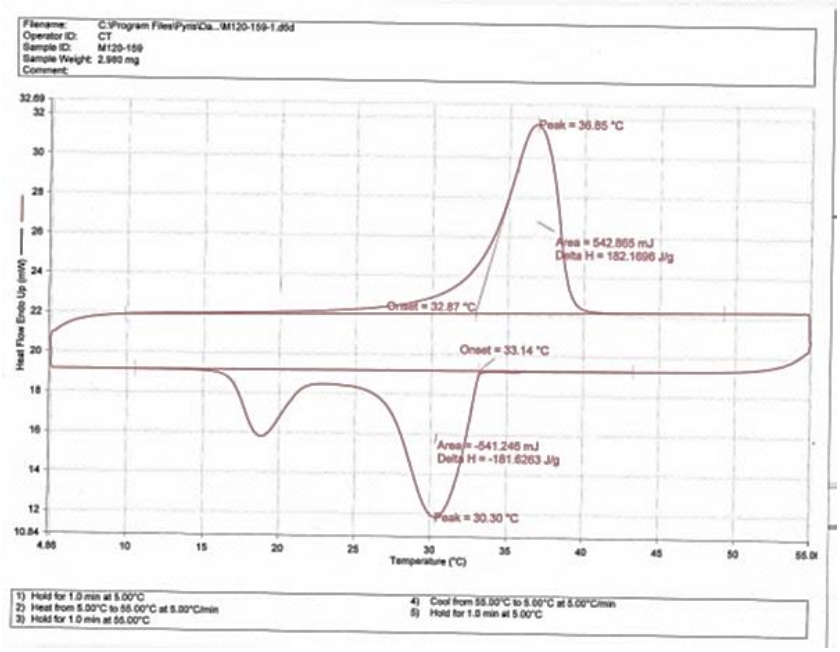

Figure 6.5 DSC curve of mPCM-37 slurry provided by Microtek Labs [www.microteklabs.com]

Table 6.2 Thermophysical properties of MPCM-37slurry

Fluid	C	ρ	k	C_p	μ
	%	kg/m^3	W/m K	J/kg K	kg/m s
Pure water	0	998.0	0.60	4180	0.00101
mPCM slurry	5	997.0	0.58	4069	0.00120
mPCM slurry	10	997.1	0.56	3959	0.00140

The temperature of mPCM slurry at the outlet should be greater than 40 ºC to ensure the complete melting of mPCM slurry. Previous studies show that the inlet temperature of mPCM slurry should be closer to the melting temperature of mPCM particles. After leaving the test section, the temperature of the MPCM-37 slurry was maintained at 28 ºC to re-solidify the mPCM particles. In order to keep the inlet temperature of MPCM-37 near the melting point, the slurry was reheated by another thermostat. After reheating, the inlet temperature of mPCM-37 slurry was set at 30 ºC. The temperature was maintained constant within the range of ±0.25 K. The photograph of experimental system for MPCM-37 slurry is shown in Figure 6.6.

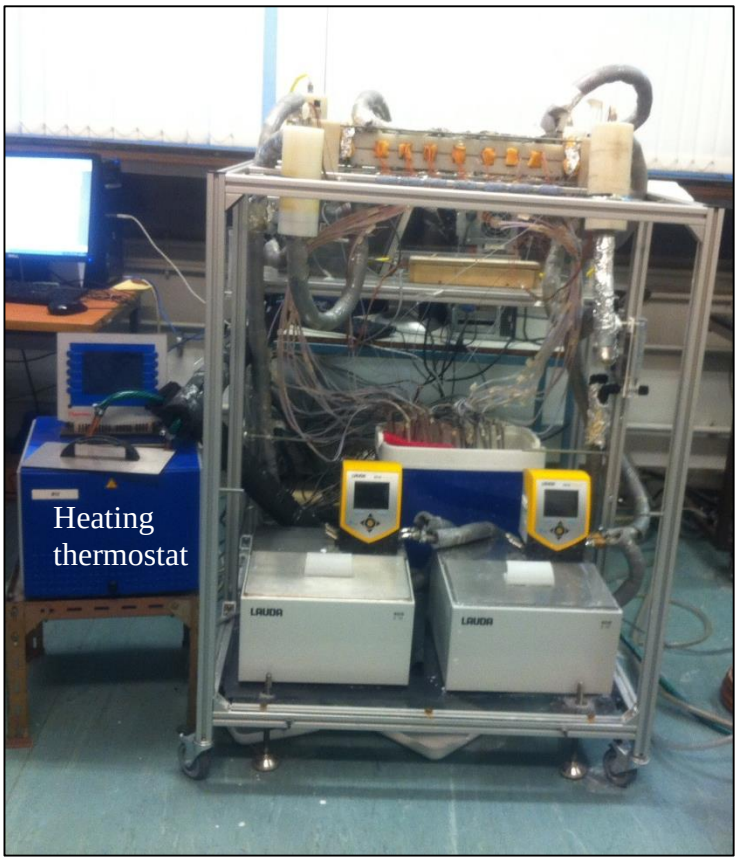

Figure 6.6 Photograph of experimental setup for MPCM-37 slurry

6.2 Energy balance for mPCM slurry

The heat transfer rate to the mPCM slurry flowing inside microchannels is the combination of sensible heat and latent heat. The heat transfer rate to the mPCM slurry, $Q_{\mathrm{s,ch}}$, was obtained by Eq. (6.1). This equation implies that all the latent heat of mPCM particles is fully utilized.

$$Q_{\mathrm{s,ch}} = m_{\mathrm{f,in}} Cp_{\mathrm{b}} \left(T_{\mathrm{out,ch}} - T_{\mathrm{in,ch}}\right) + m_{\mathrm{f,in}} ch_{\mathrm{fs}} + Q_{\mathrm{loss,jac}} \tag{6.1}$$

where $m_{\mathrm{f,in}}$ is the inlet mass flow rate of mPCM slurry, c is the mass concentration of mPCM slurry, and h_{fs} is the latent heat of mPCM slurry.

The energy balance, based on Eq. (6.1) for DS5037X slurry under different operating conditions for 5% and 10% mass concentration, is shown in Table C.3 and Table C.4,

respectively. The heat absorbed by mPCM slurry ($Q_{\mathrm{s,ch}}$) was found to be about 15% higher as compared to the amount of heat supplied by hot water($Q_{\mathrm{j,tot}}$) flowing inside the upper and lower jackets. This shows that the latent heat of mPCM particles was not fully utilized and it was likely that some of mPCM particles were still in solid or liquid state. In order to prevent the overestimation of heat absorbed by mPCM slurry, Equation (6.1) cannot be used for the present investigation. Based on the energy balance, the amount of heat absorbed by mPCM slurry was calculated by Eq. (6.2)

$$Q_{\mathrm{s,ch}} = (Q_{\mathrm{j,up}} + Q_{\mathrm{j,low}}) - Q_{\mathrm{l,tot}} \tag{6.2}$$

where $Q_{\mathrm{j,up}}$ and $Q_{\mathrm{j,low}}$ are the heat transfer rates of hot water in upper and lower jackets, and $Q_{\mathrm{l,tot}}$ is the total heat loss from the upper and lower jackets.

6.3 Comparison of experimental data for mPCM slurry with data available in literature

After the validation of experimental setup with pure water, the experimental data of mPCM slurry were also compared with data available in literature. The present experimental data could not be compared under the same operating conditions because previous research was focussed on the heat transfer performance of mPCM slurry flow under constant heat flux boundary condition. The experimental data were compared with experimental data of Wang et al. (2008) for laminar slurry flow in circular tube under the constant heat flux boundary condition. Comparing the two results, it can be seen from Figure 6.7 that the average Nusselt numbers for pure water are in good agreement till *Re* < 1200. For *Re* > 1200, the average Nusselt number measured by the present investigation is higher. As explained earlier it is believed that the working fluid is in thermally developing region. For mPCM slurry of different mass concentrations, the measured

Nusselt number in the present investigation is lower for both mass concentrations of mPCM slurry. This discrepancy is likely due to following reasons:

1. The latent heat of mPCM particles was not fully utilized due to possible incomplete solidification of mPCM particles.
2. The other possible reason for lower average Nusselt number may be owing to different boundary conditions.

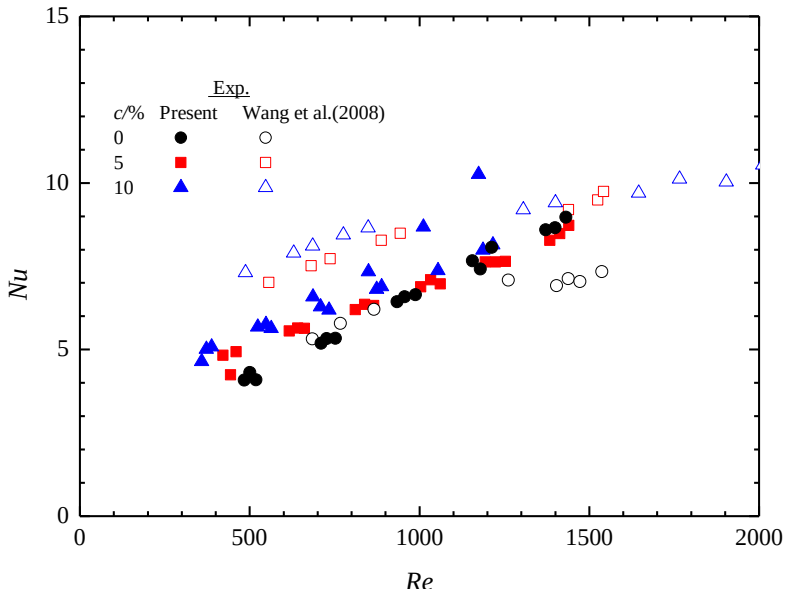

Figure 6.7 Comparison of present experimental data with experimental data of Wang et al. (2008)

Figure 6.8 shows the comparison of the ratio of Nusselt number calculated by Eq. (2.46) to the measured Nusselt number. The empirical correlation by Ho et al. (2014a) was also based on constant heat flux boundary condition. For $Re < 1200$, the computed Nusselt numbers are higher as compared to the measured Nusselt number. The maximum deviation between the predicted and measured average Nusselt numbers lies within ± 20%.

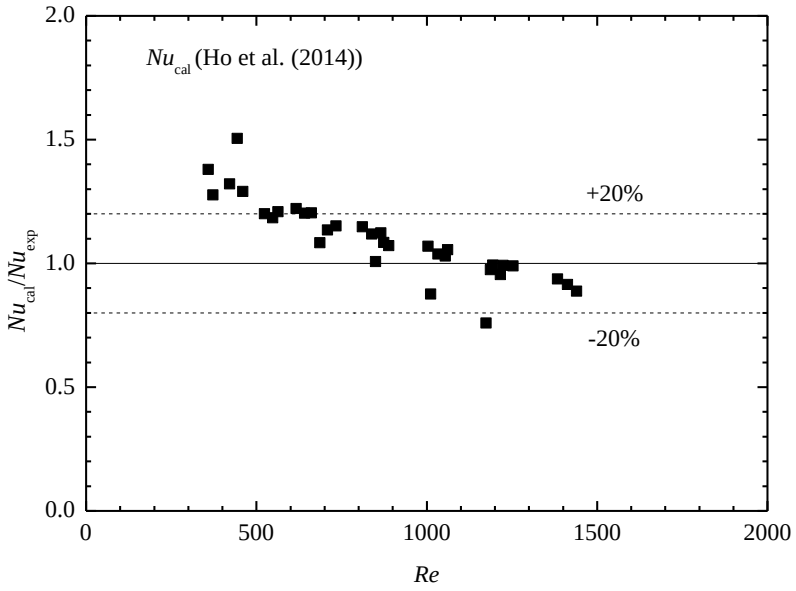

Figure 6.8 Comparison of present experimental data with empirical correlation of Ho et al. (2014a)

6.4 Local heat transfer characteristics of mPCM slurry

The local heat transfer characteristics of mPCM slurry flow in microchannels were investigated by comparing the local surface temperature, local heat flux and local Nusselt number with those of pure water. The comparisons of local surface temperature of DS5037X slurry with that of pure water under same operating conditions ($T_{h,in}$, $T_{f,in}$, $m_{h,in}$, and $m_{f,in}$) are shown in Figure 6.9 to Figure 6.14. One can see that the local surface temperature is dependent on mass flow rate of the working fluid. The variations in local surface temperature also depends on mass concentration of mPCM slurry. In all cases, the local surface temperature of the mPCM slurry was found higher. This increase in temperature is more prominent at $T_{h,in}$ (45 and 50 ºC). In Figure 6.9, at $T_{h,in}$ = 50 ºC, the surface temperature for 10% mass concentration is 2.1 K higher as compared to surface temperature of pure water. It seems possibly that this temperature rise for mPCM slurry is due to lower thermal conductivity of mPCM slurry. The heat is transferred from the hot water flowing inside the jacket to the working fluid by conduction. The decrease in

thermal conductivity of mPCM slurry deteriorates the heat transfer to the core region of the microchannel. The surface temperature further increases with the increase of mass concentration of mPCM slurry. The loading of mPCM particles at higher concentration results in further lower thermal conductivity of mPCM slurry. Similar behavior of increase of surface temperature of mPCM slurry has also been observed for MPCM-37 slurry as shown in Figure 6.15 to Figure 6.20 .

The comparison of the local heat flux for both DS5037X and MPCM-37 slurries and pure water under different operating conditions are shown in Figure 6.21 to Figure 6.32. The local heat flux was higher near the upstream and downstream of the microchannel for both mPCM slurry and pure water. This might be the jet impingement effect of the hot water as explained earlier. It can be seen that the local heat flux for mPCM slurry is lower as compared to pure water under all operating conditions. A slight increase in local heat flux of 10% mass concentration of DS5037X slurry at $T_{h,in}$ of 40 ºC was observed.

The local Nusselt number of mPCM slurry for mass concentration of 5% and 10% are also compared with pure water. The Nusselt number also considers the effect of thermal conductivity and bulk temperature rise of the working fluid. The comparison of the local Nusselt number for DS5037X slurry with pure water under different experimental conditions are represented in Figure 6.33 to Figure 6.38. One can see that the local Nusselt number increases with the mass flow rate of the working fluid. In Figure 6.33, the mPCM slurry of all mass concentrations does not behave well as compared to pure water except 10% mass concentration of mPCM slurry at $T_{h,in}$ of 40 ºC. It seems that the mPCM slurry has not completely melted due to very short residence time of mPCM slurry inside the microchannel. The local Nusselt number of mPCM slurry is higher as compared to pure water at lower mass flow rates of 6.6, 4.9 and 3.3 g/s as shown in Figure 6.36 to Figure 6.38. At lower mass flow rates of the working fluid, the residence time of mPCM particles

inside the microchannel was longer enough for almost complete melting of mPCM slurry. It is interesting to note that in Figure 6.37 at $T_{h,in}$ of 45 ºC and 50 ºC, after z = 0.3 the local Nusselt number for mPCM slurry was lower than pure water. It is believed that this decrease in Nusselt number is associated with complete melting of mPCM particles inside the microchannel. The specific heat capacity of solid and liquid mPCM particles is lower than pure water which results in poor heat transfer performance of mPCM slurry. Similar behavior of increase of the local Nusselt number for Microtek mPCM-37 slurry at lower mass flow rates is shown in Figure 6.39 to Figure 6.44.

6.5 Comparison of average Nusselt number

The comparison of the average Nusselt number obtained by the inverse method and temperature rise of the working fluid for Micronal DS5037X slurry and pure water is shown in Figure 6.45. It is observed that the average Nusselt number computed by the inverse method is within 14.6% higher as compared to temperature rise method. It can be seen from Figure 6.45 that the average Nusselt number increases with the increase of Reynolds number for both mPCM slurry and pure water. Comparing the average Nusselt number at *Re* =1200, the average Nusselt number of 5% and 10% mass concentration of mPCM slurry is 12.1% and 28.3% higher than pure water, respectively. This increase in Nusselt number is attributed to the higher latent heat of mPCM particles during the phase change.

Figure 6.46 shows the comparison of the average Nusselt number for Microtek mPCM-37 slurry with those of pure water. The average Nusselt number for mPCM slurry was found to be higher than pure water at the same Reynolds number. So, for all cases heat transfer performance of mPCM slurry was found better as compared to pure water.

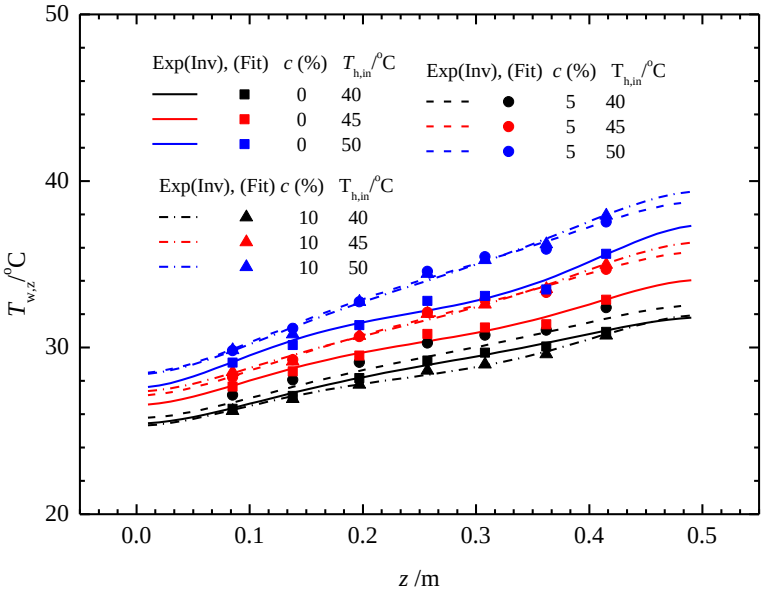

Figure 6.9 Variation of local surface temperature along the flow direction of channel. slurry: BASF, $m_{f,in}$ = 11.5 g/s ,$T_{f,in}$ = 22 ºC, $m_{h,in}$ = 24 g/s

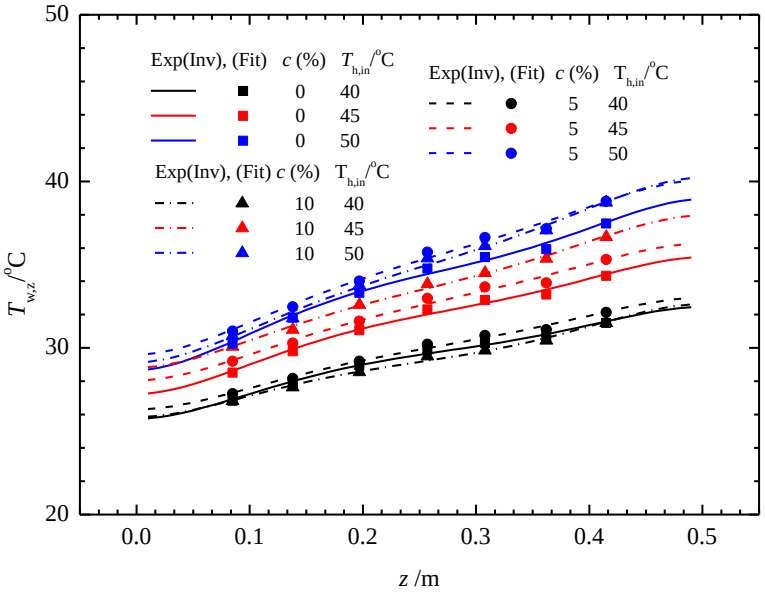

Figure 6.10 Variation of local surface temperature along the flow direction of channel. slurry: BASF, $m_{f,in}$ = 9.9 g/s ,$T_{f,in}$ = 22 ºC, $m_{h,in}$ = 24 g/s

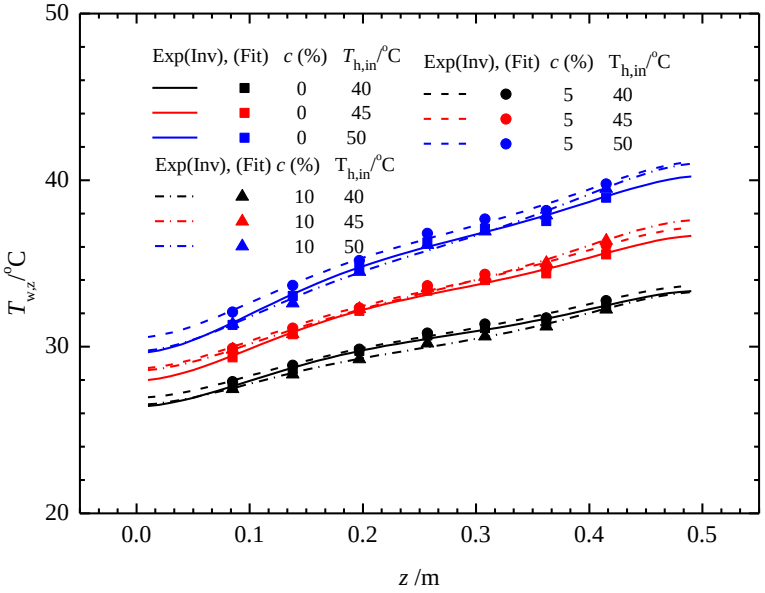

Figure 6.11 Variation of local surface temperature along the flow direction of channel. slurry: BASF, $m_{f,in}$ = 8.2 g/s ,$T_{f,in}$ = 22 ºC, $m_{h,in}$ = 24 g/s

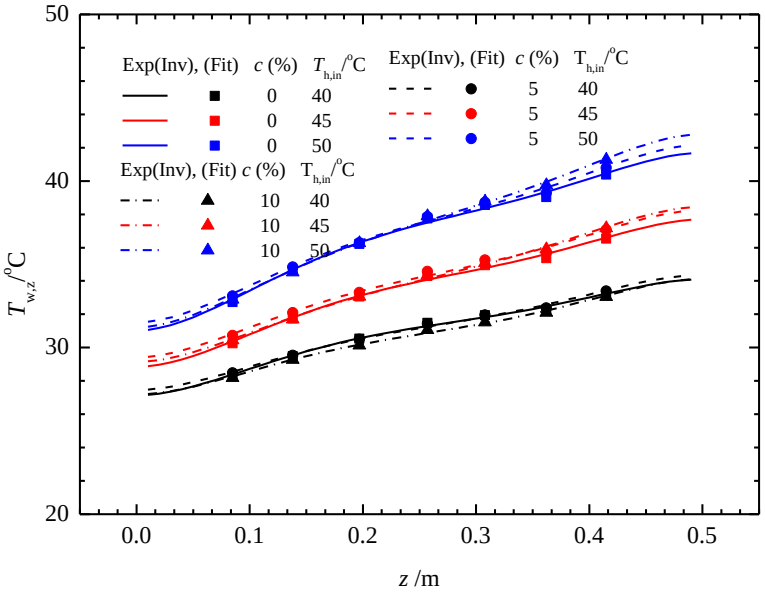

Figure 6.12 Variation of local surface temperature along the flow direction of channel. slurry: BASF, $m_{f,in}$ = 6.6 g/s ,$T_{f,in}$ = 22 ºC, $m_{h,in}$ = 24 g/s

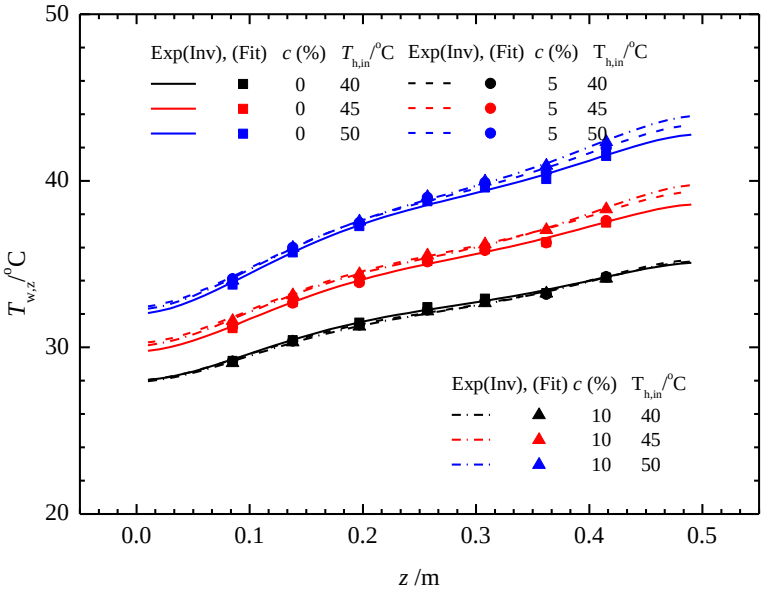

Figure 6.13 Variation of local surface temperature along the flow direction of channel. slurry: BASF, $m_{f,in}$ = 4.9 g/s ,$T_{f,in}$ = 22 ºC, $m_{h,in}$ = 24 g/s

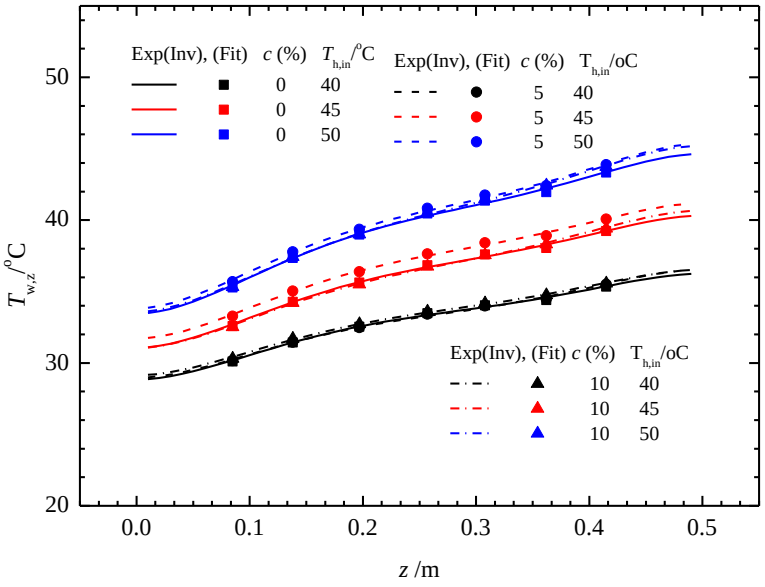

Figure 6.14 Variation of local surface temperature along the flow direction of channel. slurry: BASF, $m_{f,in}$ = 3.3 g/s ,$T_{f,in}$ = 22 ºC, $m_{h,in}$ = 24 g/s

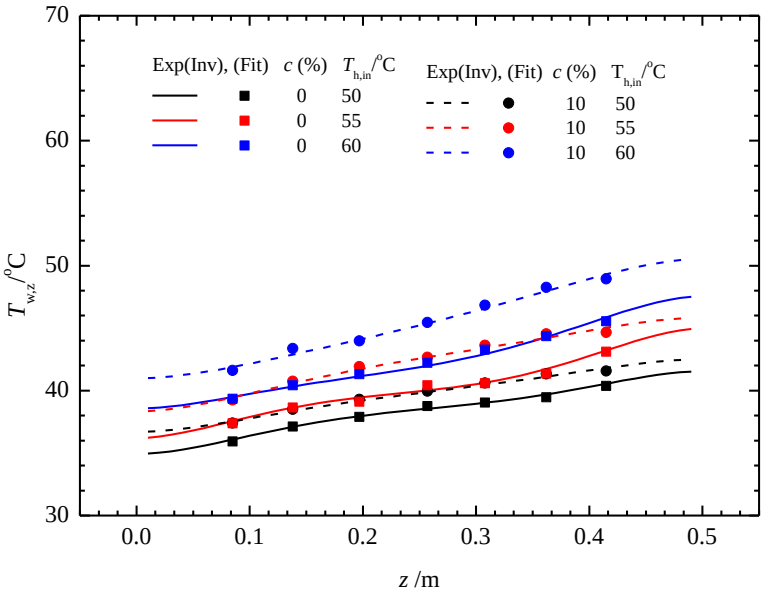

Figure 6.15 Variation of local surface temperature along the flow direction of channel. Slurry: MPCM-37, $m_{f,in}$ = 10.7 g/s ,$T_{f,in}$ = 22 ºC, $m_{h,in}$ = 24 g/s

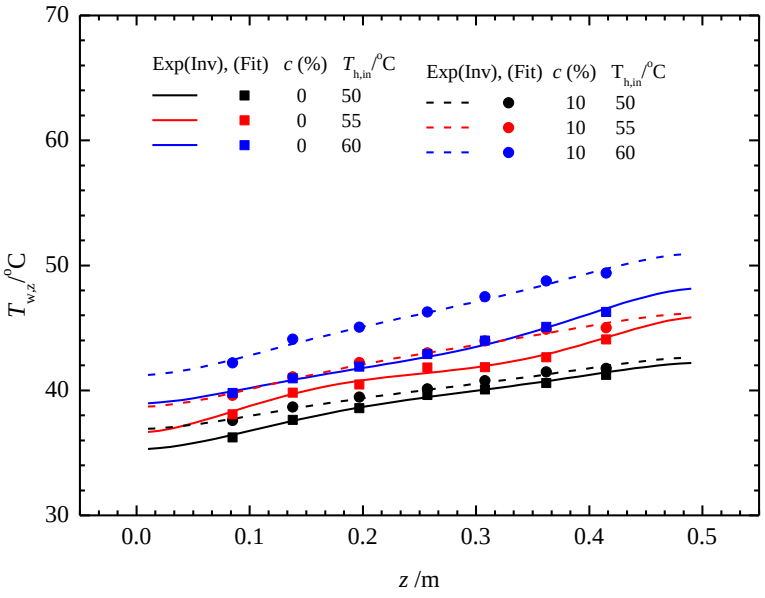

Figure 6.16 Variation of local surface temperature along the flow direction of channel. Slurry: MPCM-37, $m_{f,in}$ = 9.8 g/s ,$T_{f,in}$ = 22 ºC, $m_{h,in}$ = 24 g/s

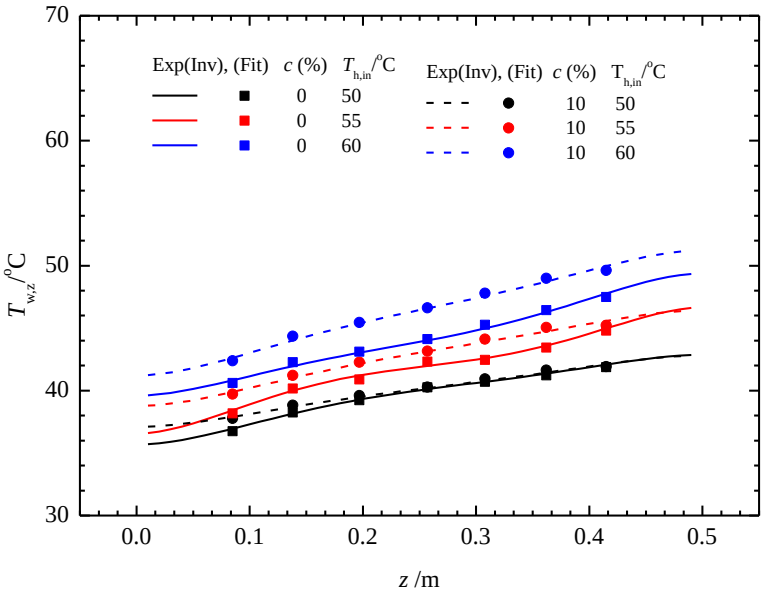

Figure 6.17 Variation of local surface temperature along the flow direction of channel.

Slurry: MPCM-37, $m_{f,in}$ = 9.0 g/s ,$T_{f,in}$ = 22 ºC, $m_{h,in}$ = 24 g/s

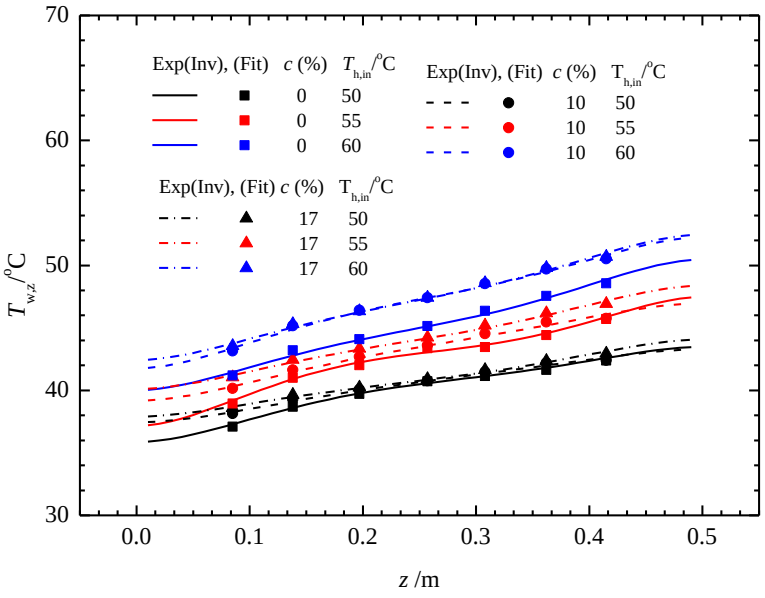

Figure 6.18 Variation of local surface temperature along the flow direction of channel.

Slurry: MPCM-37, $m_{f,in}$ = 8.2 g/s ,$T_{f,in}$ = 22 ºC, $m_{h,in}$ = 24 g/s

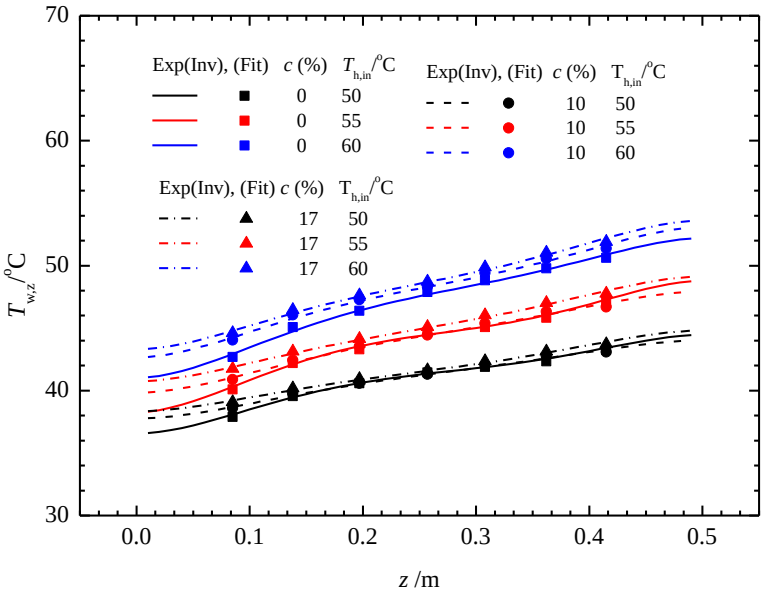

Figure 6.19 Variation of local surface temperature along the flow direction of channel.

Slurry: MPCM-37, $m_{f,in}$ = 6.6 g/s ,$T_{f,in}$ = 22 ºC, $m_{h,in}$ = 24 g/s

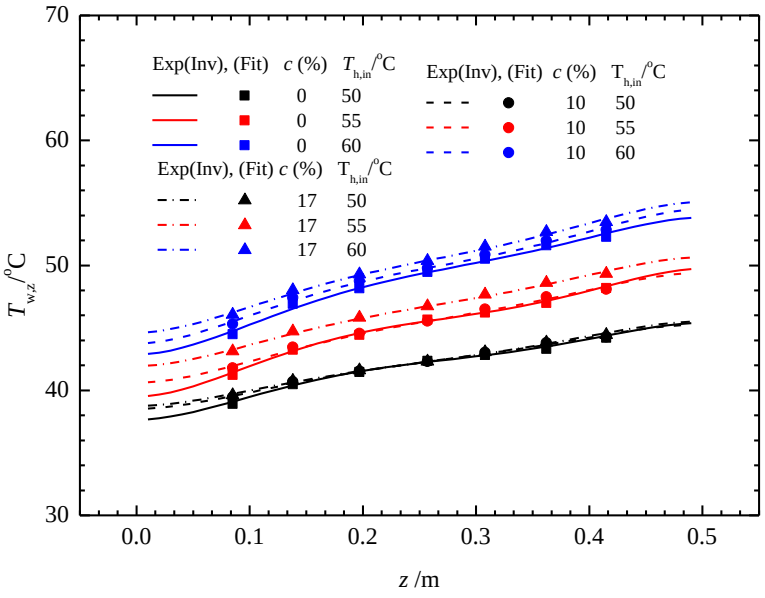

Figure 6.20 Variation of local surface temperature along the flow direction of channel.

Slurry: MPCM-37, $m_{f,in}$ = 4.9 g/s ,$T_{f,in}$ = 22 ºC, $m_{h,in}$ = 24 g/s

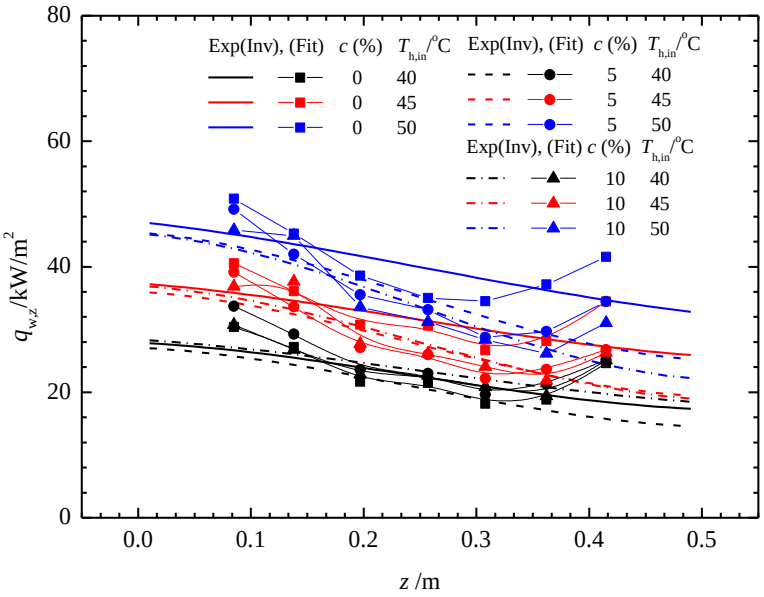

Figure 6.21 Variation of local heat flux along the flow direction of channel. slurry: BASF, $m_{f,in}$ = 11.5 g/s ,$T_{f,in}$ = 22 ºC, $m_{h,in}$ = 24 g/s

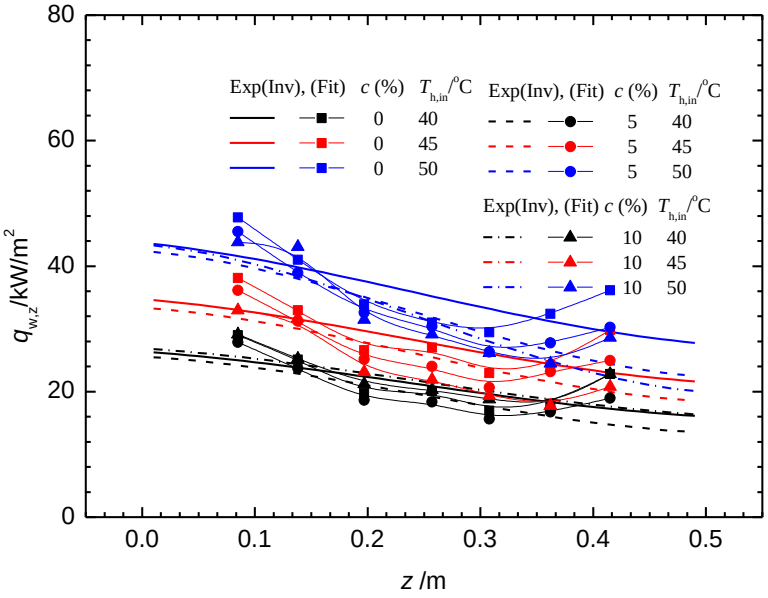

Figure 6.22 Variation of local heat flux along the flow direction of channel. slurry: BASF, $m_{f,in}$ = 9.9 g/s ,$T_{f,in}$ = 22 ºC, $m_{h,in}$ = 24 g/s

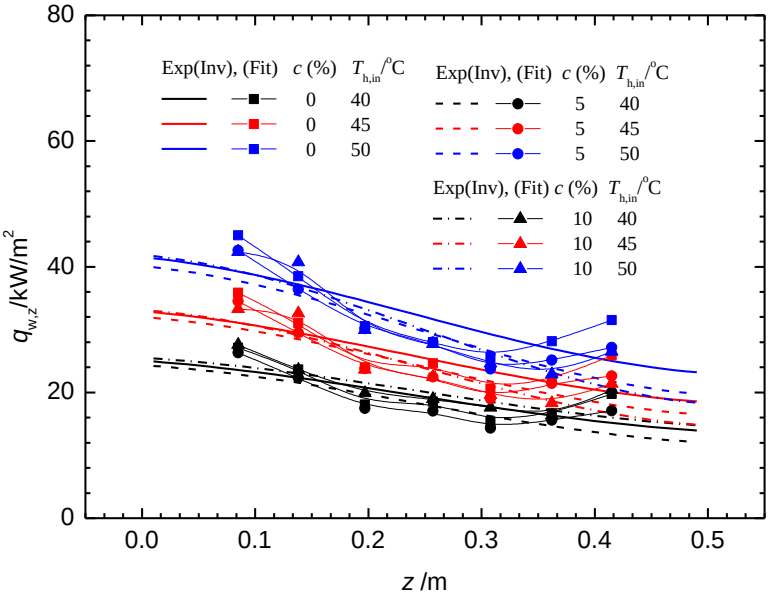

Figure 6.23 Variation of heat flux along the flow direction of channel. slurry: BASF, $m_{f,in}$ = 8.2 g/s ,$T_{f,in}$ = 22 ºC, $m_{h,in}$ = 24 g/s

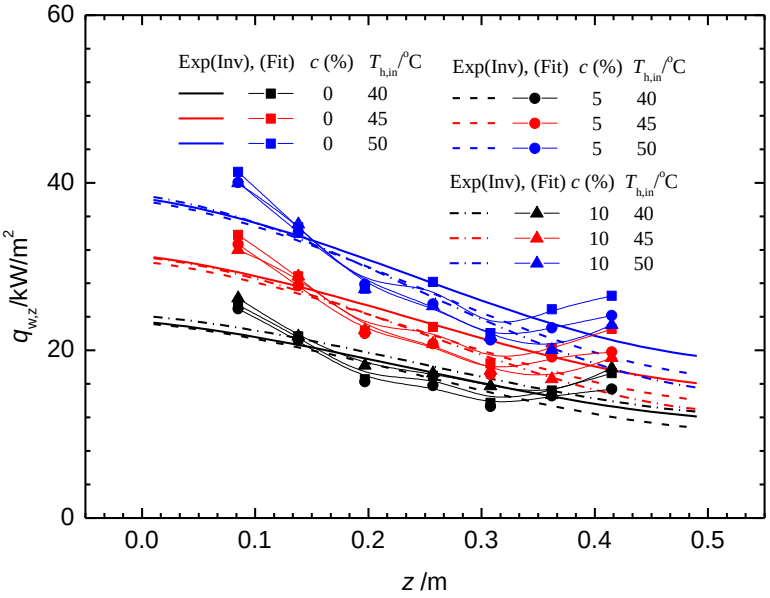

Figure 6.24 Variation of heat flux along the flow direction of channel. slurry: BASF, $m_{f,in}$ = 6.6 g/s ,$T_{f,in}$ = 22 ºC, $m_{h,in}$ = 24 g/s

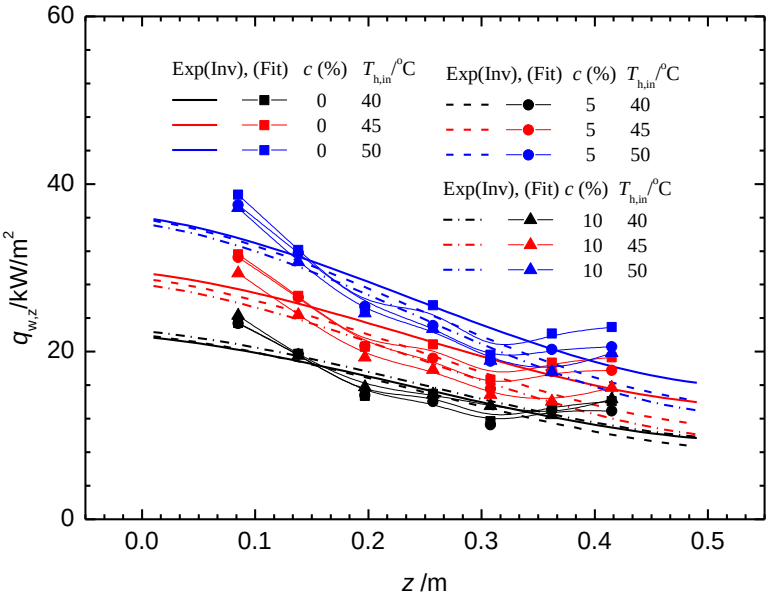

Figure 6.25 Variation of local heat flux along the flow direction of channel. slurry: BASF, $m_{f,in}$ = 4.9 g/s ,$T_{f,in}$ = 22 ºC, $m_{h,in}$ = 24 g/s

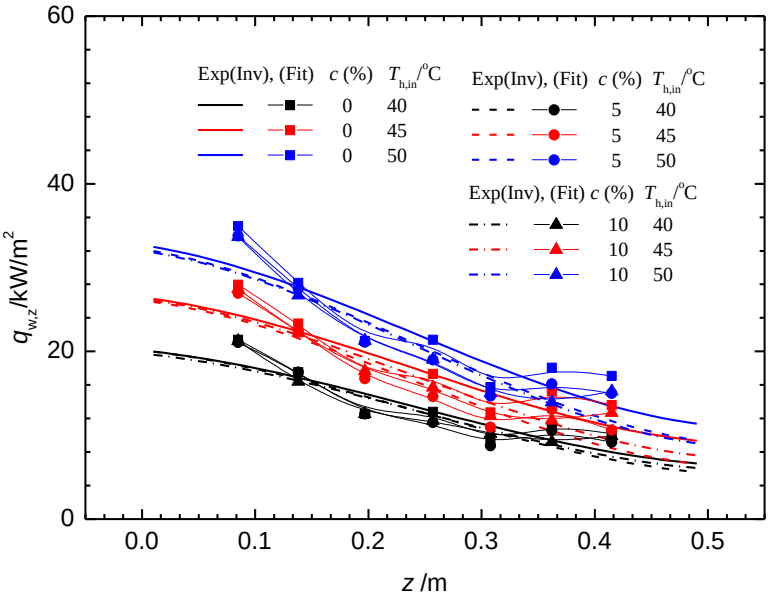

Figure 6.26 Variation of local heat flux along the flow direction of channel. slurry: BASF, $m_{f,in}$ = 3.3 g/s ,$T_{f,in}$ = 22 ºC, $m_{h,in}$ = 24 g/s

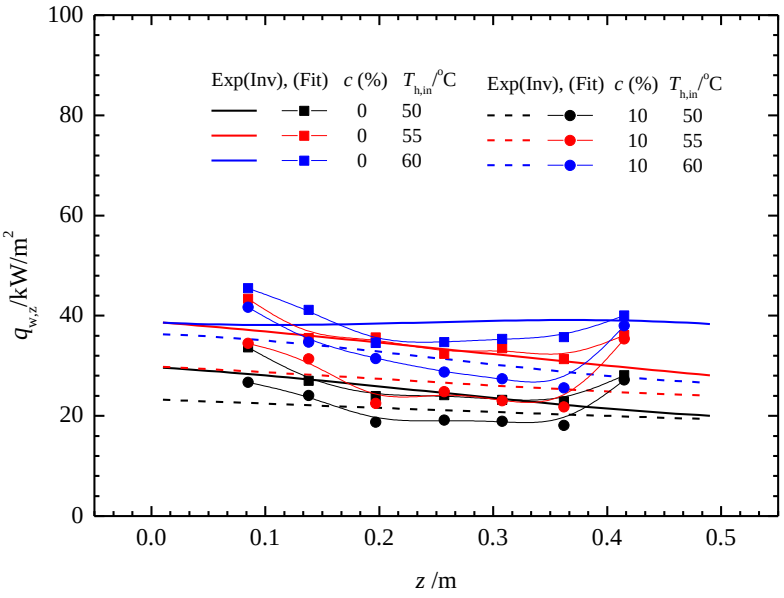

Figure 6.27 Variation of local heat flux along the flow direction of channel. slurry: MPCM-37, $m_{f,in}$ = 10.7 g/s ,$T_{f,in}$ = 22 ºC, $m_{h,in}$ = 24 g/s

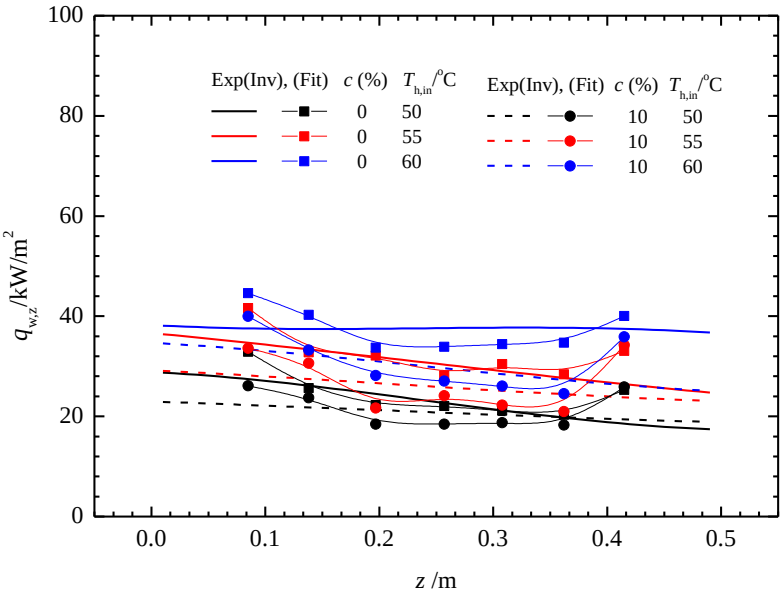

Figure 6.28 Variation of local heat flux along the flow direction of channel. slurry: MPCM-37, $m_{f,in}$ = 9.8 g/s ,$T_{f,in}$ = 22 ºC, $m_{h,in}$ = 24 g/s

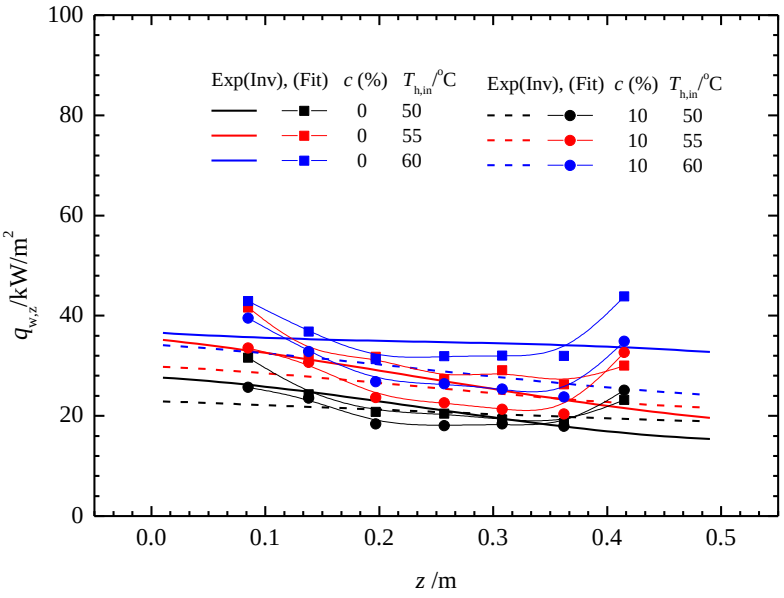

Figure 6.29 Variation of local heat flux along the flow direction of channel. slurry: MPCM-37, $m_{f,in}$ = 9.0 g/s ,$T_{f,in}$ = 22 ºC, $m_{h,in}$ = 24 g/s

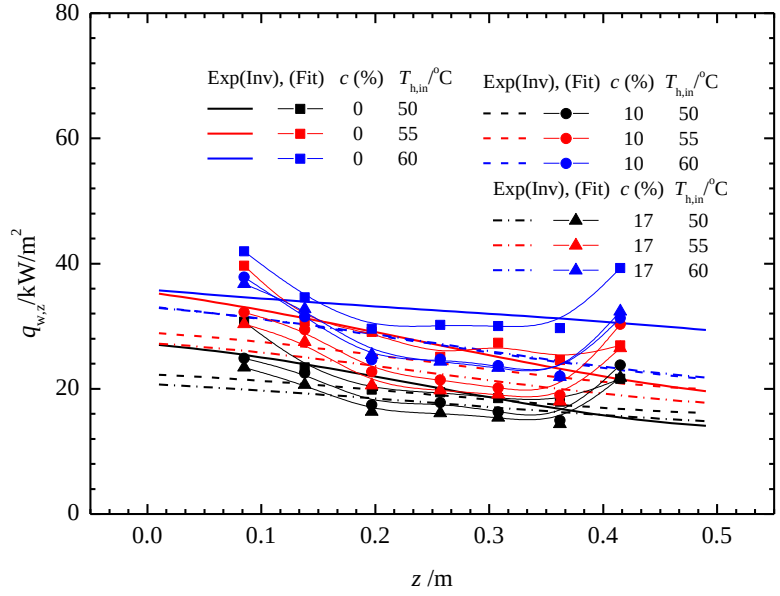

Figure 6.30 Variation of local heat flux along the flow direction of channel. slurry: MPCM-37, $m_{f,in}$ = 8.2 g/s ,$T_{f,in}$ = 22 ºC, $m_{h,in}$ = 24 g/s

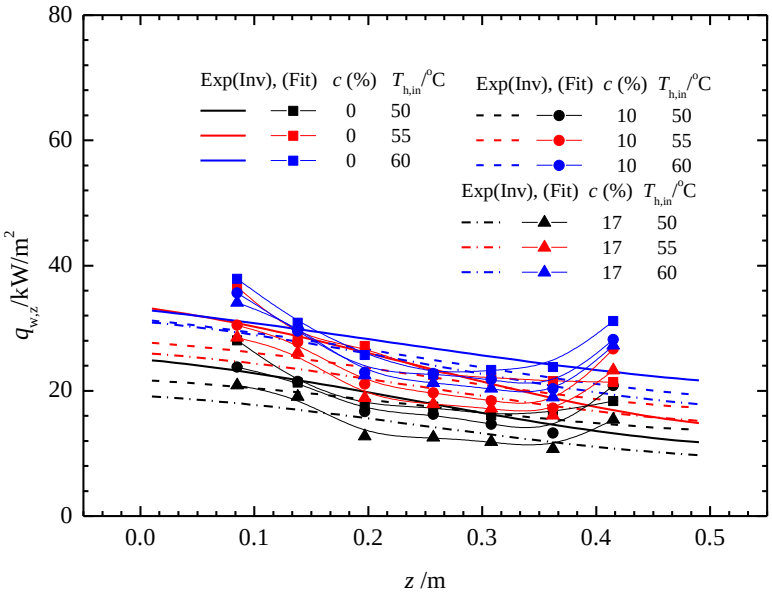

Figure 6.31 Variation of local heat flux along the flow direction of channel. slurry: MPCM-37, $m_{f,in}$ = 6.6 g/s ,$T_{f,in}$ = 22 ºC, $m_{h,in}$ = 24 g/s

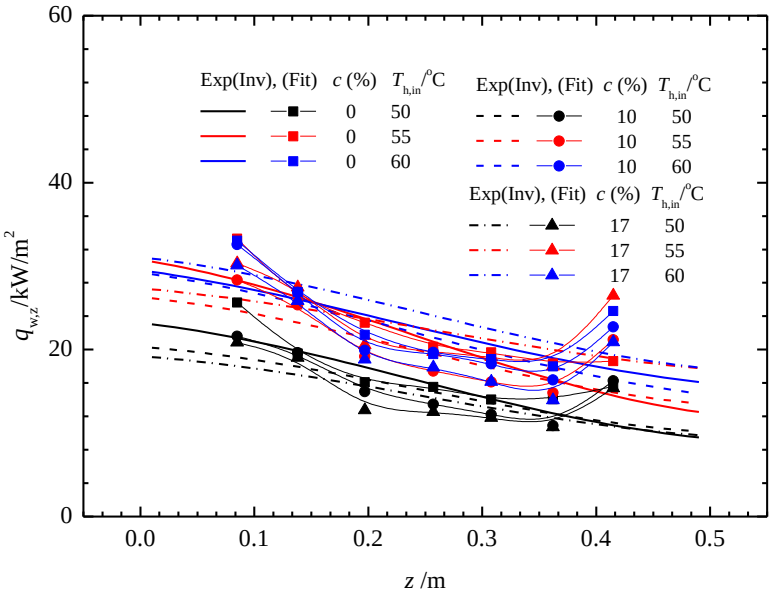

Figure 6.32 Variation of local heat flux along the flow direction of channel. $m_{f,in}$ = 4.9 g/s ,$T_{f,in}$ = 22 ºC, $m_{h,in}$ = 24 g/s

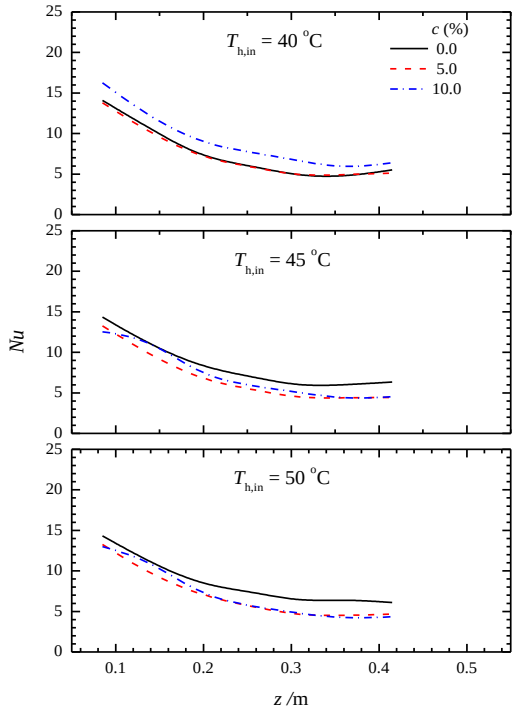

Figure 6.33 Variation of local Nusselt number along the channel. slurry: BASF, $m_{f,in}$ = 11.5 g/s ,$T_{f,in}$ = 22 ºC, $m_{h,in}$ = 24 g/s

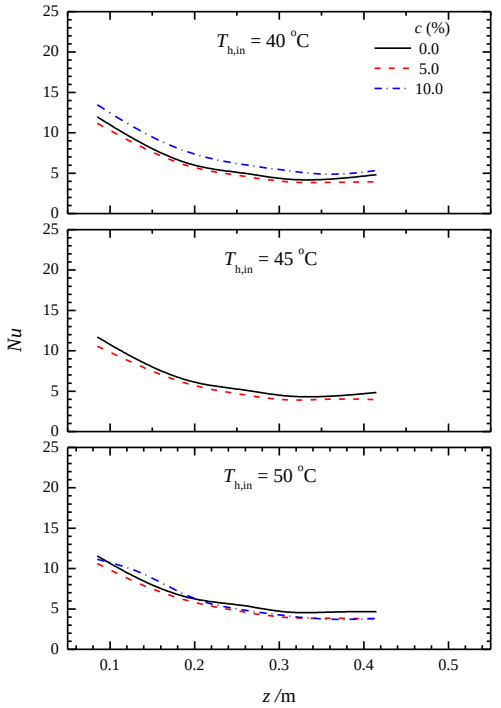

Figure 6.34 Variation of local Nusselt number along the channel. slurry: BASF, $m_{f,in}$ = 9.9 g/s ,$T_{f,in}$ = 22 ºC, $m_{h,in}$ = 24 g/s

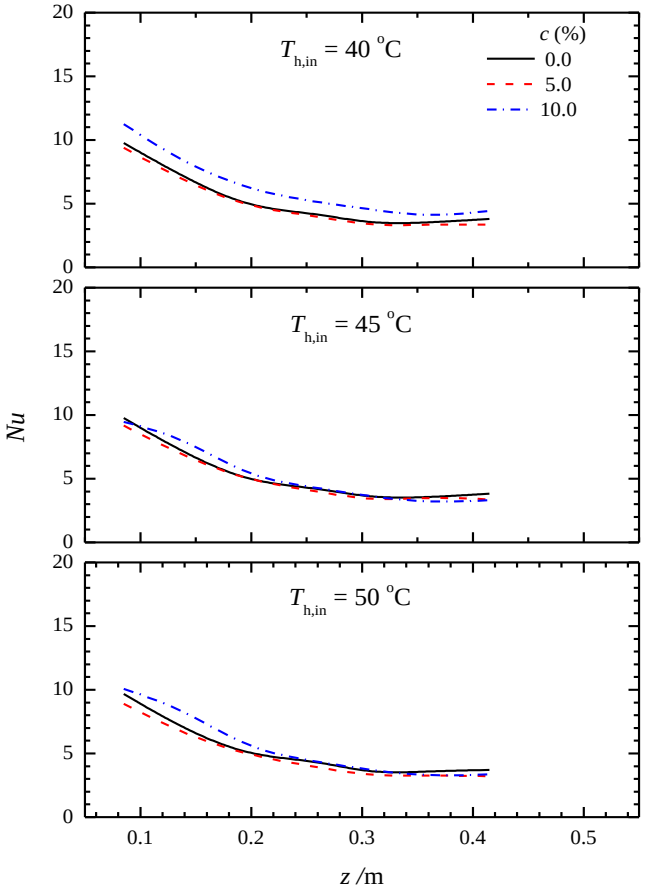

Figure 6.35 Variation of local Nusselt number along the channel. slurry: BASF, $m_{f,in}$ = 8.2 g/s ,$T_{f,in}$ = 22 ºC, $m_{h,in}$ = 24 g/s

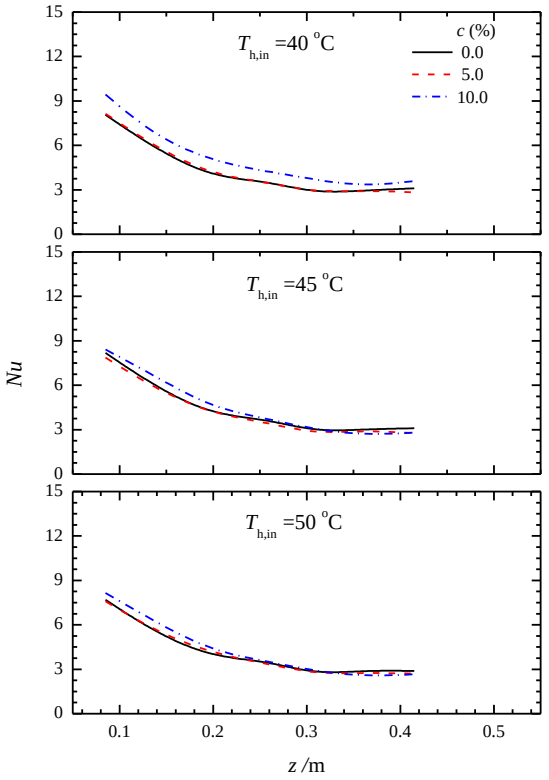

Figure 6.36 Variation of local Nusselt number along the channel. slurry: BASF, $m_{f,in}$ = 6.6 g/s ,$T_{f,in}$ = 22 ºC, $m_{h,in}$ = 24 g/s

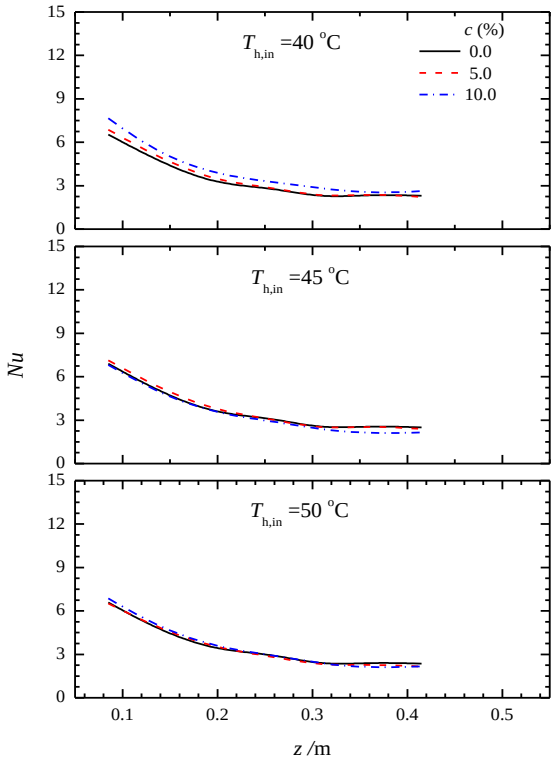

Figure 6.37 Variation of local Nusselt number along the channel. slurry: BASF, $m_{f,in}$ = 4.9 g/s ,$T_{f,in}$ = 22 ºC, $m_{h,in}$ = 24 g/s

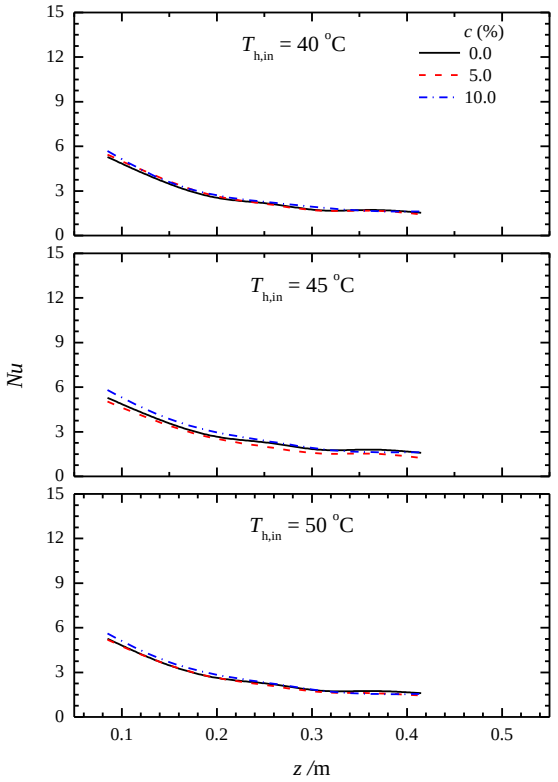

Figure 6.38 Variation of local Nusselt number along the channel. slurry: BASF, $m_{f,in}$ = 3.3 g/s ,$T_{f,in}$ = 22 ºC, $m_{h,in}$ = 24 g/s

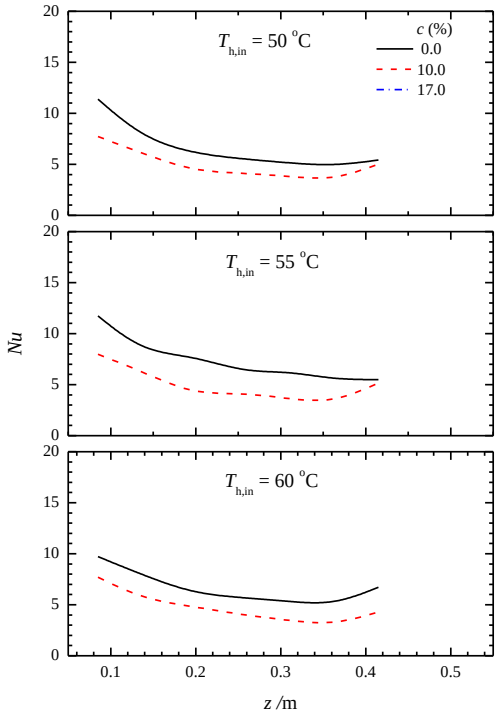

Figure 6.39 Variation of local Nusselt number along the channel. slurry: MPCM-37, $m_{f,in}$ = 10.7 g/s ,$T_{f,in}$ = 30 ºC, $m_{h,in}$ = 24 g/s

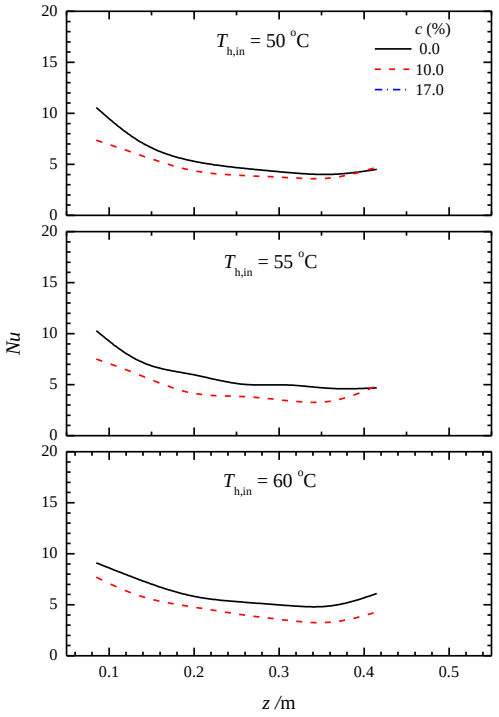

Figure 6.40 Variation of local Nusselt number along the channel. slurry: MPCM-37, $m_{f,in}$ = 9.8 g/s,$T_{f,in}$ = 30 ºC, $m_{h,in}$ = 24 g/s

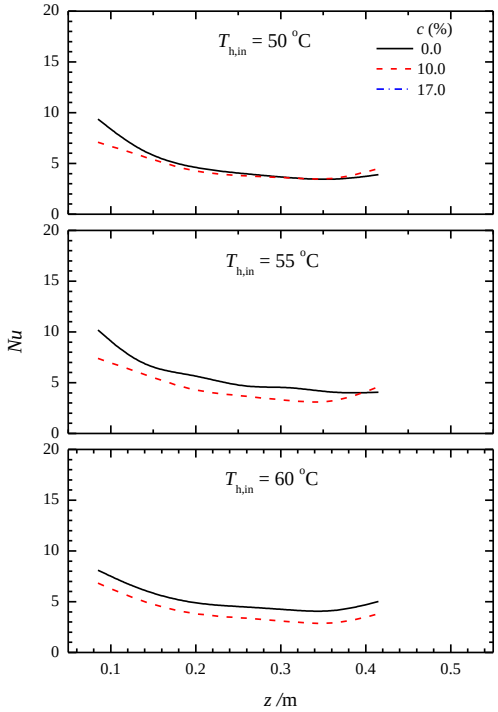

Figure 6.41 Variation of local Nusselt number along the channel. slurry: MPCM-37, $m_{f,in}$ = 9.0 g/s ,$T_{f,in}$ = 30 ºC, $m_{h,in}$ = 24 g/s

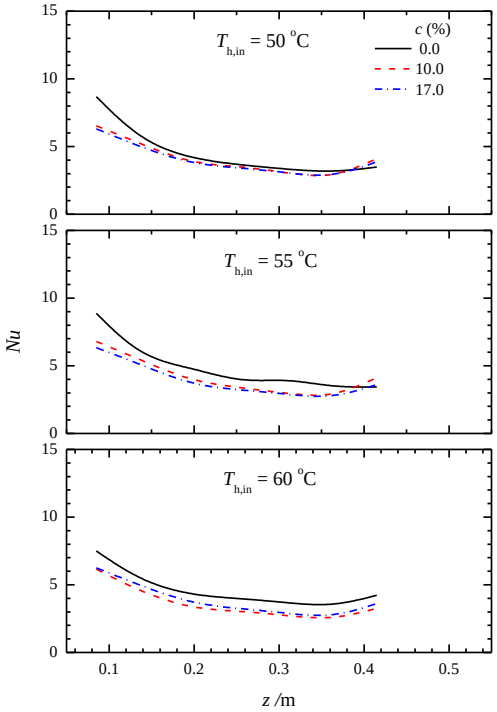

Figure 6.42 Variation of local Nusselt number along the channel. slurry: MPCM-37, $m_{f,in}$ = 8.2 g/s,$T_{f,in}$ = 30 ºC, $m_{h,in}$ = 24 g/s

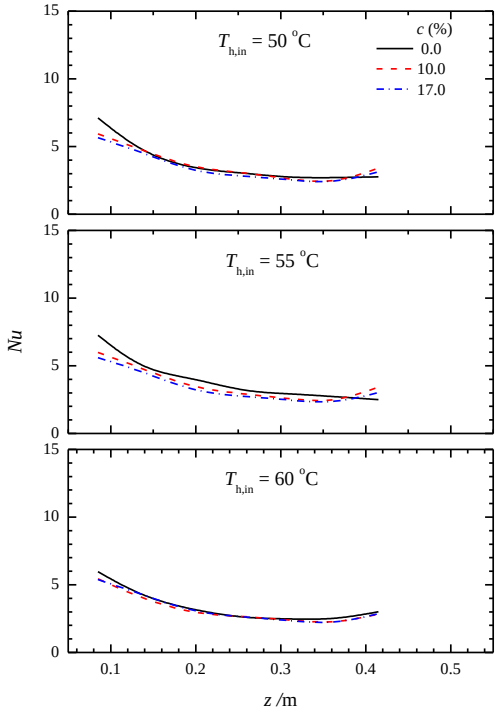

Figure 6.43 Variation of local Nusselt number along the channel. slurry: MPCM-37, $m_{f,in}$ = 6.6 g/s ,$T_{f,in}$ = 30 ºC, $m_{h,in}$ = 24 g/s

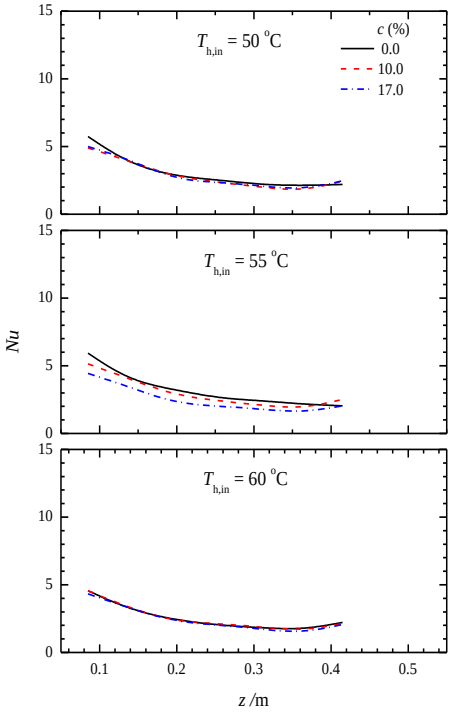

Figure 6.44 Variation of local Nusselt number along the channel. slurry: MPCM-37, $m_{f,in}$ = 4.9 g/s,$T_{f,in}$ = 30 ºC, $m_{h,in}$ = 24 g/s

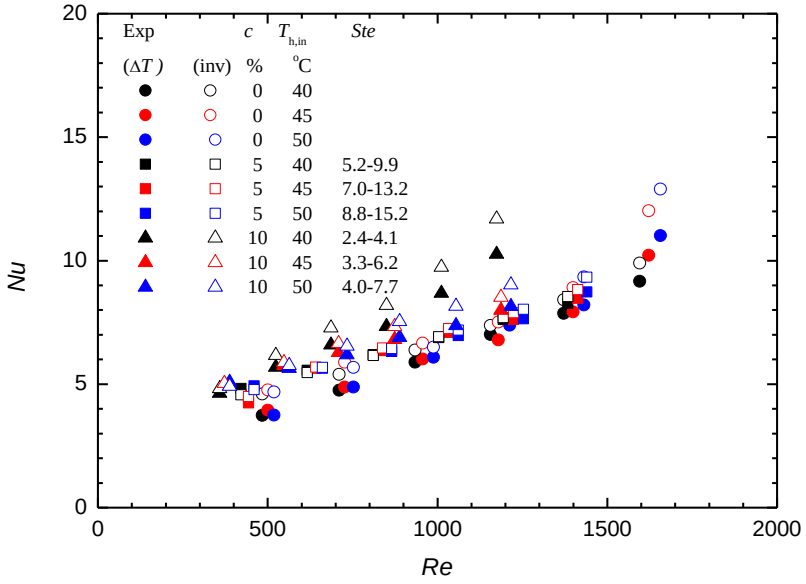

Figure 6.45 Comparison of average *Nu* of DS5037X slurry with pure water

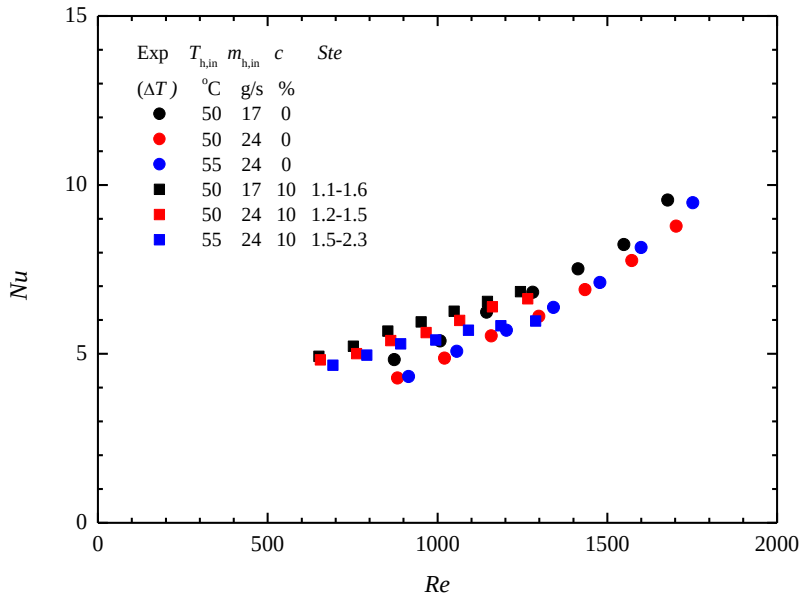

Figure 6.46 Comparison of average *Nu* of MPCM-37 slurry with pure water

6.6 Effect of Stefan number

Stefan number is the dominant parameter which affects heat transfer performance of mPCM slurry. In the present investigation, Stefan number was increased by increasing the temperature of hot water flowing inside the upper and lower jackets. It can be observed from Figure 6.45 and Figure 6.46 that the increase in hot water temperature results in lower average Nusselt number. The increase in Stefan number results in poor heat transfer performance of mPCM slurry. This is likely due to dominant sensible heating of mPCM slurry instead of latent heat of absorption.

6.7 Fluid temperature rise versus Reynolds number

The mPCM slurries as heat transfer fluid are superior to pure water due to their constant temperature during phase change. The comparison of bulk temperature rise inside the microchannel with respect to Reynolds number is shown in Figure 6.47. For the case of $T_{h,in}$ = 50 ºC, at Reynolds number, *Re*, of 1000 , the fluid temperature rises of 5% and 10% mass concentrations of mPCM slurry are 1.72 K and 3.43 K, respectively, lower than those of pure water. Because of the latent heat absorption of mPCM slurry, the temperature remains constant during the phase change which results in lower temperature rise as compared to water. This drop in temperature rise of mPCM slurry as compared to those of water, for the same heat transfer rate makes it possible to reduce the size of reservoirs for thermal energy storage.

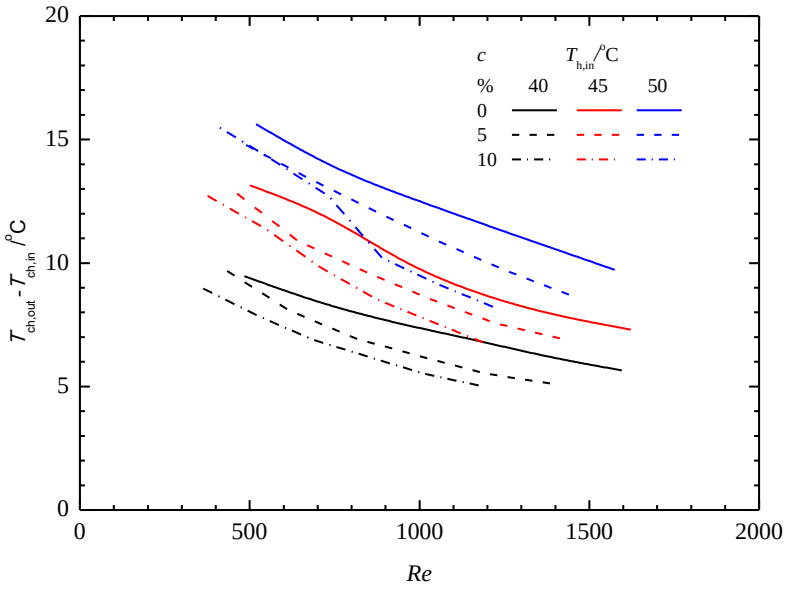

Figure 6.47 Variation of fluid temperature rise *vs Re*

6.8 Comparison of pressure drop

One of the drawback associated with phase change slurry is its higher pressure drop because of higher dynamic viscosities due to addition of mPCM particles. Figure 6.48 shows the comparison of the fanning friction factors of mPCM slurry and pure water predicted by the empirical correlation of Shah and London (1978) defined in section 5.3. It can be seen that mPCM slurry behaves as a single phase fluid in the laminar flow regime. The pressure drop of mPCM slurry was also compared with pure water at the same mass flow rate as shown in Figure 6.49. It depicts that pressure drop of mPCM slurry of 5% and 10% mass concentrations is higher than those of pure water. This is due to the addition of mPCM particles which results in flow resistance due to higher dynamic viscosities of mPCM slurry. The effect of temperature on pressure drop is not very prominent but the pressure drop decreases with the increase of temperature. It is likely that the bulk temperature rise results in lower dynamic viscosity.

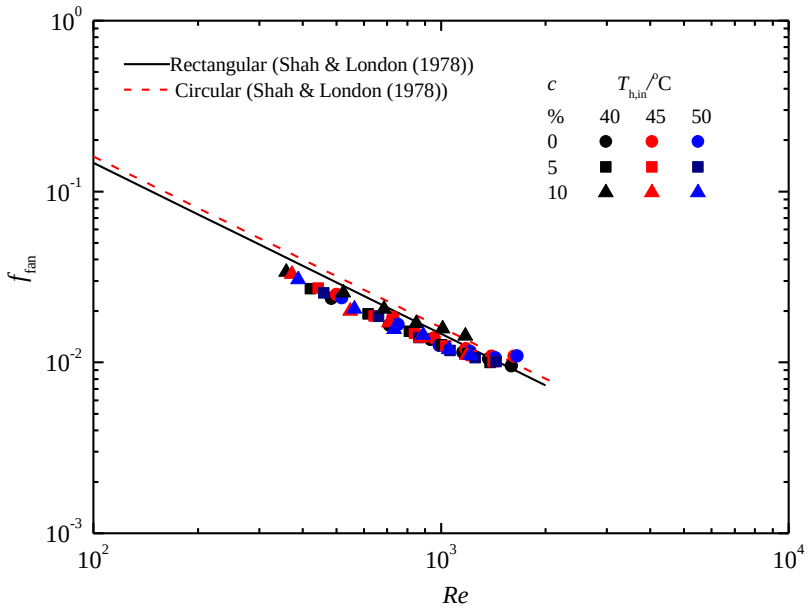

Figure 6.48 Comparison of fanning friction factor for water and mPCM slurry

One can see that in Figure 6.50 that the pressure drop of mPCM slurry was higher than pure water because of higher viscosity of mPCM slurry.

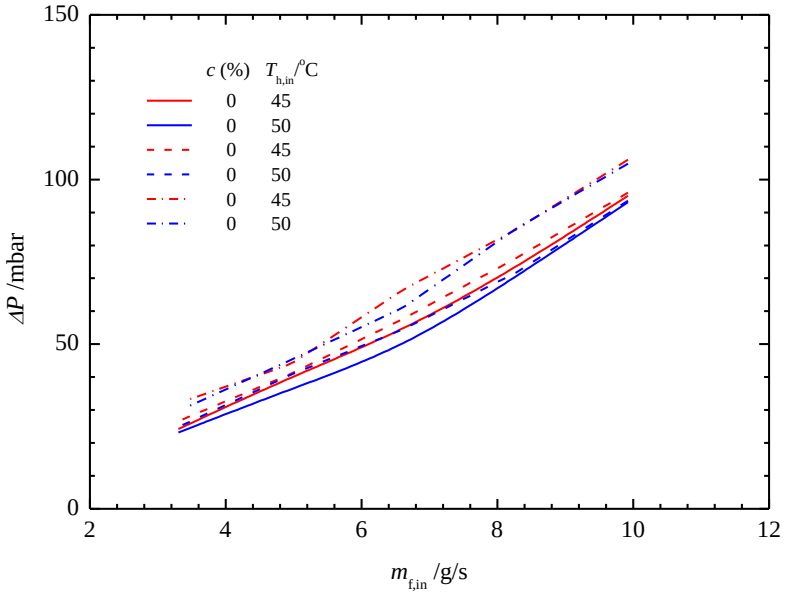

Figure 6.49 Pressure drop *vs* mass flow rate of working fluid

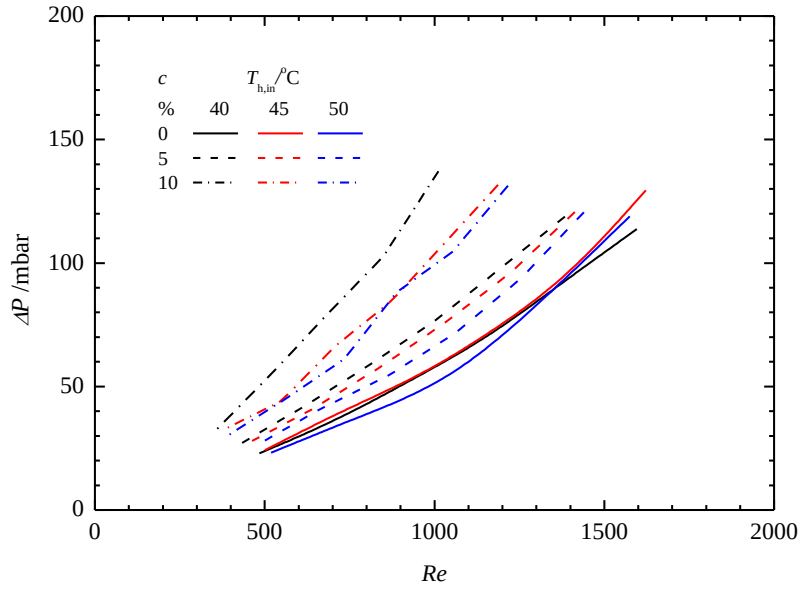

Figure 6.50 Pressure drop *vs* heat transfer rate

6.9 Development of correlation for mPCM slurry flow in microchannels under convective boundary condition

Literature review shows that heat transfer performance of mPCM slurry is dependent on mass flow rate, heat flux imposed for phase change, Stefan number and melting temperature range. A new correlation was developed for heat transfer assessment of laminar mPCM slurry flow in microchannels under convective boundary condition. For laminar flow, the general form of *Nu=f(Re,Pr,Ste)* was used to analyse the heat transfer performance of mPCM slurry under convective boundary condition. The following dimensionless parameters were taken into consideration to analyze the heat transfer characteristics of mPCM particles in laminar flow: Reynolds number($Re = \rho_b v D_h/\mu_b$), Prandtl number ($Pr = C_b\mu_b/k_b$) and Stefan number ($Ste = \dot{m}C_b(T_{ch,out} - T_{ch,in})/\dot{m}h_{fg}$).

The general form of proposed correlation is given by Eq. (6.3).

$$Nu_{\text{the}} = ARe^{b}Pr^{c}Ste^{d} \tag{6.3}$$

where *A*,*b*,*c* and *d* are the correlation coefficients which were obtained by the least-square method.

By taking natural logarithm on both sides of Eq. (6.3).

$$lnNu_{\text{the}} = a + blnRe + clnPr + dlnSte \tag{6.4}$$

The sum of square of residuals is given by following Eq. (6.5)

$$R^2 = \sum_{i=1}^{n}\left[lnNu_{\text{exp}} - lnNu_{\text{the}}\right]^2 \tag{6.5}$$

The condition for R^2 to be minimum is $\partial R^2/\partial a = \partial R^2/\partial b = \partial R^2/\partial c = \partial R^2/\partial d = 0$.

$$\frac{\partial R^2}{\partial a} = 2\sum_{i=1}^{n}\left[lnNu_{\text{exp}} - blnRe - clnPr - dlnSte - a\right](-1) = 0 \tag{6.6}$$

$$\frac{\partial R^2}{\partial b} = 2\sum_{i=1}^{n}\left[lnNu_{\text{exp}} - blnRe - clnPr - dlnSte - a\right](-lnRe) = 0 \tag{6.7}$$

$$\frac{\partial R^2}{\partial c} = 2\sum_{i=1}^{n}\left[lnNu_{\text{exp}} - blnRe - clnPr - dlnSte - a\right](-lnPr) = 0 \tag{6.8}$$

$$\frac{\partial R^2}{\partial d} = 2\sum_{i=1}^{n}\left[lnNu_{\text{exp}} - blnRe - clnPr - dlnSte - a\right](-lnSte) = 0 \tag{6.9}$$

Equations. (6.6) to (6.9) can be arranged as follows:

$$b\sum_{n=i}^{n} lnRe + c\sum_{n=i}^{n} lnPr + d\sum_{n=i}^{n} lnSte + a = \sum_{n=i}^{n} lnNu_{\exp} \tag{6.10}$$

$$b\sum_{n=i}^{n} (lnRe)^2 + c\sum_{n=i}^{n} (lnPr)(lnRe) + d\sum_{n=i}^{n} (lnSte)(LnRe) + a(lnRe) = \sum_{n=i}^{n} (lnNu_{\exp})(lnRe) \tag{6.11}$$

$$c\sum_{n=i}^{n} (lnPr)^2 + b\sum_{n=i}^{n} (lnPr)(lnRe) + d\sum_{n=i}^{n} (lnSte)(LnPr) + a(lnPr) = \sum_{n=i}^{n} (lnNu_{\exp})(lnPr) \tag{6.12}$$

$$d\sum_{n=i}^{n} (lnSte)^2 + b\sum_{n=i}^{n} (lnSte)(lnRe) + c\sum_{n=i}^{n} (lnSte)(LnPr) + a(lnSte) = \sum_{n=i}^{n} (lnNu_{\exp})(lnSte) \tag{6.13}$$

Equations (6.10) to (6.13) can be arranged into 4×4 matrix as given below:

$$\begin{bmatrix} a & \sum_{n=i}^{n} lnRe & \sum_{n=i}^{n} lnPr & \sum_{n=i}^{n} lnSte \\ (lnRe) & \sum_{n=i}^{n} (lnRe)^2 & \sum_{n=i}^{n} (lnPr)(lnRe) & \sum_{n=i}^{n} (lnSte)(LnRe) \\ (lnPr) & \sum_{n=i}^{n} (lnPr)(lnRe) & \sum_{n=i}^{n} (lnPr)^2 & \sum_{n=i}^{n} (lnSte)(LnPr) \\ (lnSte) & \sum_{n=i}^{n} (lnSte)(lnRe) & \sum_{n=i}^{n} (lnSte)(LnPr) & \sum_{n=i}^{n} (lnSte)^2 \end{bmatrix} \tag{6.14}$$

$$\begin{bmatrix} a \\ b \\ c \\ d \end{bmatrix} = \begin{bmatrix} \sum_{n=i}^{n} lnNu_{\exp} \\ \sum_{n=i}^{n} (lnNu_{\exp})(lnRe) \\ \sum_{n=i}^{n} (lnNu_{\exp})(lnPr) \\ \sum_{n=i}^{n} (lnNu_{\exp})(lnSte) \end{bmatrix}$$

The solution of Eq. (6.14) gave the coefficients *a, b, c* and *d* of the proposed correlation. Equation (6.14) was solved by Matlab software. The coefficients yield the following correlation giving the best fit with the present experimental data for 360 < *Re* < 1700, 6 < *Pr* < 14, 4< *Ste* < 16 and 0.05 < *c* < 0.10.

$$Nu = 0.10Re^{0.46}Pr^{0.53}Ste^{0.01} \tag{6.15}$$

The comparison of the measured and predicted Nusselt numbers is shown in Figure 6.51. It can be seen that all experimental data can be predicted by Eq. (6.15) with a standard deviation within ±15%.

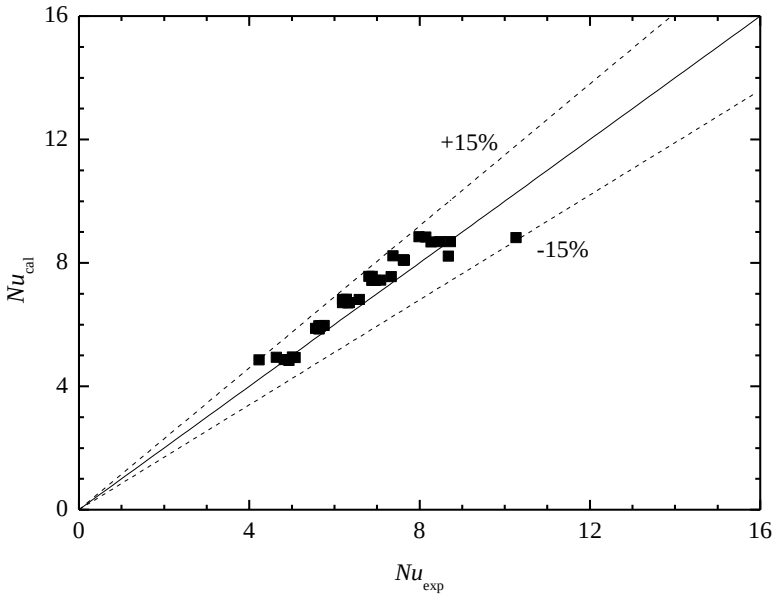

Figure 6.51 Comparison of measured and calculated Nusselt number by proposed correlation

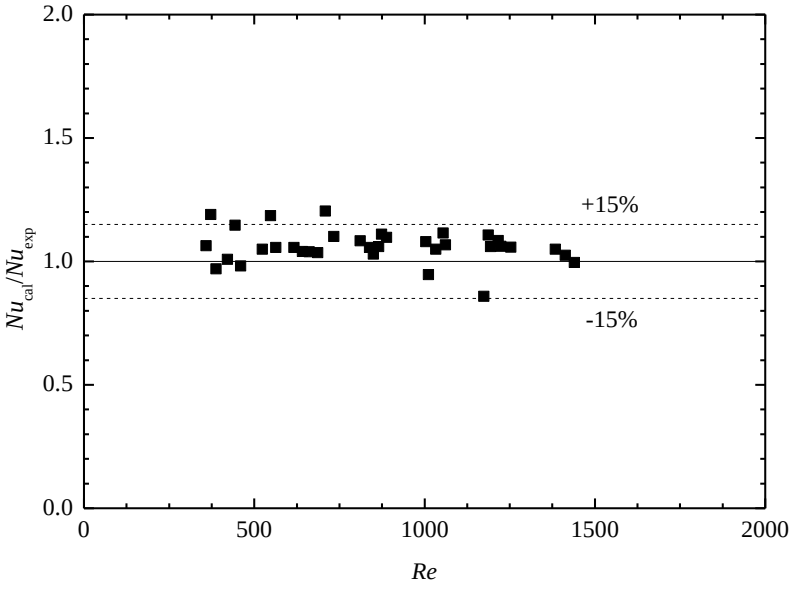

Figure 6.52 Comparison of measured and predicted Nusselt number with Reynolds number

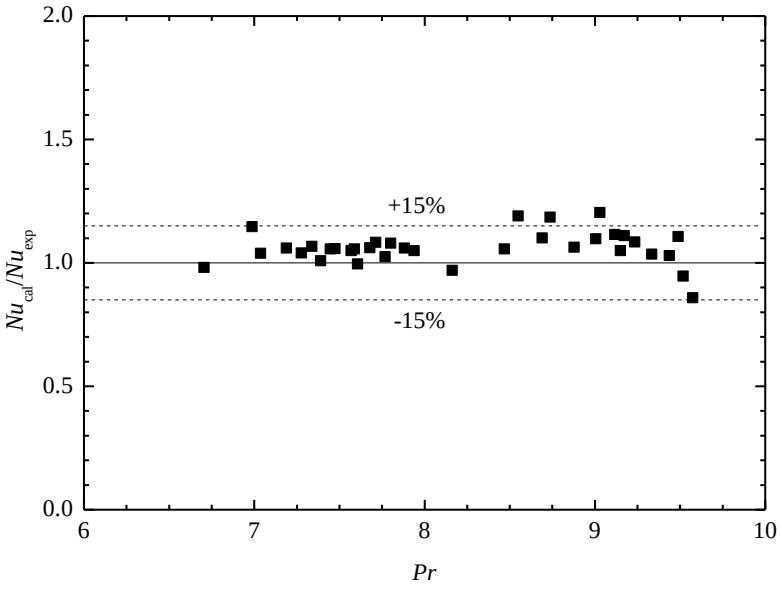

Figure 6.53 Comparison of measured and predicted Nusselt number with Prandtl number

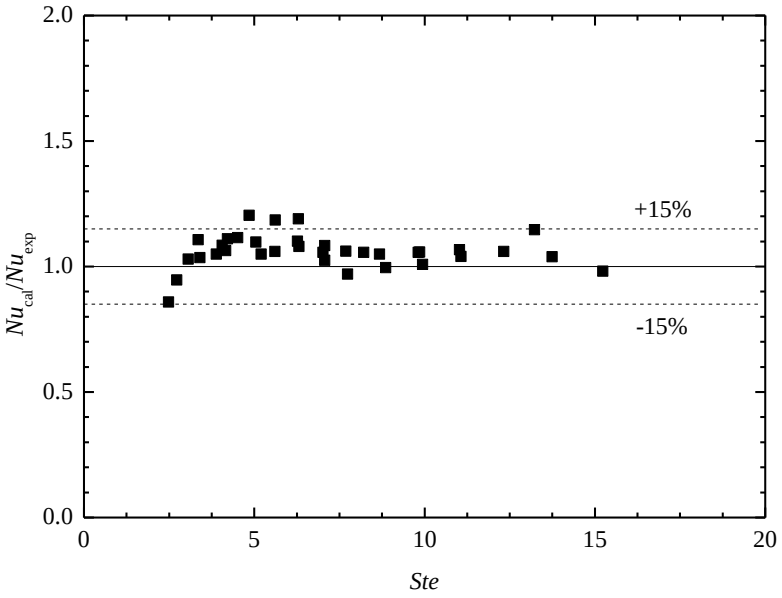

Figure 6.54 Comparison of measured and predicted Nusselt number with Stefan number

The ratios of average Nusselt number predicted by Eq. (6.15) to the measured average Nusselt number were compared with Reynolds number, Prandtl number and Stefan

number as shown in Figure 6.52 to Figure 6.54, respectively. All experimental data can be well predicted by Eq. (6.15) with a standard deviation within ±15%.

6.10 Physical stability of mPCM slurry

One of the major drawback of mPCM slurry is the rupture of mPCM particles due to pump shear force. In order to investigate the structural stability of mPCM particles, scanning electron images were taken to see the morphology of mPCM particles before and after experiments. The mPCM particles were dried to get the solid mPCM particles. The drying of mPCM slurry was done by freezer dryer as shown in Figure 6.55. The samples of 30 ml of 5% and 10% mass concentration of mPCM slurry were taken before and after experiments. Figure 6.56 and Figure 6.57 show the sample of mPCM before freezer dryer test.

Figure 6.55 Freezing/drying of mPCM slurry by liquid nitrogen

The SEM images were taken for both 5% and 10% mass concentration of Micronal DS5037X slurry at 20 µm and 50 µm scale in liquid and dried powder forms as shown in Figure 6.58 to Figure 6.69. It can be seen in both powder and liquid forms the mPCM particles were in very good shape. No rupture of particles was observed after experiments.

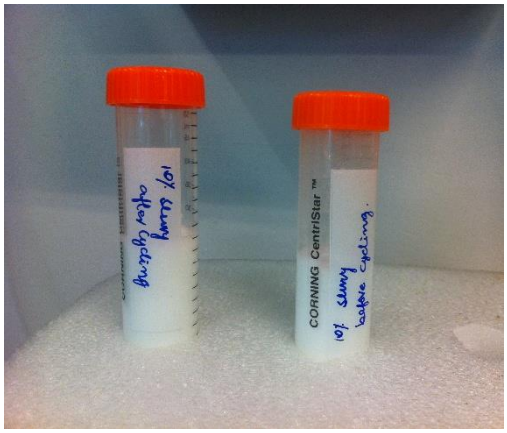

Figure 6.56 Photograph of 5% Micronal DS5037X slurry before and after experiment

Figure 6.57 Photograph of 10% Micronal BASF DS5037X slurry before and after experiment

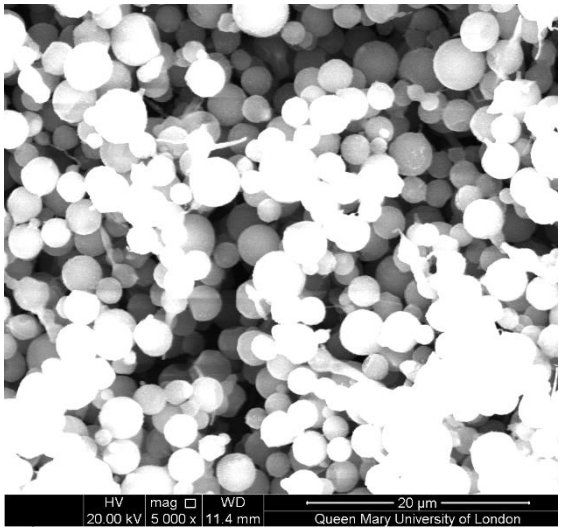

Figure 6.58 SEM image of powder Micronal BASF DS5037X slurry before experiments at 20 µm scale

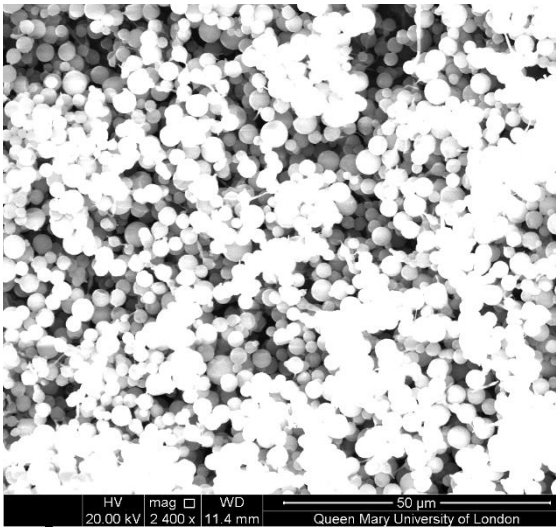

Figure 6.59 SEM image of powder Micronal BASF DS5037X slurry before thermal cycling at 50 µm scale

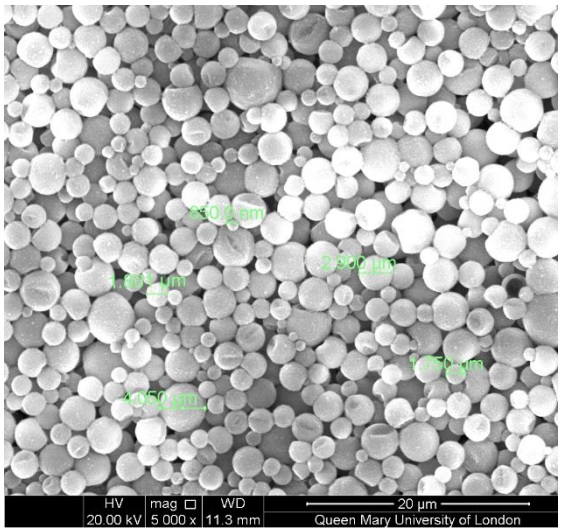

Figure 6.60 SEM image of liquid c = 42 % Micronal BASF DS5037X slurry before experiments at 20 µm scale

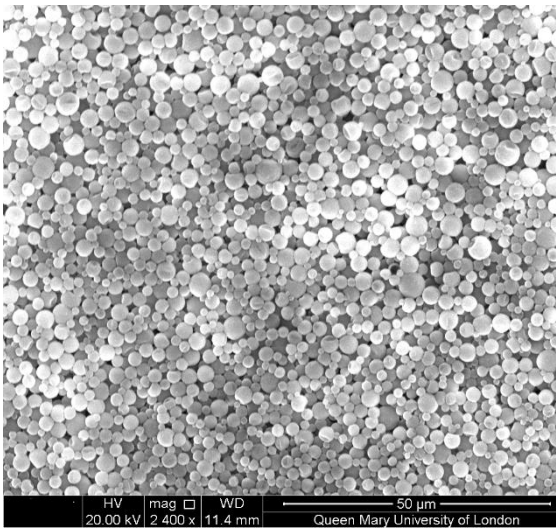

Figure 6.61 SEM image of liquid c = 42 % Micronal BASF DS5037X slurry before experiments at 50 µm scale

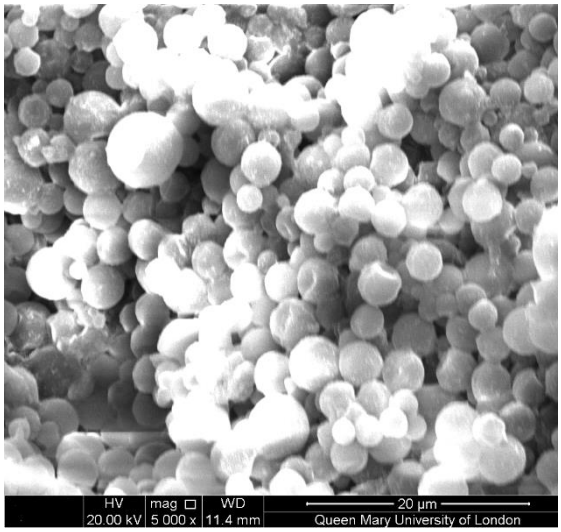

Figure 6.62 SEM image of powder c = 5 % Micronal BASF DS5037X slurry after experiments at 20 µm scale

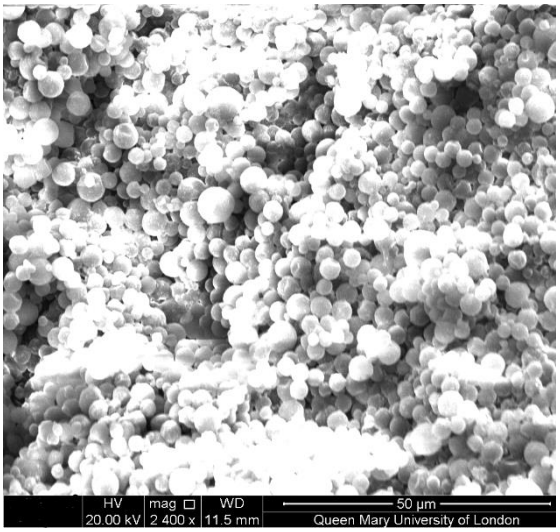

Figure 6.63 SEM image of powder c =5 % Micronal BASF DS5037X slurry after experiments at 50 µm scale

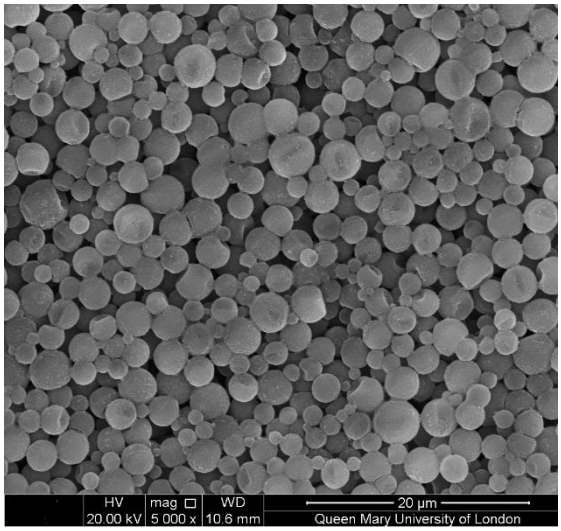

Figure 6.64 SEM image of liquid c = 5 % Micronal BASF DS5037X slurry after experiments at 20 µm scale

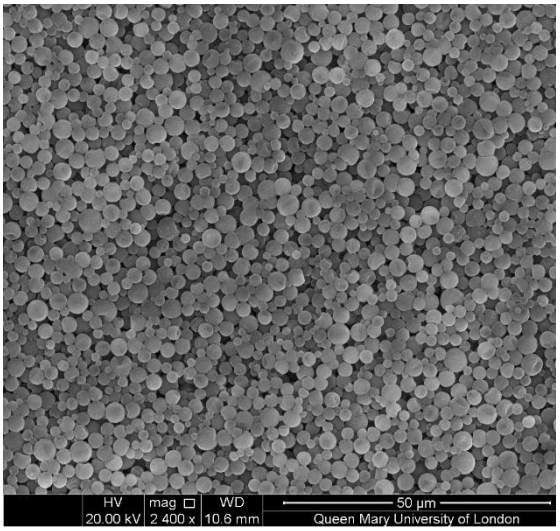

Figure 6.65 SEM image of liquid c = 5 % Micronal BASF DS5037X slurry after experiments at 50 µm scale

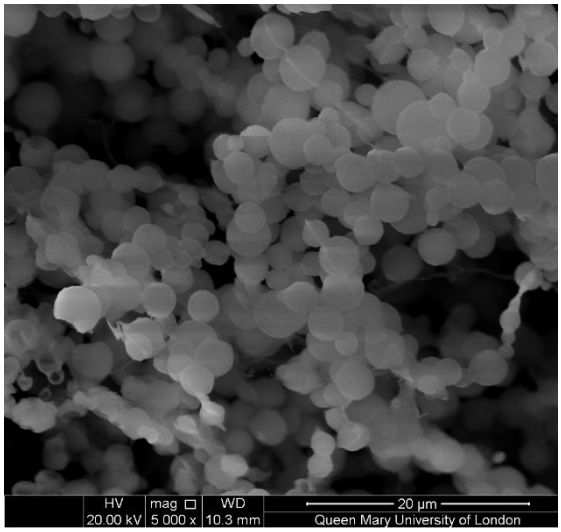

Figure 6.66 SEM image of powder *c* =10 % Micronal BASF DS5037X slurry after experiments at 20 µm scale

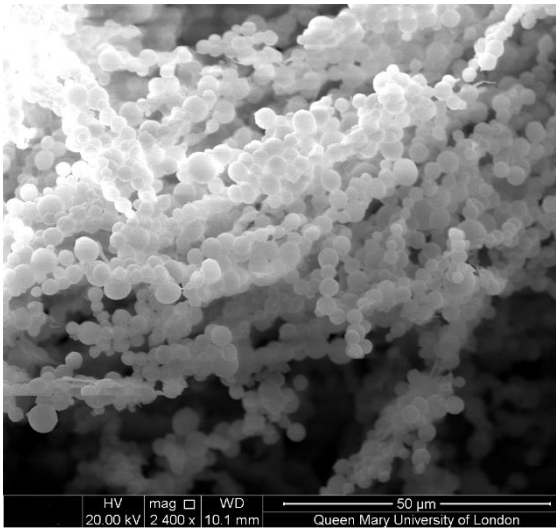

Figure 6.67 SEM image of power *c* =10 % Micronal BASF DS5037X slurry after experiments at 50 µm scale

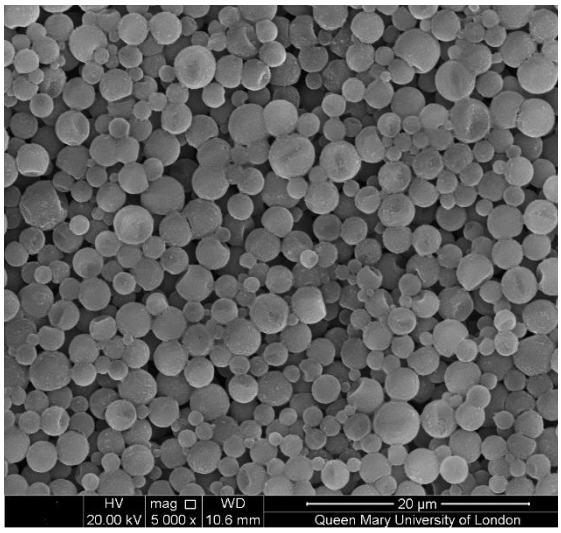

Figure 6.68 SEM image of liquid *c* =10 % Micronal BASF DS5037X slurry after experiments at 20 µm scale

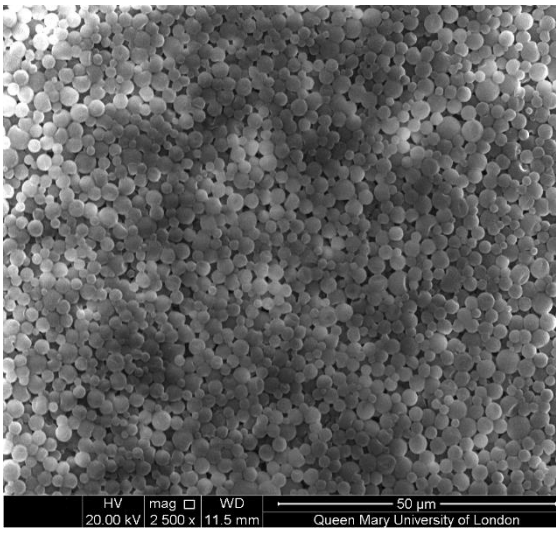

Figure 6.69 SEM image of liquid *c* =10 % Micronal BASF DS5037X slurry after experiments at 50 µm scale

6.11 Clogging of microchannels

Several operational problems were encountered during the experiments with DS5037X slurry. On one occasion the experiments were not conducted for consecutive two days. After two days large pressure drop was observed which indicated the blockage of microchannels. The blockage of microchannels was confirmed by removing one of the fitting of the mixing chamber, it was clearly seen that only one jet of mPCM slurry was coming out from microchannels. The side panel of the mixing chamber was removed and mPCM slurry thermostat was started to see the microchannels blockage. All microchannels were found to be blocked but one was open. Figure 6.70 shows the photograph of blockage of microchannels.

Figure 6.70 Photograph of blocked microchannels

After the diagnosis of blockage of channel, the whole test section was opened and cleaned thoroughly. After this incidence care was taken to avoid any deposition inside the microchannels. After finishing the daily experiments, mPCM slurry was removed from thermostat reservoir. Distilled water was circulated inside the microchannels for half an hour to avoid any PCM deposition.

6.12 Agglomeration

The water and mPCM particles remained completely dispersed during the experiments. No separation of water and PCM particles were observed. The mPCM slurry was placed inside the bottle after completing the experiments. Agglomeration of mPCM particles has been found after a week. The separation of mPCM particles is shown in Figure 6.71.

Figure 6.71 Separation of mPCM particles and water

6.13 Concluding remarks

The local and average heat transfer characteristics of mPCM slurry were compared with those of pure water under the same operating conditions. For the same *Re,* mPCM slurry of 5% and 10% mass concentrations showed enhanced local and average Nusselt numbers as compared to pure water. Owing to high latent heat of mPCM slurry bulk temperature rise of mPCM slurry was found lower than those of pure water for the same heat transfer rate. Under the some operating conditions, pressure drop for mPCM slurry was lower than those of pure water for same heat transfer rate. This reduction in fluid temperature rise and pressure drop for mPCM slurry makes it an attractive heat transfer fluid for thermal energy storage and transport. Its higher energy density results in compact devices and reduced pumping power. Operational problems during experiment were also

indicated. A new correlation was proposed to predict the heat transfer characteristics of laminar mPCM slurry flow in microchannels under convective boundary condition.

Chapter 7

Comparison of Experimental and Numerical Results for Water

In this chapter, numerical simulation of three-dimensional conjugated heat transfer of entire geometry of test section was carried out by commercial computational fluid dynamics (CFD) software FLUENT. The numerical results were compared with experimental data. The details of physical model, and simulation conditions are given in the following sections.

7.1 Physical model

The details of the test section are given in section 3.1. Due to symmetry of the test section only half of the test section was simulated in consideration of computational cost and time. Figure 7.1 shows the physical model, coordinates, and boundary conditions for three dimensional conjugated heat transfer during working fluid (water/mPCM slurry) flow in microchannels. The red line represents the microchannels. The blue sections represents the hot water flow inside the upper and lower jackets. *H, W* and *L* are the height, width and length of the test section. $T_{h,in}$, $w_{h,in}$ and $P_{h,in}$ are the temperature, velocity and pressure of the hot water at the inlet, respectively, and $T_{h,out}$ and $P_{h,out}$ are the temperature and velocity of the hot water at the outlet, respectively, for the heating water jacket. $T_{f,in}$, $w_{f,in}$ and $P_{f,in}$ are the temperature, velocity and pressure of the working fluid at the inlet, respectively, and $T_{f,out}$ and $P_{f,out}$ are the temperature and velocity of the working fluid at the outlet, respectively, for the microchannels.

Several assumptions have been made for the simplicity of the numerical model. These are as follows.

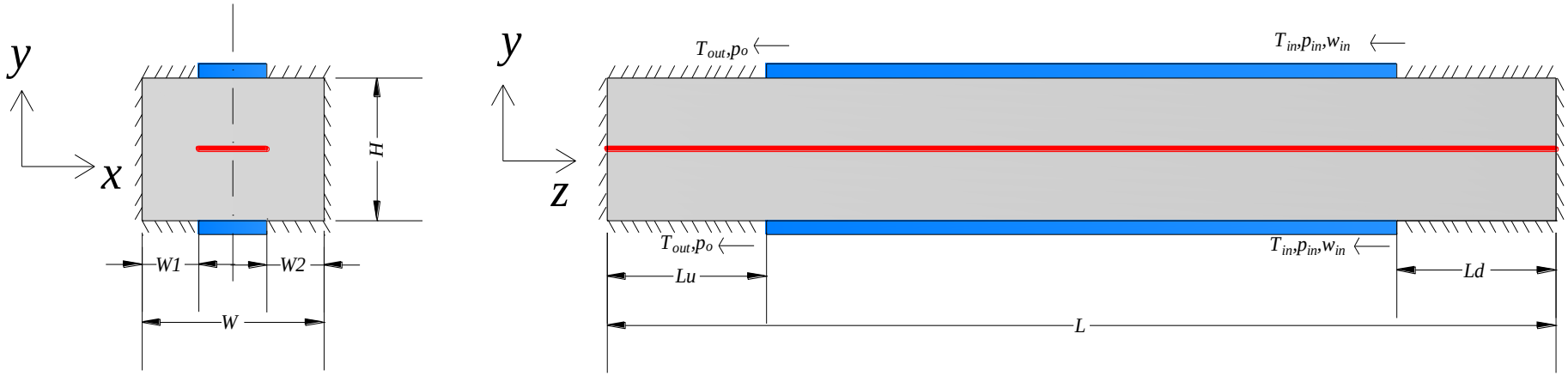

Figure 7.1 Physical model and coordinates

1. The flow of mPCM slurry inside the microchannel is steady state.
2. The mPCM slurry flow inside the microchannel is laminar.
3. Thermophysical properties of mPCM are taken to be constant except the specific heat capacity which is strongly temperature dependent.
4. The dynamic viscosity of water is set as piece linear function of water temperature.

7.2 Governing equations

The governing equations for mass, momentum and energy conservation in Cartesian coordinate are given in Eqs. (7.1) to (7.6).

Continuity equation:

$$\frac{\partial u}{\partial x}+\frac{\partial v}{\partial y}+\frac{\partial w}{\partial z}=0 \tag{7.1}$$

Momentum equations:

$$\rho_{\mathrm{b}}\left(u\frac{\partial u}{\partial x}+v\frac{\partial u}{\partial y}+w\frac{\partial u}{\partial z}\right)=-\frac{\partial P}{\partial x}+\mu_{\mathrm{b}}\left(\frac{\partial^2 u}{\partial x^2}+\frac{\partial^2 u}{\partial y^2}+\frac{\partial^2 u}{\partial z^2}\right) \tag{7.2}$$

$$\rho_{\mathrm{b}}\left(u\frac{\partial v}{\partial x}+v\frac{\partial v}{\partial y}+w\frac{\partial v}{\partial z}\right)=-\frac{\partial P}{\partial y}+\mu_{\mathrm{b}}\left(\frac{\partial^2 v}{\partial x^2}+\frac{\partial^2 v}{\partial y^2}+\frac{\partial^2 v}{\partial z^2}\right) \tag{7.3}$$

$$\rho_{\mathrm{b}}\left(u\frac{\partial w}{\partial x}+v\frac{\partial w}{\partial y}+w\frac{\partial w}{\partial z}\right)=-\frac{\partial P}{\partial z}+\mu_{\mathrm{b}}\left(\frac{\partial^2 w}{\partial x^2}+\frac{\partial^2 w}{\partial y^2}+\frac{\partial^2 w}{\partial z^2}\right) \tag{7.4}$$

Energy equation of fluid:

$$\rho_{\mathrm{b}} C_{\mathrm{b}} \left(u\frac{\partial T}{\partial x} + v\frac{\partial T}{\partial y} + w\frac{\partial T}{\partial z}\right) = k_{\mathrm{b}}\left(\frac{\partial^2 T}{\partial x^2} + \frac{\partial^2 T}{\partial y^2} + \frac{\partial^2 T}{\partial z^2}\right) \tag{7.5}$$

Energy equation for solid:

$$k_{\mathrm{s}}\left(\frac{\partial^2 T_{\mathrm{w}}}{\partial x^2} + \frac{\partial^2 T_{\mathrm{w}}}{\partial y^2} + \frac{\partial^2 T_{\mathrm{w}}}{\partial z^2}\right) = 0 \tag{7.6}$$

where u, v and w are velocity components in *x*, *y* and *z* directions. T_{f} and T_{s} are the temperatures of fluid and solid, respectively. ρ_{b} and μ_{b} are density and dynamic viscosity of the working fluid, k_{b} and k_{s} are the thermal conductivity of the working fluid and solid material (Aluminium).

7.3 Boundary conditions

The following boundary conditions were applied to the surfaces of the test section.

Fluid entered into microchannel inlet at constant velocity and temperature.

$$w = w_{\mathrm{f,in}},, u = v = 0, T_{\mathrm{fluid}} = T_{\mathrm{f,in}} \quad \text{at} \quad z = 0 \tag{7.7}$$

Hot water entered into the upper and lower jackets at constant velocity and temperature.

$$w = w_{\mathrm{h,in}},, u = v = 0, T_{\mathrm{fluid}} = T_{\mathrm{h,in}} \quad \text{at} \quad z = L - L_{\mathrm{d}} \tag{7.8}$$

A symmetry boundary condition was applied to the left side of the test section.

$$\frac{\partial T_{\mathrm{s}}}{\partial x} = 0 \quad \text{at} \quad x = 0 \tag{7.9}$$

A pressure outlet boundary condition was applied at the outlet of the microchannel.

$$p = p_o \qquad \text{at} \quad z = L \tag{7.10}$$

A pressure outlet boundary condition was also applied to the outlet of the water jacket.

$$p = p_o \qquad \text{at} \quad z = L - L_u \tag{7.11}$$

An adiabatic boundary condition was applied to the right, top and bottom surfaces.

7.4 Numerical method

The finite volume method was used to convert the partial differential equations to algebraic equations. SIMPLE algorithm was implemented for solving pressure velocity coupling. The *k*-ε turbulent model was used for turbulant flow inside the upper and lower jackets. The convergence criteria for energy, continuity and velocity equations was set at 10^{-6}. The default under relaxation factors were used for continuity (0.3), momentum (0.7) and energy (1.0) equations. Because of the geometrical symmetry of the test section only a half of the test section was chosen as the computational domain.

It is very important to mention here that this is single phase model with the properties of mPCM slurry. The properties of mPCM slurry calculated by Eqs. A.1 to A.5 was introduced into FLUENT data base.

7.5 Validation of the numerical model

The present numerical model was validated by comparing fanning friction factor for circular and rectangular channels for fully developed flow predicted by Shah and London (1978) with the numerical results. The fanning friction factor is a dimensionless parameter used for comparison at different Reynolds numbers. The maximum deviation between the numerical and empirical correlation results were within 9.1% as shown in Figure 7.2.

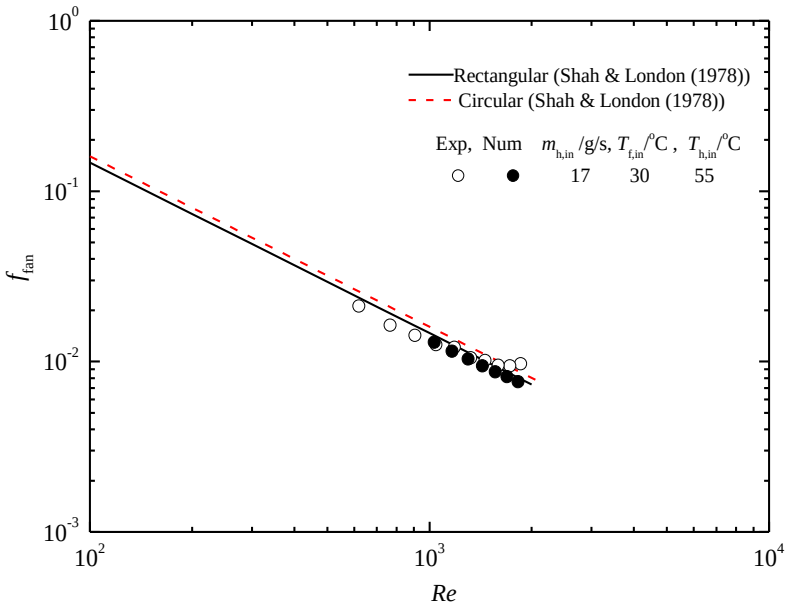

Figure 7.2 Comparison of f_{fan} with empirical correlations of Shah & London (1978)

7.6 Numerical results with pure water

Numerical results of pure water were compared with the present experimental data. Numerical simulations were performed at $T_{h,in}$= 55 ºC, $m_{h,in}$ = 17 g/s, $T_{f,in}$= 30 ºC. The inlet mass flow rate of water was varied from 4 to 11 g/s.

7.6.1 Comparison of temperature measurements inside the test block

A comparison was made for temperatures measured inside the test block, at the inlet and outlet of microchannel, at the inlet and outlet of water mixers. The comparison of temperatures measured inside the test section and those of numerical results are illustrated in Figure 7.3 to Figure 7.9. In Figure 7.3 the temperatures of the numerical results at the measured locations inside the test block are 3.6 K higher than those of the experimental data. In numerical simulation, it was assumed that there were heat losses to surroundings. In fact in the experiment there were heat losses to surroundings. This could result in the lower measured temperatures.

Figure 7.3 illustrates that the temperature gradient on upper and lower blocks is almost same for the numerical study. However, experimental data show the higher temperature gradients on lower block as compared to numerical results. This could be due to the thermal contact resistance between the lapped surfaces. However, in numerical model, the thermal contact resistance between the mating blocks was not taken into account.

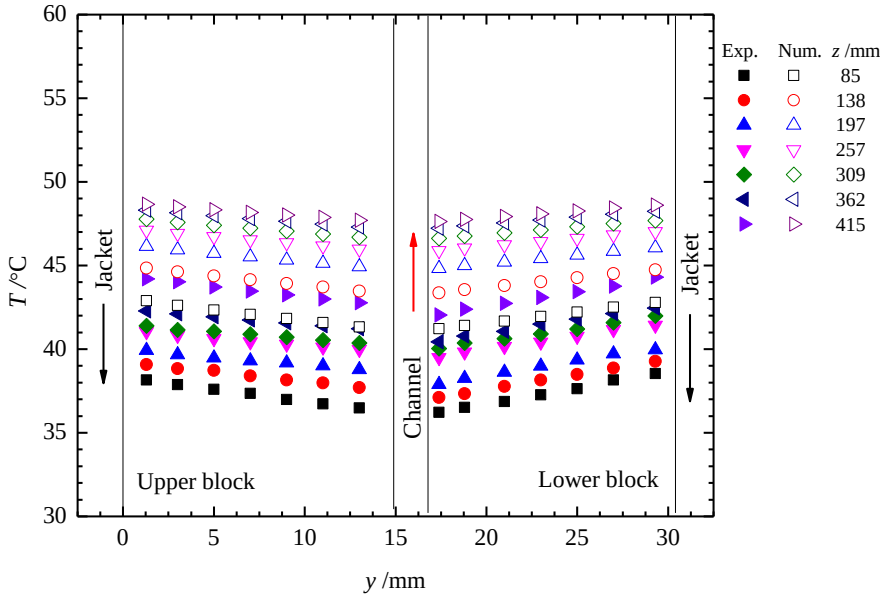

Figure 7.3 Comparison of temperature distributions inside the test block. c = 0%, $T_{h,in}$ = 55 ºC, $m_{h,in}$ = 10.7 g/s, $T_{f,in}$ = 30 ºC, $m_{h,in}$ = 17 g/s

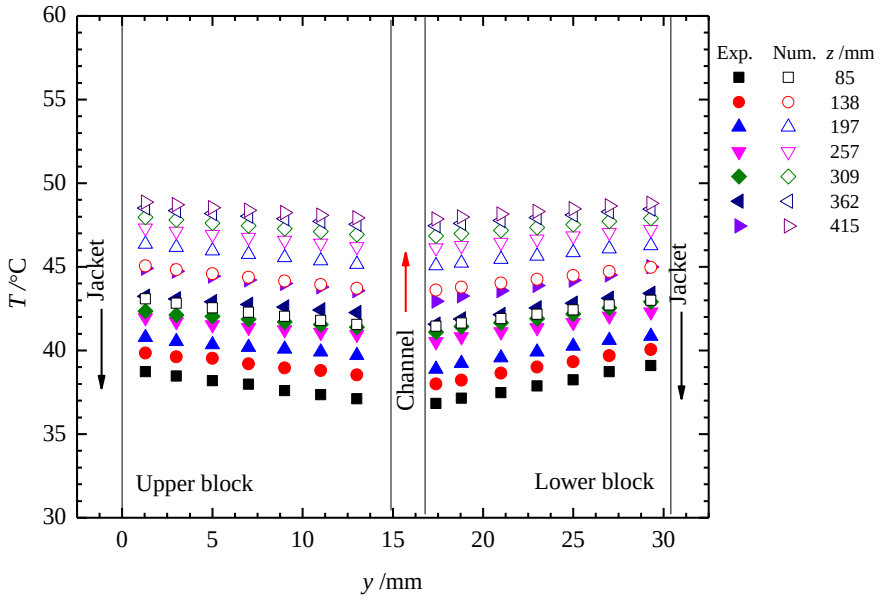

Figure 7.4 Comparison of temperature distributions inside the test block. c = 0%, $T_{h,in}$ = 55 ºC, $m_{h,in}$ = 9.8 g/s, $T_{f,in}$ = 30 ºC, $m_{h,in}$ = 17 g/s

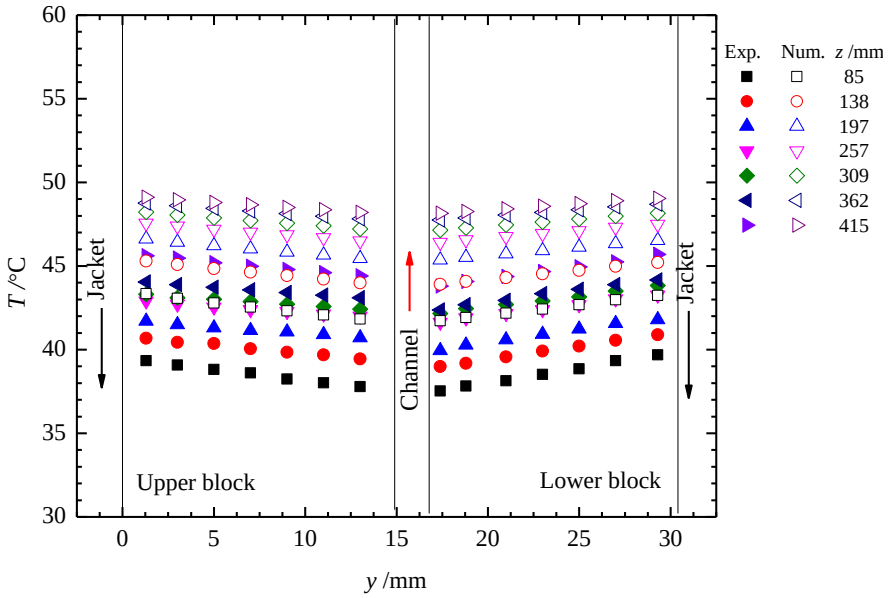

Figure 7.5 Comparison of temperature distributions inside the test block. c = 0%, $T_{h,in}$ = 55 ºC, $m_{h,in}$ = 9.0 g/s, $T_{f,in}$ = 30 ºC, $m_{h,in}$ = 17 g/s

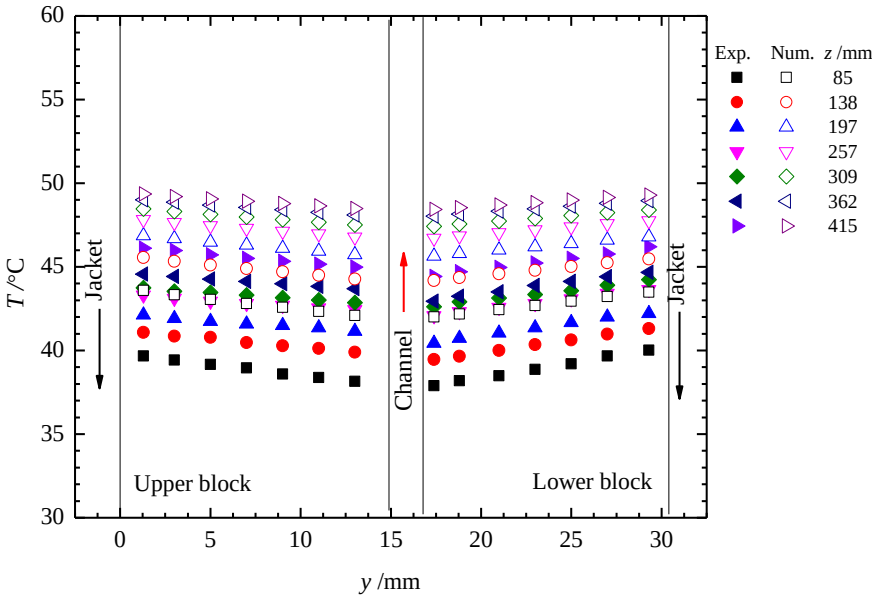

Figure 7.6 Comparison of temperature distributions inside the test block. c = 0%, $T_{h,in}$ = 55 ºC, $m_{h,in}$ = 8.2 g/s, $T_{f,in}$ = 30 ºC, $m_{h,in}$ = 17 g/s

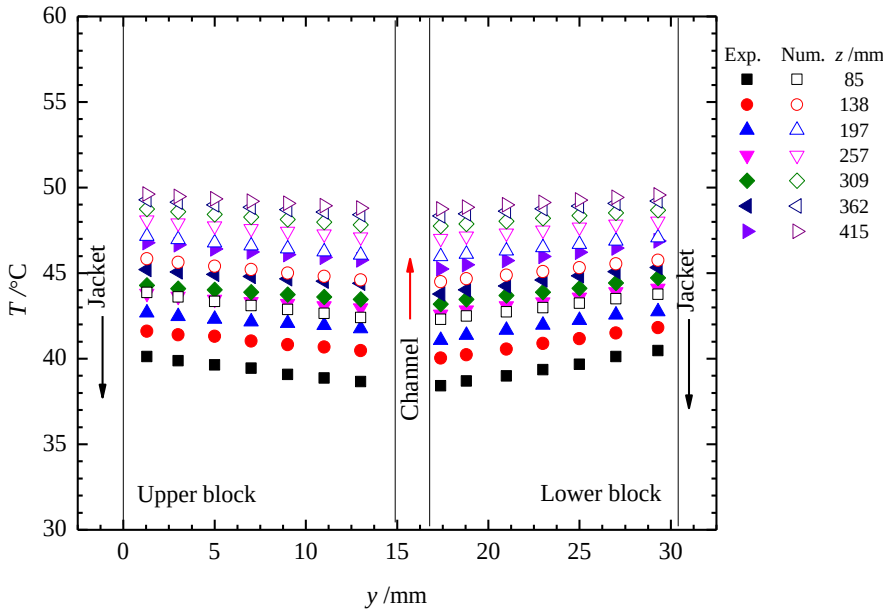

Figure 7.7 Comparison of temperature distributions inside the test block. c = 0%, $T_{h,in}$ = 55 ºC, $m_{h,in}$ = 7.4 g/s, $T_{f,in}$ = 30 ºC, $m_{h,in}$ = 17 g/s

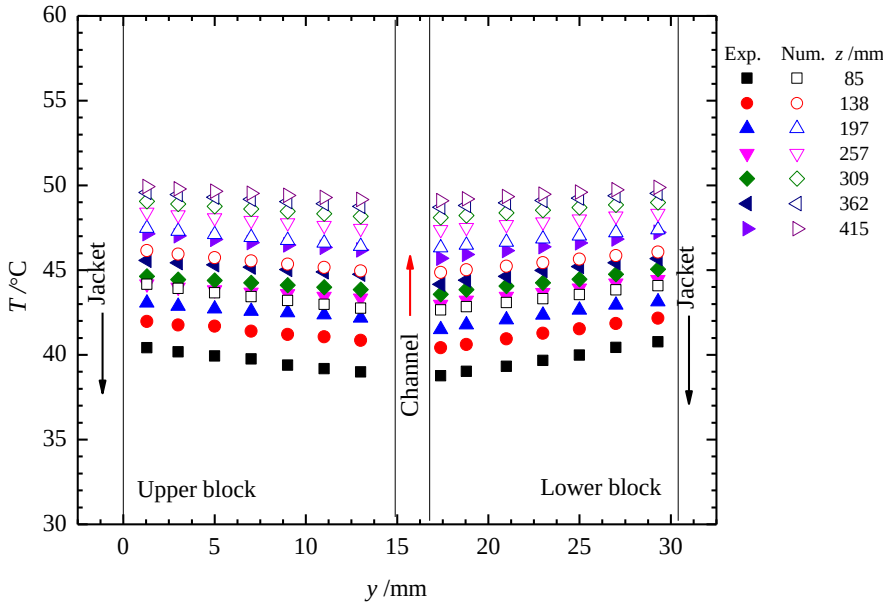

Figure 7.8 Comparison of temperature distributions inside the test block. c = 0%, $T_{h,in}$ = 55 ºC, $m_{h,in}$ = 6.6 g/s, $T_{f,in}$ = 30 ºC, $m_{h,in}$ = 17 g/s

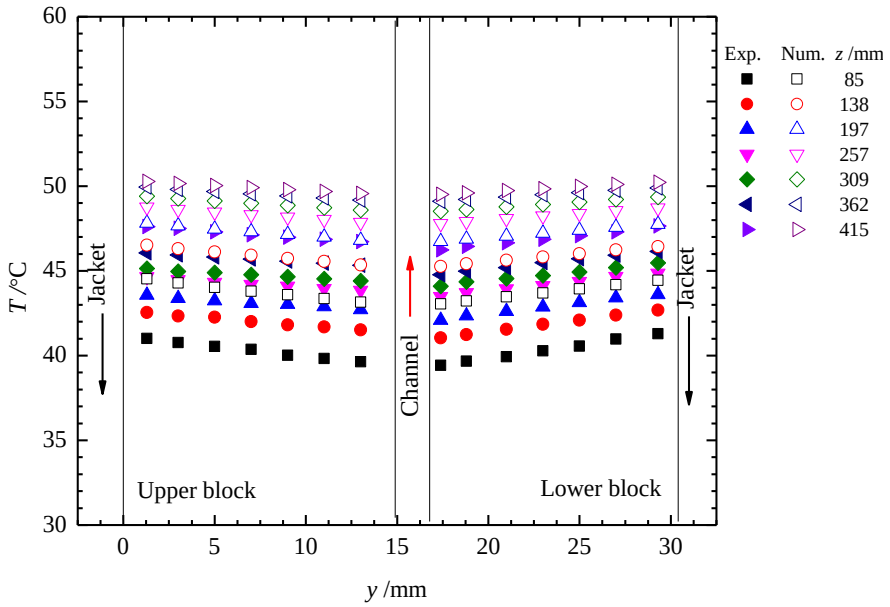

Figure 7.9 Comparison of temperature distributions inside the test block. c = 0%, $T_{h,in}$ = 55 ºC, $m_{h,in}$ = 5.7 g/s, $T_{f,in}$ = 30 ºC, $m_{h,in}$ = 17 g/s

7.6.2 Comparison of local surface temperature

Figure 7.10 shows the comparison of local surface temperature between numerical results and experimental data. In numerical simulation, the local surface temperature of the microchannel was obtained by taking the area weighted average temperature of the periphery of the microchannel. It can be seen that for $m_{f,in}$ = 10.7 g/s, till z = 0.03 m the surface temperature rises sharply due to adiabatic part of the test section. Later, the local surface temperature of the microchannel rises gradually and reaches to 47.3 ºC at z = 0.470 m. Afterwards, the local surface temperature of the microchannel decreases and reaches to 46.4 ºC due to the adiabatic section downstream. This drop in temperature is not observed in the experimental data by the inverse method. The temperatures measured are lower than numerical results by a maximum value of 4.6 K.

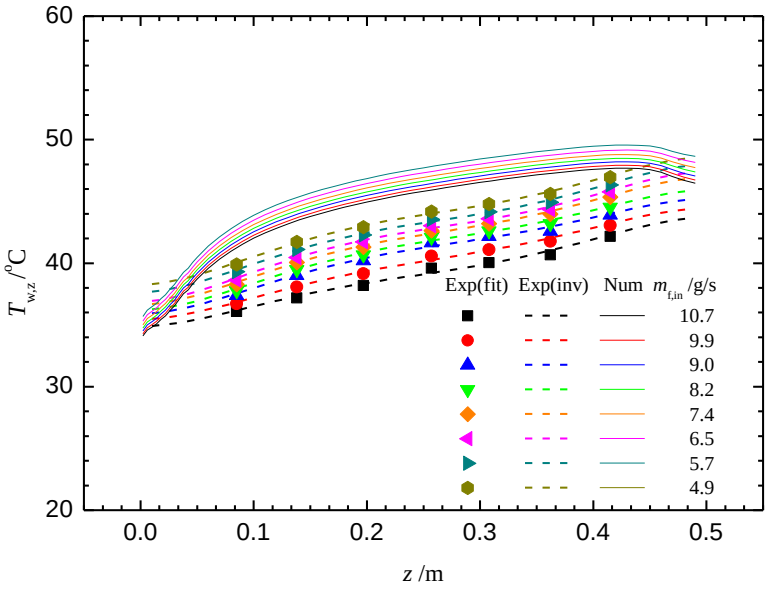

Figure 7.10 Comparison of local surface temperature. c = 0%, $T_{h,in}$ = 55 ºC, $T_{f,in}$ = 30 ºC, $m_{h,in}$ = 17 g/s

7.6.3 Comparison of local heat flux

Figure 7.11 describes the comparison of local heat flux by experiment data and numerical results. For $m_{f,in}$ = 10.7 g/s, the local heat flux by the inverse method and numerical results shows the same trend. The local heat flux till z = 0.03 m shows higher values as compared to numerical results due to ignoring the adiabatic upstream section of the test section. The numerical results clearly depicts the lower heat flux on both sides upstream and downstream adiabatic sections. Further, experimental local heat flux by linear fitting shows the similar trend of decrease in heat flux till z = 0.35 m, but afterwards local heat flux seems increasing. The increase in heat flux near the end of the test section could be due to the downstream adiabatic section and the jet impingement of hot water.

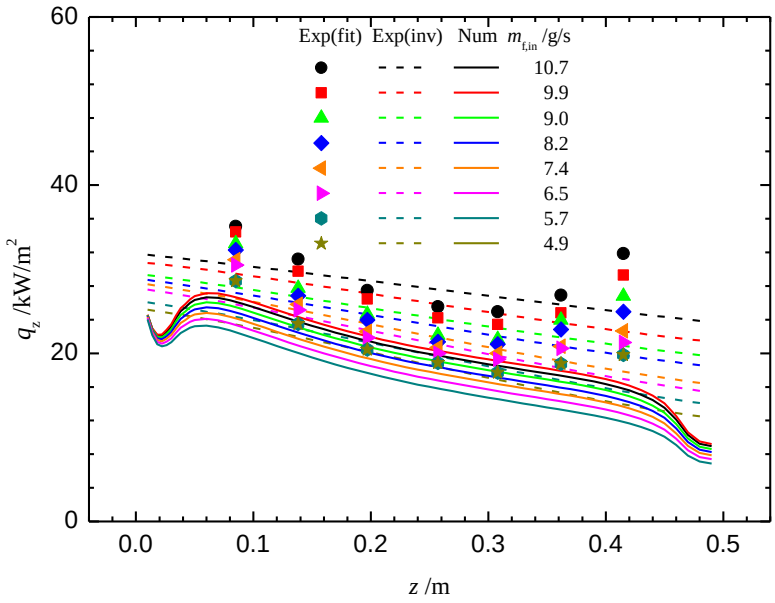

Figure 7.11 Comparison of local surface temperature. c = 0%, $T_{h,in}$ = 55 ºC, $T_{f,in}$ = 30 ºC, $m_{h,in}$ = 17 g/s

7.6.4 Comparison of outlet temperatures of microchannel, upper and lower jackets

A comparison was also made for the outlet temperatures of the channel and jackets by both the experimental data and numerical results. Figure 7.12 shows the comparison of

measured temperatures at the outlet of the microchannel. The difference between the measured temperatures at the outlet of microchannel and numerical results at 11.7 m/s was 1.8 K. Figure 7.13 shows the comparison of measured temperatures at the upper and lower jackets and obtained from numerical results. It seems a very good agreement between the numerical results and experimental data.

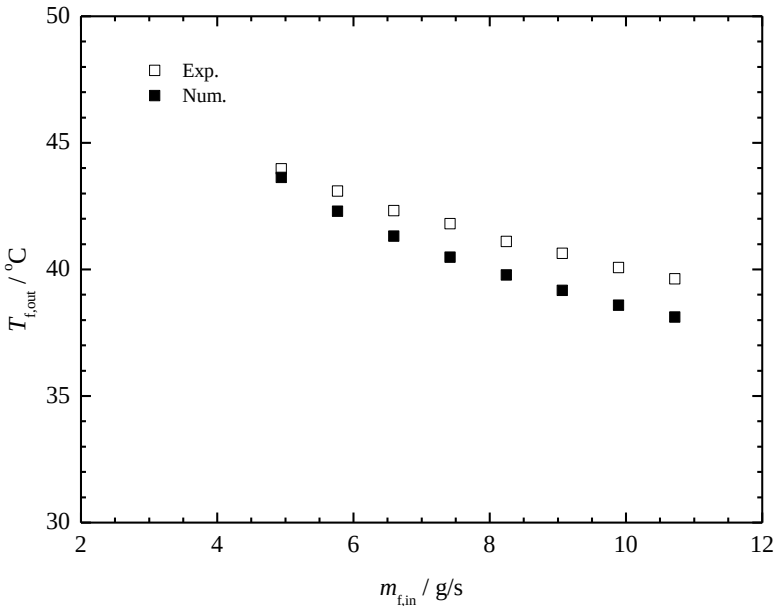

Figure 7.12 Comparison of experimental and numerical outlet temperature of fluid from microchannel

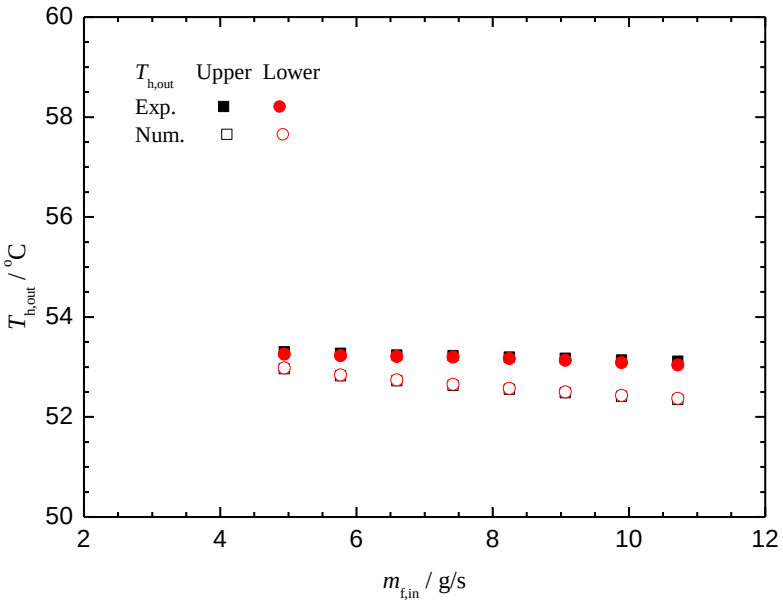

Figure 7.13 Comparison of outlet temperatures of upper and lower jacket

7.7 Summary

The numerical simulation of three-dimensional conjugated heat transfer of entire geometry of test section was performed. The numerical simulation was validated by comparing the fanning friction factor obtained from the numerical results with fanning friction factor predicted by empirical correlations. A good agreement was found. The numerical results were also compared with experimental data. The temperature obtained inside the test block from numerical results were found to be maximum 4.6 K higher than experimental data. This could be due to the heat losses to the surroundings. The numerical model was reliable and could be used for further simulation of mPCM slurry.

Chapter 8

Numerical Simulation of Heat Transfer and Pressure Drop during Melting of mPCM Slurry Flow in Microchannels

In this chapter, after the validation of numerical model, numerical simulations of three dimensional conjugated heat transfer were conducted during melting of mPCM slurry in microchannels. For validation purpose numerical simulation results were compared with experimental data of Chen et al. (2008). The physical model, boundary conditions and governing equations are the same as in Chapter 7. The effect of mPCM slurry on bulk temperature, surface temperature, Nusselt number and pressure drop were investigated.

8.1 Validation of numerical simulation for mPCM slurry

The present numerical simulation results were compared with the experimental data of Chen et al. (2008). The experiment was conducted in a circular tube of inner diameter 4 mm and length of 1.46 m. Due to the geometrical symmetry, only a half of the circular tube was simulated. The melting temperature range of mPCM slurry for the experiment was not mentioned. The melting temperature range of 14.1 ºC - 15.7 ºC was considered for the numerical simulation. The inlet temperature of mPCM slurry was taken as 11.0 ºC.

Figure 8.1 and Figure 8.2 compare the local Nusselt number and dimensionless surface temperature along dimensionless axial distance for experimental data and present numerical results. The maximum deviation between experimental and numerical results was 14.6%.

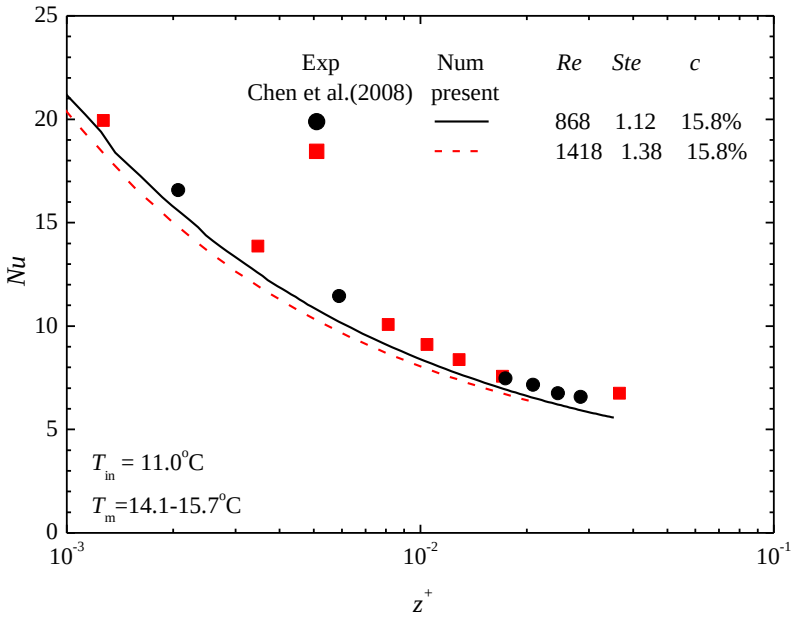

Figure 8.1 Comparison of local *Nu* along dimensionless axial distance

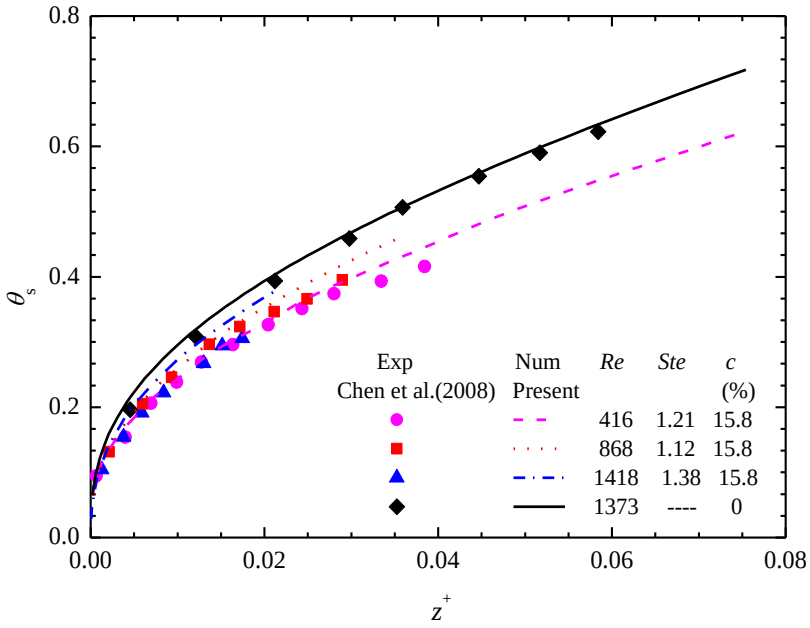

Figure 8.2 Variation of dimensionless surface temperature along dimensionless axial distance for mPCM slurry of mass concentration of 15.8%

8.2 Effective specific heat capacity model

The effective specific heat capacity model (Kondle et al. (2013)) was used for the numerical simulation of mPCM slurry flow. The specific heat capacity of mPCM slurry was strongly dependent on temperature. Eqs. (8.1) and (8.2) were used to find out the

specific heat capacity. Piecewise polynomial approach had been used in FLUENT to implement the change in specific heat capacity with temperature.

For $T_b < T_1$ or $T_b > T_2$

$$C_b = cC_p + (1-c)C_w \tag{8.1}$$

where T_b is the bulk temperature, T_1 and T_2 is the temperature where the phase change begins and completes, respectively.

For $T_1 < T_b < T_2$

$$C_b = (1-c)C_w + \frac{ch_{fs}}{(T_2 - T_1)} \tag{8.2}$$

where h_{fs} is the latent of mPCM slurry.

8.3 Fluid properties and flow parameters

The physical model and its coordinates are shown in Figure 7.1. The governing equations and boundary conditions are given in section 7.2 and section 7.3, respectively. The mPCM slurry properties of mPCM slurry are given in Table 6.2. Numerical simulations were conducted with mPCM slurry of mass concentration from 5-15%. The peak melting temperature of MPCM-37 was 36.85 ºC. The DSC curve shows that the melting temperature range of MPCM-37 was from 33-39 ºC as shown in Figure 6.5. The melting temperature range of 33 to 39 ºC was selected for numerical simulation.

Numerical simulations were conducted under the same operating conditions as water for comparison. By considering the melting temperature range of MPCM-37 slurry, the inlet temperature of mPCM slurry was taken to be 30 ºC. The inlet temperature and velocity of the hot water were taken to be 55 ºC and 0.37 m/s, respectively. In numerical simulation,

it was assumed that the mPCM slurry is completely in solid state before entering into the microchannel.

8.4 Temperature contours

Figure 8.3 illustrates temperature contours at the microchannel outlet for water and mPCM slurry of mass concentration ranging from 5 to 15%. Temperature contours show that the fluid temperature varies from the wall to the centre of the microchannel. The fluid temperature is lower in the case of mPCM slurry as compared to water. In the three-region model, it is assumed that all the mPCM particles starts to melt and to solidify at the same temperature. However, it is evident from temperature contours that the mPCM slurry near to the wall of microchannel melts before the mPCM slurry near the centre of microchannel.

Figure 8.4 represents the temperature distributions along the flow direction of the microchannel with respect to mass concentrations. It is observed that the growth of the thermal boundary is slower than that of the pure water. The thermal boundary layer extends with the increase of mass concentration of mPCM particles. This is due to the higher latent heat of mPCM slurry which elongates the thermal entry region.

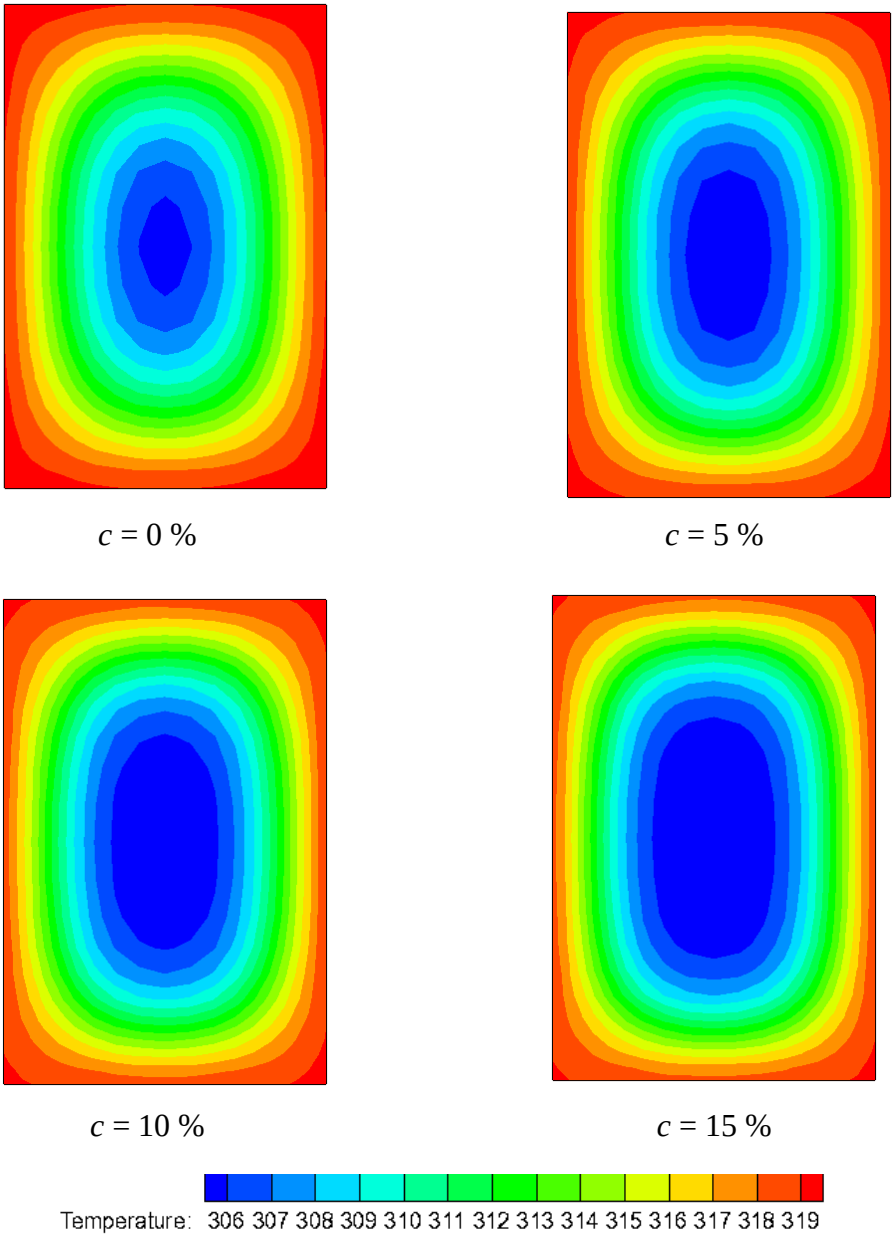

Figure 8.3 Temperature contours at the outlet of microchannel. $w_{f,in}$ = 1.2 m/s, $w_{h,in}$ = 0.37 m/s , $T_{h,in}$ = 55 ºC, $T_{f,in}$ = 30 ºC

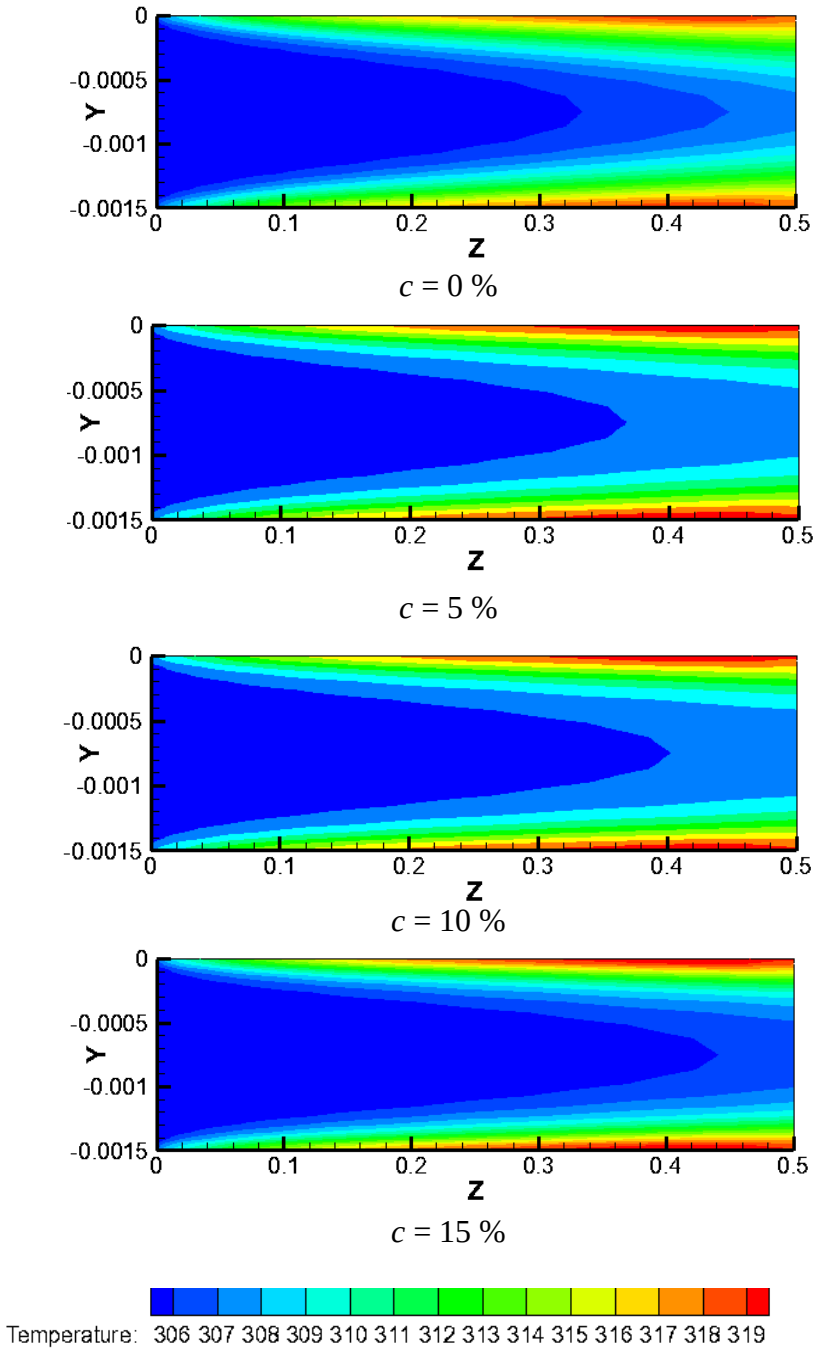

Figure 8.4 Temperature distributions along the flow direction of microchannel. $w_{f,in}$ = 1.2 m/s, $w_{h,in}$ = 0.37 m/s , $T_{h,in}$ = 55 ºC, $T_{f,in}$ = 30 ºC

8.5 Effect of mass concentration on bulk and surface temperatures

Figure 8.5 to Figure 8.9 represent the variation of the bulk temperature of pure water and mPCM slurry of 5%, 10% and 15% mass concentrations at different velocities 1.2, 1.0, 0.83, 0.65 and 0.55 m/s. In all cases, we observe that the bulk temperature of mPCM slurry are lower than that of pure water. This decrease in bulk temperature increases with the mass concentration of mPCM slurry. For v = 1.2 m/s, the bulk temperature of mPCM slurry of mass concentration 15% is 3.1 K lower than that of pure water at the outlet of the microchannel. This reduction in bulk temperature is due to the higher latent heat of mPCM slurry. Owing to the higher latent heat of mPCM slurry, it absorbs more heat and its temperature remains almost constant during phase change. Moreover, increase of mass concentration results in more loading of mPCM particles and higher latent heat, causing further reduction in bulk temperature.

The effect of mass concentration of mPCM slurry on the local surface temperature of microchannel are represented in Figure 8.10 to Figure 8.14. For all cases, the surface temperature increases sharply till z = 0.03 m because this section is adiabatic and at lower temperature the temperature rise is more prominent. From z = 0.03 to 0.47 m, there is further increase in surface temperature of microchannel, after z = 0.47 m there is sudden drop in surface temperature because of the adiabatic section of the test section downstream. For the case of v = 1.2 m/s, it can be seen that till z =0.1 m, the surface temperature of the microchannel is higher for all cases of mPCM slurry, this is because the mPCM particles were still in solid state due to insufficient heating power. The surface temperature of microchannel till z = 0.1 m has been enlarged to see more clear picture effect of mass concentration on surface temperature. It is observed that mPCM slurry with 15% concentration behaves poor than water and other concentrations. This is due to the

fact that during the solid and liquid phase of mPCM particles, the specific heat capacity is lower than that of pure water. The increase in concentration results in more mPCM particles in slurry which results in further poor performance as compared to pure water. After z = 0.1 m, the mPCM particles start melting and surface temperature starts decreasing. This decrease in surface temperature is more apparent after z = 0.38 m. It concludes that the presence of mPCM particles in slurry results in the reduction of bulk temperature and surface temperature due to enhanced specific heat capacity and latent heat of mPCM slurry during their phase change.

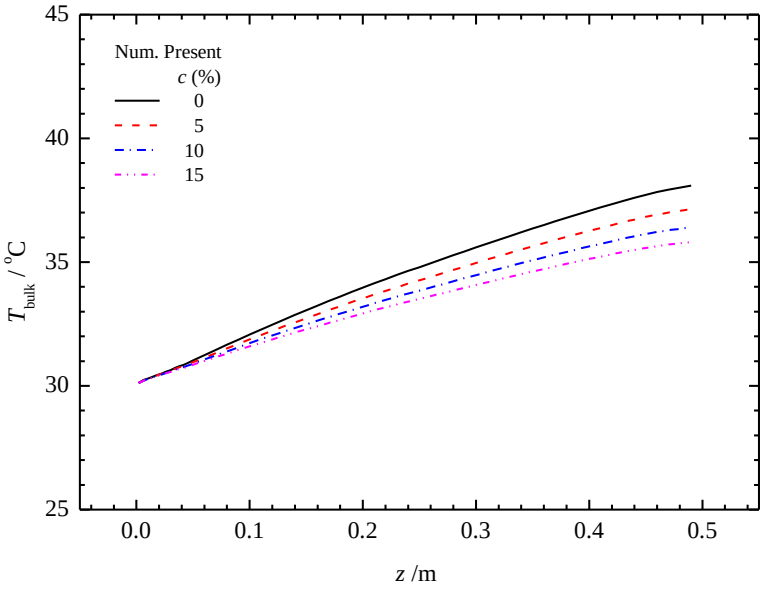

Figure 8.5 Local bulk temperature of pure water and mPCM slurry along the length of microchannel at w = 1.2 m/s

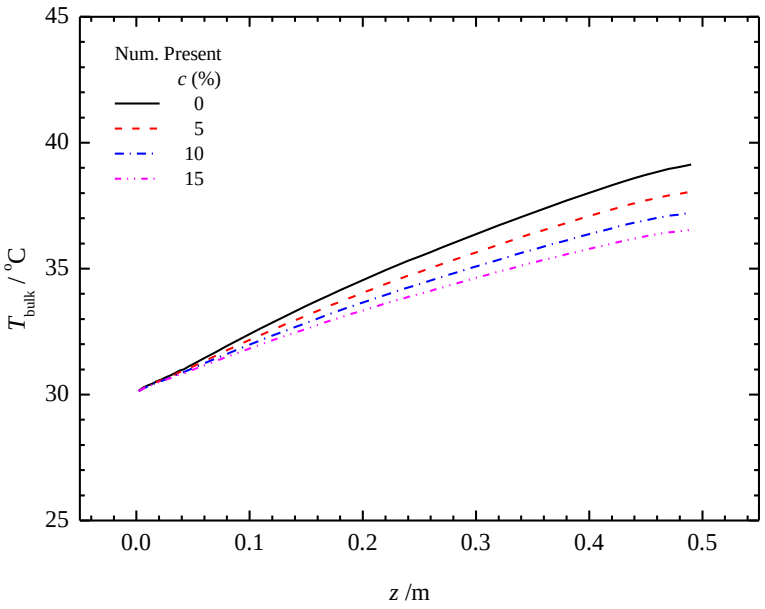

Figure 8.6 Local bulk temperature of pure water and mPCM slurry along the length of microchannel at w = 1.0 m/s

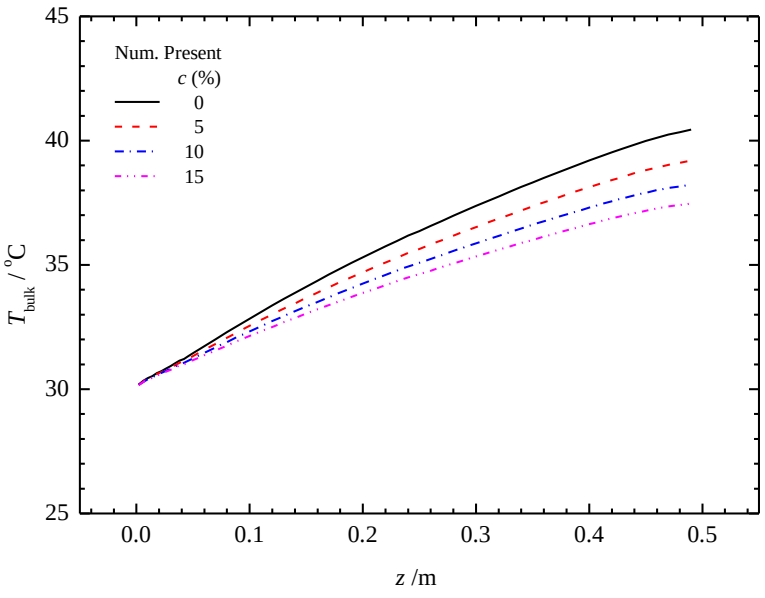

Figure 8.7 Local bulk temperature of pure water and mPCM slurry along the length of microchannel at w = 0.8 m/s

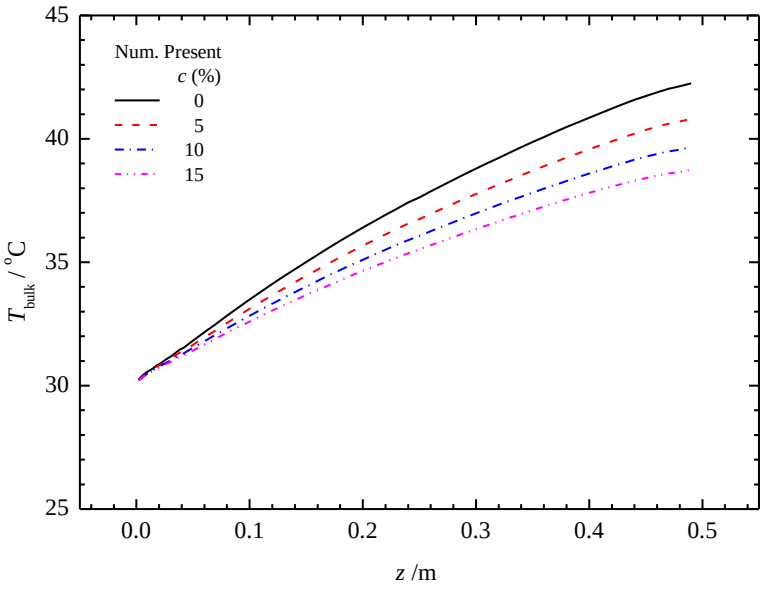

Figure 8.8 Local bulk temperature of pure water and mPCM along the length of microchannel at w = 0.65 m/s

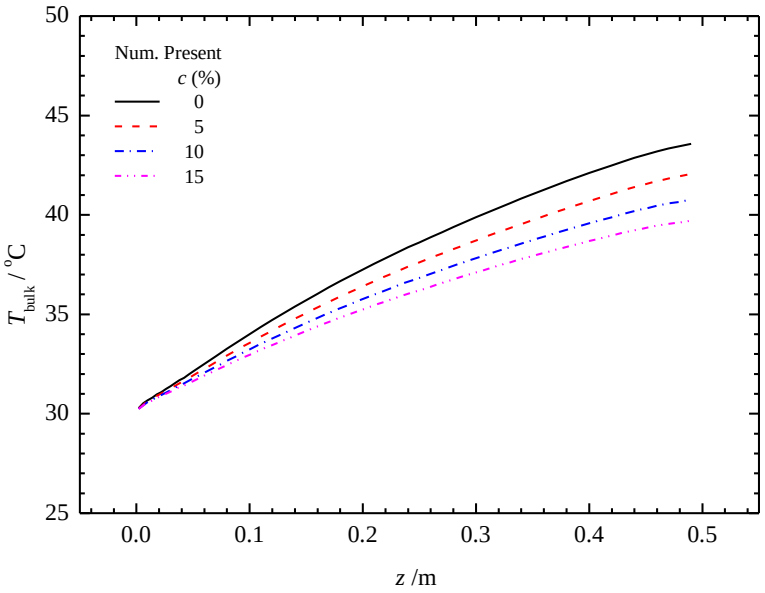

Figure 8.9 Local bulk temperature of pure water and mPCM slurry along the length of microchannel at w = 0.55 m/s

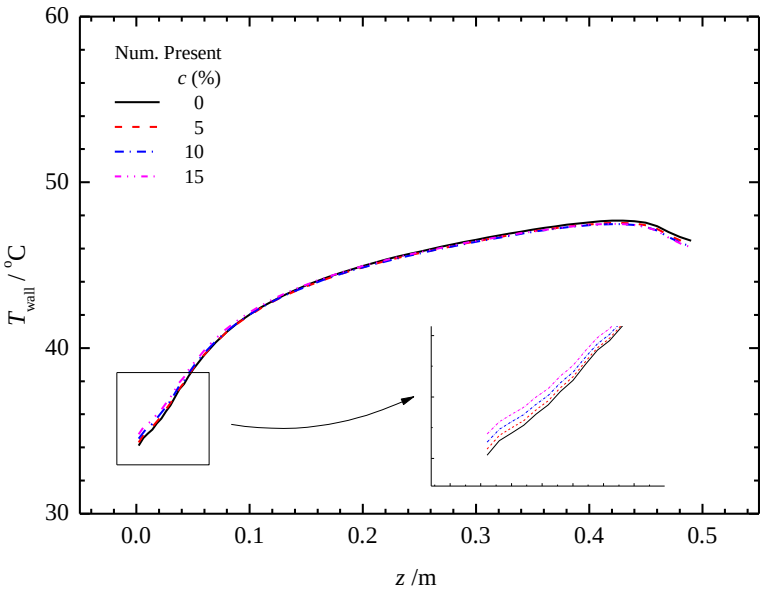

Figure 8.10 Local surface temperature of pure water and mPCM along the length of channel at w = 1.20 m/s

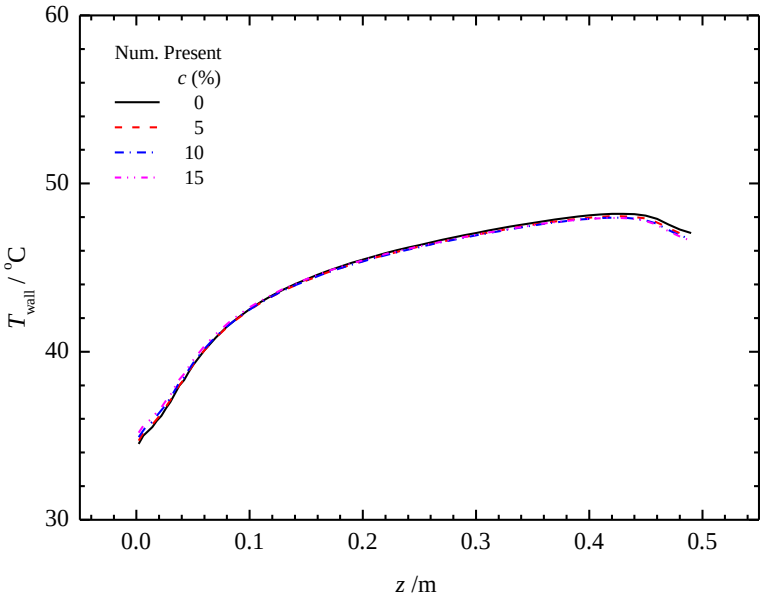

Figure 8.11 Local surface temperature of pure water and mPCM along the length of channel at w = 1.0 m/s

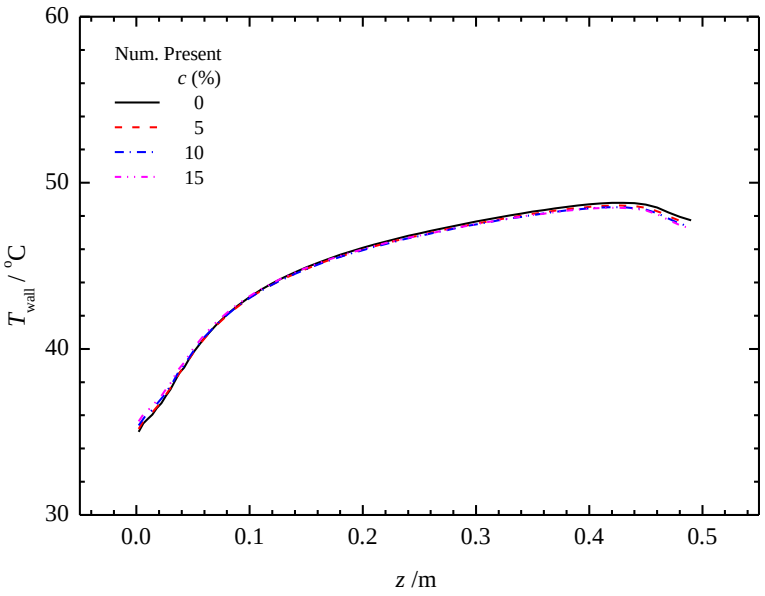

Figure 8.12 Local surface temperature of pure water and mPCM along the length of channel at w = 0.83 m/s

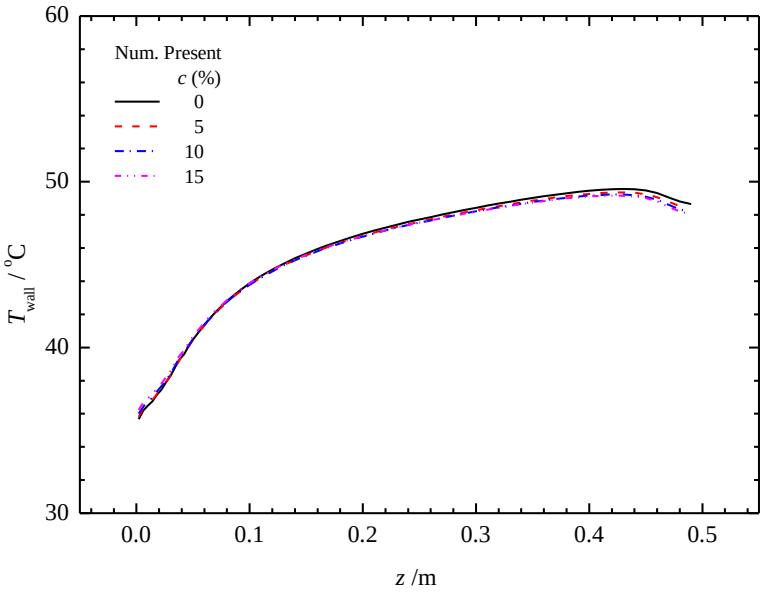

Figure 8.13 Local surface temperature of pure water and mPCM along the length of channel at w = 0.65 m/s

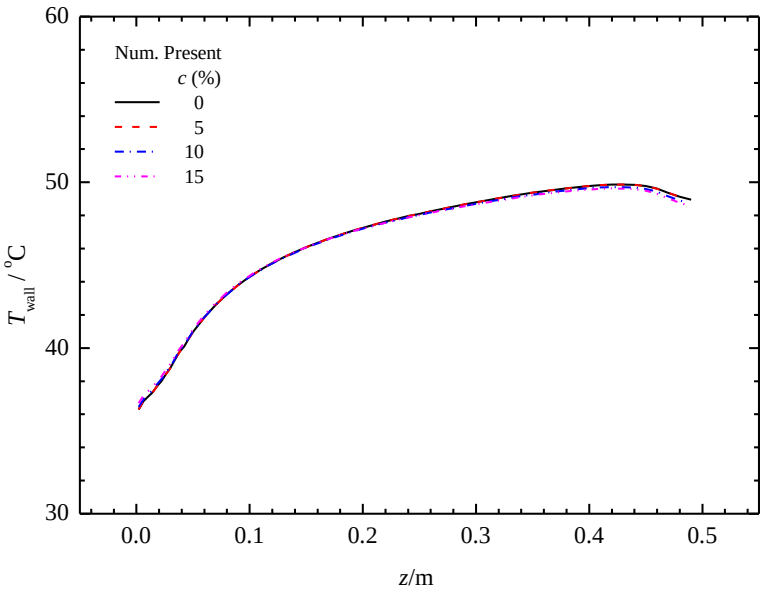

Figure 8.14 Local surface temperature of pure water and mPCM along the length of channel at w = 0.55 m/s

8.6 Variation of local Nusselt number

The Nusselt number was used to compare the performance of mPCM slurry as compared to pure water under the same operating conditions. The variation of the local Nusselt number along the flow direction of microchannel for pure water and mPCM slurry of mass concentration 5% to 15% along the length of channel under different flow conditions are presented in Figure 8.15 to Figure 8.19. The local Nusselt number is higher at the beginning due to entrance effect and then it is dropping due to development of thermal boundary layer and eventually reaches to almost a constant value. For the case of v = 1.2 m/s, the local Nusselt number for mPCM slurry of mass concentration 15% is higher than that of water and mPCM slurry of mass concentration 5 and 10%. This is because of the enhanced heat absorption due to higher latent heat of mPCM particles. At lower velocities, the increase in Nusselt number for mPCM slurry near the end of the microchannel is not very significant, this could be due to more melting of mPCM particles into liquid state.

In Figure 8.19 after z = 0.35 m the Nusselt number drops down further lower than Nusselt number of water. The possible reason for this is at lower flow rate, the residence time of mPCM particles inside the microchannel increases which results in almost complete melting of mPCM particles. The more closed observation of Nusselt number after z = 0.35 m shows that mPCM of 5% mass concentration behaves worse than all other cases. It is believed that for 5% mass concentration almost all mPCM particles undergoes the phase change. On the other hand, for higher concentrations, there could be still existence of phase changing particles. So, in order to get the full advantage of latent heat of mPCM particles, the flow rate of fluid should be adjusted.

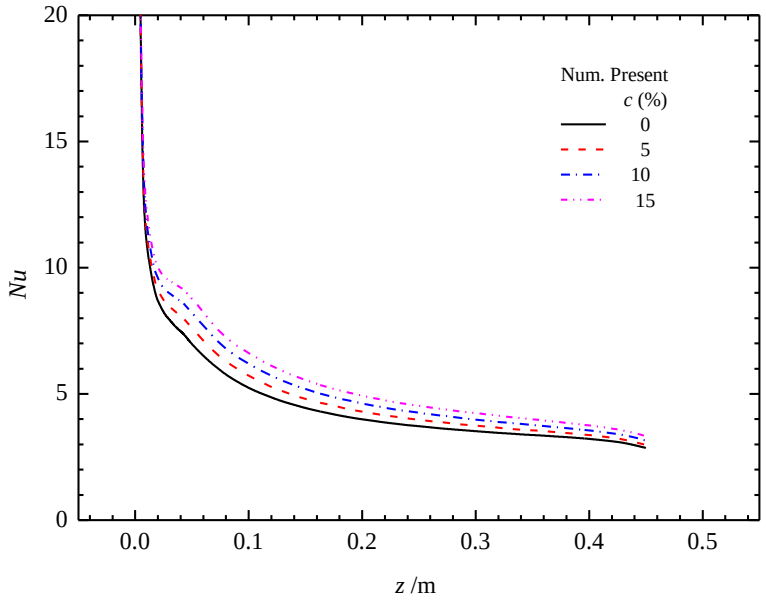

Figure 8.15 Local *Nu* of pure water and mPCM along the length of channel at w = 1.2 m/s.

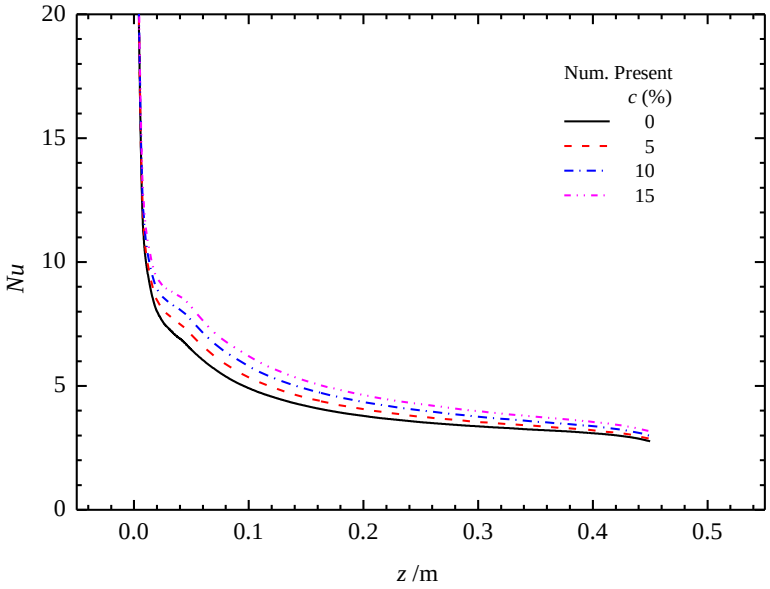

Figure 8.16 Local *Nu* of pure water and mPCM along the length of channel at *w* = 1.0 m/s

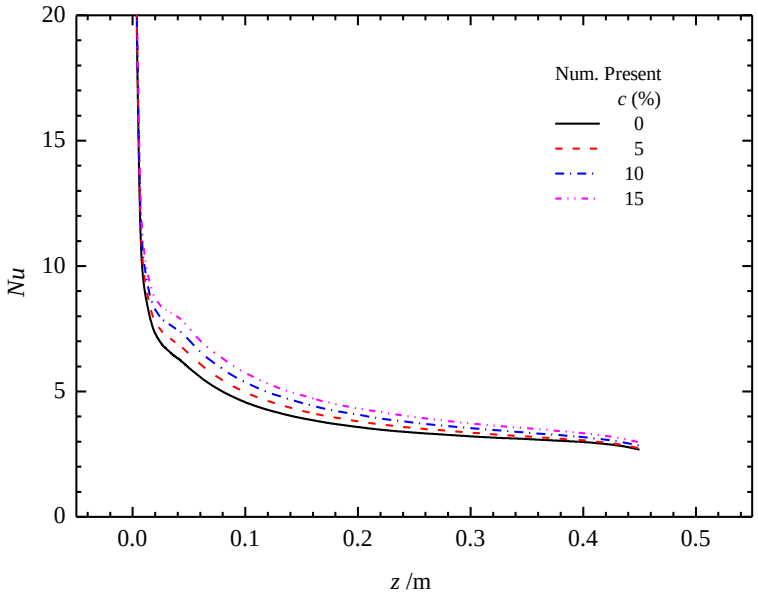

Figure 8.17 Local *Nu* of pure water and mPCM along the length of channel at *w* = 0.83 m/s

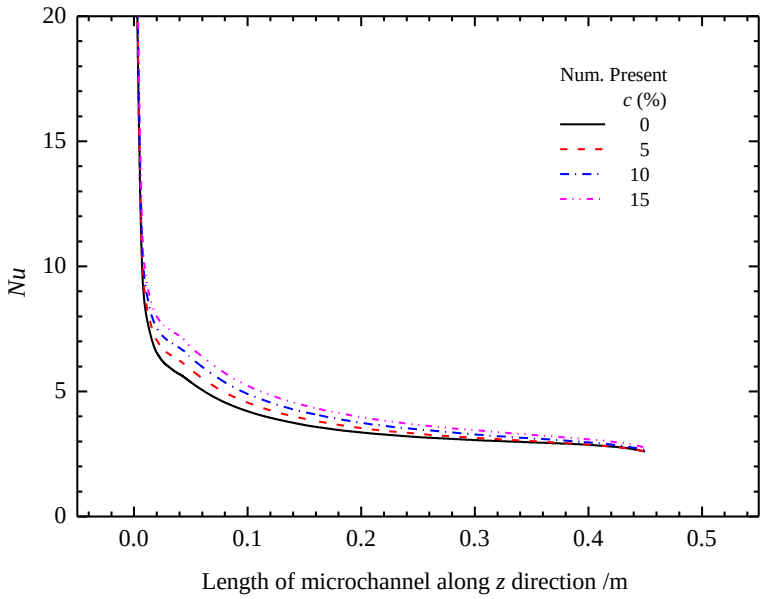

Figure 8.18 Local *Nu* of pure water and mPCM along the length of channel at *w* = 0.65 m/s

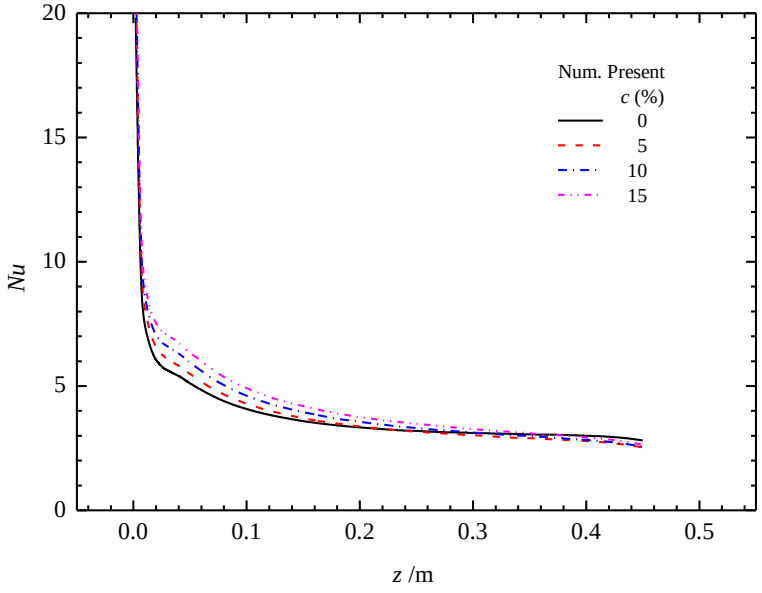

Figure 8.19 Local *Nu* of pure water and mPCM along the length of channel at *w* = 0.55 m/s

8.7 Pressure drop

The variation of pressure drop of pure water and mPCM slurry of different mass concentrations with respect to different flow rates is illustrated in Figure 8.20. It was observed that pressure drop increases with respect to flow rate for all range of mass concentrations of mPCM slurry. For the case of v = 1.2 m/s, the pressure drop for 5% 10% and 15% of mPCM slurry was 12.7%, 14.9%, and 16.7% higher than pure water, respectively. This increase in pressure drop of mPCM slurry is due to higher viscosities of mPCM slurries resulting from addition of mPCM particles.

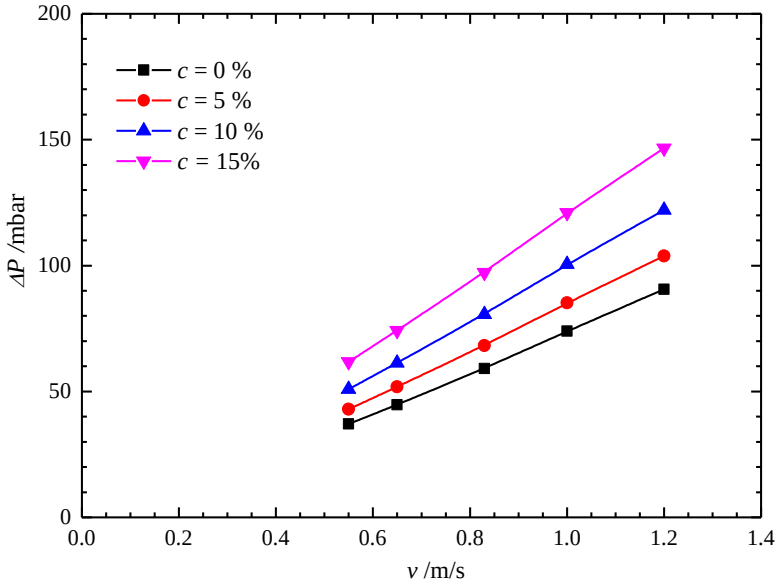

Figure 8.20 Pressure drop versus fluid velocity $T_{h,in}$ = 55 °C, $m_{f,in}$ = 17 g/s, $T_{f,in}$ = 30 °C

8.8 Concluding Remarks

The numerical model was validated by comparing the numerical results with the experimental data of Chen et al. (2008). The maximum deviation between the numerical results and experimental data was found to be 14.6%. The mechanisms of melting and solidification of mPCM slurry was observed by temperature contours at the outlet and

middle cross-section of channel. It was found that the thermal boundary layer development was slow for the mPCM slurry as compared to water. The reduction in surface temperature and bulk temperature was observed for mPCM slurry with respect to pure water.

Chapter 9

Numerical Simulation of Heat Transfer and Pressure Drop during Freezing of mPCM Slurry Flow in Microchannels

This chapter describes the numerical simulation of three-dimensional conjugated heat transfer during freezing of mPCM-37 slurry flow in microchannels. The physical model, boundary conditions and governing equations are the same as in Chapter 7. The effect of mPCM slurry on bulk temperature, surface temperature, Nusselt number and pressure drop were investigated.

9.1 Fluid properties and flow parameters

The mPCM slurry properties were based on the mPCM-37 slurry provided by Microtek Labs and calculated by equations given in Appendix A. Numerical simulations were conducted with mPCM slurry of mass concentration from 5-15%. The mPCM-37 had a subcooling of 7.8 ºC. The peak freezing temperature of mPCM-37 was 30.30 ºC. The DSC curve shows that the freezing temperature range of mPCM-37 was from 31-25 ºC. The freezing temperature range of 31 to 25 ºC were selected for numerical simulation. The inlet temperature of mPCM-37 slurry was taken to be 33 ºC. It was assumed that all the mPCM particles were completely melted before entering into the microchannels. The inlet temperature and velocity of cold water inside the upper and lower water jackets were set at 15 ºC and 0.37 m/s, respectively.

9.2 Temperature contours

The temperature contours at the outlet of the microchannel for water and mPCM slurry of mass concentration ranging from 5 to 5% are represented in Figure 9.1. It can be clearly

seen that the mPCM particles near the wall of microchannel solidifies earlier than the mPCM particles near to the centre of microchannel. The inside core of the mPCM slurry of mass concentration 15% is still in melted phase. The variation of bulk temperature along the length of microchannel is shown in Figure 9.2. The thermal boundary layer development seems to be slow down with the addition of mPCM particles. This delay further increases with the addition of mPCM particles similar to the melting of mPCM particles.

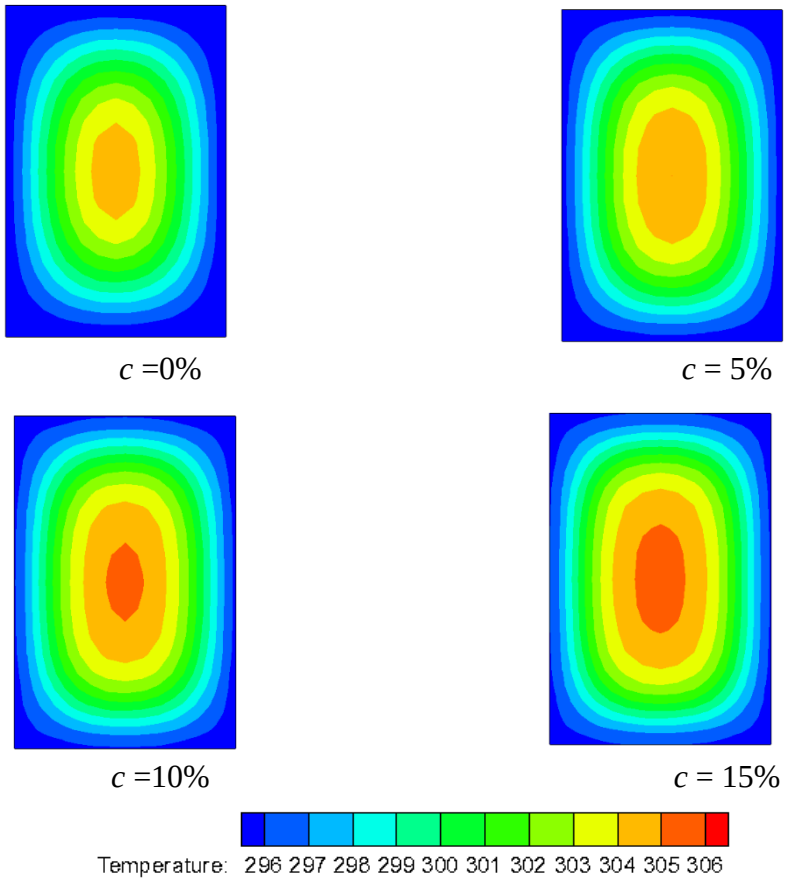

Figure 9.1 Temperature contours at the outlet of microchannel. $w_{f,in}$ = 1.2 m/s, $w_{h,in}$ = 0.37 m/s , $T_{h,in}$ = 15 ºC, $T_{f,in}$ = 33 ºC

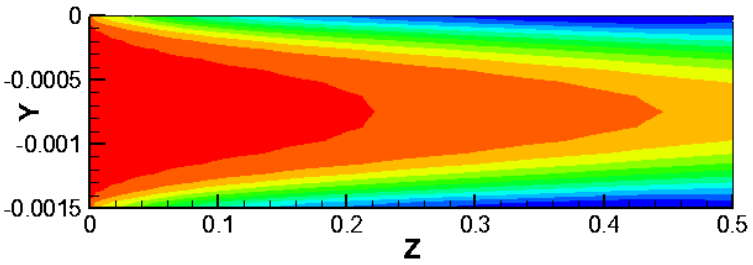

c = 0%

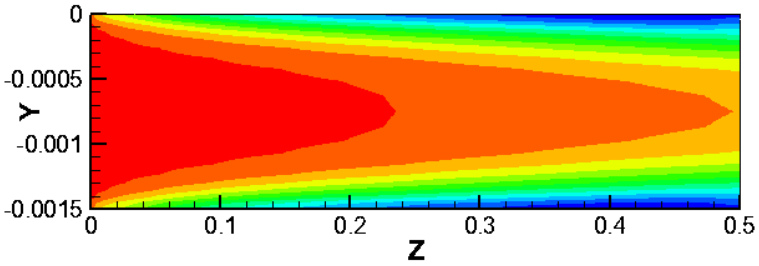

c = 5%

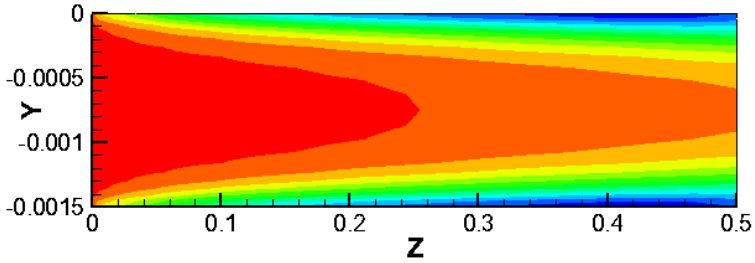

c = 10%

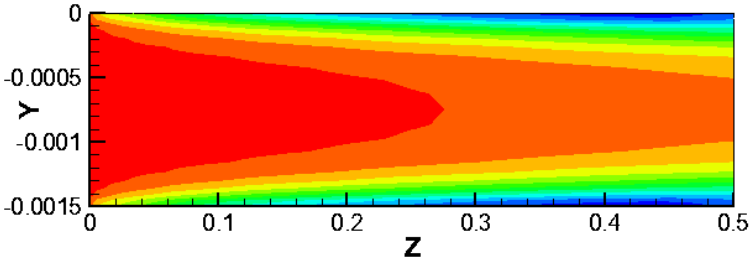

c = 15%

Figure 9.2 Temperature distributions along the flow direction of microchannel. $v_{f,in}$ = 1.2 m/s, $v_{h,in}$ = 0.37 m/s , $T_{h,in}$ = 15 ºC, $T_{f,in}$ = 33 ºC

9.3 Effect of mass concentration on bulk and surface temperature

Figure 9.3 to Figure 9.6 represent the variation of bulk temperature of pure water and mPCM slurry of 5%, 10% and 15% mass concentration at different velocities 1.2, 1.0, 0.83, 0.65 and 0.55 m/s. The bulk temperature for mPCM slurry is higher as compared to that of pure water in all cases. For the case of w = 1.2 m/s the bulk temperature for mPCM slurry of mass concentration 5%, 10% and 15% is 0.71 K, 1.24 K and 1.64 K higher at the outlet of microchannel as compared to pure water. The reason for higher temperatures are the latent heat and increase in effective specific heat capacity of mPCM slurry. During the freezing of mPCM particles, they transferred more heat as compared to the pure water. It is also noticed that the difference in bulk temperature of pure water and mPCM slurry is more with the decrease of velocity of working fluid. In Figure 9.7, at w = 0.55 m/s, the bulk temperature at the outlet of microchannel for mPCM slurry of 15% mass concentration is 3.12 K higher as compared to pure water. At lower velocities, residence time of mPCM particles inside the microchannel is higher which results in more heat transferred.

The variation of local surface temperature for pure water and mPCM slurry of mass concentration 5-15% at different fluid velocities of 1.2, 1.0, 0.83, 0.65, and 0.55 m/s are shown in Figure 9.8 to Figure 9.12. It is shown in all cases the decrease in surface temperature follows the similar trend. The surface temperature drop is sharp till z = 0.03 m due to the adiabatic section of test section upstream. After z = 0.03 m the surface temperature drops gradually along microchannel till z = 0.47 m. The abrupt increase in surface temperature is observed from z = 0.47 to 0.5 m owing to the downstream adiabatic section of test section. Figure 9.6 illustrates that till z = 0.1 m, the surface temperature is a little higher for pure water as compared to all mPCM slurries. It could be due to the fact that mPCM particles were still in melted phase and specific heat capacity of mPCM in

solid and liquid states are lower as compared to pure water. The more close examination of enlarged image shows that the drop in surface temperature is maximum for 15% mass concentration mPCM slurry. This is because increase in mass concentration results in more mPCM particles which eventually results in poor performance as compared to water and other mass concentrations of slurry. After z = 0.1 m as mPCM particles start to solidify the surface temperature for mPCM slurry starts increasing due to higher latent heat absorption of mPCM slurry.

The increase in surface temperature for different mass concentrations is more apparent at lower flow rates. Figure 9.12 depicts that mPCM slurry of mass concentration 15% shows higher surface temperatures as compared to pure water and mPCM slurry of other concentrations.

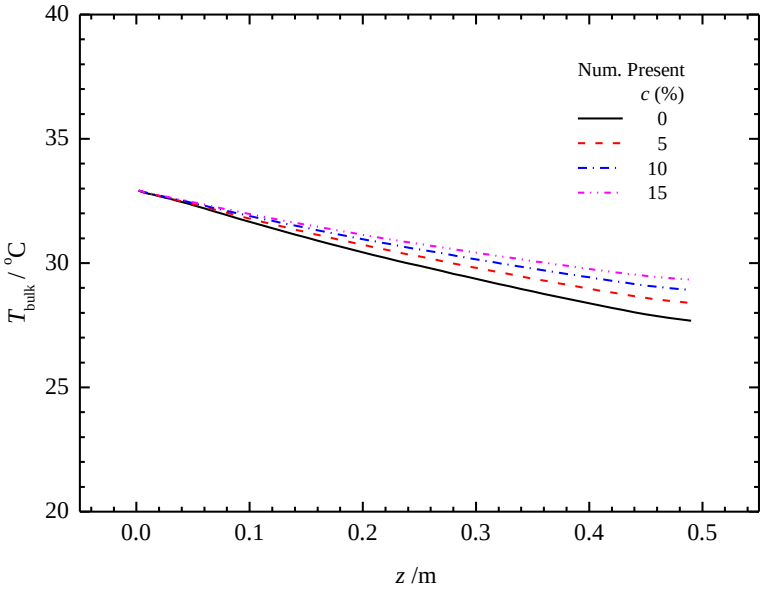

Figure 9.3 Local bulk temperature of pure water and mPCM slurry along the length of microchannel at w = 1.2 m/s

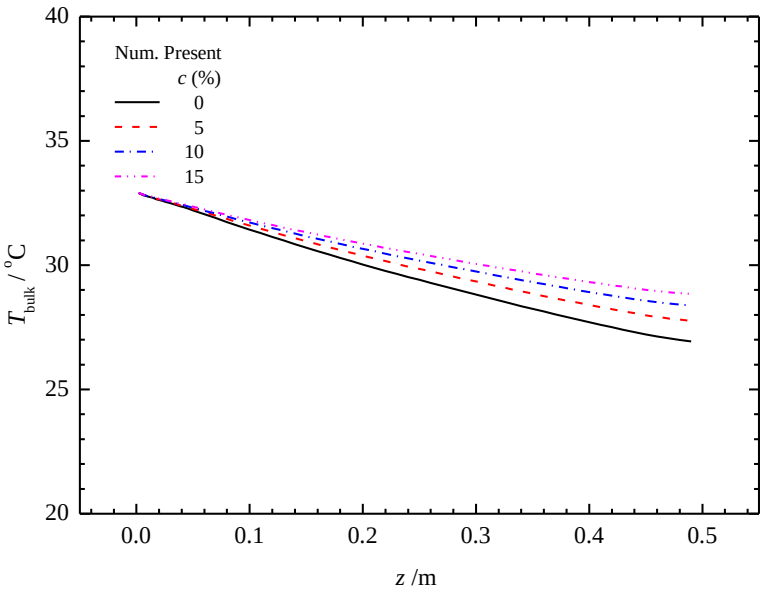

Figure 9.4 Local bulk temperature of pure water and mPCM slurry along the length of microchannel at w = 1.0 m/s

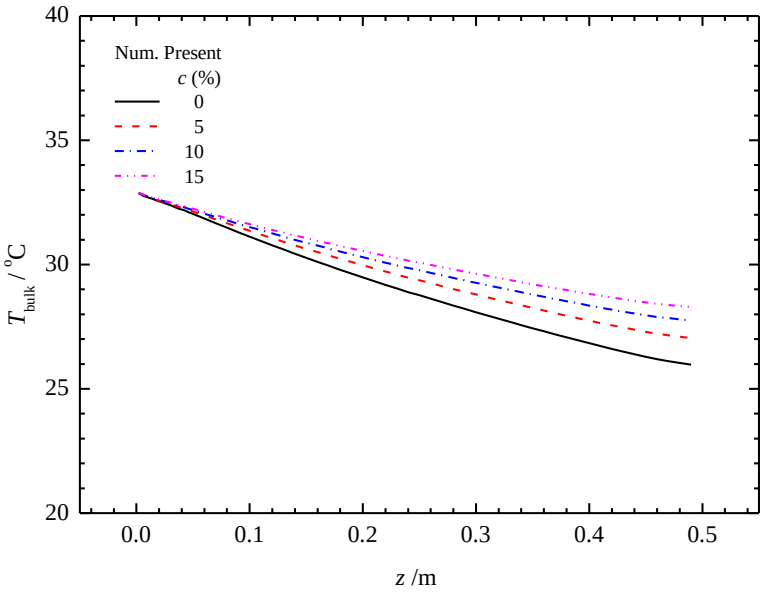

Figure 9.5 Local bulk temperature of pure water and mPCM slurry along the length of microchannel at w = 0.83 m/s

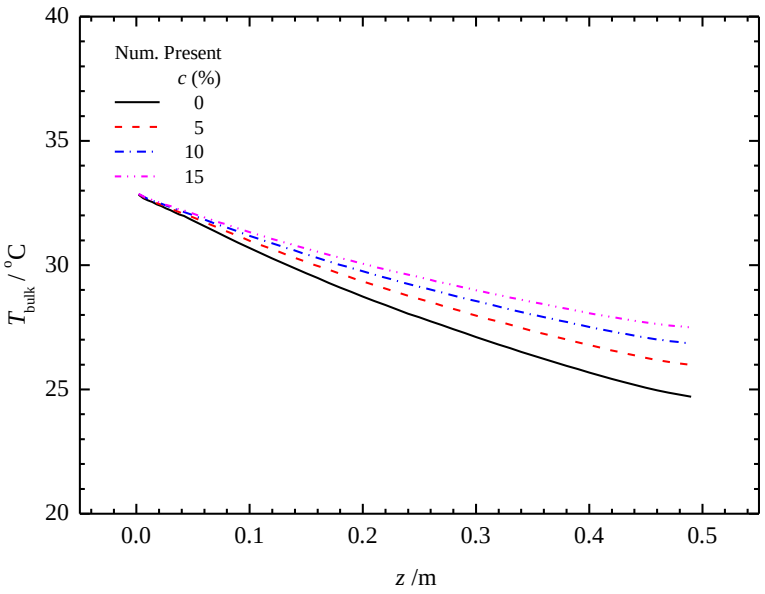

Figure 9.6 Local bulk temperature of pure water and mPCM slurry along the length of microchannel at w = 0.65 m/s

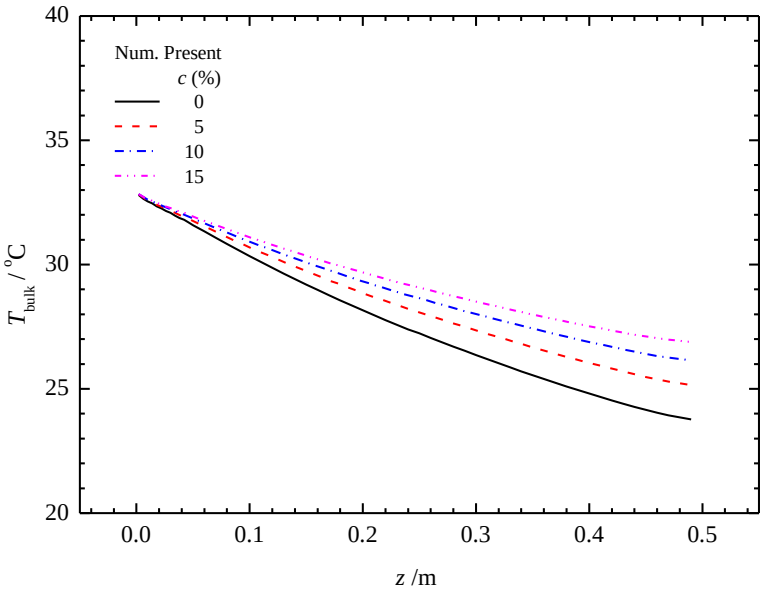

Figure 9.7 Local bulk temperature of pure water and mPCM slurry along the length of microchannel at w = 0.55 m/s

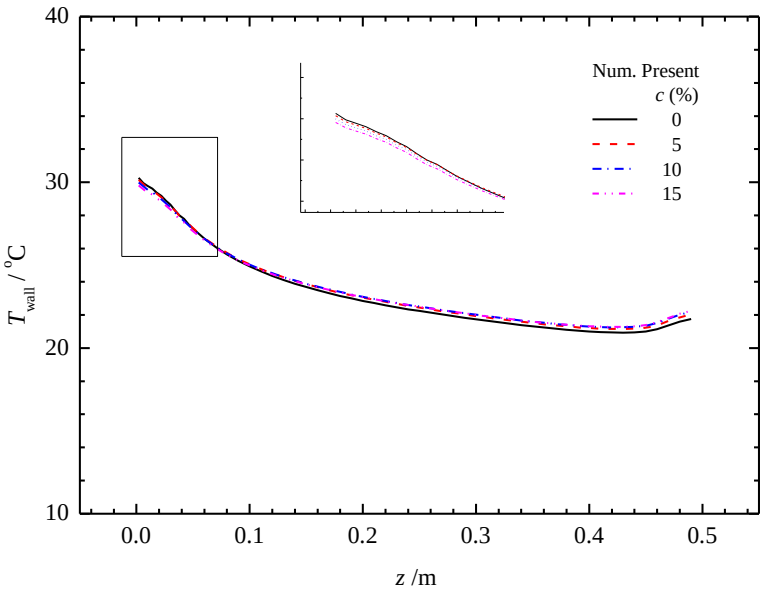

Figure 9.8 Local surface temperature of pure water and mPCM along the length of channel at w = 1.20 m/s

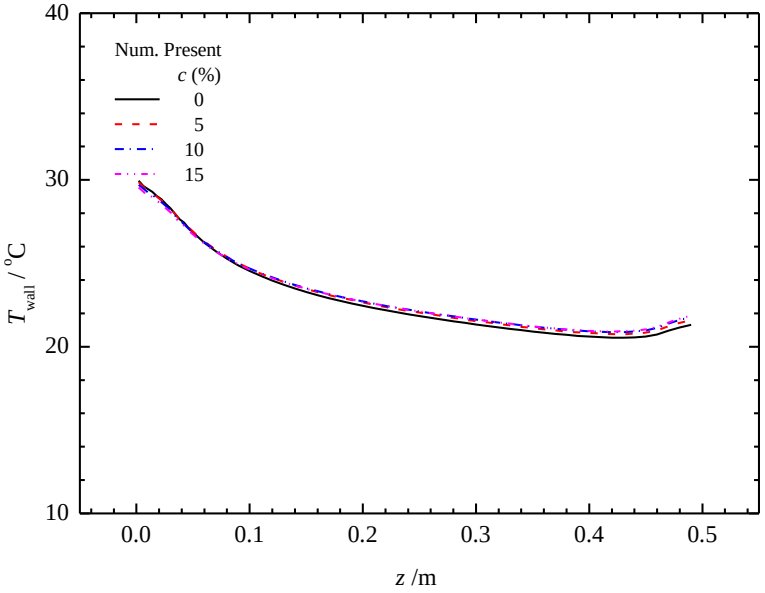

Figure 9.9 Local surface temperature of pure water and mPCM along the length of channel at w = 1.0 m/s

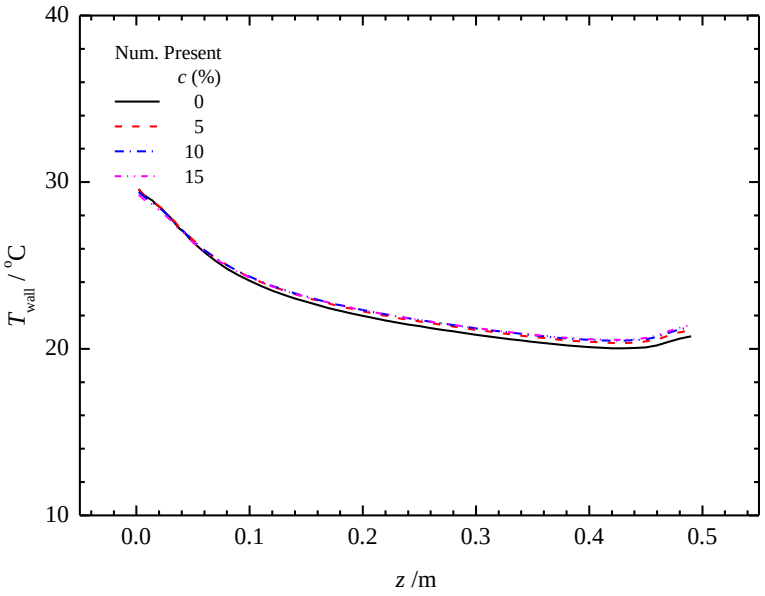

Figure 9.10 Local surface temperature of pure water and mPCM along the length of channel at w = 0.83 m/s

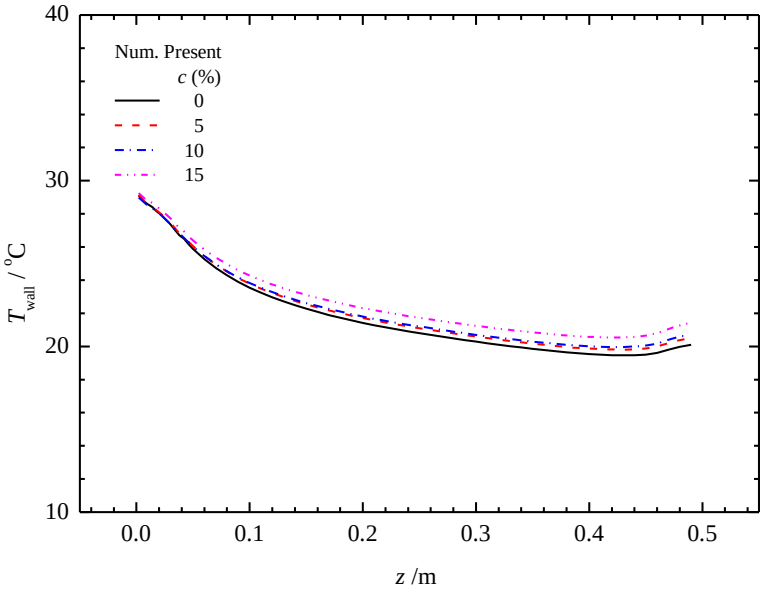

Figure 9.11 Local surface temperature of pure water and mPCM along the length of channel at w = 0.65 m/s

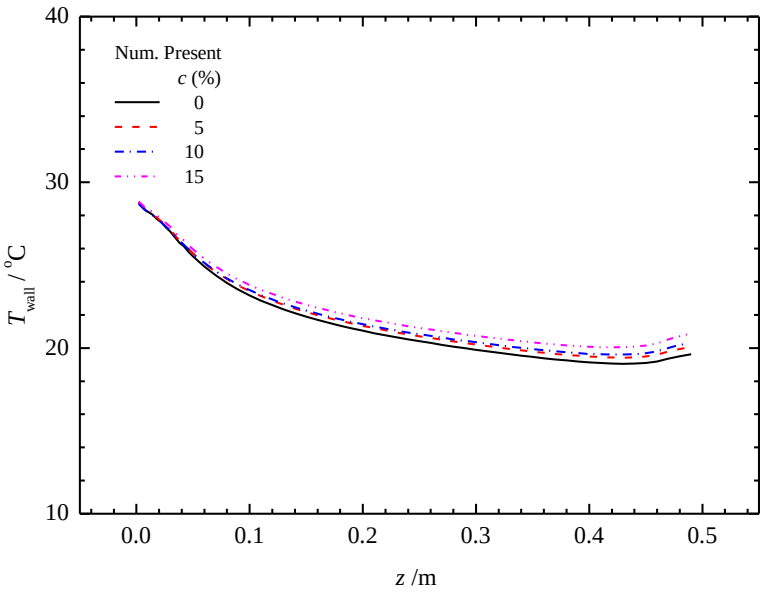

Figure 9.12 Local surface temperature of pure water and mPCM along the length of channel at w = 0.55 m/s

9.4 Local Nusselt number

The local Nusselt number was used to evaluate the performance of mPCM slurry as compared to water under the same operating conditions. The variation of local Nusselt number along the flow direction of microchannel for pure water and mPCM slurry of mass concentrations ranging from 5% to 15% are shown in Figure 9.13 to Figure 9.17. The local Nusselt number is higher at the start of microchannel due to thermal entrance effect. Then, the Nusselt number declining due to the development of thermal boundary layer. Finally, the local Nusselt number tends to be constant after the fluid approaches the fully developed flow.

In all cases of fluid velocity, the local Nusselt number is higher for mPCM slurry as compared to pure water. This increase in Nusselt number further enhances with the increase in mass concentration of mPCM slurry. This is due to the more PCM particles at

higher concentration. It is also observed that the Nusselt number starts collapsing for all mass concentrations till the end of microchannel at lower flow velocities of 0.55 and 0.65 m/s. This could be due to more mPCM particles solidified as a result of increase in residence time of slurry inside the microchannel.

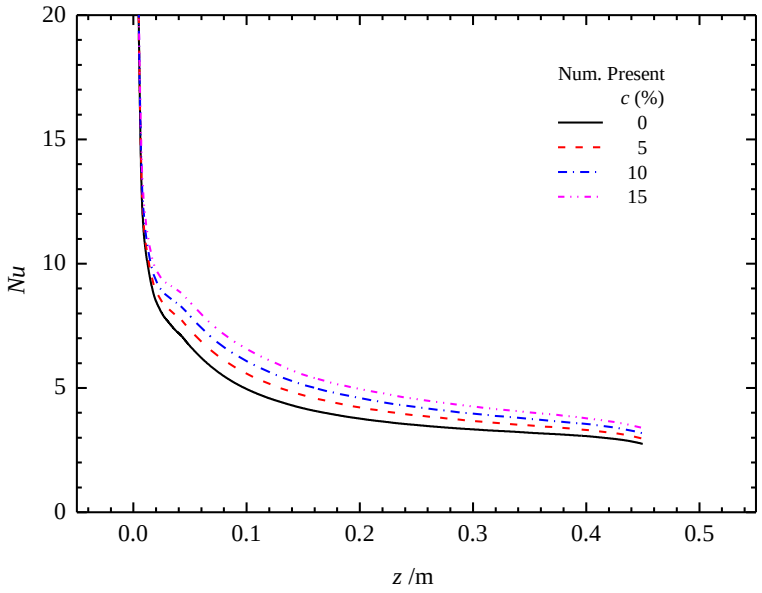

Figure 9.13 Local *Nu* of pure water and mPCM along the length of channel at w = 1.2 m/s

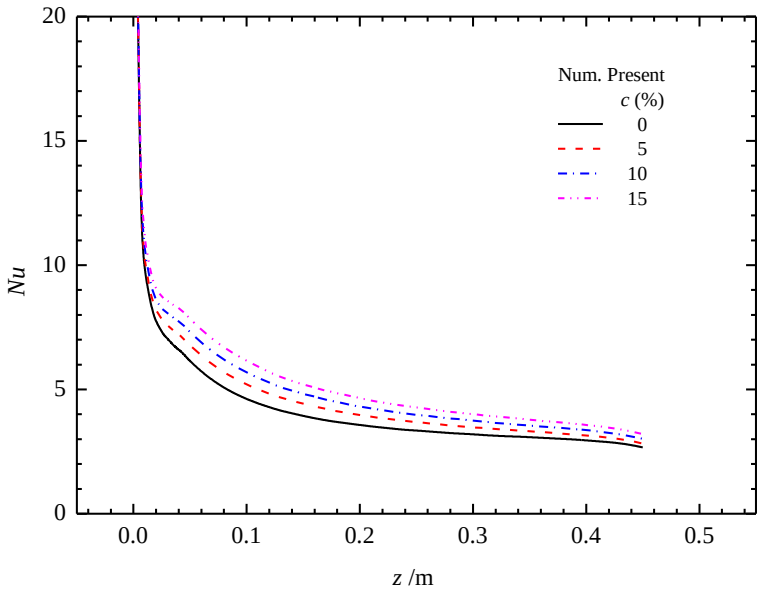

Figure 9.14 Local *Nu* of pure water and mPCM along the length of channel at *v* = 1.0 m/s

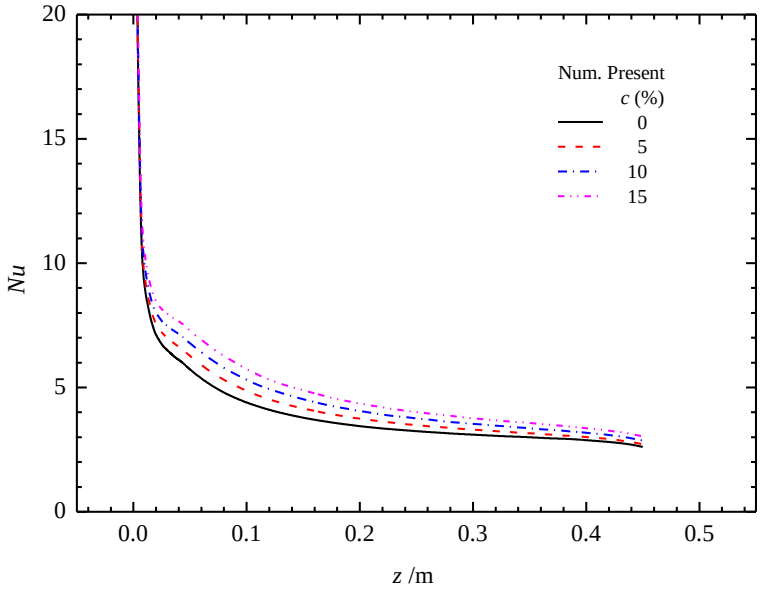

Figure 9.15 Local *Nu* of pure water and mPCM along the length of channel at *v* = 0.83 m/s

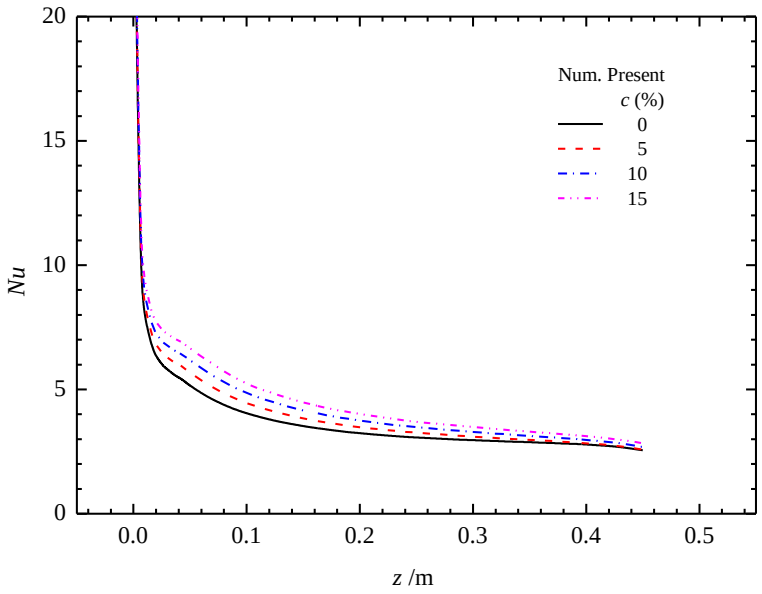

Figure 9.16 Local *Nu* of pure water and mPCM along the length of channel at *v* = 0.65 m/s

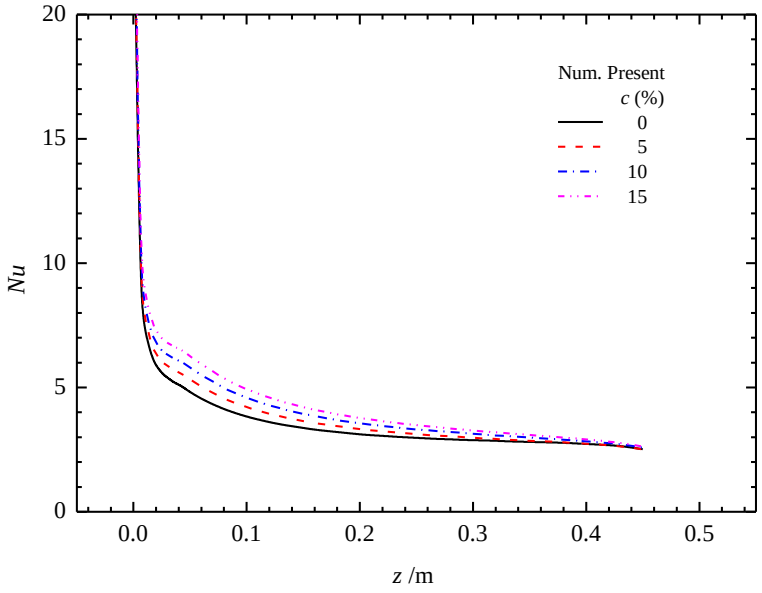

Figure 9.17 Local *Nu* of pure water and mPCM along the length of channel at *v* = 0.55 m/s

9.5 Pressure drop

One of the drawback associated with mPCM slurry is its higher pressure drop due to higher viscosities of mPCM slurry. The variation of pressure drop of pure water and mPCM slurry with different mass concentrations is illustrated in Figure 9.18. It has been observed that pressure drop increases with flow rate for all range of mass concentrations of mPCM slurry. For the case of v = 1.2 m/s, the pressure drop for 5%, 10% and 15% mass concentrations of mPCM slurry was 5.1%, 18.6% and 30.6% higher than pure water, respectively. The increase in pressure drop for 10% and 15% mass concentrations of mPCM slurry is higher during the freezing of mPCM slurry as compared to the melting of mPCM slurry. This could be due to the fact that during the melting of mPCM particles increase in bulk temperature results in lower dynamic viscosity. However, during the solidification of mPCM particles results in higher dynamic viscosities. So, the pressure drop of mPCM slurry is higher during the freezing of mPCM particles as compared to the melting of mPCM particles.

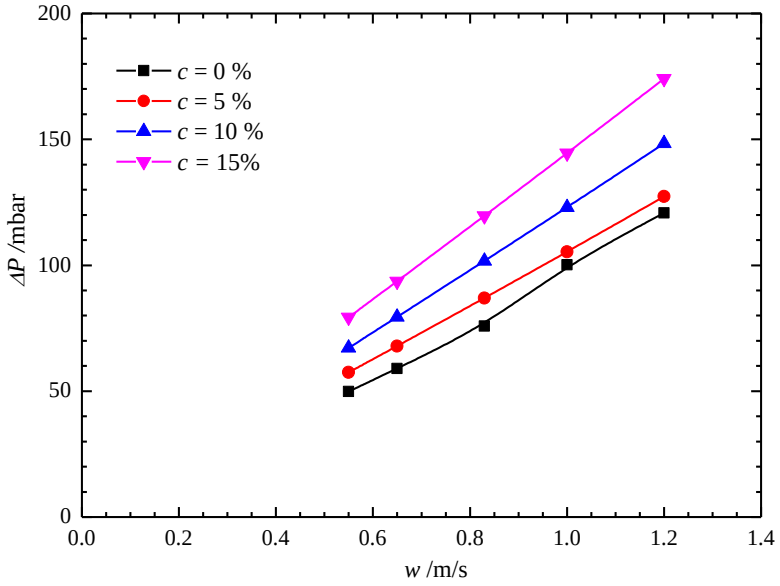

Figure 9.18 Pressure drop versus fluid velocity $T_{h,in}$ = 15 °C, $T_{f,in}$ = 33 °C

9.6 Concluding remarks

This concludes that the increase in mass concentration has positive effect on local Nusselt number. The bulk temperature and surface temperature is higher for mPCM slurry as compared to pure water during the freezing of mPCM particles inside the microchannel. The pressure drop was found higher during the freezing cycle as compared to melting cycle of mPCM slurry. In order to take the full advantage of latent heat of mPCM slurry, the mass concentration and flow rate of mPCM slurry should be adjusted for complete solidification of mPCM particles inside the microchannel.

Chapter 10

Numerical Investigation of Convective Heat Transfer during mPCM Slurry Flow in Microchannel Heat Sink

A numerical simulation of three dimensional conjugated heat transfer of microchannel heat sink was performed to analyse the effects of geometrical parameters (height and width of separating wall of channel, cross section of channel) on the heat transfer and pressure drop performance.

10.1 Physical model

The effect of geometrical parameters, height and thickness of separating wall of microchannel were investigated for circular microchannel heat sink with mPCM slurry flow. Figure 10.1 and Figure 10.2 show the physical model, coordinators and boundary conditions for three dimensional conjugated heat transfer during mPCM slurry flow in microchannel heat sinks. H, B and L are the height and width of the separating wall and the length of the microchannel heat sink, respectively. D is the diameter for the circular channel shape. a and b are the side lengths for the rectangular channel shape. The bottom surface of the heat sink is adiabatic and the constant heat flux boundary condition is applied at the top surface. T_{in}, W_{in} and P_{in} are the temperature, velocity and pressure of mPCM slurry flow at the inlet, respectively, and T_{out} and P_{out} are the temperature and pressure at the outlet, respectively.

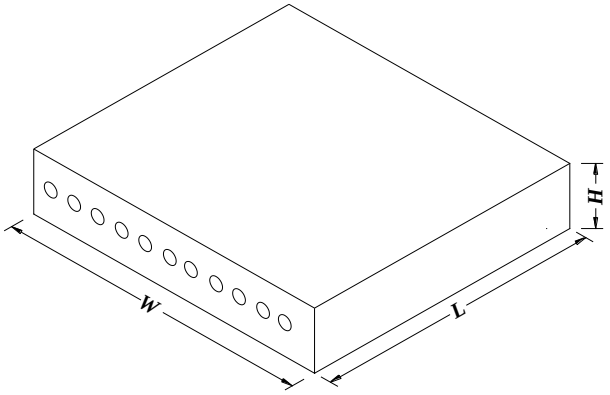

Figure 10.1 Schematic of circular microchannel heat sink

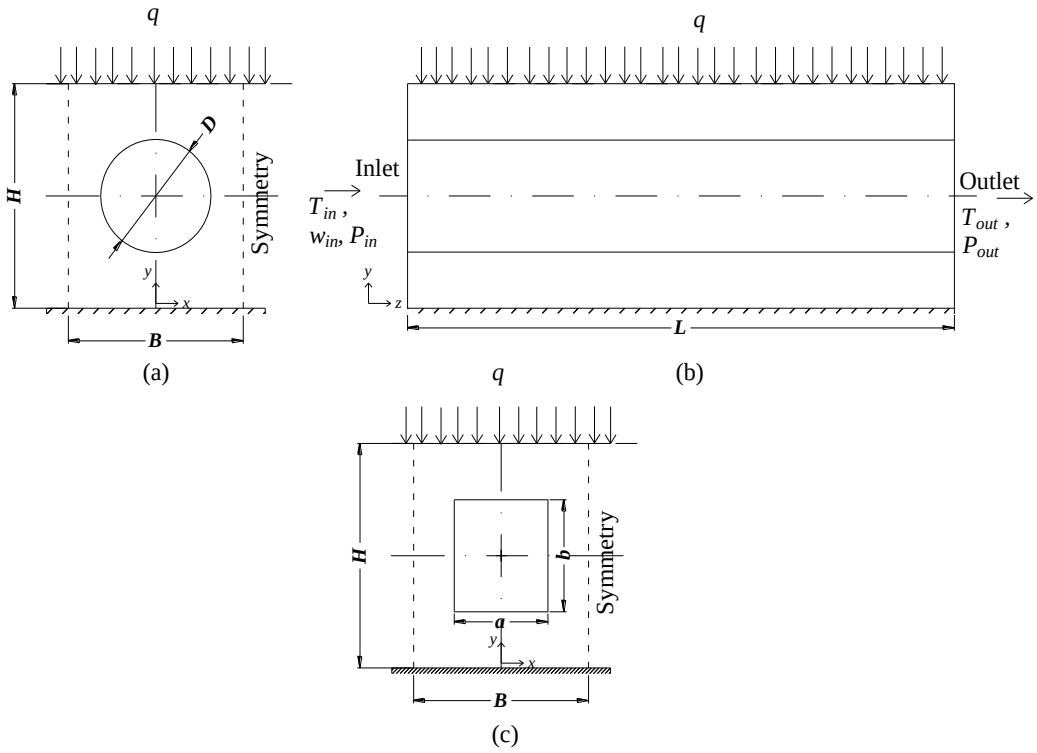

Figure 10.2 Physical model (circular and rectangular) and coordinates

The working fluid was mPCM slurry of mass concentration range of 0-20% in water. Phase change slurry enters the microchannel heat sink at constant temperature near to the melting point of mPCM slurry and constant velocity. As mPCM slurry flows in microchannel, it takes the heat from the top surface of heat sink. The phase change material starts melting when temperature of mPCM slurry reaches to its melting temperature. The temperature of mPCM slurry remains

constant during the melting region which results in more uniform surface temperature of the heat sink. It reduces thermal stresses and increases the reliability of heat sink.

10.2 Governing equations and boundary conditions

The governing equations for mass, momentum and energy conservation in Cartesian coordinate are given in Eqs. (10.1)- (10.6)

Continuity equation:

$$\frac{\partial u}{\partial x}+\frac{\partial v}{\partial y}+\frac{\partial w}{\partial z}=0 \tag{10.1}$$

Momentum equations:

$$\rho_{\mathrm{b}}\left(u\frac{\partial u}{\partial x}+v\frac{\partial u}{\partial y}+w\frac{\partial u}{\partial z}\right)=-\frac{\partial P}{\partial x}+\mu_{\mathrm{b}}\left(\frac{\partial^2 u}{\partial x^2}+\frac{\partial^2 u}{\partial y^2}+\frac{\partial^2 u}{\partial z^2}\right) \tag{10.2}$$

$$\rho_{\mathrm{b}}\left(u\frac{\partial v}{\partial x}+v\frac{\partial v}{\partial y}+w\frac{\partial v}{\partial z}\right)=-\frac{\partial P}{\partial y}+\mu_{\mathrm{b}}\left(\frac{\partial^2 v}{\partial x^2}+\frac{\partial^2 v}{\partial y^2}+\frac{\partial^2 v}{\partial z^2}\right) \tag{10.3}$$

$$\rho_{\mathrm{b}}\left(u\frac{\partial w}{\partial x}+v\frac{\partial w}{\partial y}+w\frac{\partial w}{\partial z}\right)=-\frac{\partial P}{\partial z}+\mu_{\mathrm{b}}\left(\frac{\partial^2 w}{\partial x^2}+\frac{\partial^2 w}{\partial y^2}+\frac{\partial^2 w}{\partial z^2}\right) \tag{10.4}$$

Energy equation of fluid:

$$\rho_{\mathrm{b}}C_{\mathrm{b}}\left(u\frac{\partial T}{\partial x}+v\frac{\partial T}{\partial y}+w\frac{\partial T}{\partial z}\right)=k_{\mathrm{b}}\left(\frac{\partial^2 T}{\partial x^2}+\frac{\partial^2 T}{\partial y^2}+\frac{\partial^2 T}{\partial z^2}\right) \tag{10.5}$$

Energy equation for solid:

$$k_s\left(\frac{\partial^2 T_w}{\partial x^2}+\frac{\partial^2 T_w}{\partial y^2}+\frac{\partial^2 T_w}{\partial z^2}\right)=0 \tag{10.6}$$

where u, v and w are velocity components in x, y and z directions. T_f and T_s are the temperatures of fluid and solid, respectively. ρ_b and μ_b are density and dynamic viscosity of the mPCM slurry. Following boundary conditions were applied to the surfaces of the microchannel heat sink.

At the microchannel inlet, fluid was entered microchannel at constant velocity and temperature,

$$w = w_{in}, u = v = 0, T_{fluid} = T_{in}, \quad \text{at} \quad z = 0 \tag{10.7}$$

A constant heat flux was applied at the top surface of the microchannel heat sink,

$$q = k_s \frac{\partial T_s}{\partial y} \quad \text{at} \quad y = H,\ 0 \le x \le B/2,\ 0 \le z \le L \tag{10.8}$$

A symmetry boundary condition was applied at the right and left sides of the heat sink.

$$\frac{\partial T_s}{\partial x} = 0 \quad \text{at} \quad x = B/2,\ 0 \le y \le H,\ 0 \le z \le L \tag{10.9}$$

$$\frac{\partial T_s}{\partial x} = 0 \quad \text{at} \quad x = 0,\ 0 \le y \le H,\ 0 \le z \le L \tag{10.10}$$

The adiabatic boundary condition was applied at the bottom surface and two end surfaces at the inlet and outlet.

$$\frac{\partial T_s}{\partial y} = 0 \quad \text{at} \quad y = 0,\quad 0 \le x \le B/2\,,\quad 0 \le z \le L \tag{10.11}$$

$$\frac{\partial T_s}{\partial z} = 0 \qquad \text{at } z = 0, L \tag{10.12}$$

Atmospheric pressure boundary condition was imposed at microchannel outlet

$$p = p_0 \qquad \text{at } z = L \tag{10.13}$$

where w_{in} is inlet velocity, T_{in} is inlet temperature of fluid, q is specified heat flux, and p_0 is atmospheric pressure at the outlet.

10.3 Thermophysical properties of working fluid

The effective specific heat capacity model given in section 8.2 was used. The thermophysical properties of working fluid is given in Table 10.1.

Table 10.1 Thermophysical properties of working fluid

Fluid	c %	ρ kg/m^3	k W/m K	C_p J/kg K	μ kg/m s
Pure water	0	998.0	0.6	4180	1.01×10^{-3}
mPCM slurry	5	989.6	0.57	4065	1.147×10^{-3}
mPCM slurry	10	982.3	0.54	3951	1.38×10^{-3}
mPCM slurry	20	968.0	0.48	3723	2.233×10^{-3}

10.4 Numerical methods and independence of grid

Numerical simulations were performed by commercial computational fluid dynamics software (CFD) Fluent. The finite volume method was used to convert the partial differential governing equations to algebraic equations. Second order discretization scheme was used for discretization of governing equations. The convergence criteria for energy, continuity, and velocity was set at 10^{-6}. Default under relaxation factors for continuity (0.3), momentum (0.7) and energy (1.0) equations were used.

The independency of grid was verified by measuring the variation of local Nusselt number along dimensionless length of microchannel. The variation of Nusselt number along length of microchannel for three cases (Grid 1 (77×6), Grid 2 (88× 8) and Grid 3 (109× 12) divisions in *y* and *x* directions) is shown in Figure 10.3. The maximum deviation of local Nusselt number between Grid 2 and Grid 3 was found to be 1.7%. Therefore, to save the computational cost Grid 2 was selected for further simulations.

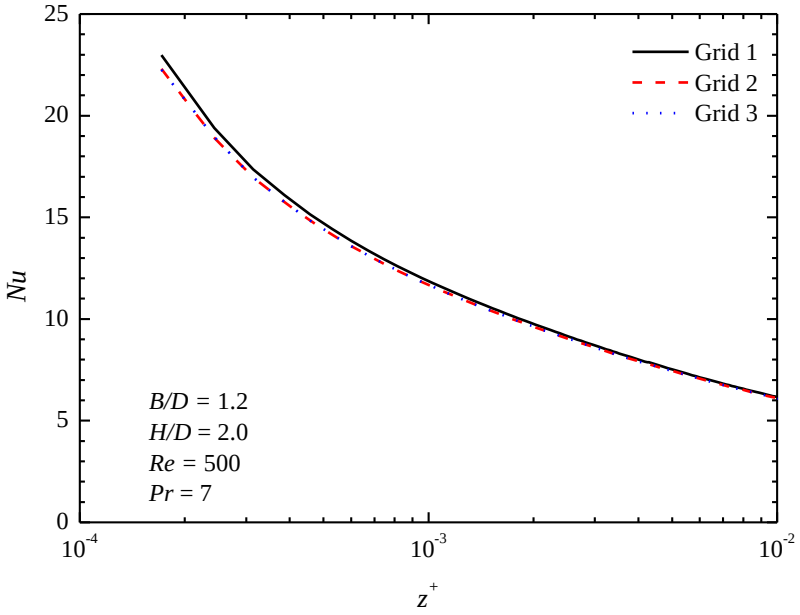

Figure 10.3 Variation of local *Nu* with dimensionless axial distance for three different grid sizes

10.5 Results and discussion

Numerical simulations were conducted with mPCM slurry of mass concentration range of 0-20%. Phase change material was taken as n-octadecane. The melting temperature of n-octadecane is 26.0 °C and latent heat is 241 kJ/kg. The melting temperature range for mPCM slurry was taken from 25.5 °C -27.5 °C. The inlet temperature of mPCM slurry was taken as 25.0 °C. The numerical results were obtained under following operating conditions: *Re* = 500.0, *L/D* = 50.0.

Numerical simulations were performed to see the effect of thickness, height, of separating wall of microchannel and geometrical shape of microchannel heat with mPCM slurry flow. Firstly, the effect of thickness and height of separating wall of microchannel on thermal performance of microchannel heat sink were investigated. The height and width of separating wall of microchannel were taken same as Kroeker et al. (2004). Secondly, numerical simulations were conducted to examine the effect of geometrical shape (circular, square, and rectangular) of microchannel on thermal and hydraulic performance of heat sink.

10.6 Heat transfer enhancement of mPCM slurry

For the analysis of mPCM slurry as heat transfer fluid, its performance was analysed by comparing the Nusselt number, surface temperature, bulk temperature as compared to water. Temperature contours for mPCM slurry and water are shown in Figure 10.5 to Figure 10.7. It can be seen that the thermal boundary layer slows down with the addition of mPCM particles in pure water. This delay increases with the increase of mass concentration. The mPCM particles are still melting at the outlet of channel. To take the full advantage of latent heat of mPCM particles the residence time of mPCM particles inside the channel should be optimized. Figure 10.7 represents the variation of temperature at different y/r = 0, 0.3, 0.5 and 0.7 locations along the length of microchannel. It depicts that during the phase change of mPCM slurry temperature remains constant. The local Nusselt number for mPCM slurry flow is higher as compared to water and further increases with increase of mass concentration of mPCM particles. The heat transfer enhances to 17% as compared to pure water as shown in Figure 10.10. This heat transfer enhancement starts declining and then mPCM slurry behaves poor as compared to water. This poor performance is owing to less specific heat capacity of PCM after complete melting of mPCM particles. The decrease in bulk and surface temperature are represented in Figure 10.11 and Figure 10.12, respectively. Figure 10.13 depicts that inlet temperature of mPCM slurry near

to melting temperature of mPCM shows higher Nusselt number. The effect of Stefan number on the heat transfer performance of mPCM slurry is depicted in Figure 10.14. It was observed that heat transfer performance declined with the increase of Stefan number

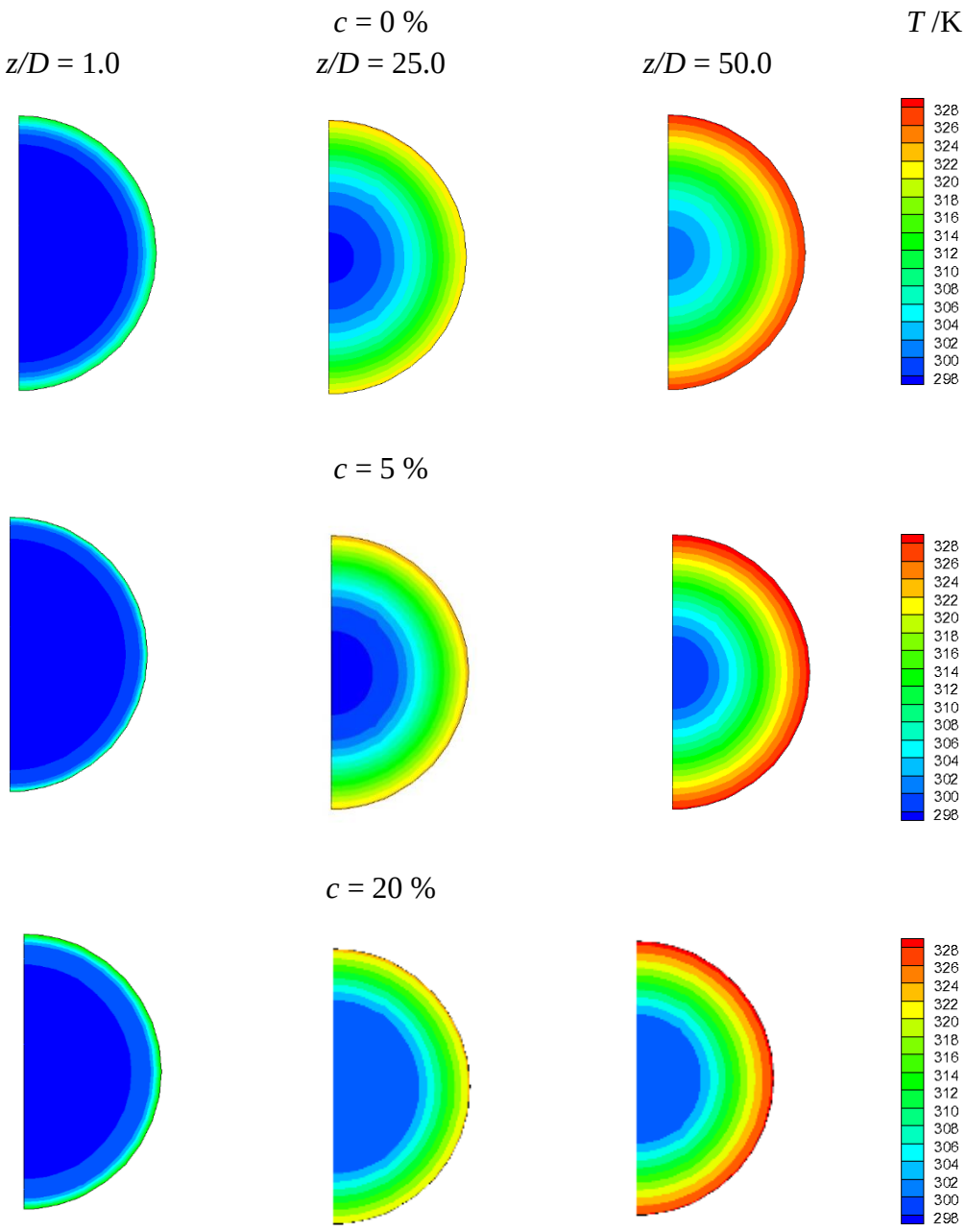

Figure 10.4 Radial temperature contours at different cross sections along the length of microchannel. q = 80 W/cm^2, T_{in} = 24 ^{o}C, w_{in} = 1.0 m/s

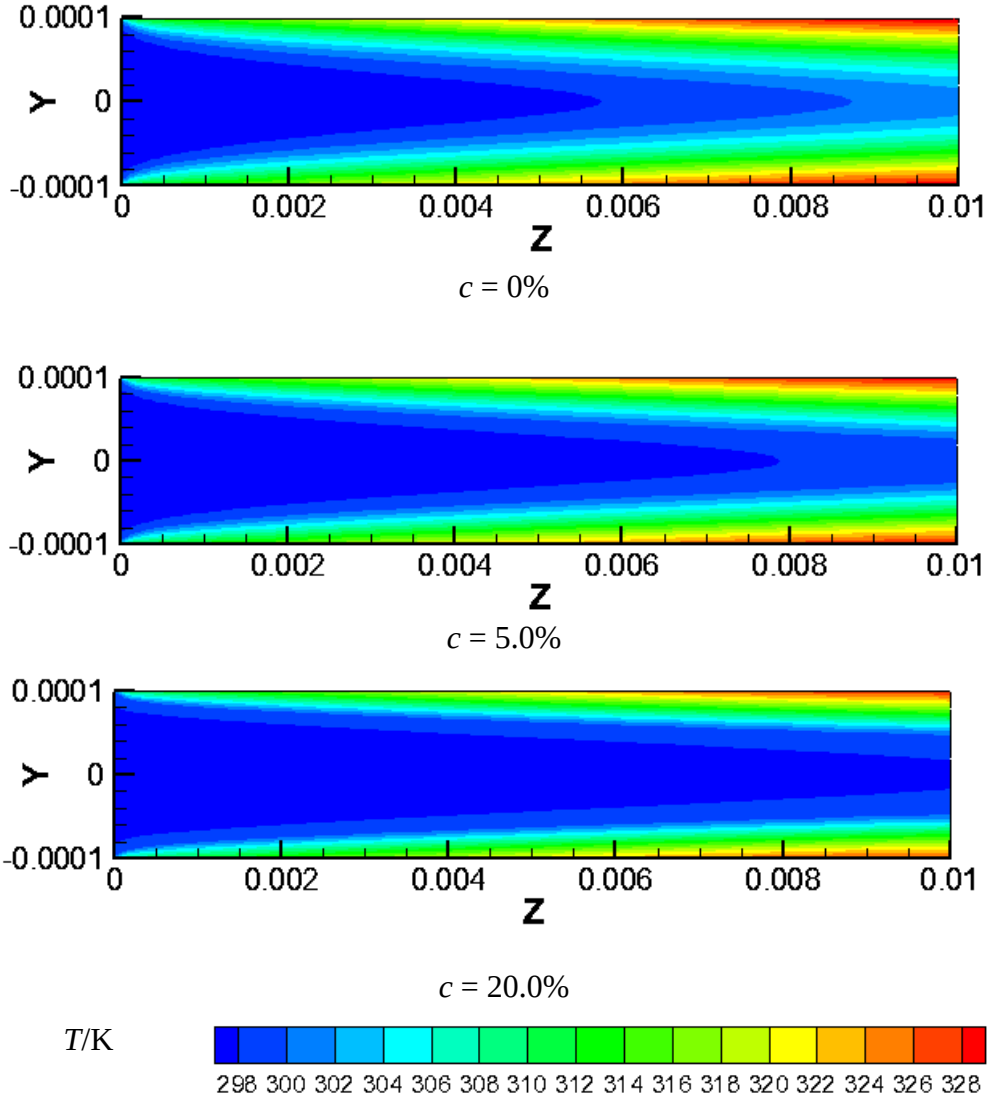

Figure 10.5 Temperature contours at middle cross section along the length of microchannel.

B/D = 1.2, H/D = 4, L/D = 50, q = 80 W/cm^2, T_{in} = 24 ^{o}C, w_{in} = 1.0 m/s

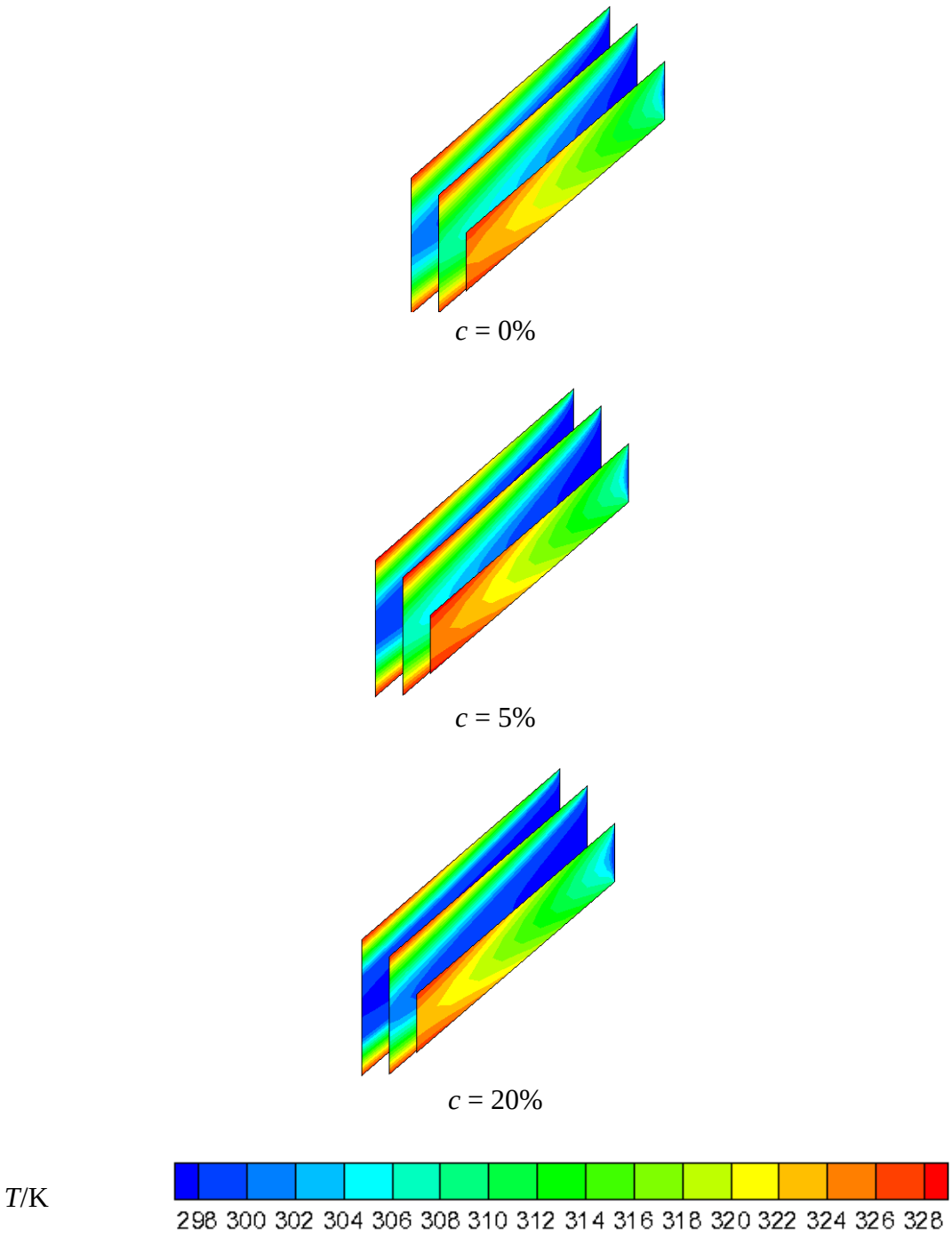

Figure 10.6 Temperature contours at different cross section along the radius of microchannel B/D = 1.2, H/D = 4, L/D = 50, q = 80 W/cm^2, T_{in} = 24 ºC, w_{in} = 1.0 m/s

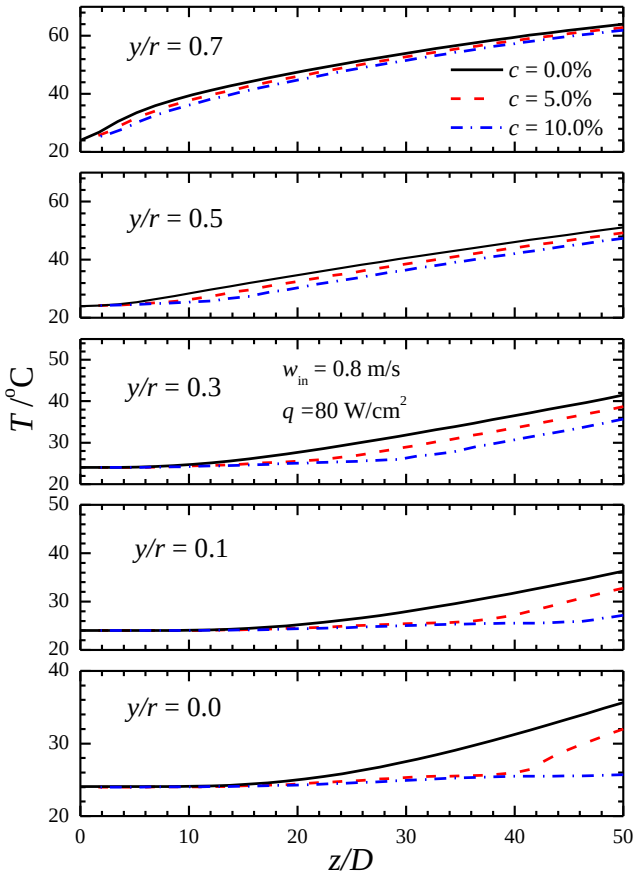

Figure 10.7 Temperature variations at different y locations along length of microchannel. B/D = 2, H/D = 4, L/D = 50, q =80 W/cm^2, w_{in} = 0.8 m/s

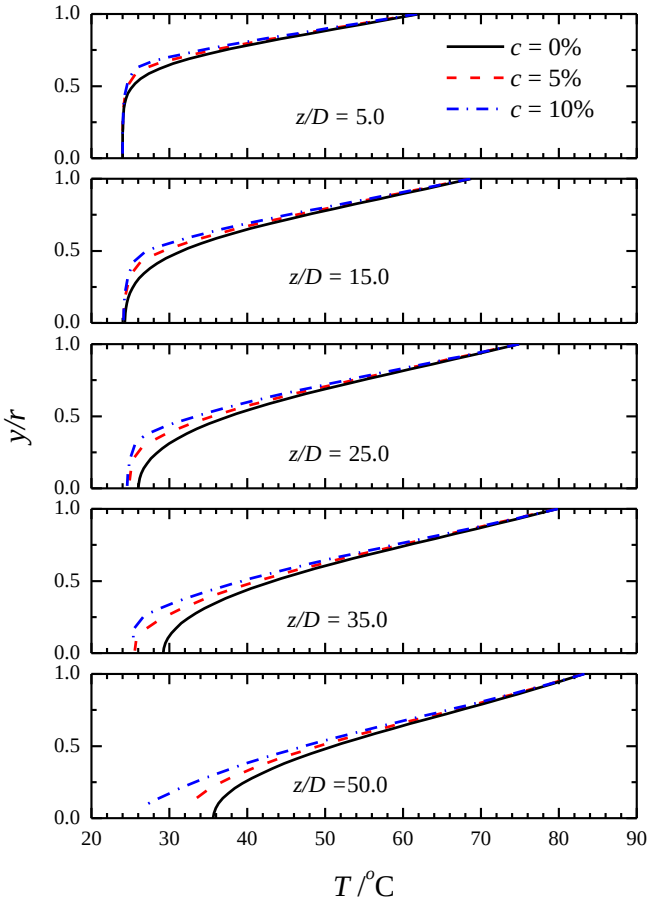

Figure 10.8 Radial Temperature variations at different z locations along length of microchannel. B/D = 2, H/D = 4, L/D = 50, q =80 W/cm^2, w_{in} = 0.8 m/s

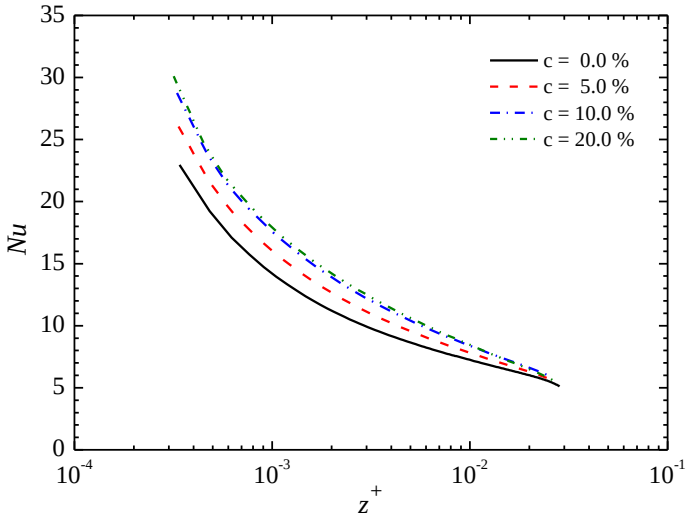

Figure 10.9 Variation of local *Nu* along the length of microchannel. *B/D* = 1.2, *H/D* = 4, *L/D* = 50, *q* = 80 W/cm^2, w_{in} = 2.53 m/s

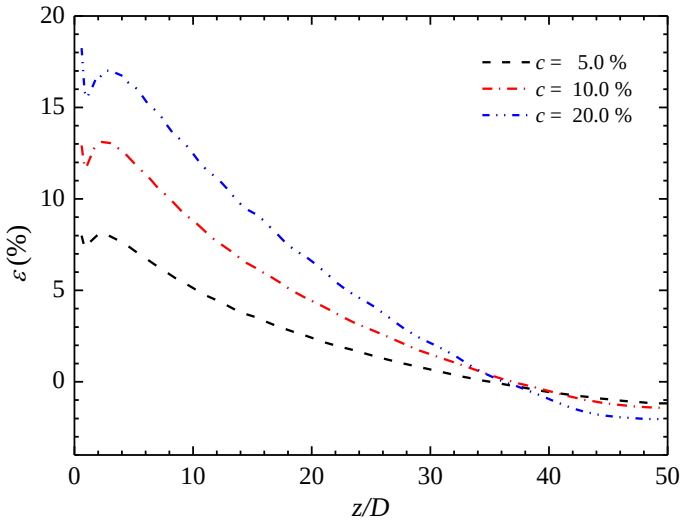

Figure 10.10 Heat transfer enhancement due to mPCM slurry flow in microchannel. *B/D* = 1.2, *H/D* = 4, *L/D* = 50, *q* =80 W/cm^2, w_{in} = 2.53 m/s

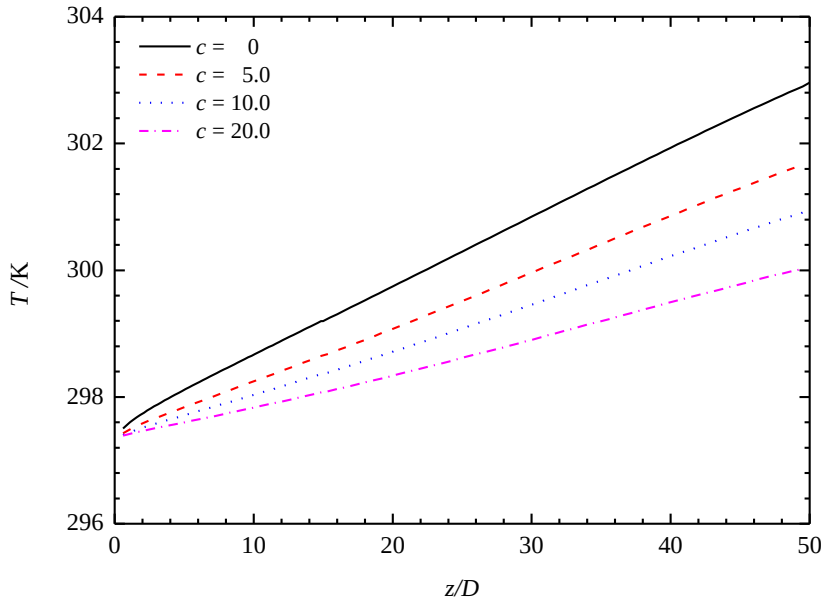

Figure 10.11 Bulk temperature rise along the length of microchannel. B/D = 1.2, H/D = 4, L/D = 50, q = 80 W/cm^2, w_{in} = 2.53 m/s

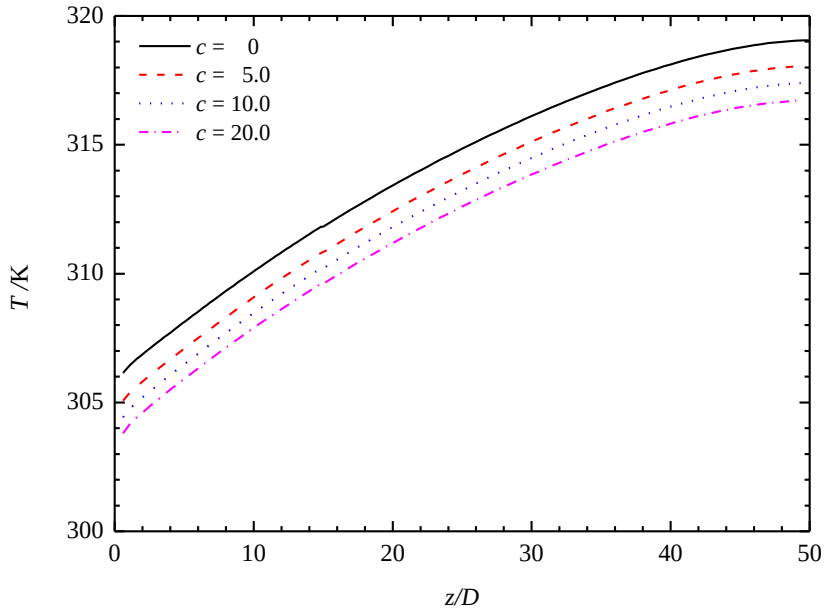

Figure 10.12 Local surface temperature rise along the length of microchannel. B/D = 1.2, H/D = 4, L/D = 50, q = 80 W/cm^2, w_{in} = 2.53 m/s

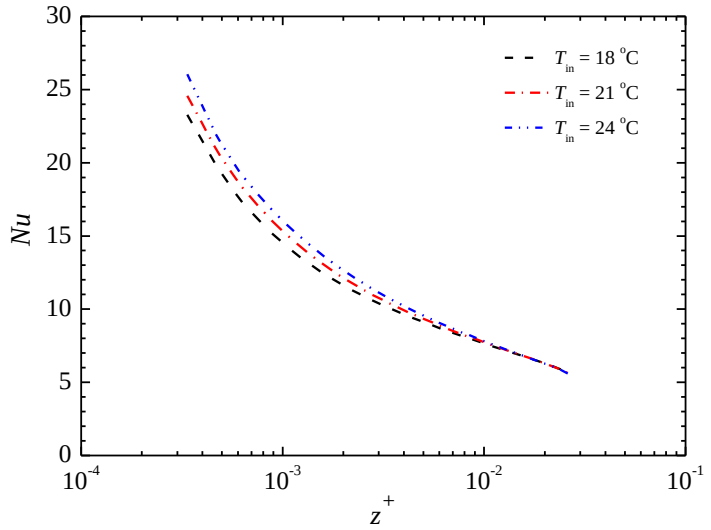

Figure 10.13 Effect of inlet temperature of mPCM slurry on local Nusselt number. *B/D* = 1.2, *H/D* = 4, *L/D* = 50, *q* =80 W/cm^2, w_{in} = 2.53 m/s, *c* = 5%

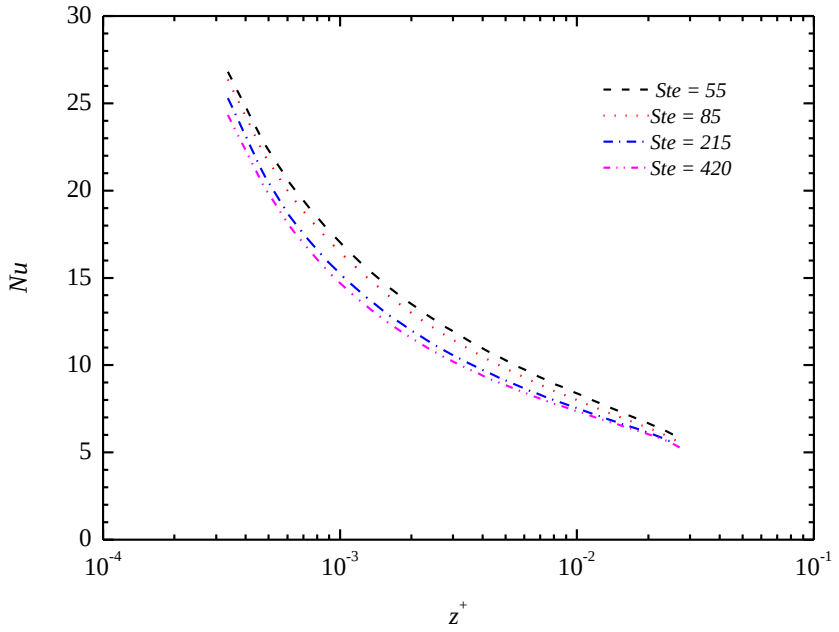

Figure 10.14 Effect of *Ste* on local *Nu* along the length of microchannel. *B/D* = 1.2, *H/D* = 4, *L/D* = 50, *q* =80 W/cm^2, w_{in} =2.53 m/s, *c* = 5%

10.7 Effect of thickness of separating wall of microchannel

Effect of thickness of separating wall of microchannel (represented by *B/D*) on surface temperature of heat sink is shown in Figure 10.15. Numerical simulations were conducted under following parameters, *Re* = 500.0, *L/D* = 50.0, and *H/D* = 4.0, *c*=0-20%. The surface temperature of the electronic devices should be maintained at safe operating temperatures. The increase in surface temperature can cause damage to electrical circuits. Therefore, it is necessary to maintain the surface temperature of top wall to reduce thermal stresses. The results shows that for mass concentration of 20% the increase in thickness of wall from 1.2 to 2.0 causes 38.5% increase in surface temperature at *z/D* = 50.0. A comparison is also made between water and mPCM slurry flow in microchannel heat sink. It has been observed for 20% mass concentration at *z/D* = 50.0, due to latent heat of mPCM slurry the dimensionless surface temperature is 28.0% less as compared to pure water. Figure 10.15 also depicts that for all cases top surface temperature decreases with the increase of mass concentration of mPCM. This is due to increase in heat capacity of mPCM slurry.

Figure 10.16 shows that thickness of separating wall has significant effect on bulk temperature. For mPCM of mass concentration 20% dimensionless bulk temperature rises to 48.0% at outlet of microchannel with the increase of *B/D* from 1.2 to 2.0. The bulk temperature gradients are less steep which shows that the bulk temperature remains constant during the phase change of mPCM particles. Similar to top surface temperature, bulk temperature decreases with the increase of mPCM mass concentration.

Thermal resistance of heat sink is also very important parameter for analysing the performance of microchannel heat sinks. Thermal resistance of heat sinks should be low to avoid thermal stresses. Effect of thickness of separating wall on thermal resistance is shown in Table 10.2. Values of thermal resistance for heat sink were calculated for *L/D*

= 50.0, *W*/D = 24.0, *Re* = 500. Table 10.2 indicates thermal resistance increases with the increase of thickness of separating wall. As thermal resistance is directly related to the surface temperature increase in surface temperature ultimately results in higher thermal resistance. Therefore, selection of optimum width of separating wall is necessary to design more efficient microchannel heat sinks.

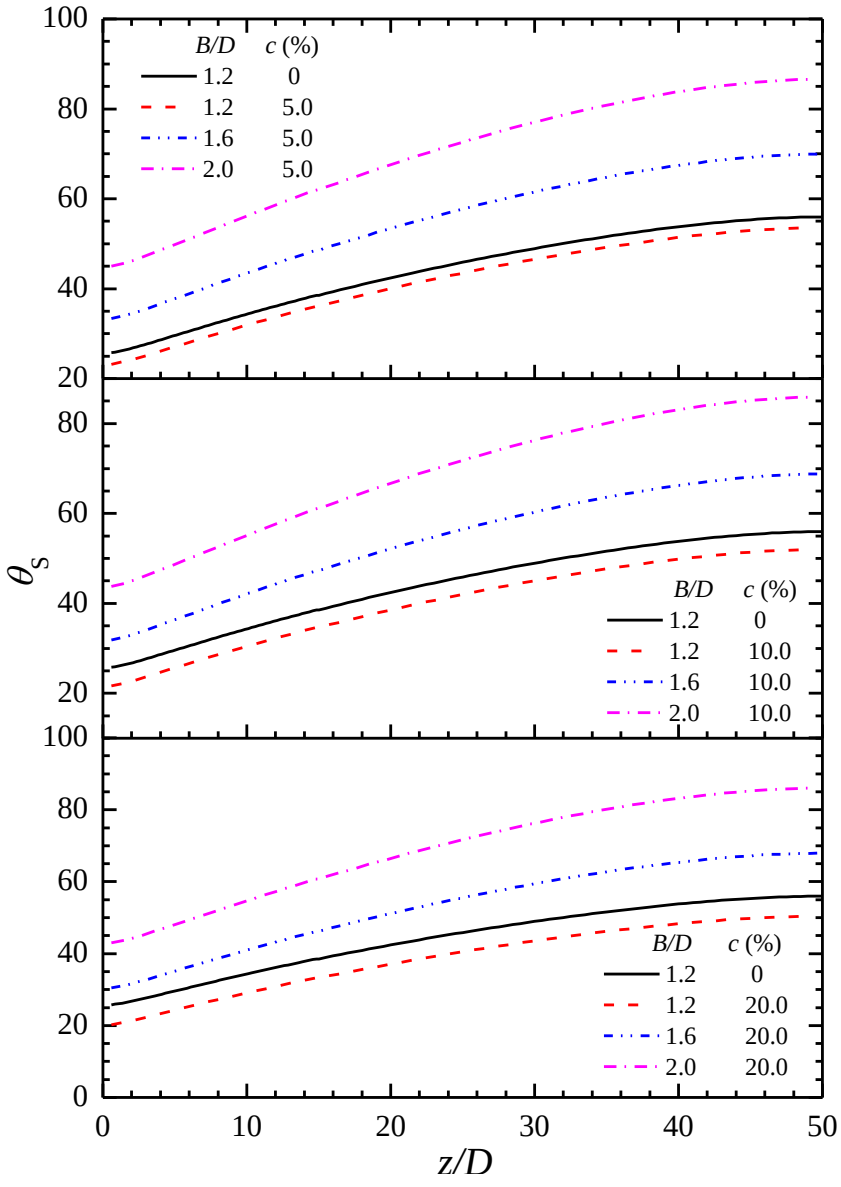

Figure 10.15 Effect of thickness *B* of separating wall on dimensionless top surface temperature of microchannel heat sink. *H/D* = 4.0, *L/D* = 50.0, w_{in} =2.53 m/s

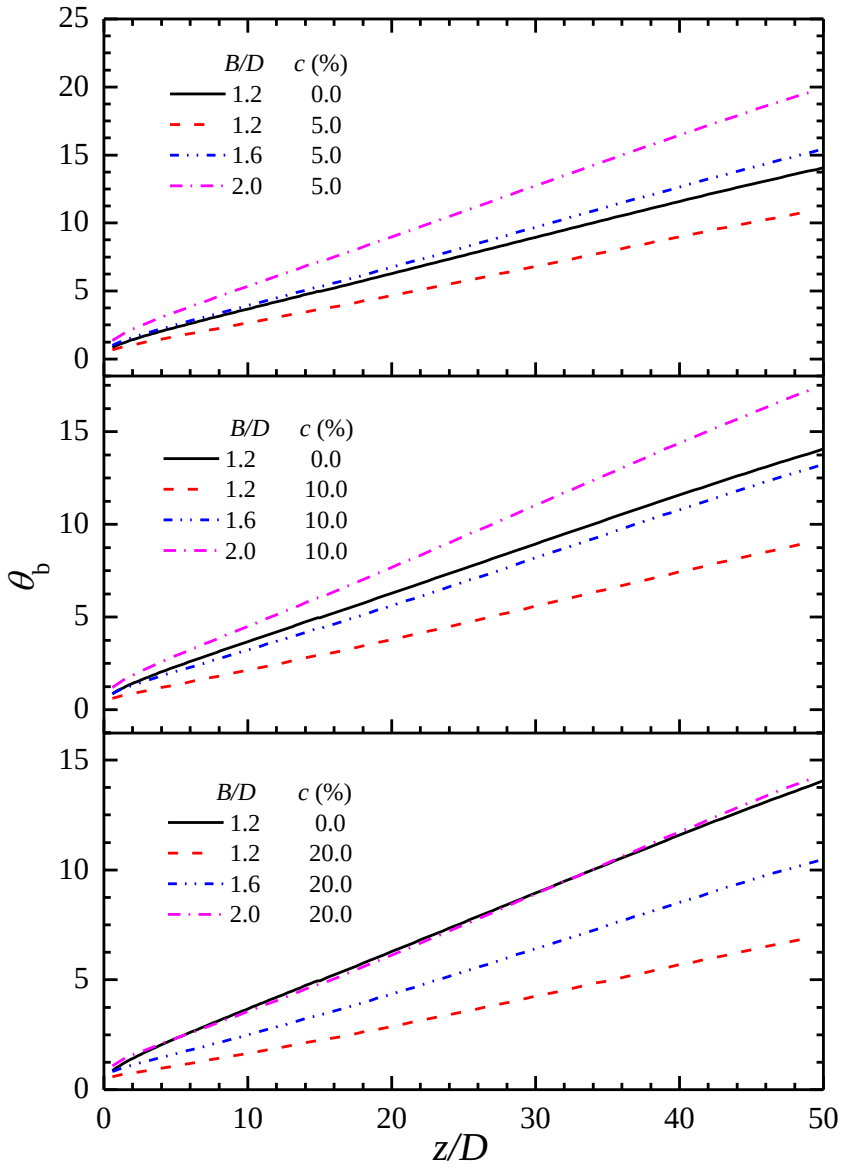

Figure 10.16 Effect of thickness *B* of separating wall on dimensionless bulk temperature of mPCM slurry along length of microchannel. *H/D* = 4.0, *L/D* = 50.0, w_{in} =2.53 m/s

Table 10.2 Effects of *H* and *B* on thermal resistance (R_{th} x10^4 /K/W) of microchannel heat sink

B/D	*H/D*	*c* (%)	
		5.0	20.0
1.2	2.0	1.169	1.106
1.2	3.0	1.154	1.092
1.2	4.0	1.152	1.083
1.6	4.0	1.506	1.460
2.0	4.0	1.862	1.849

10.8 Effect of height of separating wall of microchannel

Figure 10.17 indicates the effect of height of separating wall on top surface temperature of heat sink. The slope of the graph near the inlet of microchannel is less steep with the increase of wall height, which indicates more uniform top surface temperature. In Figure 10.17, a comparison is also made with pure water, for mass concentration of 20% latent heat of mPCM slurry causes 29.0 % reduction in dimensionless top surface temperature as compared to pure water.

Figure 10.18 represents the effect of height on dimensionless bulk temperature, it is clearly shown that change in height does not have significant effect on bulk temperature. Table 10.2 depicts that increase in height of separating wall has no effect on thermal resistance. Therefore, more uniform temperature can be attained by increasing the height of separating wall of microchannel. This increase in height will have no significant effect on thermal resistance. Similar results have also been observed by Kroeker et al. (2004).

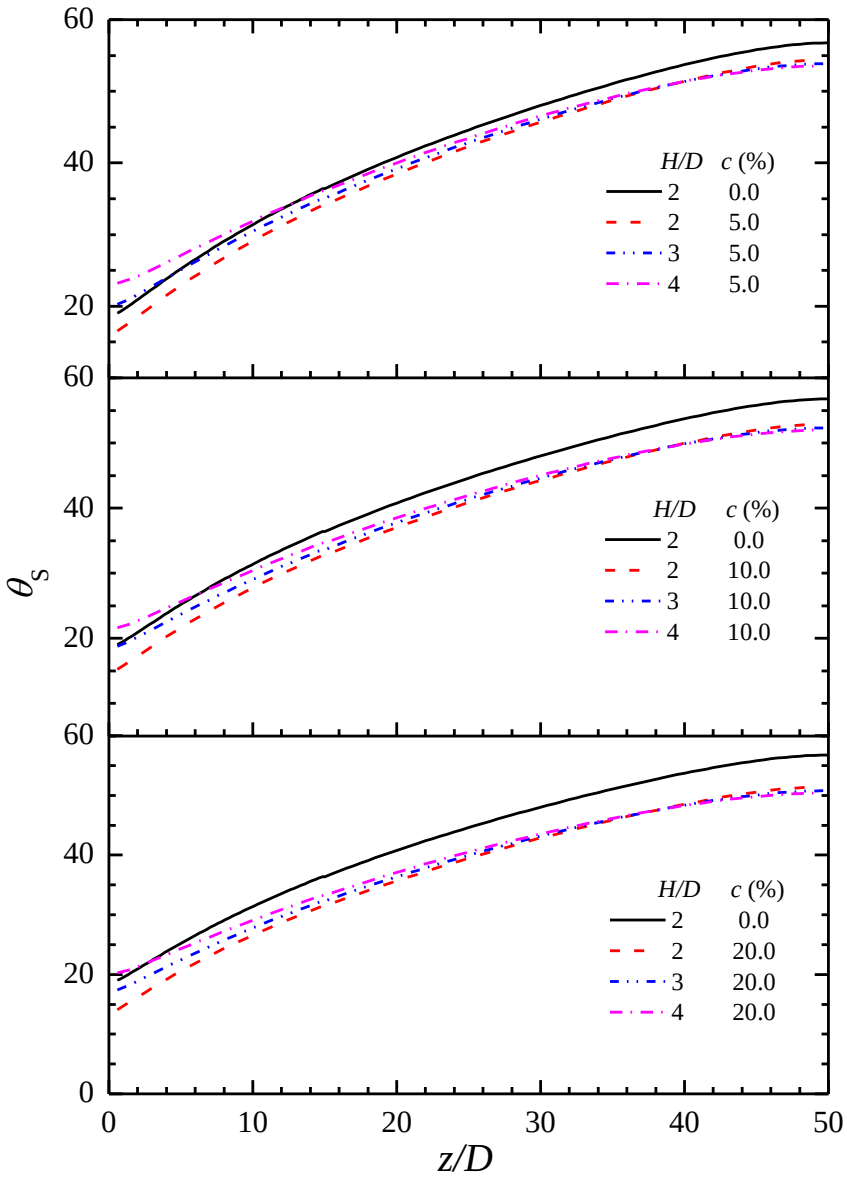

Figure 10.17 Effect of height H of separating wall of microchannel on dimensionless top surface temperature of microchannel heat sink. B/D = 1.2, L/D = 50.0, w_{in} =2.53 m/s

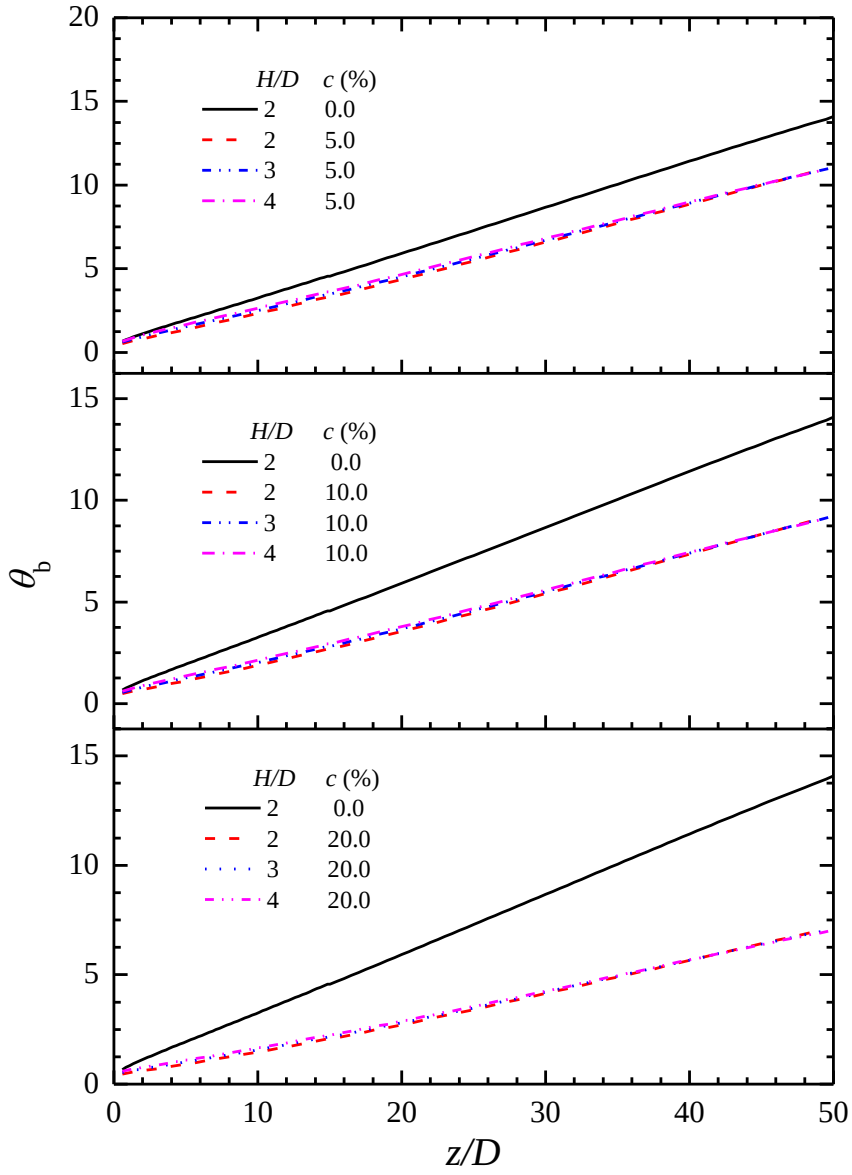

Figure 10.18 Effect of height H of separating wall of microchannel on dimensionless bulk temperature along the length of microchannel. B/D = 1.2, L/D = 50.0, w_{in} =2.53 m/s

10.9 Effect of microchannel shape

The microchannel geometry and its size have great impact on thermal and hydraulic performance of microchannel heat sinks. Numerical simulations were performed for circular, square ($\alpha = 1$) and rectangular ($\alpha = 5$) geometries having same thickness and height of separating wall of microchannel, hydraulic diameter and Reynolds number. Results were obtained by varying *Re* in range of 200 to 1000. Figure 10.19 shows the effect of microchannel geometry shape on thermal resistance of microchannel heat sink with mPCM slurry flow. Thermal resistance of rectangular microchannel was found 63% less as compared to circular microchannel at *Re* = 200. In all geometrical shapes, thermal resistance decreases with increase of Reynolds number but this decrease is not very prominent at higher Reynolds number. Pressure drop due to different microchannel shapes are illustrated in Figure 10.21. Pressure drop of rectangular microchannel is higher as compared to circular microchannel. This increase could be due to increase surface area of rectangular microchannel. The performance of microchannel heat sinks can be analysed by measuring its amount of heat dissipated per unit pumping power. Q/P_{pump} decreases with the increase of Reynolds number so low Reynolds number should be maintained to increase the performance of microchannel heat sink. Figure 10.22 shows that circular microchannel gives the best performance as compared to other microchannel geometries.

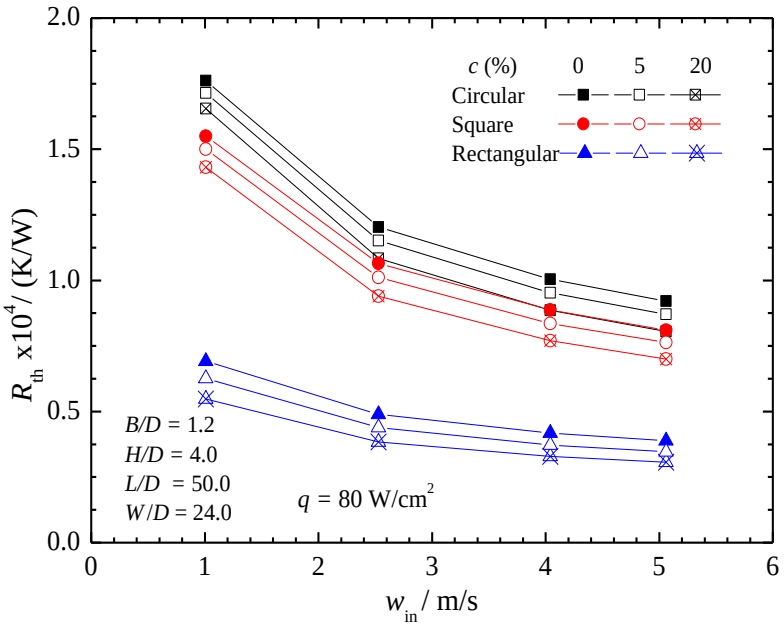

Figure 10.19 Effect of microchannel geometry on thermal resistance of microchannel heat sink

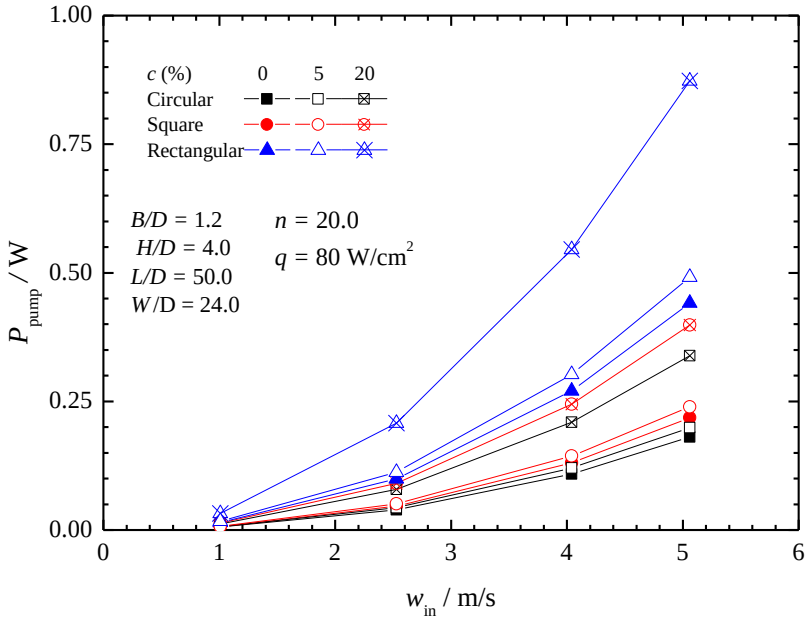

Figure 10.20 Variation of required pumping power due to different geometrical shapes of microchannels

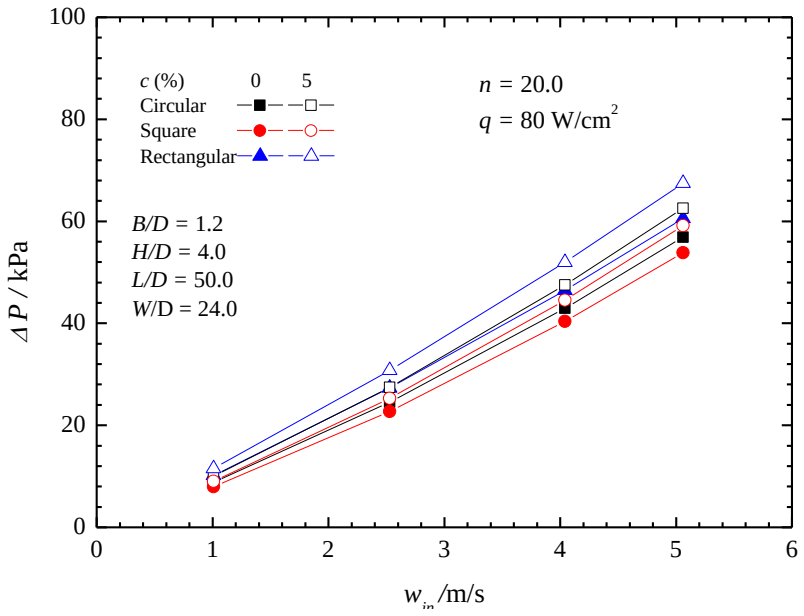

Figure 10.21 Variation of pressure drop due to different geometrical shapes of microchannel

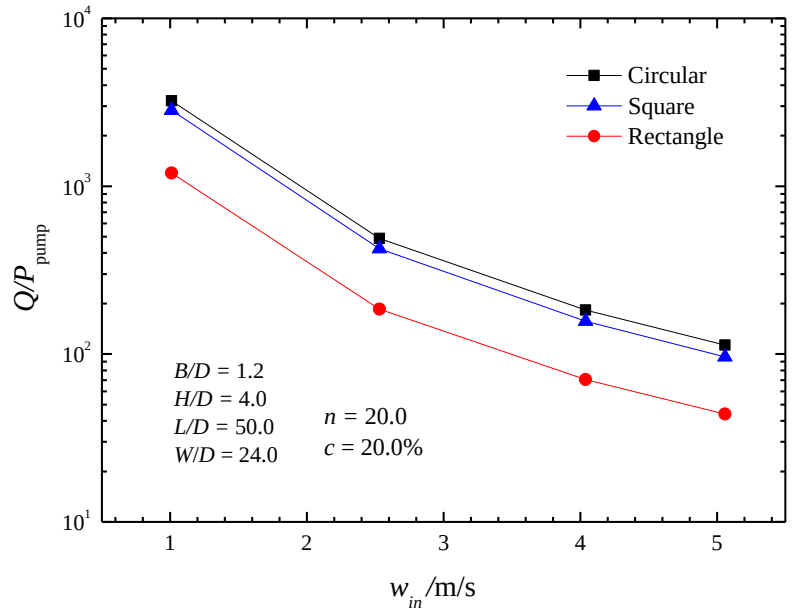

Figure 10.22 Variation of heat dissipated per unit pumping power for different shapes of microchannel

10.10 Conclusions

Numerical simulations have been performed for three dimensional conjugated heat transfer during mPCM slurry flow in microchannel heat sink to study the effects of

geometrical parameters on thermal and hydraulic performance. The following conclusions can be made:

1) Increase in thickness of separating wall of microchannel shows significant effect on dimensionless bulk temperature of slurry and surface temperature of microchannel heat sink. Increase in thickness of separating wall from 1.2 to 4.0 results in 38.5%, 48% and 41%, increase in surface temperature, bulk temperature, and thermal resistance respectively.

2) Results show that increase in height of separating wall of channel has insignificant effect on bulk temperature of slurry and thermal resistance of microchannel heat sink. The surface temperature of heat sink is found to be more uniform with increase of height so the height of the microchannel heat sink can be increased without not much effect on thermal resistance of heat sink.

3) Furthermore, a comparison is also made between the different geometrical shapes of microchannel having same hydraulic diameters and Reynolds number. Rectangular channel geometry shows maximum pressure drop inside the channel and 67% lower thermal resistance. However, circular channels show 62% more heat dissipation per unit pumping power.

Chapter 11

Conclusions

Experimental and numerical studies were conducted for analysing the local heat transfer and pressure drop characteristic of mPCM slurry flow in the microchannels under the convective boundary conditions.

11.1 Experimental measurements

A test rig has been designed and assembled to provide accurate methods for local heat flux and local surface temperature measurements. Local surface temperature and local heat flux was determined by the temperatures measured at 98 precisely known locations of thermocouples inserted in the aluminium blocks. Mixing chambers and water mixers were used to measure the accurate mean temperatures of the fluids at the inlet and outlet of microchannel and jackets, respectively. The inlet temperature of the working fluid and hot water was maintained by high accuracy thermostats (Ecogold 10, accuracy ±0.01K). An Agilent data logger was used to obtain the measurements which reduced the error of recording the measurements manually. The experiments were conducted with pure water and mPCM slurry under same operating conditions. The effects of mass concentration of mPCM slurry on local surface temperature, local heat flux, local Nusselt number, pressure drop, bulk temperature rise were investigated.

The experimental setup was validated by comparing the measured average Nusselt number and fanning friction factor with available empirical correlations. Average Nusselt number was determined and compared using two distinct methods: (i) the inverse solution of 2-D heat conduction (Yu et al. (2014)), (ii) Linear fittings of temperature measured

inside the test block. A good agreement was obtained within ± 11.1%. The following conclusions can be made from the results:

1. The local Nusselt number of mPCM slurry as compared to pure water was higher at mass flow rates of 3.3, 4.9 and 6.6 g/s. At *Re* = 1200, the average Nusselt number was found to be 12.1% and 28.3% higher than pure water for 5% and 10% mass concentrations of mPCM slurry, respectively. The increase in Nusselt number is attributed to the higher latent heat of mPCM particles during the phase change.

2. At the same heat transfer rate, *Q*, of 400 W, the fluid temperature rise of 5% and 10% mass concentration of mPCM slurry was 1.03 K and 2.68 K lower than pure water. Because of the latent heat absorption of mPCM slurry, the temperature remains constant during phase change which results in lower temperature rise as compared to water. This drop in temperature rise of fluid for same heat transfer rate makes it possible to reduce size of reservoirs for thermal energy storage.

3. It was also observed that for a particular heat transfer rate the pressure drop for mPCM slurry was lower than the pure water. Hence, decreasing the required pumping power.

4. The prediction method given by Eq. (11.1) developed for laminar mPCM slurry flow in microchannels provided ±15 % agreement with all experimental data.

$$Nu = 0.10Re^{0.46}Pr^{0.53}Ste^{0.01} \tag{11.1}$$

11.2 Numerical simulations

Numerical simulations of three-dimensional conjugated heat transfer model were carried out during melting and freezing of mPCM slurry in microchannels. It was observed that mPCM particles near the wall solidify or melt earlier as compared to mPCM slurry near

the core of microchannel. During melting of mPCM slurry significant reduction in bulk temperature rise has been observed. The surface temperature drop was not very significant. The local Nusselt number was found to be higher for mPCM slurry as compared to pure water.

Numerical simulations have been performed for three dimensional conjugated heat transfer during mPCM slurry flow in microchannel heat sink to study the effects of geometrical parameters on thermal and hydraulic performance. The following conclusions can be made:

1. Increase in thickness *B/D* from 1.2 to 4.0 results in 38.5%, 48%, 41% and 51% increase in surface temperature, bulk temperature, thermal resistance and heat transfer rate respectively.

2. As the height increases, the surface temperature appears more uniform whereas the bulk temperature, thermal resistance and heat transfer rate are almost constant.

3. At w_{in} 1m/s, for c = 20%, the rectangular shape has 67% lower thermal resistance but circular shape transferred 62% more heat per unit pumping power.

Future Work

In the present investigation, local heat transfer characteristic and pressure drop of mPCM slurry flow in microchannels have been investigated. Due to the limited cooling capacity, it is likely that PCM particles did not solidify completely during the thermal cycling. To confirm this a new slurry (MPCM-37) with higher melting temperature was purchased from Microtek but complete set of experiments have not be performed. Further experiments using MPCM-37 slurry could be done.

Thermophysical properties i.e. thermal conductivity and viscosity were not measured in present investigation and could be investigated in future.

Experiments could be conducted for higher mass concentration to further investigate the effect of mass concentration of mPCM slurry on heat transfer characteristics.

Furthermore, to analyse the durability of mPCM particles for required period of application, thermal cycling of the mPCM slurry should be carried out for few months and SEM images should be taken to see any ruptures in morphology of mPCM particles.

References

Alquaity, A. B. S., Al-Dini, S. A., Wang, E. N. & Yilbas, B. S. 2012. Numerical investigation of liquid flow with phase change nanoparticles in microchannels. *International Journal of Heat and Fluid Flow,* 38**,** 159-167.

Alvarado, J. L., Marsh, C., Sohn, C., Phetteplace, G. & Newell, T. 2007. Thermal performance of microencapsulated phase change material slurry in turbulent flow under constant heat flux. *International Journal of Heat and Mass Transfer,* 50**,** 1938-1952.

Balikowski, J. R. & Mollendorf, J. C. 2007. Performance of Phase Change Materials in a Horizontal Annulus of a Double-Pipe Heat Exchanger in a Water-Circulating Loop. *Journal of Heat Transfer,* 129**,** 265-272.

Cao, F. & Yang, B. 2014. Supercooling suppression of microencapsulated phase change materials by optimizing shell composition and structure. *Applied Energy,* 113**,** 1512-1518.

Charunyakorn, P., Sengupta, S. & Roy, S. K. 1991. Forced convection heat transfer in microencapsulated phase change material slurries: flow in circular ducts. *International Journal of Heat and Mass Transfer,* 34**,** 819-833.

Chen, B., Wang, X., Zeng, R., Zhang, Y., Wang, X., Niu, J., Li, Y. & Di, H. 2008. An experimental study of convective heat transfer with microencapsulated phase change material suspension: Laminar flow in a circular tube under constant heat flux. *Experimental Thermal and Fluid Science,* 32**,** 1638-1646.

Chen, B., Wang, X., Zhang, Y., Xu, H. & Yang, R. 2006. Experimental research on laminar flow performance of phase change emulsion. *Applied Thermal Engineering,* 26**,** 1238-1245.

Chen, L., Wang, T., Zhao, Y. & Zhang, X.-R. 2014. Characterization of thermal and hydrodynamic properties for microencapsulated phase change slurry (MPCS). *Energy Conversion and Management,* 79**,** 317-333.

Choi, E., Cho, Y. I. & Lorsch, H. G. 1994. Forced convection heat transfer with phase-change-material slurries: Turbulent flow in a circular tube. *International Journal of Heat and Mass Transfer,* 37**,** 207-215.

Choi, M. & Cho, K. 2001. Effect of the aspect ratio of rectangular channels on the heat transfer and hydrodynamics of paraffin slurry flow. *International Journal of Heat and Mass Transfer,* 44**,** 55-61.

Dammel, F. & Stephan, P. 2011. Heat Transfer to Suspensions of Microencapsulated Phase Change Material Flowing Through Minichannels. *Journal of Heat Transfer,* 134**,** 907-915.

Delgado, M., Lázaro, A., Mazo, J., Marín, J. M. & Zalba, B. 2012. Experimental analysis of a microencapsulated PCM slurry as thermal storage system and as heat transfer fluid in laminar flow. *Applied Thermal Engineering,* 36**,** 370-377.

Delgado, M., Lázaro, A., Peñalosa, C. & Zalba, B. 2014. Experimental analysis of the influence of microcapsule mass fraction on the thermal and rheological behavior of a PCM slurry. *Applied Thermal Engineering,* 63**,** 11-22.

Diaconu, B. M., Varga, S. & Oliveira, A. C. 2010. Experimental assessment of heat storage properties and heat transfer characteristics of a phase change material slurry for air conditioning applications. *Applied Energy,* 87**,** 620-628.

Farid, M., Michael, S., Rami, S. & Al Hallaj, S. 2007. Miniaturized refrigeration system with advanced PCM micro encapsulation technology. *Fifth international conference on Nanochannels, Microchannels and minichannels.* Puebla, Mexico.

Goel, M., Roy, S. K. & Sengupta, S. 1994. Laminar forced convection heat transfer in microcapsulated phase change material suspensions. *International Journal of Heat and Mass Transfer,* 37**,** 593-604.

Hasan, M. I. 2011. Numerical investigation of counter flow microchannel heat exchanger with MEPCM suspension. *Applied Thermal Engineering,* 31**,** 1068-1075.

Hassanipour, F. & Lage, J. L. 2010. Preliminary experimental study of a bio-inspired, phase-change particle capillary heat exchanger. *International Journal of Heat and Mass Transfer,* 53**,** 3300-3307.

Ho, C.-J., Chen, W.-C. & Yan, W.-M. 2013. Experimental study on cooling performance of minichannel heat sink using water-based MEPCM particles. *International Communications in Heat and Mass Transfer,* 48**,** 67-72.

Ho, C. J., Chen, W.-C. & Yan, W.-M. 2014a. Correlations of heat transfer effectiveness in a minichannel heat sink with water-based suspensions of Al2O3 nanoparticles and/or MEPCM particles. *International Journal of Heat and Mass Transfer,* 69**,** 293-299.

Ho, C. J., Chen, Y. Z., Tu, F.-J. & Lai, C.-M. 2014b. Thermal performance of water-based suspensions of phase change nanocapsules in a natural circulation loop with a mini-channel heat sink and heat source. *Applied Thermal Engineering,* 64**,** 376-384.

Hu, X. & Zhang, Y. 2002. Novel insight and numerical analysis of convective heat transfer enhancement with microencapsulated phase change material slurries: laminar flow in a circular tube with constant heat flux. *International Journal of Heat and Mass Transfer,* 45**,** 3163-3172.

Huang, Y., Xuan, Y. & Li, Q. 2012. Experimental investigation on convective heat transfer of magnetic phase change microcapsule suspension. *Applied Thermal Engineering,* 47**,** 10-17.

Inaba, H., Kim, M.-J. & Horibe, A. 2004. Melting Heat Transfer Characteristics of Microencapsulated Phase Change Material Slurries With Plural Microcapsules Having Different Diameters. *Journal of Heat Transfer,* 126**,** 558-565.

Inaba, H., Zhang, Y., Horibe, A. & Haruki, N. 2007. Numerical simulation of natural convection of latent heat phase-change-material microcapsulate slurry packed in a horizontal rectangular enclosure heated from below and cooled from above. *Heat and Mass Transfer,* 43**,** 459-470.

Incropera, F. P. & Witt, D. P. 1996. *Fundamentals of heat and mass transfer,* New York, John Wiley and sons.

Jamekhorshid, A., Sadrameli, S. M. & Farid, M. 2014. A review of microencapsulation methods of phase change materials (PCMs) as a thermal energy storage (TES) medium. *Renewable and Sustainable Energy Reviews,* 31**,** 531-542.

Jones, J. O. C. 1976. An Improvement in the Calculation of Turbulent Friction in Rectangular Ducts. *Journal of Fluids Engineering,* 98**,** 173-180.

Kays, W. M. 1966. Convective heat and mass transfer. New york: McGraw Hill book company.

Kays, W. M. & Crawford, M. E. 1993. Convective heat and mass transfer. Singapore: McGraw-Hill.

Kondle, S., Alvarado, J. & Marsh, C. 2013. Laminar flow forced convection heat transfer behavior of a phase change material fluid in microchannels. *Journal of Heat Transfer,* 135.

Krishnaswamy, S., Wang, H. S. & Rose, J. W. 2005. Condensation from gas-vapour mixtures in small non-circular tubes. *Proceesing of fifth Int. Conf on enhanced, compact andulta-compact heat exchangers: Science, Engineering and Technology*. NJ,USA.

Kroeker, C. J., Soliman, H. M. & Ormiston, S. J. 2004. Three-dimensional thermal analysis of heat sinks with circular cooling micro-channels. *International Journal of Heat and Mass Transfer,* 47**,** 4733-4744.

Kuravi, S., Kota, K. M., Du, J. & Chow, L. C. 2009. Numerical investigation of flow and heat transfer performance of nano-encapsulated phase change material slurry in microchannels. *Journal of Heat Transfer*, 131.

Lee, J. & Mudawar, I. 2007. Assessment of the effectiveness of nanofluids for single-phase and two-phase heat transfer in micro-channels. *International Journal of Heat and Mass Transfer,* 50**,** 452-463.

Lelea, D. 2010. Effects of inlet geometry on heat transfer and fluid flow of tangential micro-heat sink. *International Journal of Heat and Mass Transfer*, 53**,** 3562-3569.

Ma, X., Omer, S. A., Riffat, S. B. & Zhang, W. 2009. Investigation of energy transportation capability of a phase change slurry through a cold storage-cooling coil system. *International Journal of Energy Research,* 33**,** 999-1004.

Mehling, H. & Cabeza, L. F. 2008. *Heat and Cold storage with PCM*, Springer.

Mossaz, S., Gruss, J.-A., Ferrouillat, S., Skrzypski, J., Getto, D., Poncelet, O. & Berne, P. 2015. Experimental study on the influence of nanoparticle PCM slurry for high temperature on convective heat transfer and energetic performance in a circular tube under imposed heat flux. *Applied Thermal Engineering,* 81**,** 388-398.

Pérez-Lombard, L., Ortiz, J. & Pout, C. 2008. A review on buildings energy consumption information. *Energy and Buildings,* 40**,** 394-398.

Rajabi Far, B., Mohammadian, S. K., Khanna, S. K. & Zhang, Y. 2015. Effects of pin tip-clearance on the performance of an enhanced microchannel heat sink with oblique fins and phase change material slurry. *International Journal of Heat and Mass Transfer,* 83**,** 136-145.

Rao, Y., Dammel, F., Stephan, P. & Lin, G. 2006. Flow frictional characteristics of microencapsulated phase change material suspensions flowing through rectangular minichannels. *Science in China Series E: Technological Sciences,* 49**,** 445-456.

Rao, Y., Dammel, F., Stephan, P. & Lin, G. 2007. Convective heat transfer characteristics of microencapsulated phase change material suspensions in minichannels. *Heat and Mass Transfer,* 44**,** 175-186.

Ravi, G. 2008. *Study of laminar flow forced convection heat transfer behavior of a phase change material fluid.* Anna University.

Roy, S. K. & Avanic, B. L. 1997. Laminar forced convection heat transfer with phase change material emulsions. *International Communications in Heat and Mass Transfer,* 24**,** 653-662.

Roy, S. K. & Avanic, B. L. 2001. Turbulent heat transfer with phase change material suspensions. *International Journal of Heat and Mass Transfer,* 44**,** 2277-2285.

Royon, L. & Guiffant, G. 2008. Forced convection heat transfer with slurry of phase change material in circular ducts: A phenomenological approach. *Energy Conversion and Management,* 49**,** 928-932.

Sabbah, R., Farid, M. M. & Al-Hallaj, S. 2008. Micro-channel heat sink with slurry of water with micro-encapsulated phase change material: 3D-numerical study. *Applied Thermal Engineering,* 29**,** 445-454.

Sabbah, R., Seyed-Yagoobi, J. & Al-Hallaj, S. 2011. Heat Transfer Characteristics of Liquid Flow With Micro-Encapsulated Phase Change Material: Numerical Study. *Journal of Heat Transfer,* 133**,** 121702-10.

Seyf, H. R., Zhou, Z., Ma, H. B. & Zhang, Y. 2013. Three dimensional numerical study of heat-transfer enhancement by nano-encapsulated phase change material slurry in microtube heat sinks with tangential impingement. *International Journal of Heat and Mass Transfer,* 56**,** 561-573.

Shah, R. K. & London, A. L. 1978. Laminar flow forced convection in ducts. New york: Academic press.

Song, S.-H., Liao, Q. & Shen, W.-D. 2013a. Laminar heat transfer and friction characteristics of microencapsulated phase change material slurry in a circular tube with twisted tape inserts. *Applied Thermal Engineering,* 50**,** 791-798.

Song, S., Liao, Q., Shen, W., Ruan, Y. & Xu, J. 2013b. Numerical study on laminar convective heat transfer enhancement of microencapsulated phase change material slurry using liquid metal with low melting point as carrying fluid. *International Journal of Heat and Mass Transfer,* 62**,** 286-294.

Wang, L. & Lin, G. 2012. Experimental study on the convective heat transfer behavior of microencapsulated phase change material suspensions in rectangular tube of small aspect ratio. *Heat and Mass Transfer,* 48**,** 83-91.

Wang, X., Niu, J., Li, Y., Wang, X., Chen, B., Zeng, R., Song, Q. & Zhang, Y. 2007. Flow and heat transfer behaviors of phase change material slurries in a horizontal circular tube. *International Journal of Heat and Mass Transfer,* 50**,** 2480-2491.

Wang, X., Niu, J., Li, Y., Zhang, Y., Wang, X., Chen, B., Zeng, R. & Song, Q. 2008. Heat transfer of microencapsulated PCM slurry flow in a circular tube. *AIChE Journal,* 54**,** 1110-1120.

Wu, W., Bostanci, H., Chow, L. C., Hong, Y., Wang, C. M., Su, M. & Kizito, J. P. 2013. Heat transfer enhancement of PAO in microchannel heat exchanger using nano-encapsulated phase change indium particles. *International Journal of Heat and Mass Transfer,* 58**,** 348-355.

Xing, K. Q., Tao, Y. X. & Hao, Y. L. 2005. Performance Evaluation of Liquid Flow With PCM Particles in Microchannels. *Journal of Heat Transfer,* 127**,** 931-940.

Yamagishi, Y., Takeuchi, H., Pyatenko, A. T. & Kayukawa, N. 1999. Characteristics of microencapsulated PCM slurry as a heat-transfer fluid. *AIChE Journal,* 45**,** 696-707.

Yang, R., Xu, H. & Zhang, Y. 2003. Preparation, physical property and thermal physical property of phase change microcapsule slurry and phase change emulsion. *Solar Energy Materials and Solar Cells,* 80**,** 405-416.

Yu, G. X., Sun, J., Wang, H. S., Wen, P. H. & Rose, J. W. 2014. Meshless inverse method to determine temperature and heat flux at boundaries for 2D steady-state heat conduction problems. *Experimental Thermal and Fluid Science,* 52**,** 156-163.

Zalba, B., Marıin, J. M., Cabeza, L. F. & Mehling, H. 2003. Review on thermal energy storage with phase change: materials, heat transfer analysis and applications. *Applied Thermal Engineering,* 23**,** 251-283.

Zeng, R., Wang, X., Chen, B., Zhang, Y., Niu, J., Wang, X. & Di, H. 2009. Heat transfer characteristics of microencapsulated phase change material slurry in laminar flow under constant heat flux. *Applied Energy,* 86**,** 2661-2670.

Zhang, Y., Hu, X. & Wang, X. 2003. Theoretical analysis of convective heat transfer enhancement of microencapsulated phase change material slurries. *Heat and Mass Transfer,* 40**,** 59-66.

Zou, D., Feng, Z., Xiao, R., Qin, K., Zhang, J., Song, W. & Tu, Q. 2010. Preparation and flow characteristic of a novel phase change fluid for latent heat transfer. *Solar Energy Materials and Solar Cells,* 94**,** 2292-2297.

Appendix A

Thermophysical Properties of mPCM Slurry

For experimentation, thermophysical properties of mPCM slurry are needed. The methods for calculating the thermophysical properties of slurry are given in Eqs. A.1 to A.5 (Kondle et al. (2013))

(a) Heat capacity of mPCM slurry

$$C_{\mathrm{pb}} = cC_{\mathrm{pp}} + (1 - \mathrm{c})C_{\mathrm{pw}} \tag{A.1}$$

where $C_{\mathrm{pb}}, C_{\mathrm{pp}}, C_{\mathrm{pw}}$ are the specific heat capacities of slurry, PCM inside the shell and water respectively, and φ is the mass concentration of mPCM slurry.

(b) Density of mPCM slurry

$$\rho_{\mathrm{b}} = \mathrm{c}\rho_{\mathrm{p}} + (1 - \mathrm{c})\rho_{\mathrm{w}} \tag{A.2}$$

where $\rho_{\mathrm{b}}, \rho_{\mathrm{p}}, \rho_{\mathrm{w}}$ are the densities of slurry, PCM inside the shell and water respectively, and φ is the mass concentration of mPCM slurry.

(c) Thermal conductivity of mPCM slurry

$$k_{\mathrm{b}} = k_{\mathrm{w}}.\frac{k_{\mathrm{w}} + k_{\mathrm{p}} + 2\varphi(k_{\mathrm{p}} - k_{\mathrm{w}})}{k_{\mathrm{w}} + k_{\mathrm{p}} - \varphi(k_{\mathrm{p}} - k_{\mathrm{w}})} \tag{A.3}$$

where k_{b} , $k_{\mathrm{w}}, k_{\mathrm{p}}$ are the thermal conductivities of slurry, water and PCM inside the shell, ω is the volume concentration of mPCM slurry.

(d) Dynamic viscosity of mPCM slurry

$$\mu_{\mathrm{b}} = \mu_{\mathrm{w}}(1 + 2.5\varphi + 10.05\varphi^2 + 0.00273e^{16.6\varphi}) \tag{A.4}$$

where $\mu_{\mathrm{b}}, \mu_{\mathrm{w}}$ are the dynamic viscosities of mPCM slurry and water respectively.

(e) Latent heat mPCM capacity

The phase change temperature of the mPCM suspension is same as that of the mPCM particles so the latent heat capacity of mPCM suspension is calculated by Eq. (A.5j)

$$h_{\mathrm{bfs}} = c h_{\mathrm{fs}} \tag{A.5}$$

where h_{bfs} is the bulk latent heat capacity of slurry and h_{fs} is the latent heat capacity of PCM particle inside the shell.

Appendix B

Heat Loss Tests

The heat loss from the nylon jackets to the surroundings were carried out by flowing the pure water in upper and lower jackets when the apparatus was at room temperature. The inlet temperature of the hot water was varied from 35 °C to 60 °C. The volume flow rate of the hot water was taken at 1000 ccm and 1500 ccm. The inlet and outlet temperature of the hot water was measured by two T-type thermocouples inserted inside the water mixers. It is shown in Table B.1 that the heat losses increases with the increase of hot water temperature.

Table B.1 Data for heat loss

Run No.	$T_{h,in}$	$V_{h,in}$	T_{amb}	$T_{h,in,up}$	$T_{h,out,up}$	$T_{h,in,low}$	$T_{b,out,low}$	$Q_{l,up}$	$Q_{l,low}$
	°C	ccm	°C	°C	°C	°C	°C	W	W
hl-1b	35	1000	23.42	33.94	33.87	33.97	33.88	4.96	6.59
hl-1c	35	1500	23.72	33.94	33.91	33.96	33.91	3.05	5.71
hl-2b	40	1000	24.34	38.92	38.81	38.95	38.81	7.73	9.36
hl-2c	40	1500	24.01	38.92	38.84	38.96	38.86	7.93	10.76
hl-3b	45	1000	24.14	43.92	43.76	43.96	43.78	10.73	12.78
hl-3c	45	1500	24.33	43.92	43.83	43.97	43.84	9.26	12.91
hl-4b	50	1000	23.97	48.94	48.73	48.99	48.74	14.39	16.65
hl-4c	50	1500	24.09	48.95	48.81	49.01	48.83	14.26	18.35
hl-5b	55	1000	24.13	53.99	53.70	54.07	53.73	20.30	23.81
hl-5c	55	1500	24.17	53.98	53.81	54.07	53.85	17.18	22.21
hl-5b	60	1000	24.37	59.02	58.70	59.10	58.74	22.25	24.85
hl-5c	60	1500	24.29	59.05	58.82	59.15	58.87	24.05	29.16

Appendix C

Data Tables of Experimental Results

Table C.2 Data of pure water (conditions for comparison with DS5037X slurry)

c = 0 %, m_{jac} = 29 g/s, T_{jac} = 40 °C ,T_{ch} = 22 °C

No.	m_{ch} g/s	ΔT_m °C	ΔT_{ch} °C	$Q_{\Delta T,m}$ W	$Q_{\Delta T,ch}$ W	$Q_{l,tot}$ W	$Q_{\Delta T+l,m}$ W	$Q_{\Delta T+l,ch}$ W	$\Delta T_{j,up}$ °C	$\Delta T_{j,low}$ °C	$Q_{\Delta T,j,up}$ W	$Q_{\Delta T,j,low}$ W	$Q_{\Delta T,j,tot}$ W	$Q_{\Delta T,j,tot}$/ $Q_{\Delta T,ch,tot}$ %	$Q_{inv,ch}$ W	$Q_{\Delta T,j,tot}$/ $Q_{inv,ch}$ %
	Flow inside microchannels								Flow inside jackets							
W-1	11.58	5.67	5.65	274.68	273.56	20.43	295.10	293.99	1.50	1.49	155.86	154.31	310.18	5.22	338.07	-8.99
W-2	9.92	5.51	6.21	228.65	257.53	20.33	248.98	277.87	1.42	1.39	147.94	144.66	292.60	5.04	316.57	-8.19
W-3	8.27	5.98	6.92	206.84	239.17	20.25	227.09	259.41	1.34	1.29	139.46	133.98	273.44	5.13	290.20	-6.13
W-4	6.61	6.97	7.55	192.81	208.79	20.10	212.91	228.89	1.26	1.19	130.47	124.07	254.55	10.08	264.08	-3.75
W-5	4.96	7.89	8.35	163.58	173.07	20.11	183.69	193.18	1.13	1.08	117.61	111.90	229.51	15.83	233.41	-1.70
W-6	3.31	9.61	9.46	132.75	130.76	19.84	152.59	150.60	1.02	0.94	105.67	97.32	202.99	25.81	197.60	2.65

c = 0 %, m_{jac} = 29 g/s, T_{jac} = 45 °C ,T_{ch} = 22 °C

No.	m_{ch} g/s	ΔT_m °C	ΔT_{ch} °C	$Q_{\Delta T,m}$ W	$Q_{\Delta T,ch}$ W	$Q_{l,tot}$ W	$Q_{\Delta T+l,mix}$ W	$Q_{\Delta T+l,ch}$ W	$\Delta T_{j,up}$ °C	$\Delta T_{j,low}$ °C	$Q_{\Delta T,j,up}$ W	$Q_{\Delta T,j,low}$ W	$Q_{\Delta T,j,tot}$ W	$Q_{\Delta T,j,tot}$/ $Q_{\Delta T,ch,tot}$ %	$Q_{inv,ch}$ W	$Q_{\Delta T,j,tot}$/ $Q_{inv,ch}$ %
	Flow inside microchannels								Flow inside jackets							
W-7	11.58	7.22	7.30	349.51	353.10	24.85	374.36	377.95	2.03	2.04	210.95	211.73	422.67	10.58	473.18	-11.95
W-8	9.92	7.26	7.86	301.02	326.04	24.78	325.80	350.82	1.88	1.86	195.60	192.71	388.31	9.66	419.86	-8.12
W-9	8.27	7.97	8.69	275.54	300.44	24.74	300.28	325.18	1.76	1.72	183.31	178.83	362.14	10.21	383.01	-5.76
W-10	6.61	9.14	9.93	252.57	274.49	24.56	277.13	299.05	1.64	1.60	170.75	165.71	336.47	11.12	351.94	-4.60
W-11	4.96	9.27	10.93	192.17	226.55	24.52	216.69	251.07	1.64	1.48	169.92	153.43	323.35	22.35	322.23	0.35
W-12	3.30	11.31	13.14	156.24	181.44	24.24	180.47	205.68	1.43	1.26	148.96	130.36	279.32	26.36	264.66	5.25

c = 0 %, m_{jac} = 29 g/s, T_{jac} = 50 °C ,T_{ch} = 22 °C

No.	m_{ch}	ΔT_m	ΔT_{ch}	$Q_{\Delta T,m}$	$Q_{\Delta T,ch}$	$Q_{l,tot}$	$Q_{\Delta T+l,mix}$	$Q_{\Delta T+l,ch}$	$\Delta T_{j,up}$	$\Delta T_{j,low}$	$Q_{\Delta T,j,up}$	$Q_{\Delta T,j,low}$	$Q_{\Delta T,j,tot}$	$Q_{\Delta T,j,tot}$/ $Q_{\Delta T,ch,tot}$	$Q_{inv,ch}$	$Q_{\Delta T,j,tot}$/ $Q_{inv,ch}$
	g/s	°C	°C	W	W	W	W	W	°C	°C	W	W	W	%	W	%
	Flow inside microchannels								Flow inside jackets							
W-13	11.57	10.07	9.34	487.16	451.77	28.91	516.07	480.68	2.53	2.57	262.79	267.26	530.05	9.31	598.91	-12.99
W-14	9.92	10.21	9.92	423.16	411.45	28.96	452.12	440.41	2.32	2.33	241.44	241.70	483.15	8.85	533.18	-10.36
W-15	8.26	10.31	11.45	356.26	395.49	28.93	385.19	424.42	2.17	2.14	225.30	221.88	447.19	5.09	481.44	-7.66
W-16	6.61	11.92	12.56	329.33	346.98	28.60	357.93	375.58	1.98	1.94	205.86	201.80	407.65	7.87	427.03	-4.75
W-17	4.96	13.25	13.75	274.47	284.83	28.87	303.34	313.70	1.99	1.79	206.85	186.40	393.26	20.23	387.94	1.35
W-18	3.30	13.93	15.62	192.27	215.63	29.14	221.41	244.77	1.79	1.57	186.13	163.21	349.34	29.93	325.87	6.72

Table C.3 Data of 5% mass concentration of mPCM DS5037X slurry

c = 5 %, $m_{h,in}$ = 24 g/s, $T_{h,in}$ = 40 °C ,$T_{f,in}$ = 22 °C

No.	m_{ch} g/s	ΔT_m °C	ΔT_{ch} °C	$Q_{\Delta T,m}$ W	$Q_{\Delta T,ch}$ W	$Q_{l,tot}$ W	$Q_{\Delta T+l,mix}$ W	$Q_{s,ch}$ W	$\Delta T_{j,up}$ °C	$\Delta T_{j,low}$ °C	$Q_{\Delta T,j,up}$ W	$Q_{\Delta T,j,low}$ W	$Q_{\Delta T,j,tot}$ W	$Q_{\Delta T,j,tot}/Q_{s,ch,tot}$ %	$Q_{inv,ch}$ W	$Q_{\Delta T,j,tot}/Q_{inv,ch}$ %
	Flow inside microchannels								Flow inside jackets							
s5-1	11.58	4.88	5.12	280.19	294.20	20.50	300.69	314.71	1.53	1.40	158.80	144.91	303.72	-3.62	311.03	-2.41
s5-2	9.93	5.65	5.52	275.20	268.76	20.40	295.60	289.16	1.48	1.33	154.10	138.27	292.36	1.10	291.76	0.21
s5-3	8.27	5.81	6.21	231.72	247.87	20.42	252.14	268.29	1.40	1.24	145.44	129.05	274.50	2.26	271.61	1.05
s5-4	6.61	6.51	6.95	204.91	218.75	20.42	225.34	239.18	1.33	1.17	138.42	121.52	259.94	7.99	253.43	2.51
s5-5	4.96	8.06	8.08	186.97	187.34	20.27	207.24	207.61	1.23	1.06	127.76	110.43	238.19	12.84	227.82	4.35
s5-6	3.31	9.69	9.78	147.02	148.39	20.17	167.19	168.56	1.10	0.91	114.40	94.87	209.26	19.45	190.37	9.03

c = 5 %, $m_{h,in}$ = 24 g/s, $T_{h,in}$ = 45 °C ,$T_{f,in}$ = 22 °C

No.	m_{ch} g/s	ΔT_m °C	ΔT_{ch} °C	$Q_{\Delta T,m}$ W	$Q_{\Delta T,ch}$ W	$Q_{l,tot}$ W	$Q_{\Delta T+l,mix}$ W	$Q_{s,ch}$ W	$\Delta T_{j,up}$ °C	$\Delta T_{j,low}$ °C	$Q_{\Delta T,j,up}$ W	$Q_{\Delta T,j,low}$ W	$Q_{\Delta T,j,tot}$ W	$Q_{\Delta T,j,tot}/Q_{s,ch,tot}$ %	$Q_{inv,ch}$ W	$Q_{\Delta T,j,tot}/Q_{inv,ch}$ %
	Flow inside microchannels								Flow inside jackets							
s5-7	11.58	6.68	6.96	379.65	394.51	24.93	404.59	419.45	2.00	1.84	207.73	191.18	398.91	-5.15	414.24	-3.84
s5-8	9.92	7.46	7.56	359.09	363.26	24.89	383.98	388.15	1.89	1.74	196.23	180.36	376.58	-3.07	387.15	-2.81
s5-9	8.27	8.28	8.54	327.05	336.28	24.71	351.77	361.00	1.80	1.64	187.45	170.11	357.56	-0.96	361.71	-1.16
s5-10	6.61	9.60	9.66	298.77	299.95	24.73	323.50	324.68	1.69	1.51	175.76	156.57	332.33	2.30	332.64	-0.09
s5-11	4.96	11.30	10.89	260.44	250.48	24.59	285.03	275.07	1.56	1.35	161.84	140.53	302.37	9.03	297.83	1.50
s5-12	3.30	14.83	13.02	224.26	196.25	24.53	248.80	220.79	1.24	1.05	128.86	109.12	237.97	7.22	241.17	-1.34

c = 5 %, $m_{h,in}$ = 24 g/s, $T_{h,in}$ = 50 °C ,$T_{f,in}$ = 22 °C

No.	m_{ch}	ΔT_m	ΔT_{ch}	$Q_{\Delta T,m}$	$Q_{\Delta T,ch}$	$Q_{l,tot}$	$Q_{\Delta T+l,mix}$	$Q_{s,ch}$	$\Delta T_{j,up}$	$\Delta T_{j,low}$	$Q_{\Delta T,j,up}$	$Q_{\Delta T,j,low}$	$Q_{\Delta T,j,tot}$	$Q_{\Delta T,j,tot}/Q_{s,ch,tot}$	$Q_{inv,ch}$	$Q_{\Delta T,j,tot}/Q_{inv,ch}$
	g/s	°C	°C	W	W	W	W	W	°C	°C	W	W	W	%	W	%
	Flow inside microchannels								Flow inside jackets							
s5-13	11.57	8.51	8.72	468.84	479.70	29.68	498.51	509.38	2.46	2.30	255.42	238.45	493.87	-3.14	414.24	16.12
s5-14	9.92	9.35	9.70	436.50	451.71	29.43	465.94	481.15	2.32	2.14	241.06	221.85	462.91	-3.94	414.24	10.52
s5-15	8.26	10.58	10.85	406.80	416.06	29.47	436.27	445.53	2.20	2.00	228.21	207.79	436.00	-2.19	414.24	4.99
s5-16	6.61	11.95	12.13	363.80	368.02	29.47	393.27	397.49	2.06	1.86	213.54	193.26	406.80	2.29	414.24	-1.83
s5-17	4.96	13.91	13.52	314.57	304.84	29.28	343.86	334.12	1.92	1.70	199.93	176.13	376.05	11.15	414.24	-10.15
s5-18	3.30	16.99	14.99	254.12	223.38	29.45	283.57	252.83	1.71	1.45	177.44	150.89	328.32	22.99	414.24	-26.17

Table C.4 Data of 10% mass concentration of mPCM DS5037X slurry

c = 10 %, $m_{h,in}$ = 24 g/s, $T_{h,in}$ = 40 °C ,$T_{f,in}$ = 22 °C

No.	m_{ch} g/s	ΔT_m °C	ΔT_{ch} °C	$Q_{\Delta T,m}$ W	$Q_{\Delta T,ch}$ W	$Q_{l,tot}$ W	$Q_{\Delta T+l,mix}$ W	$Q_{s,ch}$ W	$\Delta T_{j,up}$ °C	$\Delta T_{j,low}$ °C	$Q_{\Delta T,j,up}$ W	$Q_{\Delta T,j,low}$ W	$Q_{\Delta T,j,tot}$ W	$Q_{\Delta T,j,tot}/Q_{s,ch,tot}$ %	$Q_{inv,ch}$ W	$Q_{\Delta T,j,tot}/Q_{inv,ch}$ %
	Flow inside microchannels								Flow inside jackets							
s10-19	11.58	5.20	5.04	346.97	336.53	16.63	363.60	353.16	1.47	1.49	152.28	154.35	306.62	-15.18	351.43	-14.61
s10-20	9.93	5.83	5.53	324.84	308.67	16.84	341.68	325.51	1.38	1.39	143.50	144.53	288.03	-13.01	323.75	-12.40
s10-21	8.27	6.58	6.20	297.40	280.45	16.73	314.13	297.18	1.30	1.31	134.81	135.70	270.51	-9.86	301.40	-11.42
s10-22	6.62	7.49	6.89	264.31	243.54	16.67	280.98	260.21	1.20	1.21	124.74	125.73	250.47	-3.89	274.74	-9.69
s10-23	4.96	8.92	7.87	229.60	202.81	16.72	246.32	219.52	1.08	1.08	112.67	112.02	224.68	2.30	240.21	-6.91
s10-24	3.31	11.29	8.42	191.13	142.84	16.64	207.77	159.49	0.92	0.90	95.82	93.49	189.32	15.76	190.82	-0.79

c = 10 %, $m_{h,in}$ = 24 g/s, $T_{h,in}$ = 45 °C ,$T_{f,in}$ = 22 °C

No.	m_{ch} g/s	ΔT_m °C	ΔT_{ch} °C	$Q_{\Delta T,m}$ W	$Q_{\Delta T,ch}$ W	$Q_{l,tot}$ W	$Q_{\Delta T+l,mix}$ W	$Q_{s,ch}$ W	$\Delta T_{j,up}$ °C	$\Delta T_{j,low}$ °C	$Q_{\Delta T,j,up}$ W	$Q_{\Delta T,j,low}$ W	$Q_{\Delta T,j,tot}$ W	$Q_{\Delta T,j,tot}/Q_{s,ch,tot}$ %	$Q_{inv,ch}$ W	$Q_{\Delta T,j,tot}/Q_{inv,ch}$ %
	Flow inside microchannels								Flow inside jackets							
s10-25	11.58	6.15	6.78	382.25	420.94	23.55	405.80	444.49	1.89	1.89	196.14	196.80	392.94	-13.12	419.03	-6.64
s10-27	8.27	8.02	8.53	339.94	360.89	22.62	362.56	383.52	1.62	1.61	168.40	167.04	335.44	-14.33	358.24	-6.80
s10-28	6.61	9.30	9.81	308.01	324.11	22.43	330.45	346.55	1.52	1.51	157.69	157.36	315.05	-10.00	328.95	-4.41
s10-29	4.96	11.77	11.37	285.62	275.29	22.47	308.09	297.76	1.38	1.36	142.98	140.97	283.95	-4.86	283.67	0.10
s10-30	3.30	13.79	12.74	219.71	202.39	22.55	242.26	224.94	1.26	1.22	130.47	126.61	257.08	12.50	250.61	2.52

c = 10 %, $m_{h,in}$ = 24 g/s, $T_{h,in}$ = 50 °C ,$T_{f,in}$ = 22 °C

No.	m_{ch}	ΔT_m	ΔT_{ch}	$Q_{\Delta T,m}$	$Q_{\Delta T,ch}$	$Q_{l,tot}$	$Q_{\Delta T+l,mix}$	$Q_{s,ch}$	$\Delta T_{j,up}$	$\Delta T_{j,low}$	$Q_{\Delta T,j,up}$	$Q_{\Delta T,j,low}$	$Q_{\Delta T,j,tot}$	$Q_{\Delta T,j,tot}/Q_{s,ch,tot}$	$Q_{inv,ch}$	$Q_{\Delta T,j,tot}/Q_{inv,ch}$
	g/s	°C	°C	W	W	W	W	W	°C	°C	W	W	W	%	W	%
	Flow inside microchannels								Flow inside jackets							
s10-31	11.57	7.83	8.22	467.68	490.52	27.01	494.69	517.53	2.17	2.21	225.63	229.49	455.12	-13.71	504.64	-10.88
s10-32	9.92	8.73	9.14	438.88	458.33	26.94	465.82	485.27	2.07	2.08	214.87	215.70	430.58	-12.70	474.59	-10.22
s10-33	8.26	9.71	10.22	399.30	419.07	27.12	426.42	446.19	1.98	2.00	205.70	207.85	413.55	-7.89	449.51	-8.69
s10-34	6.61	12.15	12.70	387.32	403.78	27.52	414.84	431.30	1.85	1.86	192.06	193.30	385.36	-11.92	402.61	-4.48
s10-35	4.96	14.15	14.21	333.65	333.87	27.47	361.12	361.34	1.73	1.71	179.63	177.97	357.60	-1.05	358.53	-0.26
s10-36	3.30	17.29	15.68	268.63	242.81	27.49	296.12	270.31	1.58	1.53	164.39	158.66	323.05	16.33	303.81	5.96

Table C.5 Data of pure water (conditions for comparison with MPCM-37 slurry)

c = 0 %, $m_{h,in}$ = 24 g/s, $T_{h,in}$ = 50 °C ,$T_{f,in}$ = 30 °C

No.	m_{ch}	ΔT_m	ΔT_{ch}	$Q_{\Delta T,m}$	$Q_{\Delta T,ch}$	$Q_{\Delta T+l,ch}$	$\Delta T_{j,up}$	$\Delta T_{j,low}$	$Q_{\Delta T,j,up}$	$Q_{\Delta T,j,low}$	$Q_{\Delta T,j,tot}$	$Q_{\Delta T,j,tot}/Q_{\Delta T,ch,tot}$
	g/s	°C	°C	W	W	W	°C	°C	W	W	W	%
	Flow inside microchannels						Flow inside jackets					
w-1a	10.72	6.71	6.14	300.88	275.11	305.28	1.43	1.63	148.61	169.71	318.32	4.10
w-2a	9.90	6.77	6.40	279.83	264.51	294.89	1.35	1.54	140.06	159.72	299.78	1.63
w-3a	9.07	6.70	6.53	253.99	247.63	278.13	1.28	1.45	132.80	150.74	283.54	1.91
w-4a	8.24	6.83	6.76	235.28	232.81	262.81	1.23	1.39	127.82	144.33	272.15	3.43
w-5a	7.42	7.43	7.01	230.33	217.56	247.78	1.16	1.31	120.06	136.31	256.37	3.35
w-6a	6.60	7.81	7.16	215.41	197.28	227.61	1.12	1.28	116.70	132.48	249.18	8.66
w-7a	5.77	8.59	7.38	207.11	178.09	208.35	1.06	1.19	109.82	124.00	233.82	10.89
w-8a	4.95	9.32	7.59	192.63	156.91	187.22	1.00	1.14	104.03	118.37	222.40	15.82

c = 0 %, $m_{h,in}$ = 24 g/s, $T_{h,in}$ = 55 °C ,$T_{f,in}$ = 30 °C

No.	m_{ch}	ΔT_m	ΔT_{ch}	$Q_{\Delta T,m}$	$Q_{\Delta T,ch}$	$Q_{\Delta T+l,ch}$	$\Delta T_{j,up}$	$\Delta T_{j,low}$	$Q_{\Delta T,j,up}$	$Q_{\Delta T,j,low}$	$Q_{\Delta T,j,tot}$	$Q_{\Delta T,j,tot}/Q_{\Delta T,ch,tot}$
	g/s	°C	°C	W	W	W	°C	°C	W	W	W	%
	Flow inside microchannels						Flow inside jackets					
w-9a	11.54	8.81	7.88	424.87	380.32	418.16	1.97	2.21	204.93	229.58	434.51	3.76
w-10a	10.72	9.01	8.14	403.79	364.52	402.31	1.89	2.11	196.22	219.63	415.85	3.26
w-11a	9.89	8.96	8.33	370.52	344.44	381.76	1.77	1.98	183.56	205.95	389.51	1.99
w-12a	9.07	9.35	8.70	354.34	329.92	367.04	1.71	1.91	177.96	198.36	376.31	2.47
w-13a	8.24	9.37	8.67	322.80	298.83	335.94	1.60	1.78	166.36	184.52	350.89	4.26
w-14a	7.42	10.05	9.07	311.45	281.34	318.31	1.52	1.68	157.57	174.56	332.13	4.16
w-15a	6.59	10.49	9.44	289.18	260.02	296.94	1.44	1.59	149.44	165.23	314.68	5.64
w-16a	5.77	11.42	9.89	275.43	238.50	274.78	1.38	1.53	143.70	159.06	302.76	9.24
w-17a	4.94	12.19	9.99	251.89	206.50	242.91	1.28	1.46	133.30	151.38	284.68	14.67

c = 0 %, $m_{h,in}$ = 17 g/s, $T_{h,in}$ = 50 °C ,$T_{f,in}$ = 30 °C

No.	m_{ch}	ΔT_m	ΔT_{ch}	$Q_{\Delta T,m}$	$Q_{\Delta T,ch}$	$Q_{\Delta T+l,ch}$	$\Delta T_{j,up}$	$\Delta T_{j,low}$	$Q_{\Delta T,j,up}$	$Q_{\Delta T,j,low}$	$Q_{\Delta T,j,tot}$	$Q_{\Delta T,j,tot}/Q_{\Delta T,ch,tot}$
	g/s	°C	°C	W	W	W	°C	°C	W	W	W	%
	Flow inside microchannels						Flow inside jackets					
w-18a	10.72	5.70	5.52	255.52	247.38	266.88	1.90	2.07	131.26	143.01	274.27	2.69
w-19a	9.90	5.92	5.75	244.95	237.66	256.88	1.78	1.94	123.20	134.57	257.77	0.35
w-20a	9.07	6.23	5.99	236.20	227.11	246.16	1.67	1.82	115.60	125.77	241.37	1.98
w-21a	8.25	6.42	6.22	221.40	214.55	233.62	1.62	1.76	112.21	121.83	234.04	0.18
w-22a	7.42	6.89	6.48	213.77	200.85	219.86	1.56	1.68	107.85	116.50	224.35	2.00
w-23a	6.60	7.33	6.72	202.03	185.15	204.01	1.51	1.65	104.39	114.23	218.63	6.69
w-24a	5.77	7.78	6.87	187.60	165.61	184.40	1.43	1.56	99.25	108.10	207.35	11.07
w-25a	4.95	8.35	7.17	172.56	148.20	166.78	1.37	1.48	94.85	102.72	197.57	15.59

c = 0 %, $m_{h,in}$ = 17 g/s, $T_{h,in}$ = 55 °C ,$T_{f,in}$ = 30 °C

No.	m_{ch}	ΔT_m	ΔT_{ch}	$Q_{\Delta T,m}$	$Q_{\Delta T,ch}$	$Q_{\Delta T+l,ch}$	$\Delta T_{j,up}$	$\Delta T_{j,low}$	$Q_{\Delta T,j,up}$	$Q_{\Delta T,j,low}$	$Q_{\Delta T,j,tot}$	$Q_{\Delta T,j,tot}/Q_{\Delta T,ch,tot}$
	g/s	°C	°C	W	W	W	°C	°C	W	W	W	%
	Flow inside microchannels						Flow inside jackets					
w-26a	10.72	7.62	7.29	341.63	326.43	340.15	2.41	2.63	166.90	182.00	348.91	2.51
w-27a	9.89	7.84	7.40	324.37	306.05	319.87	2.29	2.49	158.87	172.31	331.18	3.41
w-28a	9.07	8.10	7.62	307.11	288.99	302.69	2.16	2.34	149.43	161.75	311.18	2.73
w-29a	8.24	8.40	7.88	289.31	271.60	285.32	2.09	2.26	144.79	156.45	301.24	5.28
w-30a	7.42	8.88	8.28	275.40	256.76	270.44	2.00	2.17	138.44	150.22	288.66	6.31
w-31a	6.59	9.24	8.58	254.65	236.37	250.08	1.94	2.11	134.43	145.93	280.36	10.80
w-32a	5.77	10.04	8.90	242.20	214.52	228.21	1.86	2.04	128.59	141.16	269.75	15.40
w-33a	4.94	11.05	9.31	228.31	192.36	206.04	1.76	1.93	121.94	133.60	255.54	19.37

c = 0 %, $m_{h,in}$ = 17 g/s, $T_{h,in}$ = 50 °C ,$T_{f,in}$ = 32 °C

No.	m_{ch}	ΔT_m	ΔT_{ch}	$Q_{\Delta T,m}$	$Q_{\Delta T,ch}$	$Q_{\Delta T+l,ch}$	$\Delta T_{j,up}$	$\Delta T_{j,low}$	$Q_{\Delta T,j,up}$	$Q_{\Delta T,j,low}$	$Q_{\Delta T,j,tot}$	$Q_{\Delta T,j,tot}/Q_{\Delta T,ch,tot}$
	g/s	°C	°C	W	W	W	°C	°C	W	W	W	%
	Flow inside microchannels						Flow inside jackets					
w-34a	10.72	5.30	4.99	237.33	223.66	246.73	1.73	1.92	120.04	132.65	252.68	2.35
w-35a	9.89	5.33	5.21	220.57	215.51	238.39	1.62	1.79	112.22	124.09	236.31	0.88
w-36a	9.07	5.44	5.50	206.35	208.61	231.40	1.54	1.70	106.33	117.40	223.72	3.43
w-37a	8.24	5.66	5.72	195.08	196.95	219.76	1.47	1.62	101.61	112.34	213.95	2.72
w-38a	7.42	6.10	5.95	189.09	184.49	207.18	1.41	1.56	97.72	108.17	205.89	0.62
w-39a	6.59	6.48	6.08	178.60	167.53	190.07	1.37	1.50	94.79	104.19	198.97	4.48
w-40a	5.77	7.08	6.29	170.63	151.75	174.23	1.32	1.44	91.35	99.93	191.28	8.91
w-41a	4.94	7.62	6.55	157.38	135.34	158.10	1.26	1.40	87.50	97.01	184.51	14.32

c = 0 %, $m_{h,in}$ = 17 g/s, $T_{h,in}$ = 55 °C ,$T_{f,in}$ = 32 °C

No.	m_{ch}	ΔT_m	ΔT_{ch}	$Q_{\Delta T,m}$	$Q_{\Delta T,ch}$	$Q_{\Delta T+l,ch}$	$\Delta T_{j,up}$	$\Delta T_{j,low}$	$Q_{\Delta T,j,up}$	$Q_{\Delta T,j,low}$	$Q_{\Delta T,j,tot}$	$Q_{\Delta T,j,tot}/Q_{\Delta T,ch,tot}$
	g/s	°C	°C	W	W	W	°C	°C	W	W	W	%
	Flow inside microchannels						Flow inside jackets					
w-42a	10.71	7.01	6.52	313.72	291.82	318.62	2.22	2.45	153.86	169.58	323.44	1.49
w-43a	9.89	7.08	6.78	292.50	280.32	306.88	2.12	2.33	147.10	161.06	308.16	0.41
w-44a	9.06	7.27	7.11	275.30	269.18	295.83	2.02	2.23	139.82	154.40	294.22	0.55
w-45a	8.24	7.58	7.39	261.01	254.50	281.28	1.90	2.09	131.75	144.76	276.51	1.73
w-46a	7.41	8.13	7.81	251.95	242.13	268.86	1.85	2.04	128.19	141.28	269.46	0.22
w-47a	6.59	8.61	8.03	237.23	221.08	247.56	1.80	1.99	124.57	137.55	262.12	5.55
w-48a	5.77	9.50	8.40	229.03	202.52	229.19	1.72	1.90	119.41	131.56	250.97	8.68
w-49a	4.94	10.31	8.74	213.05	180.45	207.31	1.64	1.82	113.57	126.06	239.63	13.49

c = 0 %, $m_{h,in}$ = 24 g/s, $T_{h,in}$ = 50 °C ,$T_{f,in}$ = 32 °C

No.	m_{ch} g/s	ΔT_m °C	ΔT_{ch} °C	$Q_{\Delta T,m}$ W	$Q_{\Delta T,ch}$ W	$Q_{\Delta T+l,ch}$ W	$\Delta T_{j,up}$ °C	$\Delta T_{j,low}$ °C	$Q_{\Delta T,j,up}$ W	$Q_{\Delta T,j,low}$ W	$Q_{\Delta T,j,tot}$ W	$Q_{\Delta T,j,tot}/Q_{\Delta T,ch,tot}$ %
	Flow inside microchannels						Flow inside jackets					
w-50a	10.72	6.21	5.53	277.94	247.80	270.16	1.31	1.46	135.62	152.11	287.73	6.11
w-51a	9.89	6.22	5.59	257.22	231.10	253.33	1.25	1.39	129.43	144.38	273.81	7.48
w-52a	9.07	6.40	5.83	242.54	220.99	242.43	1.14	1.27	118.52	132.07	250.59	3.25
w-53a	8.24	6.44	5.90	221.69	203.09	224.37	1.08	1.21	112.18	125.76	237.94	5.70
w-54a	7.42	6.85	6.05	212.37	187.41	208.58	1.03	1.16	107.05	120.74	227.80	8.44
w-55a	6.59	7.19	6.12	198.08	168.62	189.58	0.98	1.12	101.71	115.86	217.57	12.87
w-56a	5.77	7.69	6.29	185.51	151.70	172.51	0.94	1.06	97.18	110.35	207.53	16.87
w-57a	4.94	8.30	6.59	171.53	136.09	156.85	0.90	1.01	92.98	105.17	198.15	20.85

c = 0 %, $m_{h,in}$ = 24 g/s, $T_{h,in}$ = 55 °C ,$T_{f,in}$ = 32 °C

No.	m_{ch} g/s	ΔT_m °C	ΔT_{ch} °C	$Q_{\Delta T,m}$ W	$Q_{\Delta T,ch}$ W	$Q_{\Delta T+l,ch}$ W	$\Delta T_{j,up}$ °C	$\Delta T_{j,low}$ °C	$Q_{\Delta T,j,up}$ W	$Q_{\Delta T,j,low}$ W	$Q_{\Delta T,j,tot}$ W	$Q_{\Delta T,j,tot}/Q_{\Delta T,ch,tot}$ %
	Flow inside microchannels						Flow inside jackets					
w-58a	10.71	8.34	7.28	373.17	326.12	365.10	1.74	1.96	180.82	203.71	384.53	5.05
w-59a	9.89	8.38	7.47	346.43	308.55	347.54	1.64	1.85	169.91	191.97	361.88	3.96
w-60a	9.06	8.44	7.66	319.83	290.32	329.61	1.55	1.76	161.50	183.24	344.75	4.39
w-61a	8.24	8.73	7.75	300.67	266.80	306.18	1.45	1.63	150.17	169.26	319.43	4.15
w-62a	7.41	9.07	7.92	281.01	245.38	284.76	1.39	1.56	144.05	162.06	306.12	6.98
w-63a	6.59	9.57	8.06	263.50	222.13	261.69	1.32	1.49	136.61	155.10	291.72	10.29
w-64a	5.76	10.44	8.37	251.47	201.67	241.44	1.25	1.41	129.58	146.71	276.29	12.61
w-65a	4.94	11.24	8.67	232.11	179.02	218.86	1.19	1.36	123.61	141.05	264.66	17.30

Table C.6 Data of MPCM-37 slurry

c = 10 %, $m_{h,in}$ = 17 g/s, $T_{h,in}$ = 50 °C ,$T_{f,in}$ = 30 °C

	m_{ch}	ΔT_m	ΔT_{ch}	$Q_{\Delta T,m}$	$Q_{\Delta T,ch}$	$Q_{s,ch}$	$\Delta T_{j,up}$	$\Delta T_{j,low}$	$Q_{\Delta T,j,up}$	$Q_{\Delta T,j,low}$	$Q_{\Delta T,j,tot}$	$Q_{\Delta T,j,tot}/Q_{s,ch,tot}$
	g/s	°C	°C	W	W	W	°C	°C	W	W	W	%
	Flow inside microchannels						Flow inside jackets					
s10-1a	9.90	3.66	5.11	277.78	387.74	418.70	1.62	1.79	112.12	124.02	236.14	-77.31
s10-2a	9.07	3.91	5.32	267.24	363.13	393.78	1.58	1.75	109.61	121.53	231.14	-70.36
s10-3a	8.25	4.48	5.53	273.23	337.25	367.80	1.54	1.71	106.48	118.13	224.61	-63.75
s10-4a	7.42	5.25	5.90	280.55	315.14	345.52	1.48	1.65	102.82	114.11	216.93	-59.28
s10-5a	6.60	5.97	6.26	276.67	290.02	320.06	1.43	1.58	98.76	109.74	208.50	-53.50
s10-6a	5.77	7.08	6.83	277.39	267.42	297.21	1.36	1.51	94.17	104.45	198.62	-49.64
s10-7a	4.95	7.98	7.21	262.47	237.06	266.75	1.30	1.46	90.27	100.81	191.08	-39.60
s10-8a	4.12	9.68	7.84	257.34	208.36	237.86	1.20	1.34	82.93	92.59	175.52	-35.52
s10-9a	3.30	11.37	8.44	235.74	174.95	204.36	1.06	1.24	73.42	85.79	159.22	-28.35

c = 10 %, $m_{h,in}$ = 24 g/s, $T_{h,in}$ = 50 °C ,$T_{f,in}$ = 30 °C

	m_{ch}	ΔT_m	ΔT_{ch}	$Q_{\Delta T,m}$	$Q_{\Delta T,ch}$	$Q_{s,ch}$	$\Delta T_{j,up}$	$\Delta T_{j,low}$	$Q_{\Delta T,j,up}$	$Q_{\Delta T,j,low}$	$Q_{\Delta T,j,tot}$	$Q_{\Delta T,j,tot}/Q_{sch,tot}$
	g/s	°C	°C	W	W	W	°C	°C	W	W	W	%
	Flow inside microchannels						Flow inside jackets					
s10-10a	9.89	4.62	5.59	336.44	407.20	439.13	1.21	1.38	125.49	142.85	268.34	-63.65
s10-11a	9.07	5.02	5.75	331.58	379.32	411.28	1.20	1.35	124.24	140.22	264.46	-55.52
s10-12a	8.24	5.82	6.05	341.52	355.24	387.19	1.14	1.29	118.43	134.38	252.81	-53.16
s10-13a	7.42	6.55	6.35	339.43	329.16	360.92	1.09	1.24	113.48	128.71	242.19	-49.02
s10-14a	6.59	7.10	6.52	323.36	297.12	328.93	1.06	1.21	110.35	125.65	235.99	-39.38
s10-15a	5.77	8.03	6.93	312.72	269.88	301.54	1.00	1.14	104.01	118.72	222.73	-35.39
s10-16a	4.95	8.43	7.07	279.22	234.20	265.97	0.98	1.12	101.37	116.08	217.45	-22.31
s10-17a	4.12	10.42	8.11	273.54	213.08	244.99	0.85	0.98	88.70	101.34	190.04	-28.92
s10-18a	3.30	12.60	8.60	259.48	177.10	208.76	0.77	0.89	79.57	92.44	172.00	-21.37

c = 10 %, $m_{h,in}$ = 24 g/s, $T_{h,in}$ = 55 °C ,$T_{f,in}$ = 30 °C

	m_{ch}	ΔT_m	ΔT_{ch}	$Q_{\Delta T,m}$	$Q_{\Delta T,ch}$	$Q_{s,ch}$	$\Delta T_{j,up}$	$\Delta T_{j,low}$	$Q_{\Delta T,j,up}$	$Q_{\Delta T,j,low}$	$Q_{\Delta T,j,tot}$	$Q_{\Delta T,j,tot}/Q_{s,ch,tot}$
	g/s	°C	°C	W	W	W	°C	°C	W	W	W	%
	Flow inside microchannels						Flow inside jackets					
s10-19a	10.72	5.68	6.70	418.47	490.83	523.00	1.52	1.88	157.96	195.38	353.34	-48.02
s10-20a	9.89	6.28	7.06	418.38	468.18	500.53	1.47	1.81	152.99	188.42	341.40	-46.61
s10-21a	9.07	6.80	7.24	411.52	435.83	468.57	1.44	1.77	149.69	184.37	334.06	-40.27
s10-22a	8.24	7.45	7.84	397.87	416.76	449.52	1.40	1.72	145.84	179.10	324.94	-38.34
s10-23a	7.42	8.31	8.33	391.59	390.25	423.09	1.34	1.65	139.66	171.58	311.24	-35.94
s10-24a	6.59	9.01	8.91	368.76	362.88	395.32	1.31	1.62	135.74	167.76	303.50	-30.26
s10-25a	5.77	10.10	9.37	355.86	328.58	361.24	1.24	1.52	128.50	157.81	286.31	-26.17
s10-26a	4.94	11.19	10.53	326.33	305.56	338.04	1.16	1.44	120.44	149.14	269.58	-25.40

Appendix D

D.1 Temperature profiles for Run No. w-1 to Run No. w-6

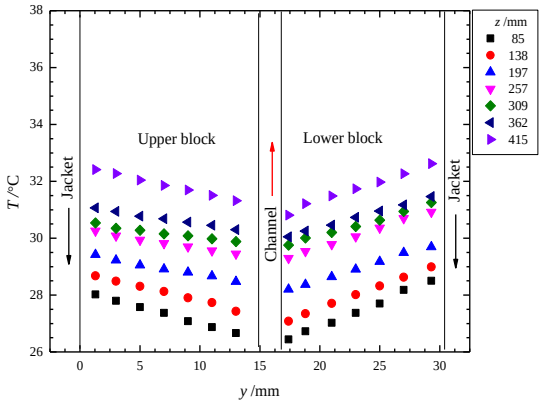

Figure D.1 Temperature distributions inside the block. c = 0 %, $T_{h,in}$ = 40 °C, $T_{f,in}$ = 22 °C, $m_{h,in}$ = 24 g/s, $m_{f,in}$ = 11.5 g/s

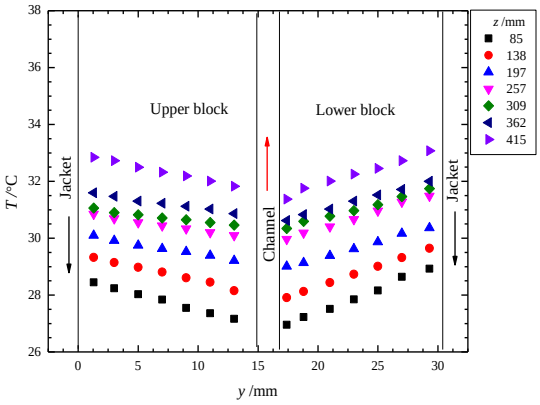

Figure D.2 Temperature distributions inside the block. c = 0 %, $T_{h,in}$ = 40 °C, $T_{f,in}$ = 22 °C, $m_{h,in}$ = 24 g/s, $m_{f,in}$ = 9.9 g/s

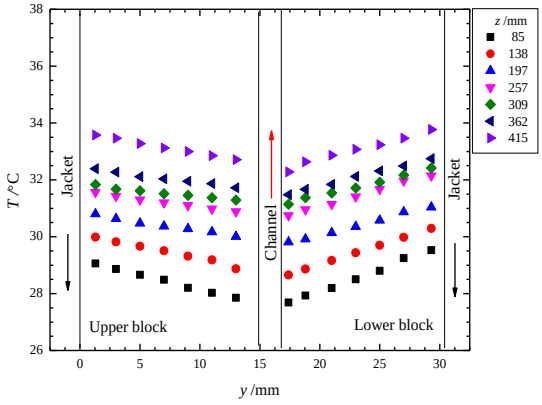

Figure D.3 Temperature distributions inside the block. c = 0 %, $T_{h,in}$ = 40 °C, $T_{f,in}$ = 22 °C, $m_{h,in}$ = 24 g/s, $m_{f,in}$ = 8.2 g/s

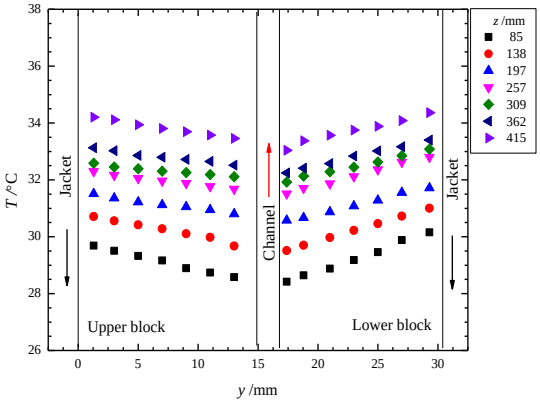

Figure D.4 Temperature distributions inside the block. c = 0 %, $T_{h,in}$ = 40 °C, $T_{f,in}$ = 22 °C, $m_{h,in}$ = 24 g/s, $m_{f,in}$ = 6.6 g/s

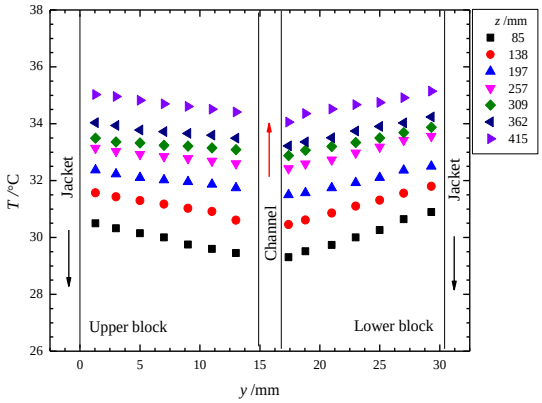

Figure D.5 Temperature distributions inside the block. c = 0 %, $T_{h,in}$ = 40 °C, $T_{f,in}$ = 22 °C, $m_{h,in}$ = 24 g/s, $m_{f,in}$ = 4.9 g/s

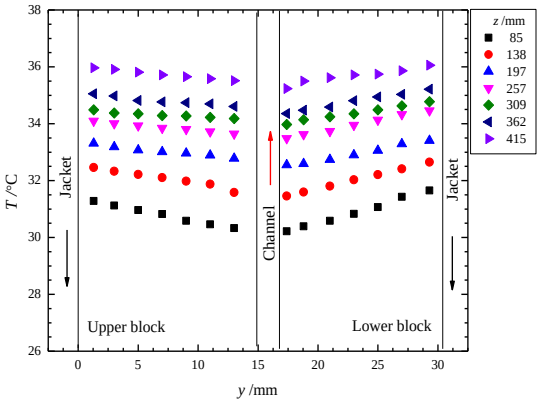

Figure D.6 Temperature distributions inside the block. c = 0 %, $T_{h,in}$ = 40 °C, $T_{f,in}$ = 22 °C, $m_{h,in}$ = 24 g/s, $m_{f,in}$ = 3.3 g/s

D.2 Temperature profiles for Run No. w-7 to Run No. w-12

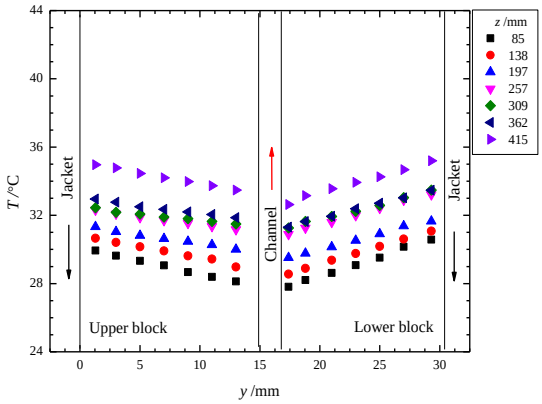

Figure D.7 Temperature distributions inside the block. c = 0 %, $T_{h,in}$ = 45 °C, $T_{f,in}$ = 22 °C, $m_{h,in}$ = 24 g/s, $m_{f,in}$ = 11.5 g/s

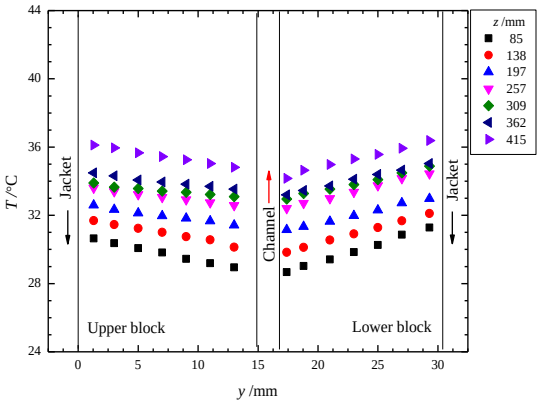

Figure D.8 Temperature distributions inside the block. c = 0 %, $T_{h,in}$ = 45 °C, $T_{f,in}$ = 22 °C, $m_{h,in}$ = 24 g/s, $m_{f,in}$ = 9.9 g/s

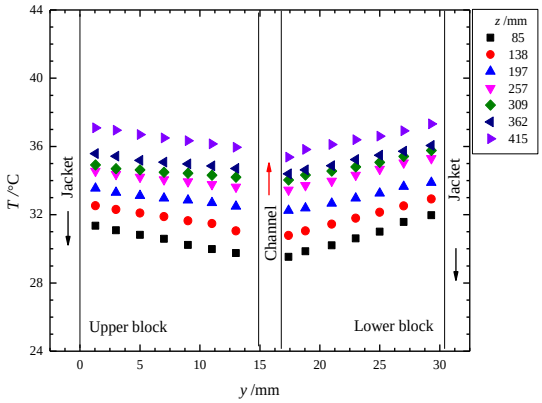

Figure D.9 Temperature distributions inside the block. c = 0 %, $T_{h,in}$ = 45 °C, $T_{f,in}$ = 22 °C, $m_{h,in}$ = 24 g/s, $m_{f,in}$ = 8.2 g/s

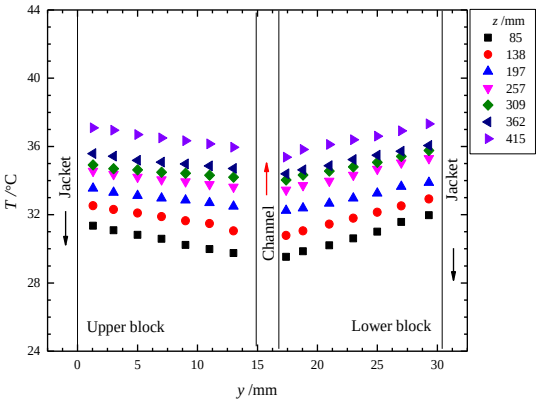

Figure D.10 Temperature distributions inside the block. c = 0 %, $T_{h,in}$ = 45 °C, $T_{f,in}$ = 22 °C, $m_{h,in}$ = 24 g/s, $m_{f,in}$ = 6.6 g/s

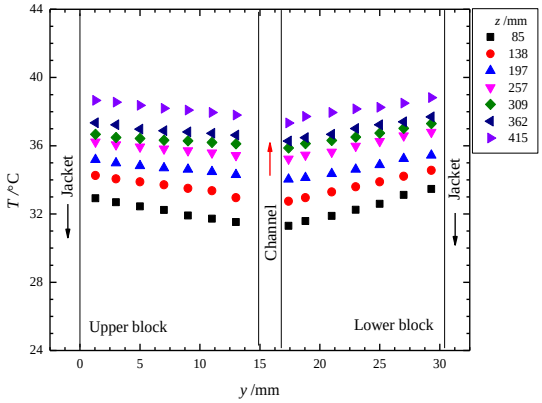

Figure D.11 Temperature distributions inside the block. c = 0 %, $T_{h,in}$ = 45 °C, $T_{f,in}$ = 22 °C, $m_{h,in}$ = 24 g/s, $m_{f,in}$ = 4.9 g/s

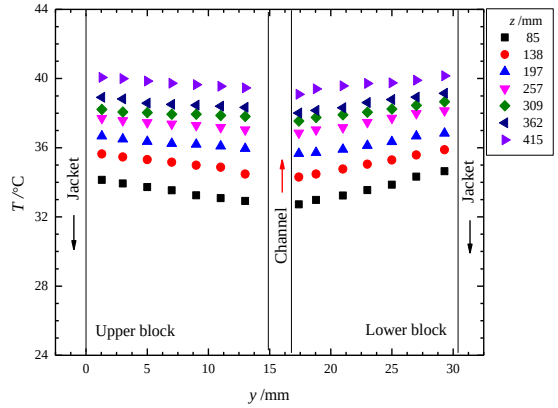

Figure D.12 Temperature distributions inside the block. c = 0 %, $T_{h,in}$ = 45 °C, $T_{f,in}$ = 22 °C, $m_{h,in}$ = 24 g/s, $m_{f,in}$ = 3.3 g/s

D.4 Temperature profiles for Run No. w-13 to Run No. w-18

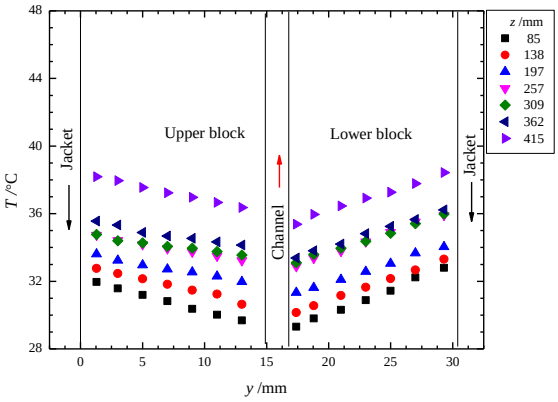

Figure D.13 Temperature distributions inside the block. c = 0 %, $T_{h,in}$ = 50 °C, $T_{f,in}$ = 22 °C, $m_{h,in}$ = 24 g/s, $m_{f,in}$ = 11.5 g/s

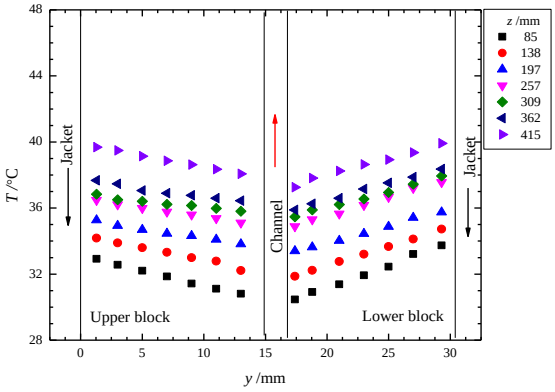

Figure D.14 Temperature distributions inside the block. c = 0 %, $T_{h,in}$ = 50 °C, $T_{f,in}$ = 22 °C, $m_{h,in}$ = 24 g/s, $m_{f,in}$ = 9.9 g/s

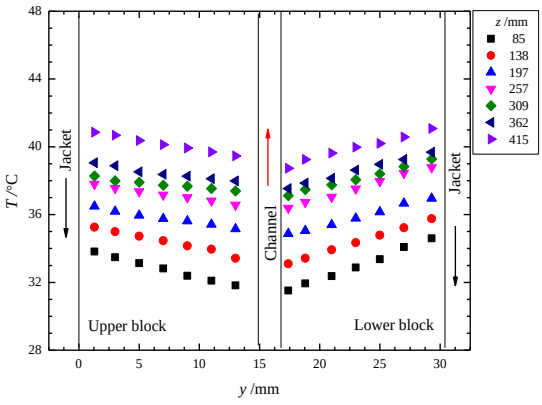

Figure D.15 Temperature distributions inside the block. c = 0 %, $T_{h,in}$ = 50 °C, $T_{f,in}$ = 22 °C, $m_{h,in}$ = 24 g/s, $m_{f,in}$ = 8.2 g/s

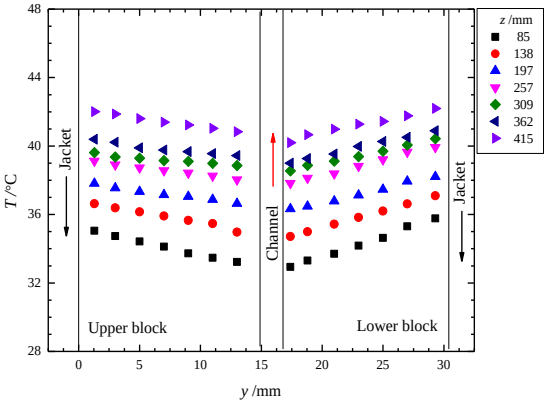

Figure D.16 Temperature distributions inside the block. c = 0 %, $T_{h,in}$ = 50 °C, $T_{f,in}$ = 22 °C, $m_{h,in}$ = 24 g/s, $m_{f,in}$ = 6.6 g/s

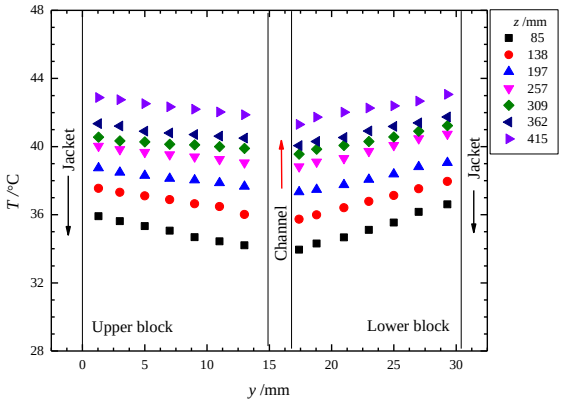

Figure D.17 Temperature distributions inside the block. c = 0 %, $T_{h,in}$ = 50 °C, $T_{f,in}$ = 22 °C, $m_{h,in}$ = 24 g/s, $m_{f,in}$ = 4.9 g/s

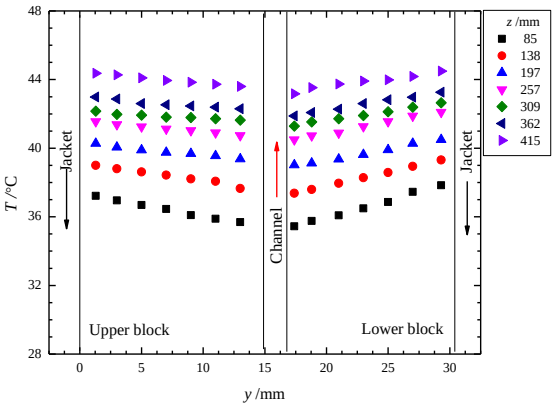

Figure D.18 Temperature distributions inside the block. c = 0 %, $T_{h,in}$ = 50 °C, $T_{f,in}$ = 22 °C, $m_{h,in}$ = 24 g/s, $m_{f,in}$ = 3.3 g/s

D.5 Temperature profiles for Run No. s5-1 to Run No. s5-6

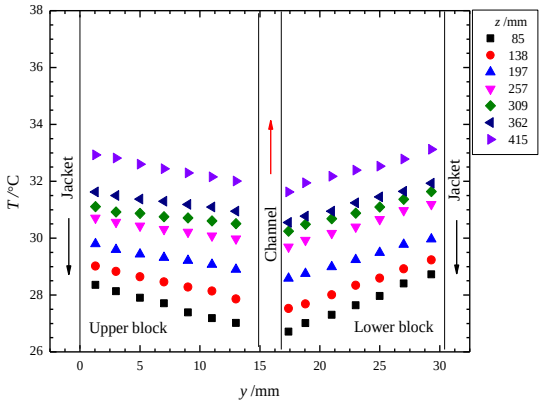

Figure D.19 Temperature distributions inside the block. c = 5 %, $T_{h,in}$ = 40 °C, $T_{f,in}$ = 22 °C, $m_{h,in}$ = 24 g/s, $m_{f,in}$ = 11.5 g/s

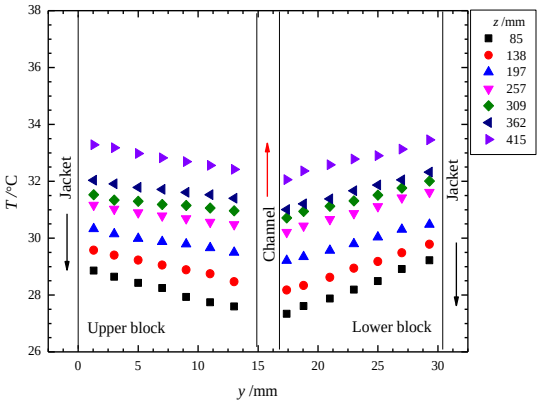

Figure D.20 Temperature distributions inside the block. c = 5 %, $T_{h,in}$ = 40 °C, $T_{f,in}$ = 22 °C, $m_{h,in}$ = 24 g/s, $m_{f,in}$ = 9.9 g/s

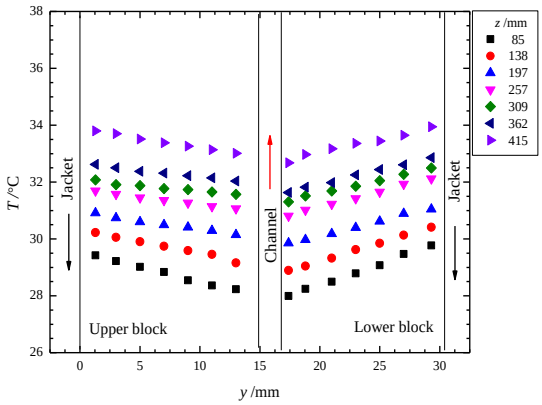

Figure D.21 Temperature distributions inside the block. c = 5 %, $T_{h,in}$ = 40 °C, $T_{f,in}$ = 22 °C, $m_{h,in}$ = 24 g/s, $m_{f,in}$ = 8.2 g/s

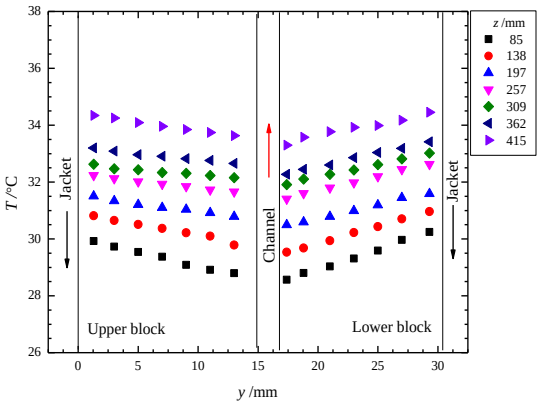

Figure D.22 Temperature distributions inside the block. c = 5 %, $T_{h,in}$ = 40 °C, $T_{f,in}$ = 22 °C, $m_{h,in}$ = 24 g/s, $m_{f,in}$ = 6.6 g/s

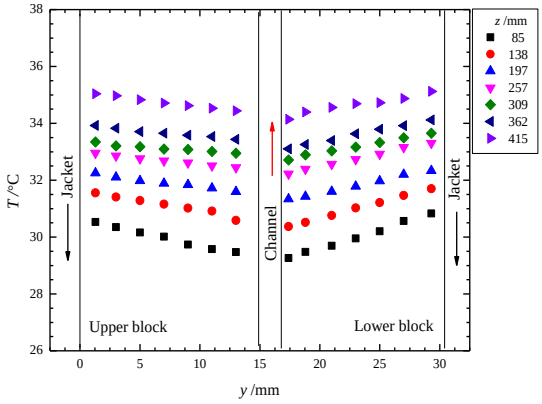

Figure D.23 Temperature distributions inside the block. c = 5 %, $T_{h,in}$ = 40 °C, $T_{f,in}$ = 22 °C, $m_{h,in}$ = 24 g/s, $m_{f,in}$ = 4.9 g/s

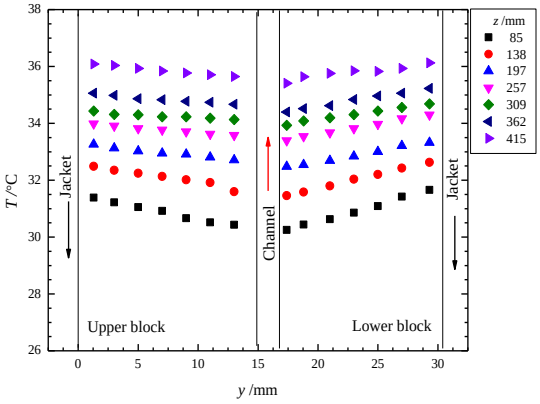

Figure D.24 Temperature distributions inside the block. c = 5 %, $T_{h,in}$ = 40 °C, $T_{f,in}$ = 22 °C, $m_{h,in}$ = 24 g/s, $m_{f,in}$ = 3.3 g/s

D.6 Temperature profiles for Run No. s5-7 to Run No. s5-12

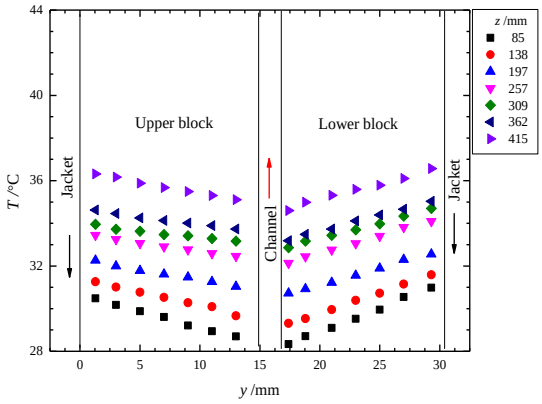

Figure D.25 Temperature distributions inside the block. c = 5 %, $T_{h,in}$ = 45 °C, $T_{f,in}$ = 22 °C, $m_{h,in}$ = 24 g/s, $m_{f,in}$ = 11.5 g/s

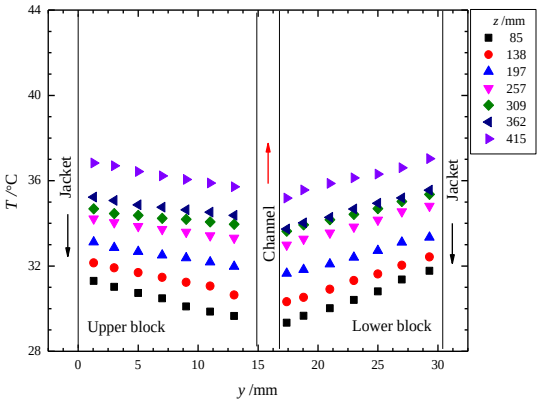

Figure D.26 Temperature distributions inside the block. c = 5 %, $T_{h,in}$ = 45 °C, $T_{f,in}$ = 22 °C, $m_{h,in}$ = 24 g/s, $m_{f,in}$ = 9.9 g/s

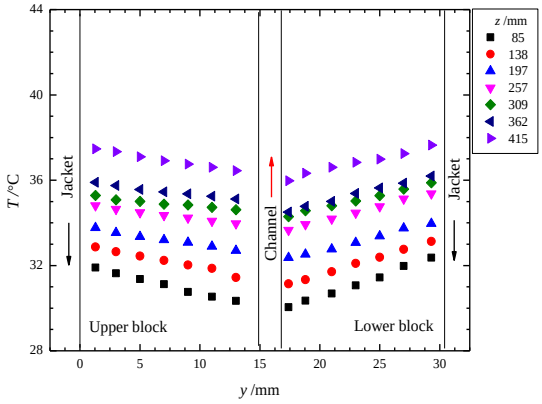

Figure D.27 Temperature distributions inside the block. c = 5 %, $T_{h,in}$ = 45 °C, $T_{f,in}$ = 22 °C, $m_{h,in}$ = 24 g/s, $m_{f,in}$ = 8.2 g/s

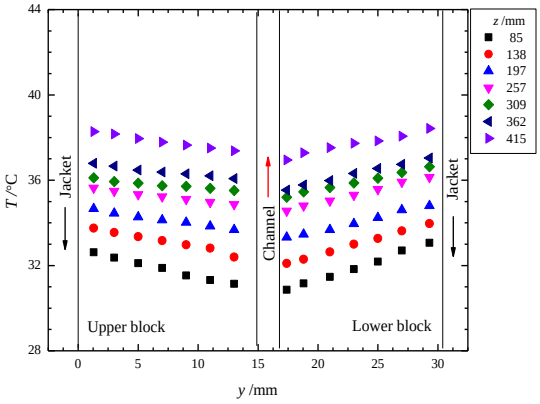

Figure D.28 Temperature distributions inside the block. c = 5 %, $T_{h,in}$ = 45 °C, $T_{f,in}$ = 22 °C, $m_{h,in}$ = 24 g/s, $m_{f,in}$ = 6.6 g/s

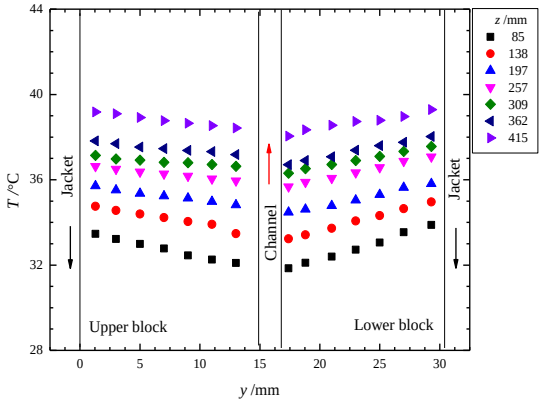

Figure D.29 Temperature distributions inside the block. c = 5 %, $T_{h,in}$ = 45 °C, $T_{f,in}$ = 22 °C, $m_{h,in}$ = 24 g/s, $m_{f,in}$ = 4.9 g/s

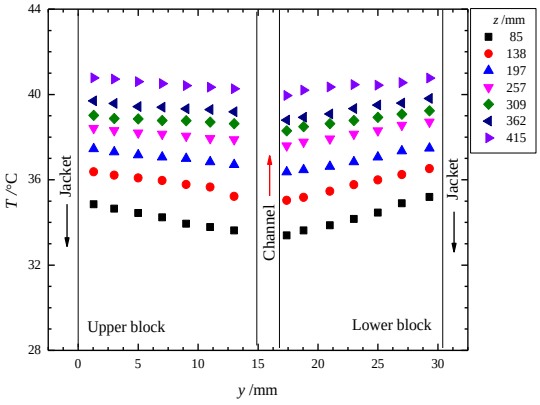

Figure D.30 Temperature distributions inside the block. c = 5 %, $T_{h,in}$ = 45 °C, $T_{f,in}$ = 22 °C, $m_{h,in}$ = 24 g/s, $m_{f,in}$ = 3.3 g/s

D.7 Temperature profiles for Run No. s5-13 to Run No. s5-18

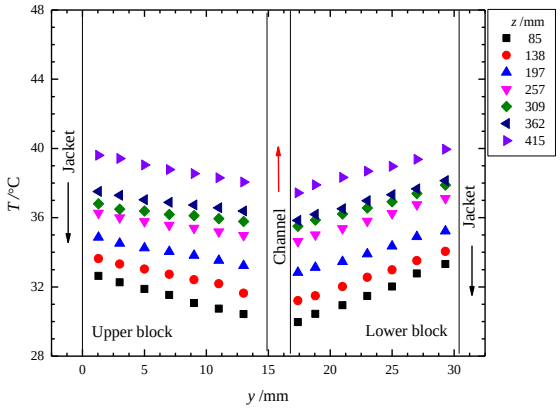

Figure D.31 Temperature distributions inside the block. c = 5 %, $T_{h,in}$ = 50 °C, $T_{f,in}$ = 22 °C, $m_{h,in}$ = 24 g/s, $m_{f,in}$ = 11.5 g/s

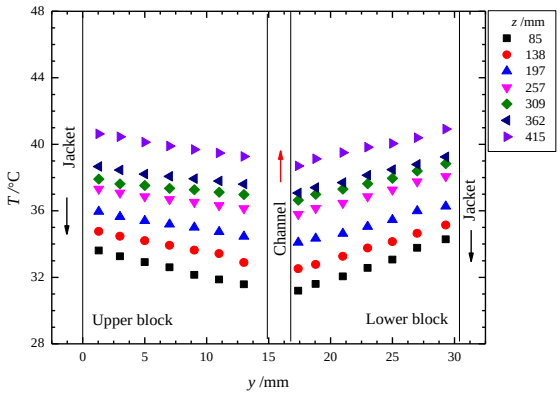

Figure D.32 Temperature distributions inside the block. c = 5 %, $T_{h,in}$ = 50 °C, $T_{f,in}$ = 22 °C, $m_{h,in}$ = 24 g/s, $m_{f,in}$ = 9.9 g/s

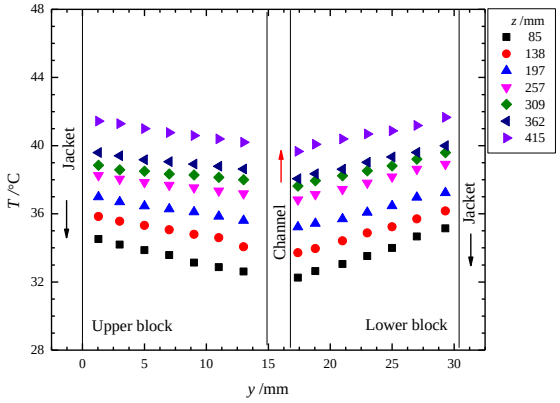

Figure D.33 Temperature distributions inside the block. c = 5 %, $T_{h,in}$ = 50 °C, $T_{f,in}$ = 22 °C, $m_{h,in}$ = 24 g/s, $m_{f,in}$ = 8.2 g/s

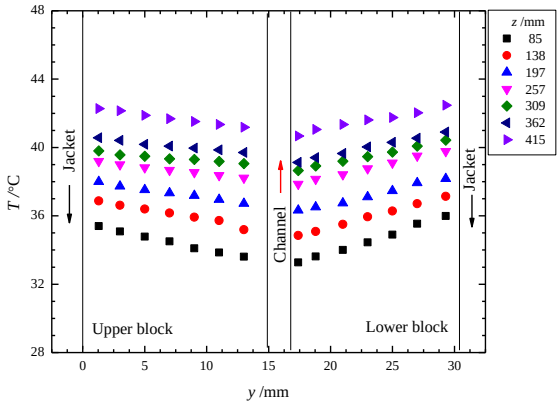

Figure D.34 Temperature distributions inside the block. c = 5 %, $T_{h,in}$ = 50 °C, $T_{f,in}$ = 22 °C, $m_{h,in}$ = 24 g/s, $m_{f,in}$ = 6.6 g/s

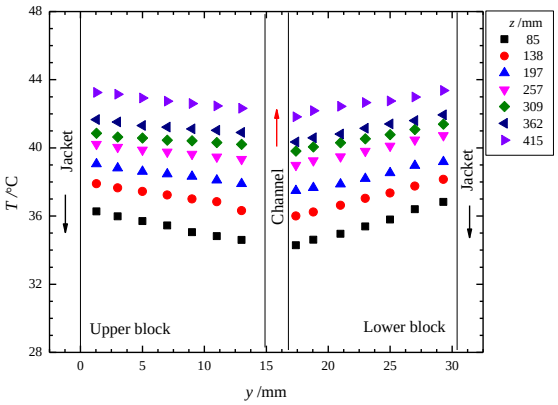

Figure D.35 Temperature distributions inside the block. c = 5 %, $T_{h,in}$ = 50 °C, $T_{f,in}$ = 22 °C, $m_{h,in}$ = 24 g/s, $m_{f,in}$ = 4.9 g/s

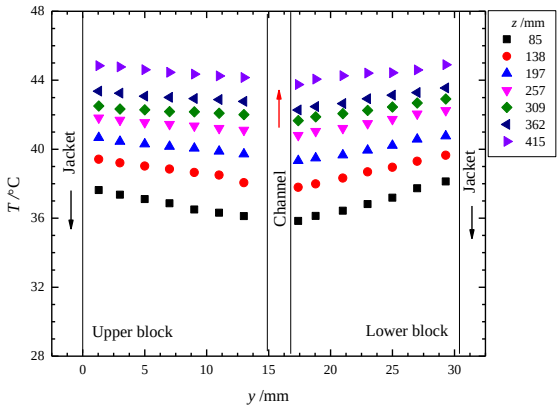

Figure D.36 Temperature distributions inside the block. c = 5 %, $T_{h,in}$ = 50 °C, $T_{f,in}$ = 22 °C, $m_{h,in}$ = 24 g/s, $m_{f,in}$ = 3.3 g/s

D.8 Temperature profiles for Run No. s10-19 to Run No. s10-24

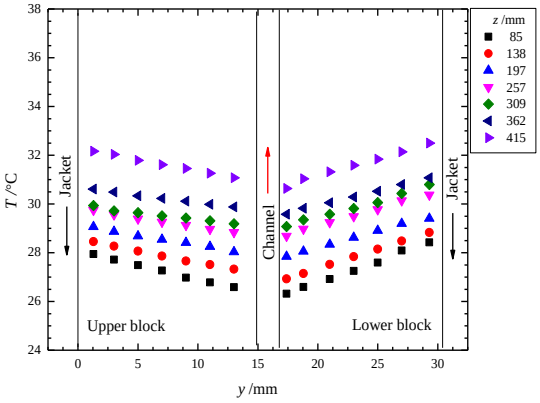

Figure D.37 Temperature distributions inside the block. c = 10 %, $T_{h,in}$ = 40 °C, $T_{f,in}$ = 22 °C, $m_{h,in}$ = 24 g/s, $m_{f,in}$ = 11.5 g/s

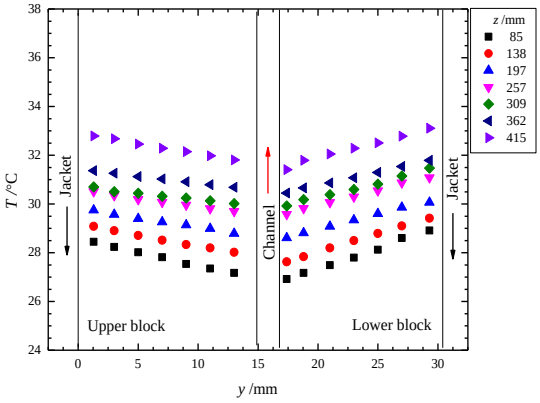

Figure D.38 Temperature distributions inside the block. c = 10 %, $T_{h,in}$ = 40 °C, $T_{f,in}$ = 22 °C, $m_{h,in}$ = 24 g/s, $m_{f,in}$ = 9.9 g/s

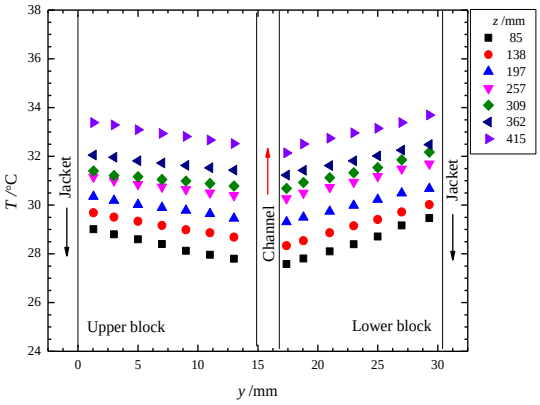

Figure D.39 Temperature distributions inside the block. c = 10 %, $T_{h,in}$ = 40 °C, $T_{f,in}$ = 22 °C, $m_{h,in}$ = 24 g/s, $m_{f,in}$ = 8.2 g/s

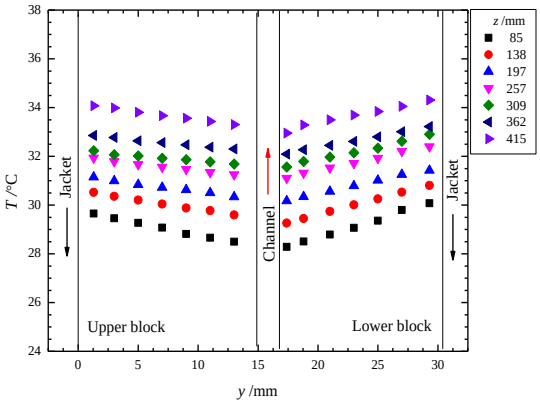

Figure D.40 Temperature distributions inside the block. c = 10 %, $T_{h,in}$ = 40 °C, $T_{f,in}$ = 22 °C, $m_{h,in}$ = 24 g/s, $m_{f,in}$ = 6.6 g/s

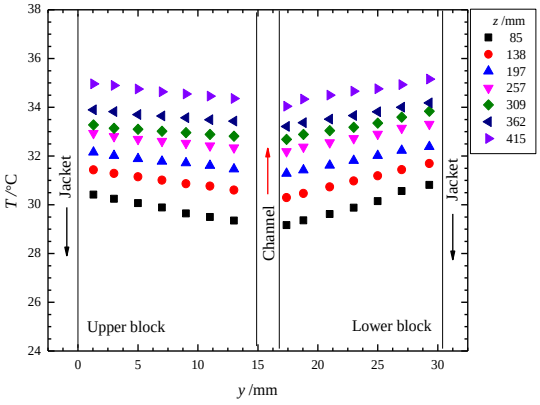

Figure D.41 Temperature distributions inside the block. c = 10 %, $T_{h,in}$ = 40 °C, $T_{f,in}$ = 22 °C, $m_{h,in}$ = 24 g/s, $m_{f,in}$ = 4.9 g/s

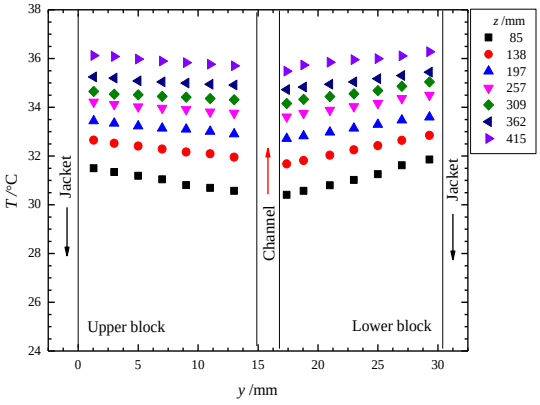

Figure D.42 Temperature distributions inside the block. c = 10 %, $T_{h,in}$ = 40 °C, $T_{f,in}$ = 22 °C, $m_{h,in}$ = 24 g/s, $m_{f,in}$ = 3.3 g/s

D.9 Temperature profiles for Run No. s10-25 to Run No. s10-30

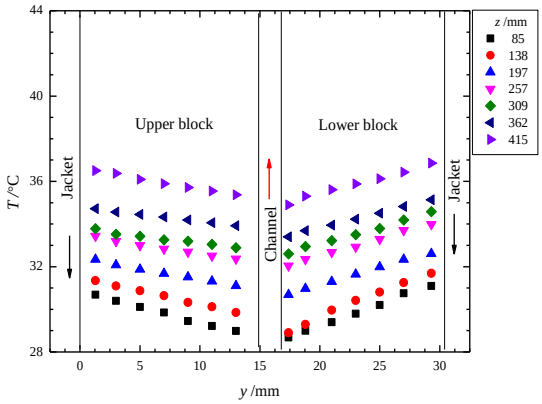

Figure D.43 Temperature distributions inside the block. c = 10 %, $T_{h,in}$ = 45 °C, $T_{f,in}$ = 22 °C, $m_{h,in}$ = 24 g/s, $m_{f,in}$ = 11.5 g/s

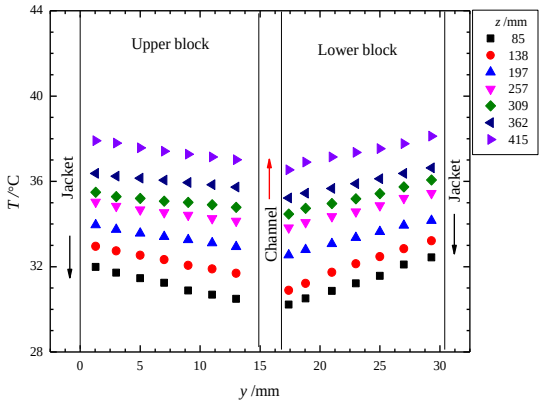

Figure D.44 Temperature distributions inside the block. c = 10 %, $T_{h,in}$ = 45 °C, $T_{f,in}$ = 22 °C, $m_{h,in}$ = 24 g/s, $m_{f,in}$ = 9.9 g/s

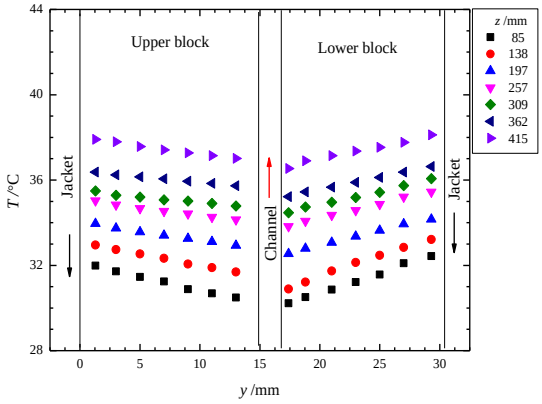

Figure D.45 Temperature distributions inside the block. c = 10 %, $T_{h,in}$ = 45 °C, $T_{f,in}$ = 22 °C, $m_{h,in}$ = 24 g/s, $m_{f,in}$ = 8.2 g/s

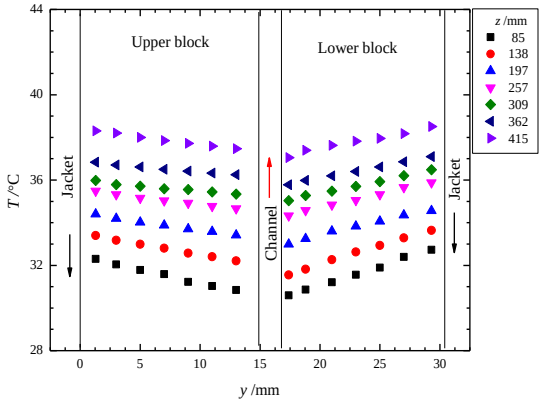

Figure D.46 Temperature distributions inside the block. c = 10 %, $T_{h,in}$ = 45 °C, $T_{f,in}$ = 22 °C, $m_{h,in}$ = 24 g/s, $m_{f,in}$ = 6.6 g/s

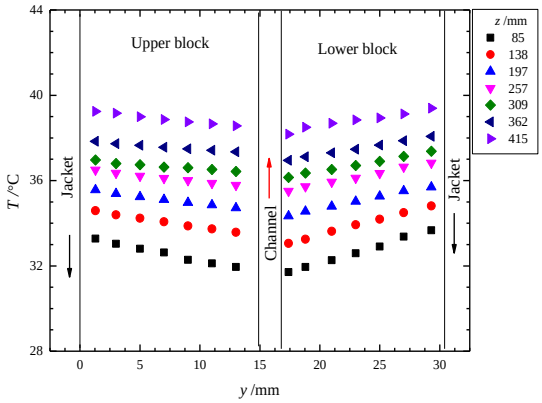

Figure D.47 Temperature distributions inside the block. c = 10 %, $T_{h,in}$ = 45 °C, $T_{f,in}$ = 22 °C, $m_{h,in}$ = 24 g/s, $m_{f,in}$ = 4.9 g/s

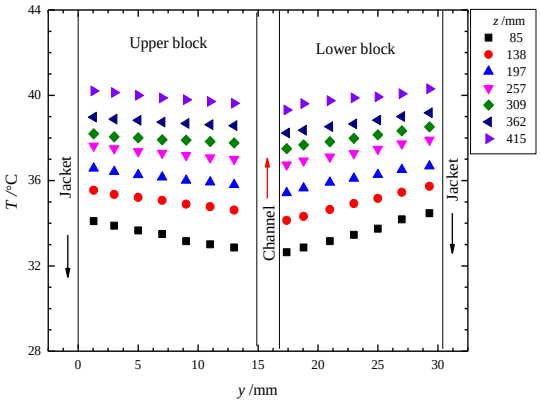

Figure D.48 Temperature distributions inside the block. c = 10 %, $T_{h,in}$ = 45 °C, $T_{f,in}$ = 22 °C, $m_{h,in}$ = 24 g/s, $m_{f,in}$ = 3.3 g/s

D.10 Temperature profiles for Run No. s10-31 to Run No. s10-36

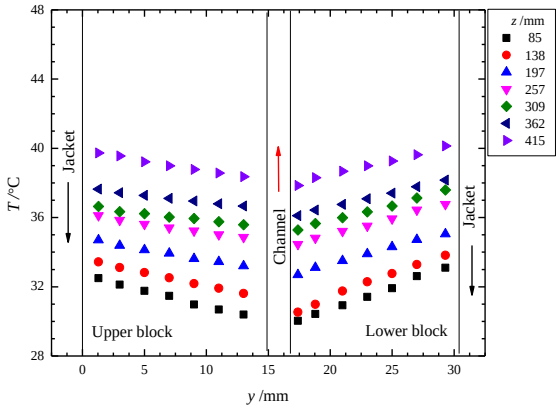

Figure D.49 Temperature distributions inside the block. c = 10 %, $T_{h,in}$ = 50 °C, $T_{f,in}$ = 22 °C, $m_{h,in}$ = 24 g/s, $m_{f,in}$ = 11.5 g/s

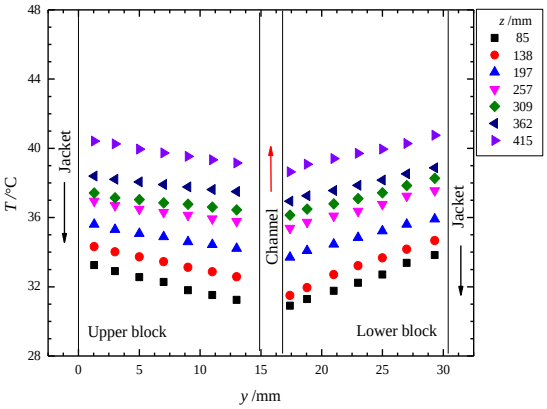

Figure D.50 Temperature distributions inside the block. c = 10 %, $T_{h,in}$ = 50 °C, $T_{f,in}$ = 22 °C, $m_{h,in}$ = 24 g/s, $m_{f,in}$ = 9.9 g/s

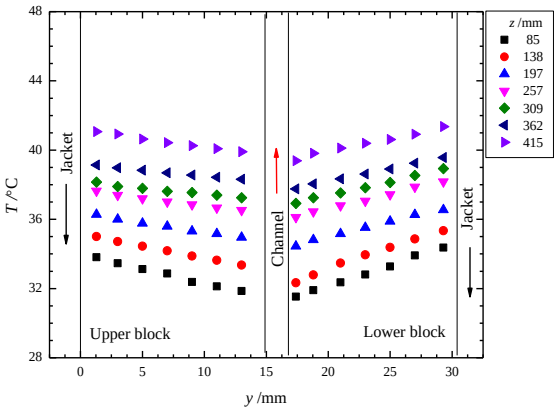

Figure D.51 Temperature distributions inside the block. c = 10 %, $T_{h,in}$ = 50 °C, $T_{f,in}$ = 22 °C, $m_{h,in}$ = 24 g/s, $m_{f,in}$ = 8.2 g/s

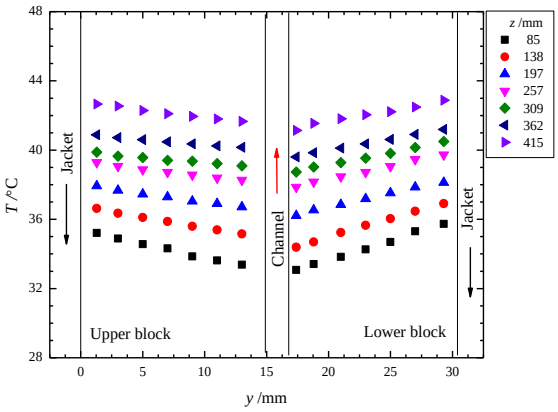

Figure D.52 Temperature distributions inside the block. c = 10 %, $T_{h,in}$ = 50 °C, $T_{f,in}$ = 22 °C, $m_{h,in}$ = 24 g/s, $m_{f,in}$ = 6.6 g/s

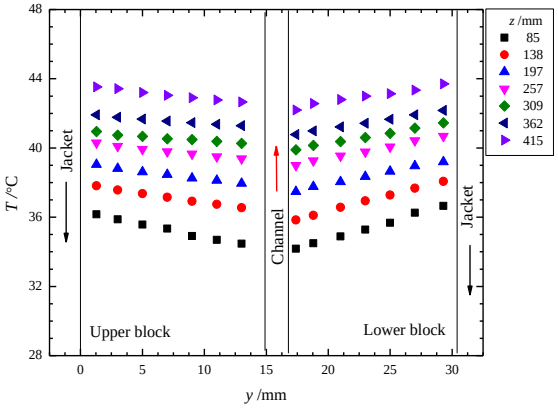

Figure D.53 Temperature distributions inside the block. c = 10 %, $T_{h,in}$ = 50 °C, $T_{f,in}$ = 22 °C, $m_{h,in}$ = 24 g/s, $m_{f,in}$ = 4.9 g/s

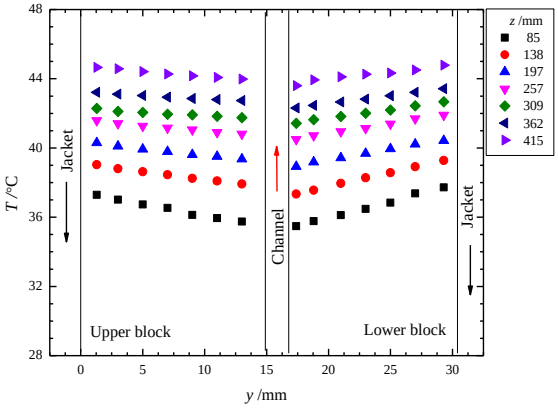

Figure D.54 Temperature distributions inside the block. c = 10 %, $T_{h,in}$ = 50 °C, $T_{f,in}$ = 22 °C, $m_{h,in}$ = 24 g/s, $m_{f,in}$ = 3.3 g/s

D.11 Temperature profiles for Run No. w-1a to Run No. w-8a

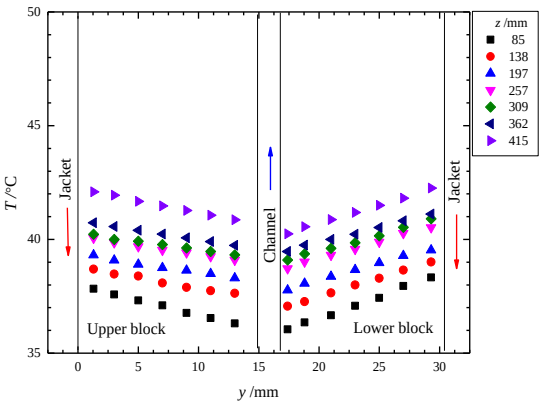

Figure D.55 Temperature distributions inside the test block. c = 0 %, $T_{h,in}$ = 50 °C, $T_{f,in}$ = 30 °C, $m_{h,in}$ = 24 g/s, $m_{f,in}$ = 10.7 g/s

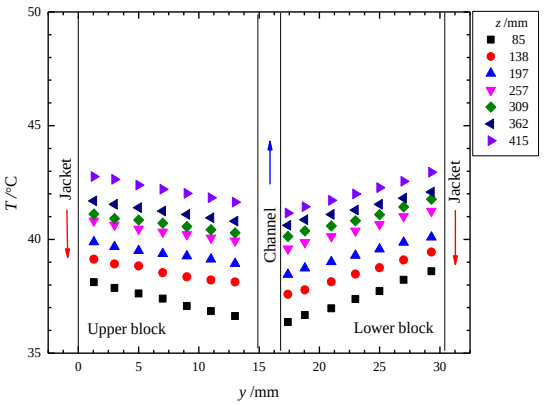

Figure D.56 Temperature distributions inside the test block. c = 0 %, $T_{h,in}$ = 50 °C, $T_{f,in}$ = 30 °C, $m_{h,in}$ = 24 g/s, $m_{f,in}$ = 9.9 g/s

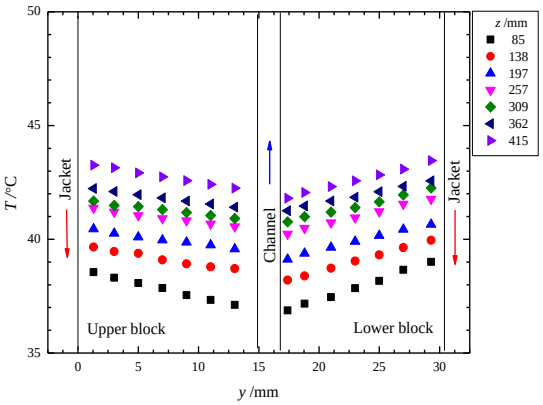

Figure D.57 Temperature distributions inside the test block. c = 0 %, $T_{h,in}$ = 50 °C, $T_{f,in}$ = 30 °C, $m_{h,in}$ = 24 g/s, $m_{f,in}$ = 9.0 g/s

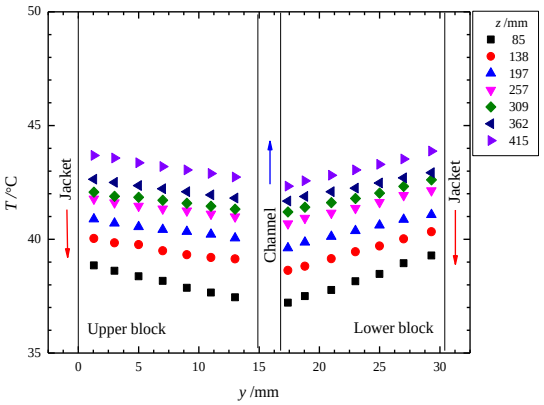

Figure D.58 Temperature distributions inside the test block. c = 0 %, $T_{h,in}$ = 50 °C, $T_{f,in}$ = 30 °C, $m_{h,in}$ = 24 g/s, $m_{f,in}$ = 8.2 g/s

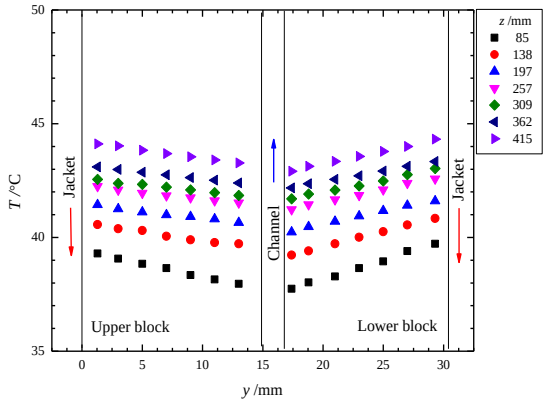

Figure D.59 Temperature distributions inside the test block. c = 0 %, $T_{h,in}$ = 50 °C, $T_{f,in}$ = 30 °C, $m_{h,in}$ = 24 g/s, $m_{f,in}$ = 7.4 g/s

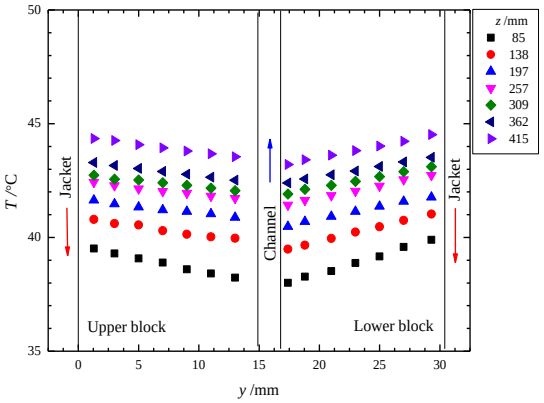

Figure D.60 Temperature distributions inside the test block. c = 0 %, $T_{h,in}$ = 50 °C, $T_{f,in}$ = 30 °C, $m_{h,in}$ = 24 g/s, $m_{f,in}$ = 6.6 g/s

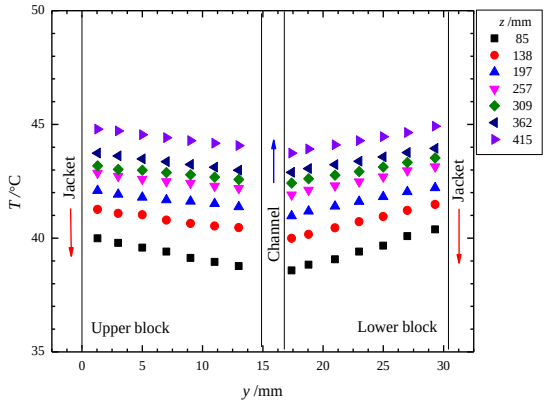

Figure D.61 Temperature distributions inside the test block. c = 0 %, $T_{h,in}$ = 50 °C, $T_{f,in}$ = 30 °C, $m_{h,in}$ = 24 g/s, $m_{f,in}$ = 5.8 g/s

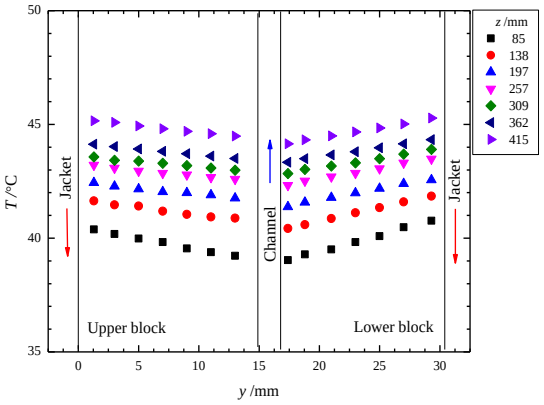

Figure D.62 Temperature distributions inside the test block. c = 0 %, $T_{h,in}$ = 50 °C, $T_{f,in}$ = 30 °C, $m_{h,in}$ = 24 g/s, $m_{f,in}$ = 4.9 g/s

D.12 Temperature profiles for Run No. w-9a to Run No. w-17a

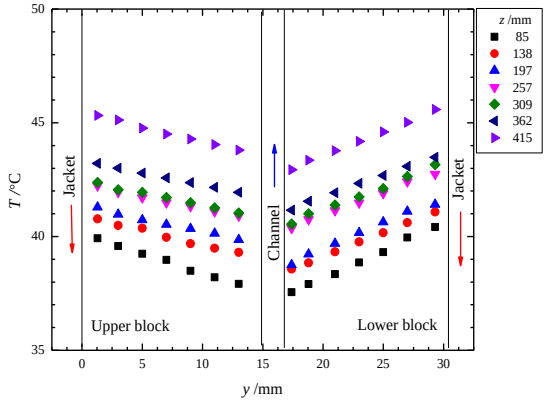

Figure D.63 Temperature distributions inside the test block. c = 0 %, $T_{h,in}$ = 55 °C, $T_{f,in}$ = 30 °C, $m_{h,in}$ = 24 g/s, $m_{f,in}$ = 10.7 g/s

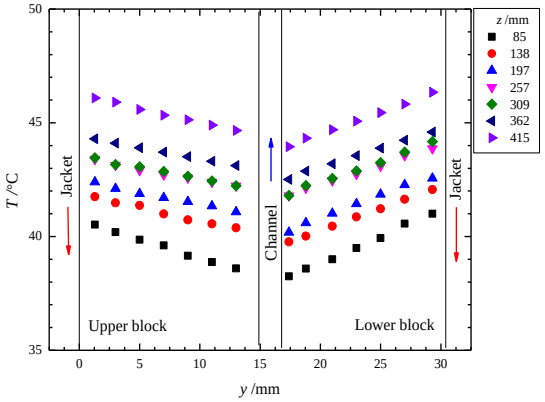

Figure D.64 Temperature distributions inside the test block. c = 0 %, $T_{h,in}$ = 55 °C, $T_{f,in}$ = 30 °C, $m_{h,in}$ = 24 g/s, $m_{f,in}$ = 9.9 g/s

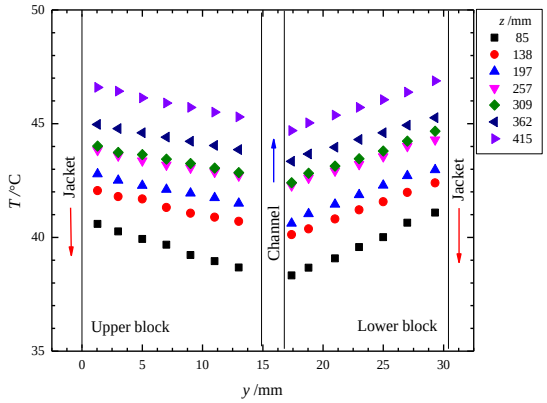

Figure D.65 Temperature distributions inside the test block. c = 0 %, $T_{h,in}$ = 55 °C, $T_{f,in}$ = 30 °C, $m_{h,in}$ = 24 g/s, $m_{f,in}$ = 9.0 g/s

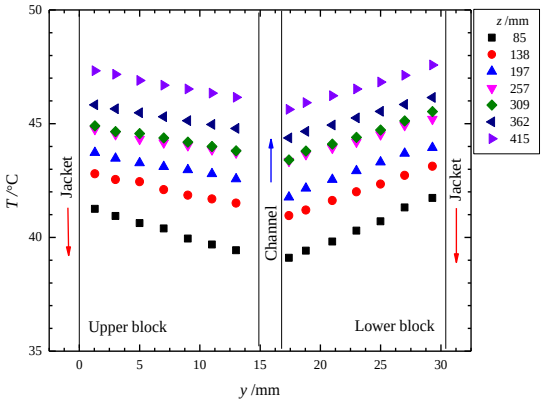

Figure D.66 Temperature distributions inside the test block. c = 0 %, $T_{h,in}$ = 55 °C, $T_{f,in}$ = 30 °C, $m_{h,in}$ = 24 g/s, $m_{f,in}$ = 8.2 g/s

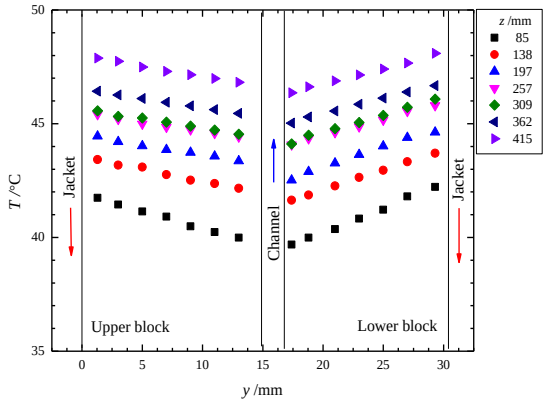

Figure D.67 Temperature distributions inside the test block. c = 0 %, $T_{h,in}$ = 55 °C, $T_{f,in}$ = 30 °C, $m_{h,in}$ = 24 g/s, $m_{f,in}$ = 7.4 g/s

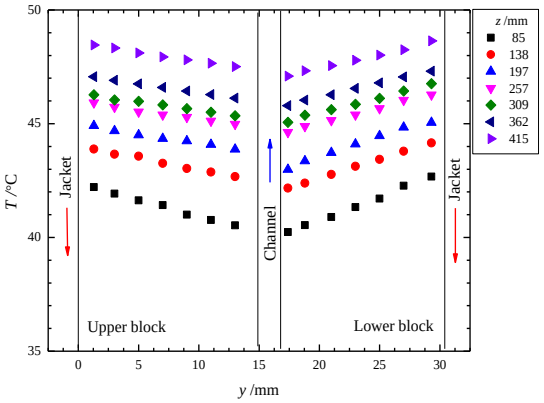

Figure D.68 Temperature distributions inside the test block. c = 0 %, $T_{h,in}$ = 55 °C, $T_{f,in}$ = 30 °C, $m_{h,in}$ = 24 g/s, $m_{f,in}$ = 6.6 g/s

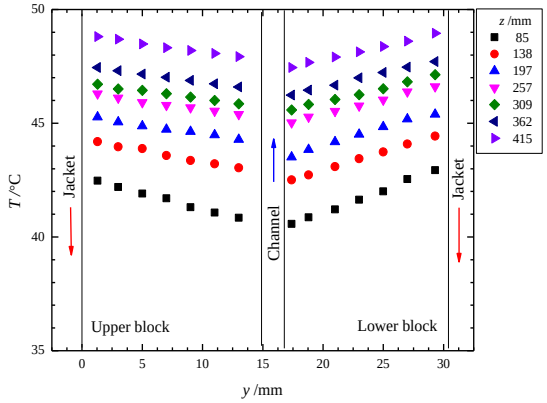

Figure D.69 Temperature distributions inside the test block. c = 0 %, $T_{h,in}$ = 55 °C, $T_{f,in}$ = 30 °C, $m_{h,in}$ = 24 g/s, $m_{f,in}$ = 5.8 g/s

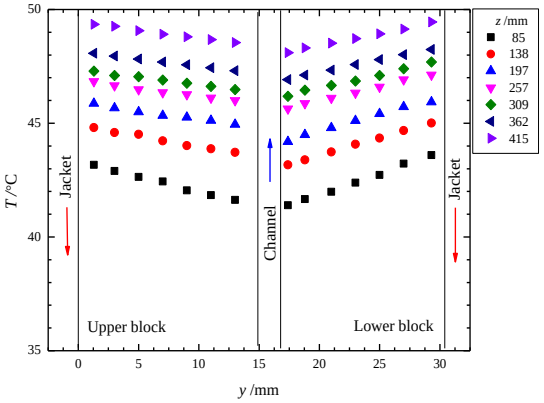

Figure D.70 Temperature distributions inside the test block. c = 0 %, $T_{h,in}$ = 55 °C, $T_{f,in}$ = 30 °C, $m_{h,in}$ = 24 g/s, $m_{f,in}$ = 4.9 g/s

D.13 Temperature profiles for Run No. w-18a to Run No. w-25a

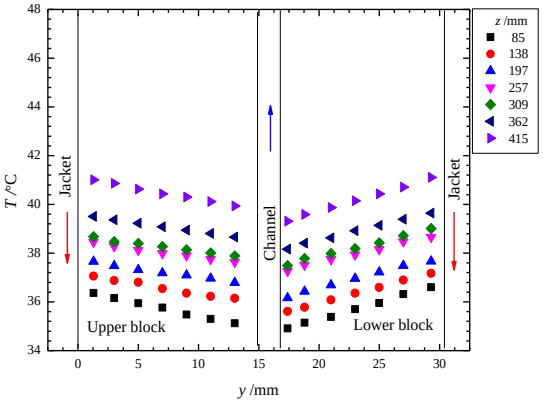

Figure D.71 Temperature distributions inside the test block. c = 0 %, $T_{h,in}$ = 50 °C, $T_{f,in}$ = 30 °C, $m_{h,in}$ = 17 g/s, $m_{f,in}$ = 10.7 g/s

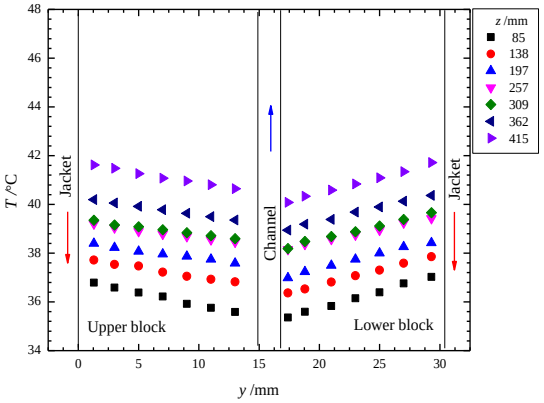

Figure D.72 Temperature distributions inside the test block. c = 0 %, $T_{h,in}$ = 50 °C, $T_{f,in}$ = 30 °C, $m_{h,in}$ = 17 g/s, $m_{f,in}$ = 9.9 g/s

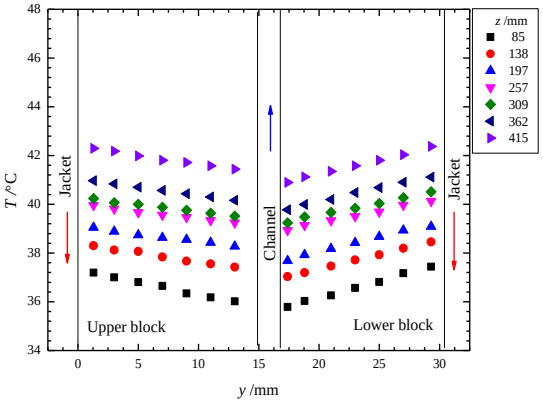

Figure D.73 Temperature distributions inside the test block. c = 0 %, $T_{h,in}$ = 50 °C, $T_{f,in}$ = 30 °C, $m_{h,in}$ = 17 g/s, $m_{f,in}$ = 9.0 g/s

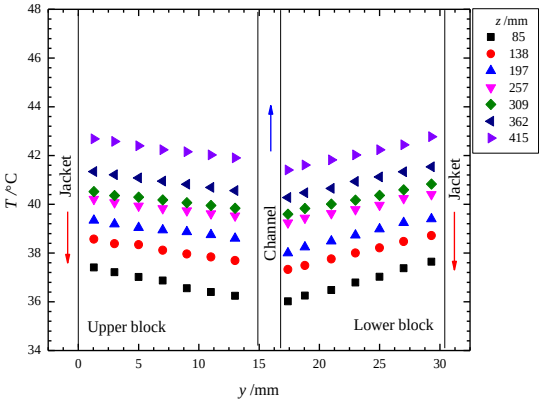

Figure D.74 Temperature distributions inside the test block. c = 0 %, $T_{h,in}$ = 50 °C, $T_{f,in}$ = 30 °C, $m_{h,in}$ = 17 g/s, $m_{f,in}$ = 8.2 g/s

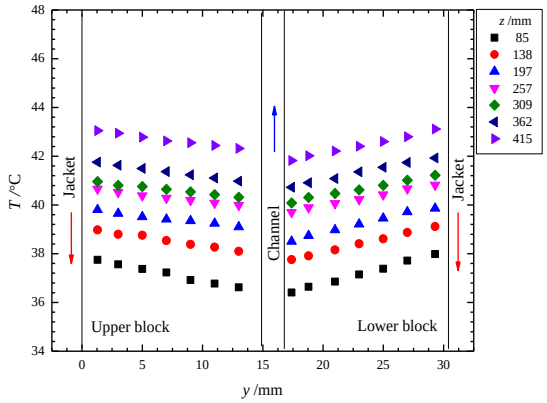

Figure D.75 Temperature distributions inside the test block. c = 0 %, $T_{h,in}$ = 50 °C, $T_{f,in}$ = 30 °C, $m_{h,in}$ = 17 g/s, $m_{f,in}$ = 7.4 g/s

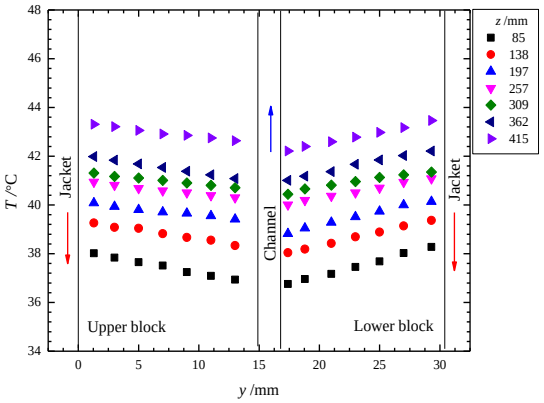

Figure D.76 Temperature distributions inside the test block. c = 0 %, $T_{h,in}$ = 50 °C, $T_{f,in}$ = 30 °C, $m_{h,in}$ = 17 g/s, $m_{f,in}$ = 6.6 g/s

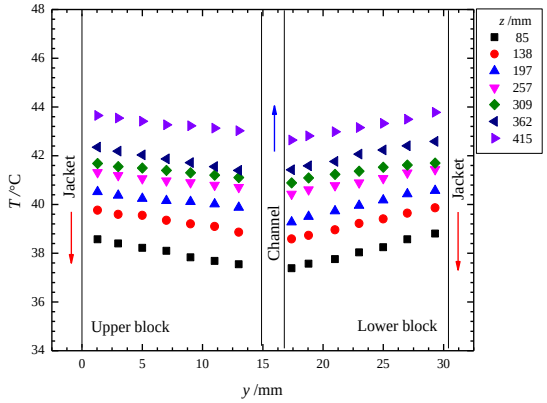

Figure D.77 Temperature distributions inside the test block. c = 0 %, $T_{h,in}$ = 50 °C, $T_{f,in}$ = 30 °C, $m_{h,in}$ = 17 g/s, $m_{f,in}$ = 5.8 g/s

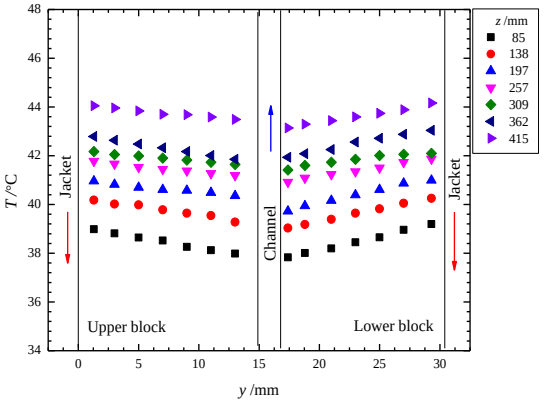

Figure D.78 Temperature distributions inside the test block. c = 0 %, $T_{h,in}$ = 50 °C, $T_{f,in}$ = 30 °C, $m_{h,in}$ = 17 g/s, $m_{f,in}$ = 4.9 g/s

D.14 Temperature profiles for Run No. w-26a to Run No. w-33a

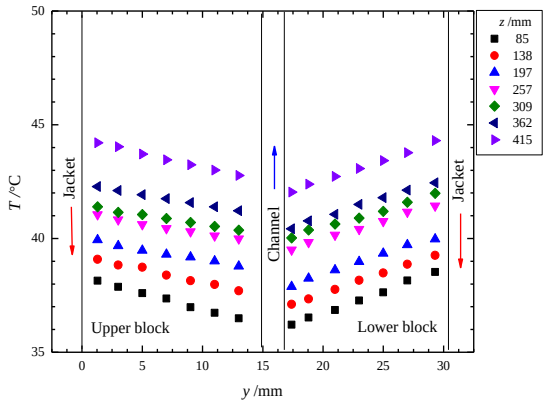

Figure D.79 Temperature distributions inside the test block. c = 0 %, $T_{h,in}$ = 55 °C, $T_{f,in}$ = 30 °C, $m_{h,in}$ = 17 g/s, $m_{f,in}$ = 10.7 g/s

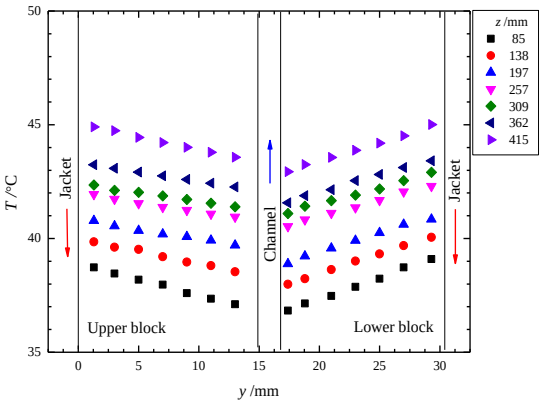

Figure D.80 Temperature distributions inside the test block. c = 0 %, $T_{h,in}$ = 55 °C, $T_{f,in}$ = 30 °C, $m_{h,in}$ = 17 g/s, $m_{f,in}$ = 9.9 g/s

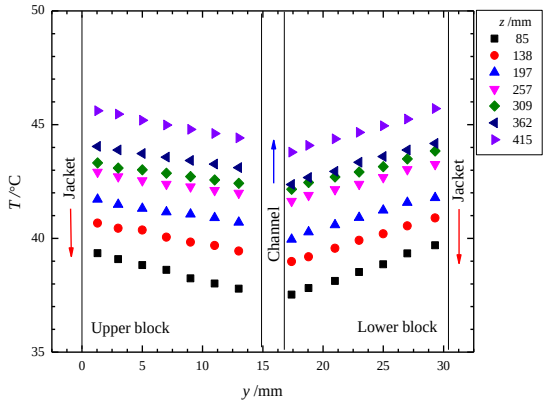

Figure D.81 Temperature distributions inside the test block. c = 0 %, $T_{h,in}$ = 55 °C, $T_{f,in}$ = 30 °C, $m_{h,in}$ = 17 g/s, $m_{f,in}$ = 9.0 g/s

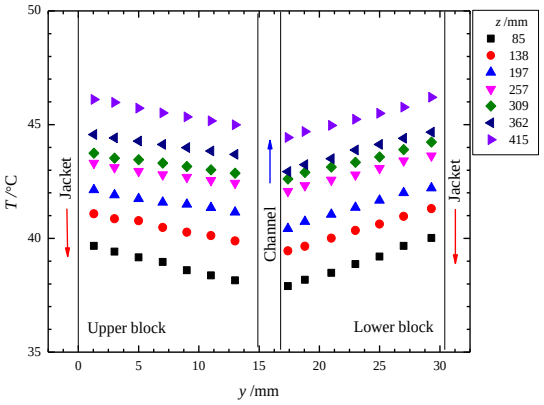

Figure D.82 Temperature distributions inside the test block. c = 0 %, $T_{h,in}$ = 55 °C, $T_{f,in}$ = 30 °C, $m_{h,in}$ = 17 g/s, $m_{f,in}$ = 8.2 g/s

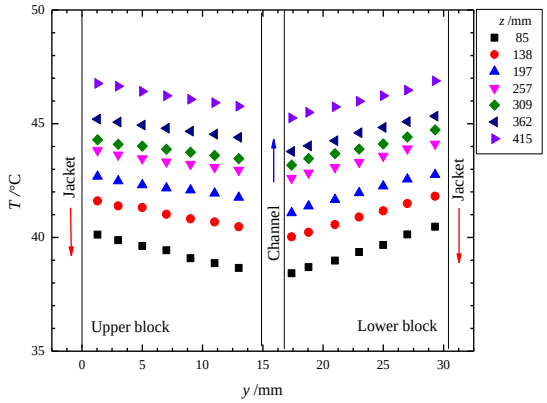

Figure D.83 Temperature distributions inside the test block. c = 0 %, $T_{h,in}$ = 55 °C, $T_{f,in}$ = 30 °C, $m_{h,in}$ = 17 g/s, $m_{f,in}$ = 7.4 g/s

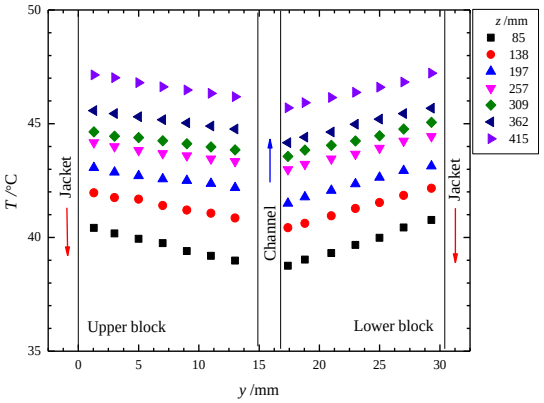

Figure D.84 Temperature distributions inside the test block. c = 0 %, $T_{h,in}$ = 55 °C, $T_{f,in}$ = 30 °C, $m_{h,in}$ = 17 g/s, $m_{f,in}$ = 6.6 g/s

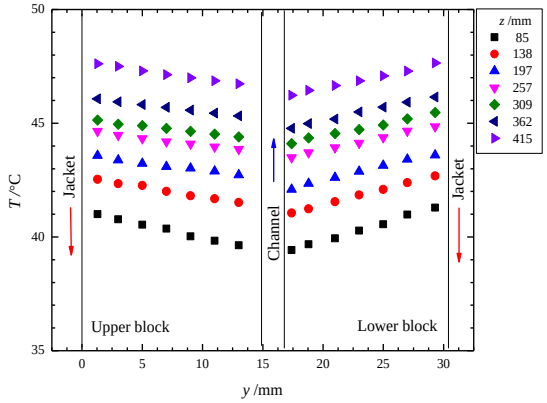

Figure D.85 Temperature distributions inside the test block. c = 0 %, $T_{h,in}$ = 55 °C, $T_{f,in}$ = 30 °C, $m_{h,in}$ = 17 g/s, $m_{f,in}$ = 5.8 g/s

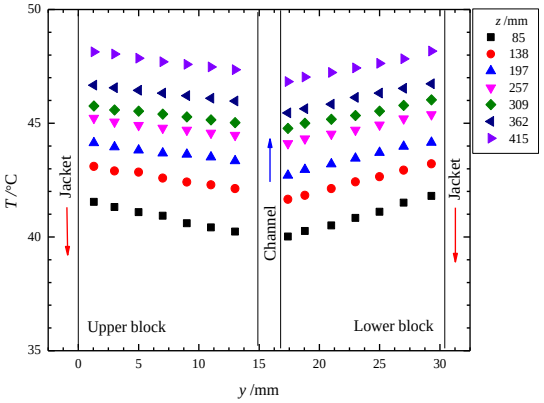

Figure D.86 Temperature distributions inside the test block. c = 0 %, $T_{h,in}$ = 55 °C, $T_{f,in}$ = 30 °C, $m_{h,in}$ = 17 g/s, $m_{f,in}$ = 4.9 g/s

D.15 Temperature profiles for Run No. w-34a to Run No. w-41a

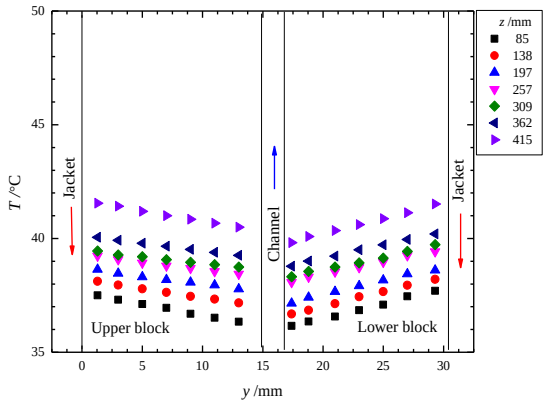

Figure D.87 Temperature distributions inside the test block. c = 0 %, $T_{h,in}$ = 50 °C, $T_{f,in}$ = 32 °C, $m_{h,in}$ = 17 g/s, $m_{f,in}$ = 10.7 g/s

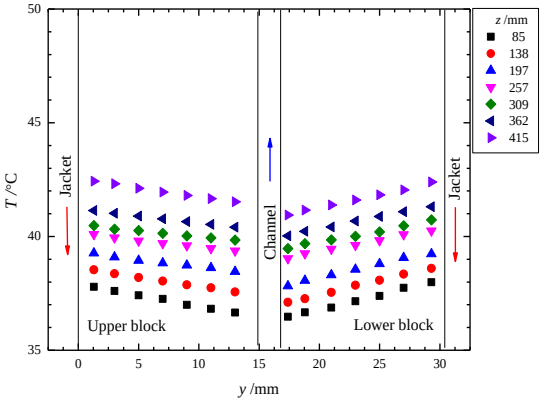

Figure D.88 Temperature distributions inside the test block. c = 0 %, $T_{h,in}$ = 50 °C, $T_{f,in}$ = 32 °C, $m_{h,in}$ = 17 g/s, $m_{f,in}$ = 9.9 g/s

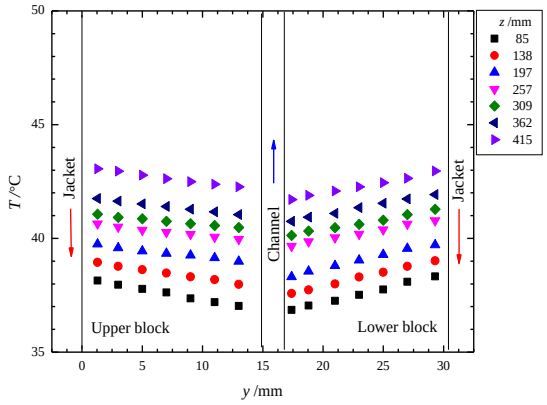

Figure D.89 Temperature distributions inside the test block. c = 0 %, $T_{h,in}$ = 50 °C, $T_{f,in}$ = 32 °C, $m_{h,in}$ = 17 g/s, $m_{f,in}$ = 9.0 g/s

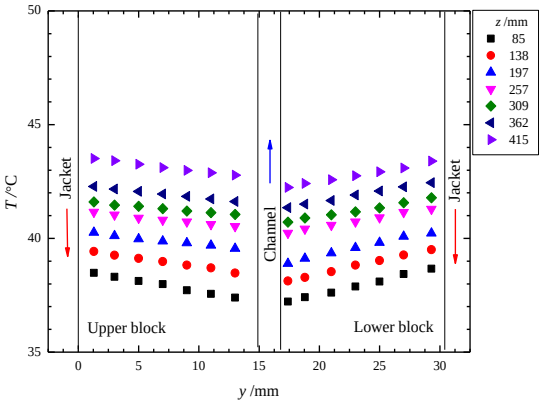

Figure D.90 Temperature distributions inside the test block. c = 0 %, $T_{h,in}$ = 50 °C, $T_{f,in}$ = 32 °C, $m_{h,in}$ = 17 g/s, $m_{f,in}$ = 8.2 g/s

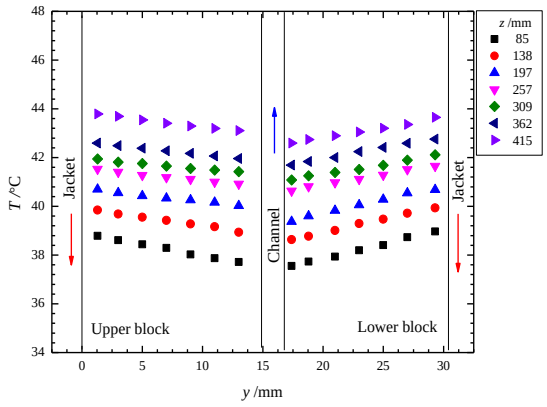

Figure D.91 Temperature distributions inside the test block. c = 0 %, $T_{h,in}$ = 50 °C, $T_{f,in}$ = 32 °C, $m_{h,in}$ = 17 g/s, $m_{f,in}$ = 7.4 g/s

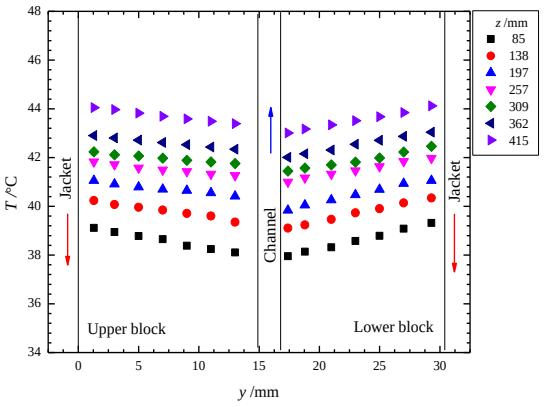

Figure D.92 Temperature distributions inside the test block. c = 0 %, $T_{h,in}$ = 50 °C, $T_{f,in}$ = 32 °C, $m_{h,in}$ = 17 g/s, $m_{f,in}$ = 6.6 g/s

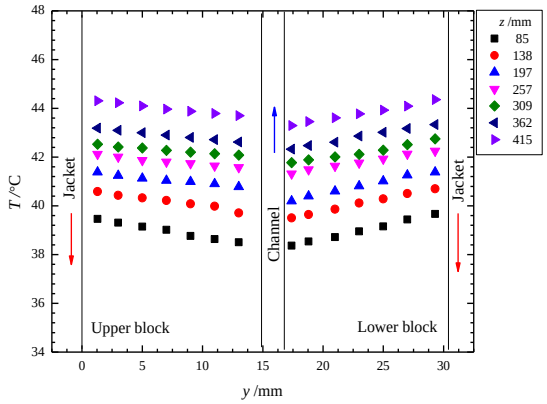

Figure D.93 Temperature distributions inside the test block. c = 0 %, $T_{h,in}$ = 50 °C, $T_{f,in}$ = 32 °C, $m_{h,in}$ = 17 g/s, $m_{f,in}$ = 5.8 g/s

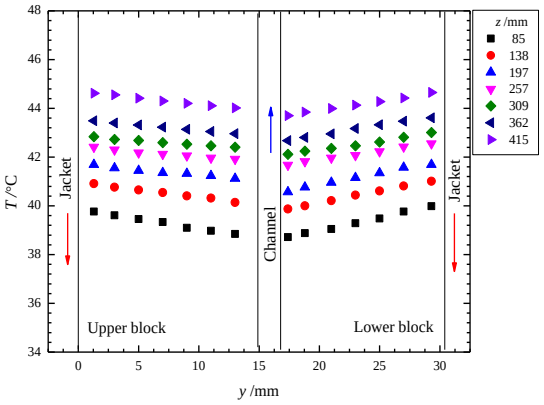

Figure D.94 Temperature distributions inside the test block. c = 0 %, $T_{h,in}$ = 50 °C, $T_{f,in}$ = 32 °C, $m_{h,in}$ = 17 g/s, $m_{f,in}$ = 4.9 g/s

D.16 Temperature profiles for Run No. w-42a to Run No. w-49a

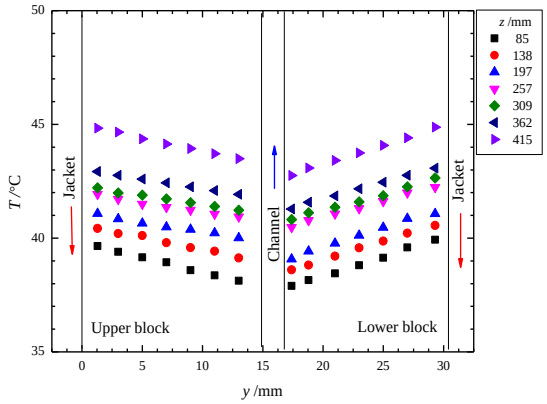

Figure D.95 Temperature distributions inside the test block. c = 0 %, $T_{h,in}$ = 55 °C, $T_{f,in}$ = 32 °C, $m_{h,in}$ = 17 g/s, $m_{f,in}$ = 10.7 g/s

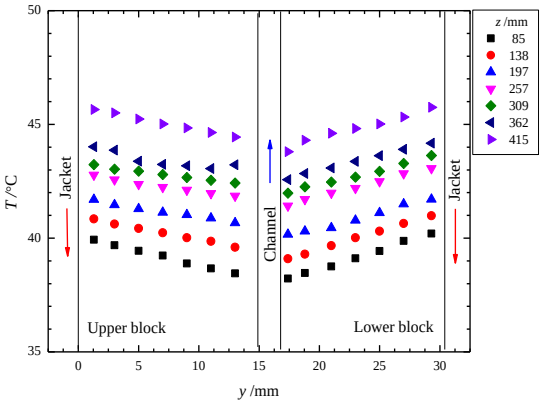

Figure D.96 Temperature distributions inside the test block. c = 0 %, $T_{h,in}$ = 55 °C, $T_{f,in}$ = 32 °C, $m_{h,in}$ = 17 g/s, $m_{f,in}$ = 9.9 g/s

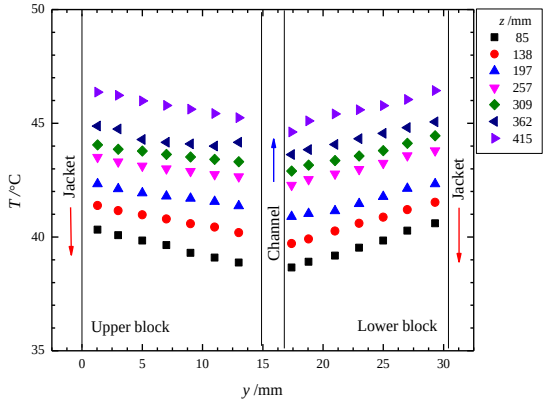

Figure D.97 Temperature distributions inside the test block. c = 0 %, $T_{h,in}$ = 55 °C, $T_{f,in}$ = 32 °C, $m_{h,in}$ = 17 g/s, $m_{f,in}$ = 9.0 g/s

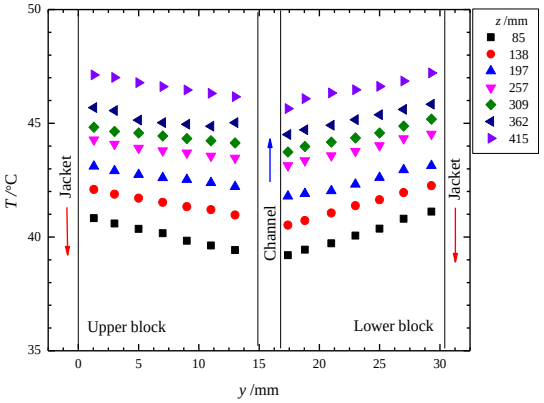

Figure D.98 Temperature distributions inside the test block. c = 0 %, $T_{h,in}$ = 55 °C, $T_{f,in}$ = 32 °C, $m_{h,in}$ = 17 g/s, $m_{f,in}$ = 8.2 g/s

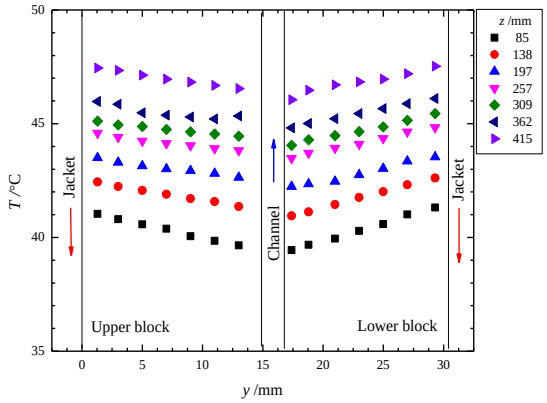

Figure D.99 Temperature distributions inside the test block. c = 0 %, $T_{h,in}$ = 55 °C, $T_{f,in}$ = 32 °C, $m_{h,in}$ = 17 g/s, $m_{f,in}$ = 7.4 g/s

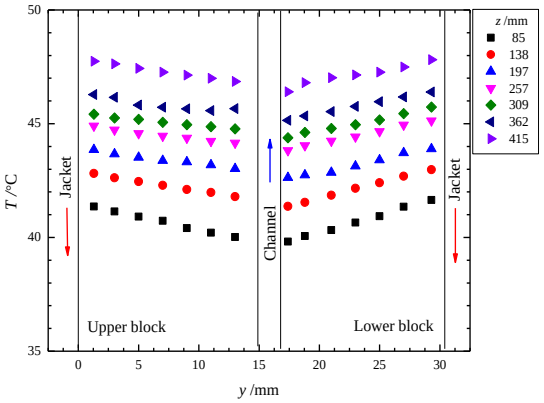

Figure D.100 Temperature distributions inside the test block. c = 0 %, $T_{h,in}$ = 55 °C, $T_{f,in}$ = 32 °C, $m_{h,in}$ = 17 g/s, $m_{f,in}$ = 6.6 g/s

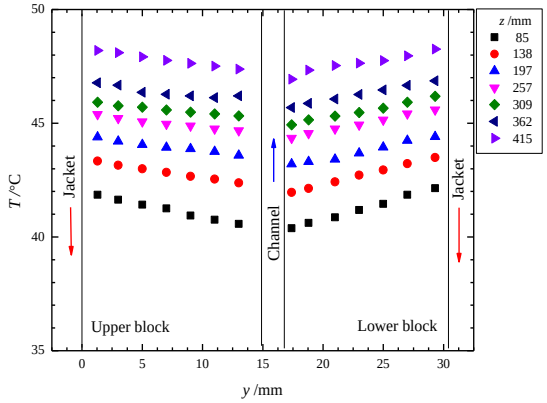

Figure D.101 Temperature distributions inside the test block. c = 0 %, $T_{h,in}$ = 55 °C, $T_{f,in}$ = 32 °C, $m_{h,in}$ = 17 g/s, $m_{f,in}$ = 5.8 g/s

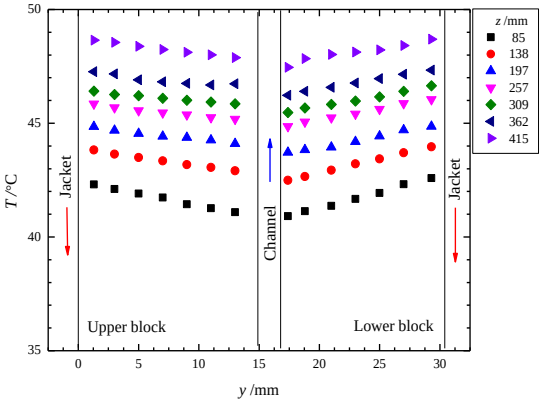

Figure D.102 Temperature distributions inside the test block. c = 0 %, $T_{h,in}$ = 55 °C, $T_{f,in}$ = 32 °C, $m_{h,in}$ = 17 g/s, $m_{f,in}$ = 4.9 g/s

D.17 Temperature profiles for Run No. w-50a to Run No. w-57a

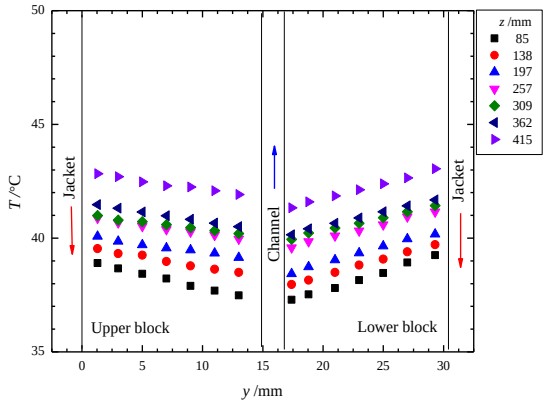

Figure D.103 Temperature distributions inside the test block. c = 0 %, $T_{h,in}$ = 50 °C, $T_{f,in}$ = 32 °C, $m_{h,in}$ = 24 g/s, $m_{f,in}$ = 10.7 g/s

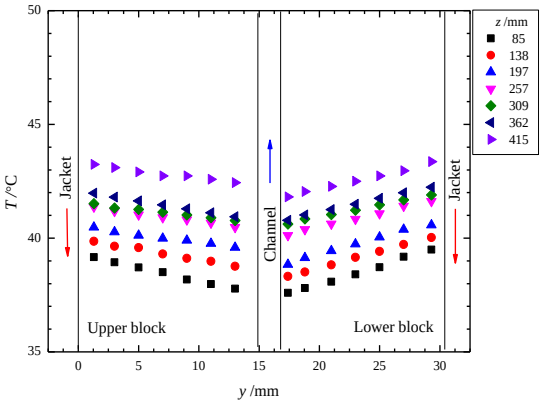

Figure D.104 Temperature distributions inside the test block. c = 0 %, $T_{h,in}$ = 50 °C, $T_{f,in}$ = 32 °C, $m_{h,in}$ = 24 g/s, $m_{f,in}$ = 9.9 g/s

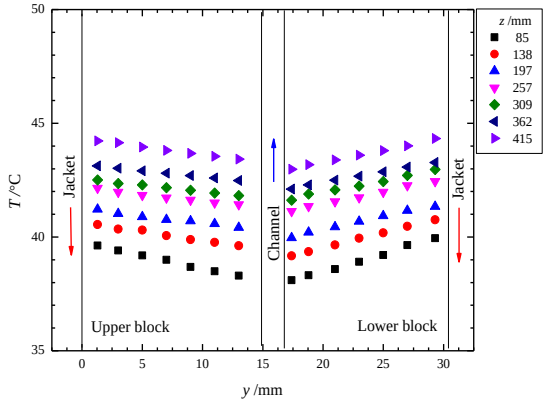

Figure D.105 Temperature distributions inside the test block. c = 0 %, $T_{h,in}$ = 50 °C, $T_{f,in}$ = 32 °C, $m_{h,in}$ = 24 g/s, $m_{f,in}$ = 9.0 g/s

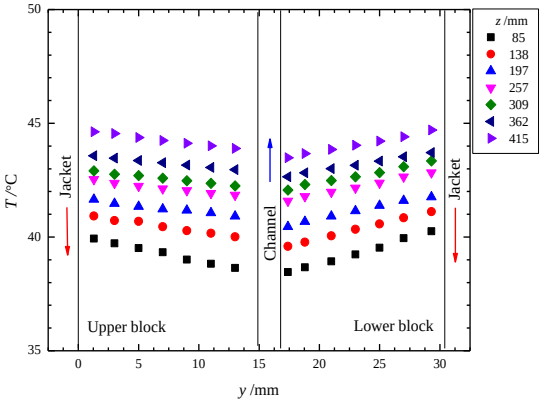

Figure D.106 Temperature distributions inside the test block. c = 0 %, $T_{h,in}$ = 50 °C, $T_{f,in}$ = 32 °C, $m_{h,in}$ = 24 g/s, $m_{f,in}$ = 8.2 g/s

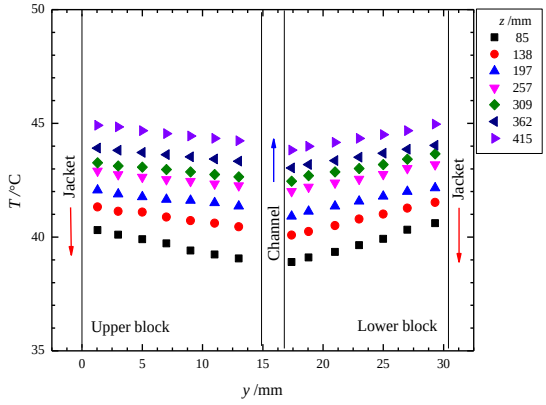

Figure D.107 Temperature distributions inside the test block. c = 0 %, $T_{h,in}$ = 55 °C, $T_{f,in}$ = 32 °C, $m_{h,in}$ = 24 g/s, $m_{f,in}$ = 7.4 g/s

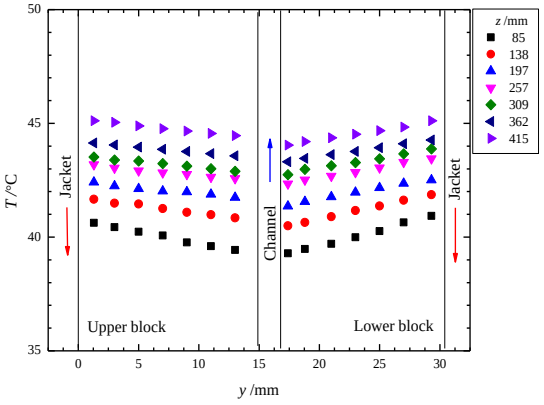

Figure D.108 Temperature distributions inside the test block. c = 0 %, $T_{h,in}$ = 55 °C, $T_{f,in}$ = 32 °C, $m_{h,in}$ = 24 g/s, $m_{f,in}$ = 6.6 g/s

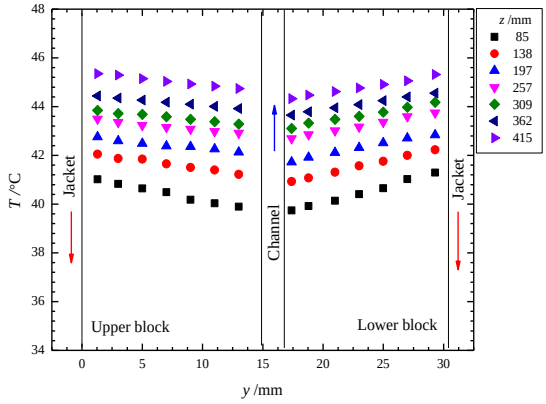

Figure D.109 Temperature distributions inside the test block. c = 0 %, $T_{h,in}$ = 50 °C, $T_{f,in}$ = 32 °C, $m_{h,in}$ = 24 g/s, $m_{f,in}$ = 5.8 g/s

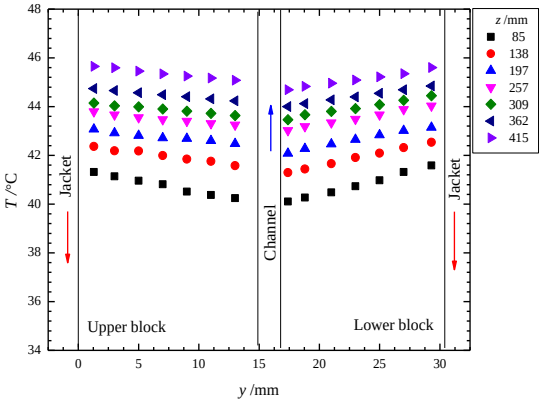

Figure D.110 Temperature distributions inside the test block. c = 0 %, $T_{h,in}$ = 50 °C, $T_{f,in}$ = 32 °C, $m_{h,in}$ = 24 g/s, $m_{f,in}$ = 4.9 g/s

D.18 Temperature profiles for Run No. w-58a to Run No. w-65a

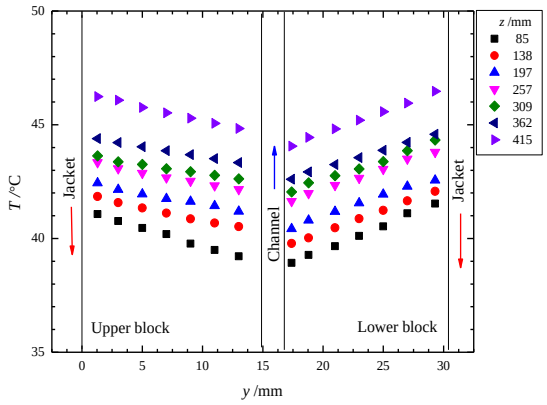

Figure D.111 Temperature distributions inside the test block. c = 0 %, $T_{h,in}$ = 55 °C, $T_{f,in}$ = 32 °C, $m_{h,in}$ = 24 g/s, $m_{f,in}$ = 10.7 g/s

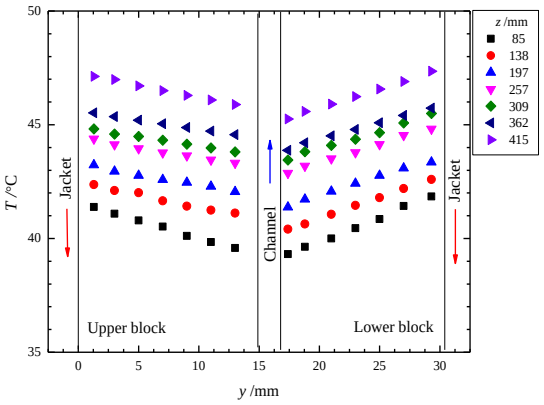

Figure D.112 Temperature distributions inside the test block. c = 0 %, $T_{h,in}$ = 55 °C, $T_{f,in}$ = 32 °C, $m_{h,in}$ = 24 g/s, $m_{f,in}$ = 9.9 g/s

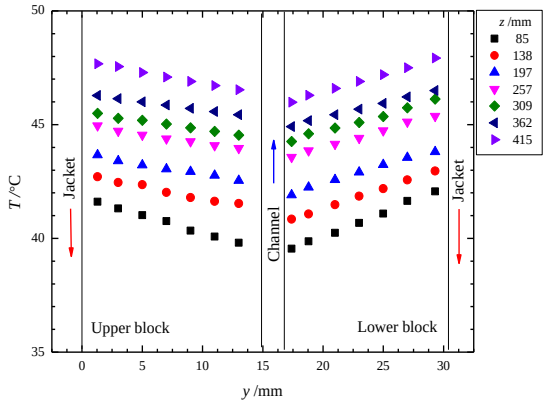

Figure D.113 Temperature distributions inside the test block. c = 0 %, $T_{h,in}$ = 55 °C, $T_{f,in}$ = 32 °C, $m_{h,in}$ = 24 g/s, $m_{f,in}$ = 9.0 g/s

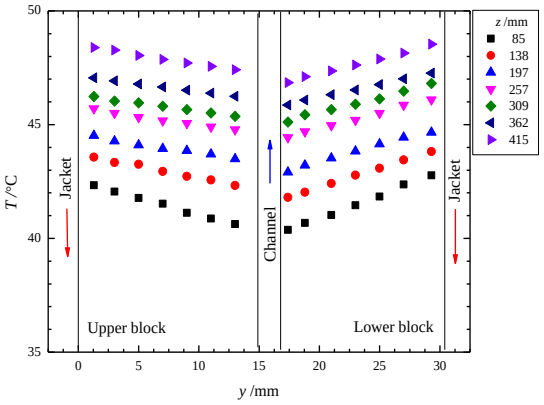

Figure D.114 Temperature distributions inside the test block. c = 0 %, $T_{h,in}$ = 55 °C, $T_{f,in}$ = 32 °C, $m_{h,in}$ = 24 g/s, $m_{f,in}$ = 8.2 g/s

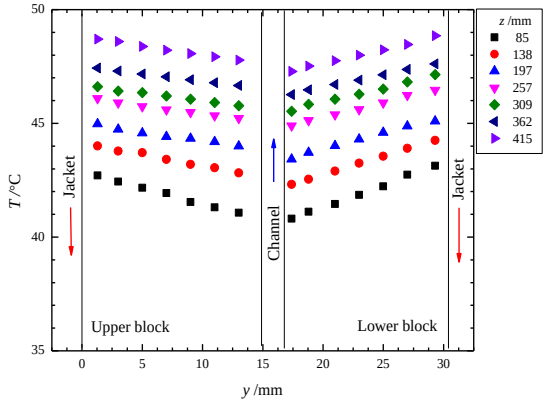

Figure D.115 Temperature distributions inside the test block. c = 0 %, $T_{h,in}$ = 55 °C, $T_{f,in}$ = 32 °C, $m_{h,in}$ = 24 g/s, $m_{f,in}$ = 7.4 g/s

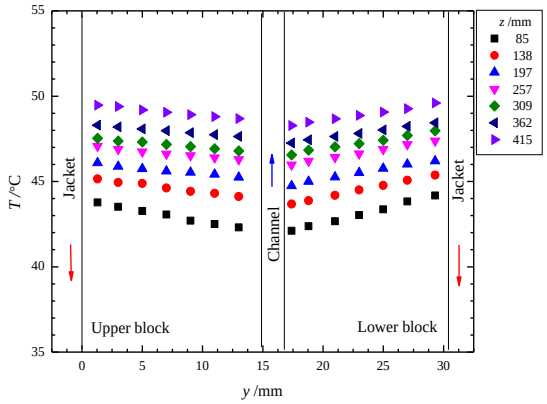

Figure D.116 Temperature distributions inside the test block. c = 0 %, $T_{h,in}$ = 55 °C, $T_{f,in}$ = 32 °C, $m_{h,in}$ = 24 g/s, $m_{f,in}$ = 5.8 g/s

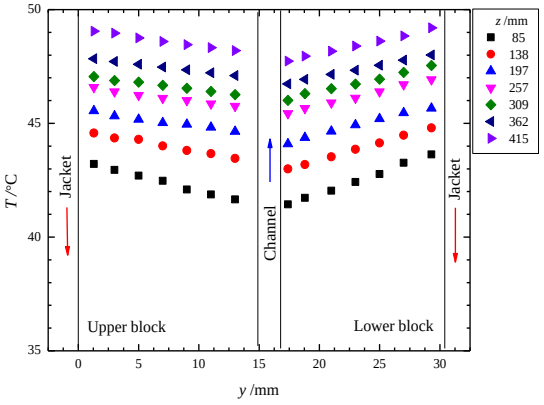

Figure D.117 Temperature distributions inside the test block. c = 0 %, $T_{h,in}$ = 55 °C, $T_{f,in}$ = 32 °C, $m_{h,in}$ = 24 g/s, $m_{f,in}$ = 6.6 g/s

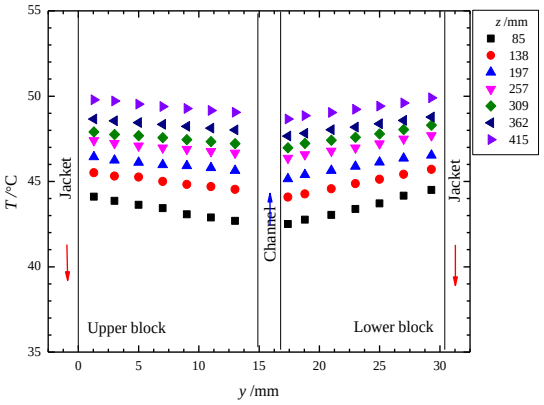

Figure D.118 Temperature distributions inside the test block. c = 0 %, $T_{h,in}$ = 55 °C, $T_{f,in}$ = 32 °C, $m_{h,in}$ = 24 g/s, $m_{f,in}$ = 4.9 g/s

List of Publications

Conference

1. Shaukat, R, Kamran, M.S., Jivani, S.R., Chai, L., Sun, J., Yang, T., and Wang, H.S. Experimental study of Heat Transfer during mPCM Slurry Flow in Microchannels. *Proc. 14th International Conference on Sustainable Energy Technologies*. 25-27 August, 2015. Nottingham, UK.

2. Shaukat, R., Kamran, M.S., Chai, L., Sun, J., and Wang, H.S. Numerical Investigation of Convective Heat Transfer during Microencapsulated Phase Change Slurry Flow in Microchannels. *Proc. International Conference on Sustainable Thermal Energy Management.*7-8 July, 2015. Newcastle Upon Tyne. UK.

Journal

1. Shaukat, R., Kamran, M.S., Jivani, S.R., Chai. L., Sun. J., Yang, T., and Wang. H.S. Numerical Investigation of Convective Heat Transfer during Microencapsulated Phase Change Slurry Flow in Microchannels. *Applied Energy.* 2015, invited submission in a special issue.

2. Shaukat, R., Kamran, M.S., Jivani, S.R., Chai. L., Sun. J., and Wang. H.S. Experimental study on Heat Transfer and Pressure Drop of mPCM Slurry flow in Microchannels. *Applied Thermal Engineering.* To be submitted.

3. Shaukat, R., Kamran, M.S., Jivani, S.R., Chai. L., Sun. J., and Wang. H.S. Experimental and Numerical study on Heat Transfer and Pressure Drop of mPCM Slurry flow in Microchannels. *Applied Thermal Engineering.* To be submitted.